UNIVERSITY OF BIRMINGHAM

# AZOPHOSPHINES: SYNTHESIS, COORDINATION CHEMISTRY AND CATALYSIS

by

EMMA JANE JORDAN-ROSE

A thesis submitted to the University of Birmingham for the degree of

DOCTOR OF PHILOSOPHY

School of Chemistry

College of Engineering and Physical Sciences

University of Birmingham

February 2025

## ABSTRACT

The conceptual replacement of nitrogen with phosphorus in common organic functional groups unlocks new properties and reactivity. Azophosphines, the phosphorus-containing analogues of triazenes, are underexplored but offer great potential as flexible and small bite-angle ligands.

Chapter 1 introduces the concept of phosphorus-analogues of common functional groups and considers the application of azophosphines as novel hybrid ligands.

Chapter 2 explores the synthesis and characterisation of a family of air-stable azophosphine-borane complexes, and their subsequent deprotection to the free azophosphines.

Chapter 3 demonstrates that the azophosphine synthesis can tolerate substituents with strongly electron-donating and electron-withdrawing *para*-Z groups and that the nature of this Z group can affect the spectroscopic and structural properties of the azophosphines. Highlighted is the availability of the phosphorus lone pair for coordination. Azophosphines are shown to be relatively weak phosphine donors, but the donor properties can be fine-tuned within this area of chemical space.

Chapter 4 provides evidence for this by demonstrating that neutral azophosphines can coordinate as ligands to a range of transition metal centres, with a focus on Ru(II) and Au(I) complexes, and can coordinate as monodentate, bidentate or bridging ligands in a controlled manner, in contrast to their nitrogen analogues.

Chapter 5 describes the culmination of the research on azophosphines presented in this thesis in the first use of the Ru- and Au-azophosphine complexes as catalysts in which additive-free transformations were achieved.

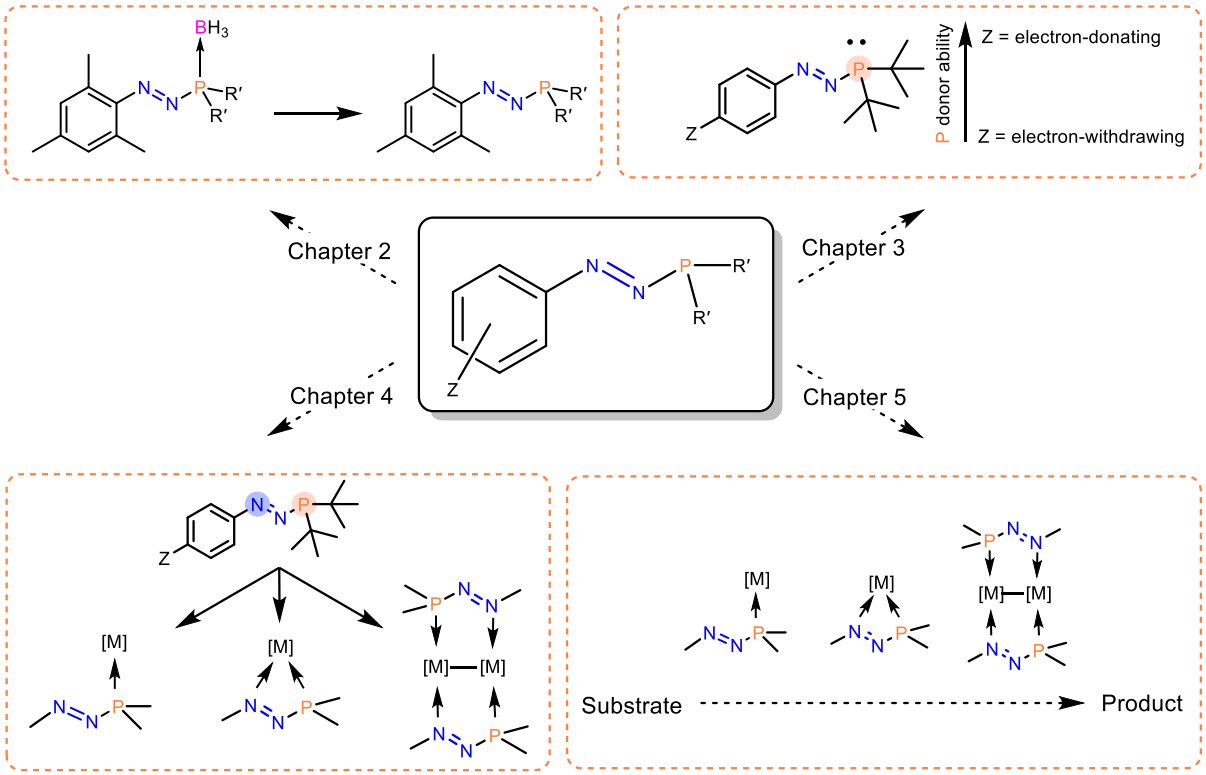

## ACKNOWLEDGEMENTS

Thank you to my supervisor, Dr Andrew Jupp. Such simple words do not seem fitting enough to acknowledge the breadth of support Andy has provided to me as a scientist and researcher, but also as a person. His genuine enthusiasm for chemistry and research can be infectious after discussing the latest lab results whether they are good, bad or unexpected. For his advice on chemistry, the time spent to offer thorough, constructive feedback, and his overall belief in me as a researcher throughout my PhD, I thank Andy enormously.

Next, I'd like to thank the Jupp group. Ethan, a fellow PhD researcher of azophosphines, for contributing the computational insight that was so pertinent to my research. Alastair, who was a pleasure to share time with and was always on hand to offer tech support or for cat chat; Kimberly, for never failing to make me laugh; and Sandro, although we didn't get to spend much time in the group together, his second-to-none humour made the time great fun. Finally, thank you to Laura. I only regret that I didn't spend the duration of my PhD with Laura as a group member. I am immensely grateful for the kindness, help and advice that she has consistently given to me, and for her invaluable feedback in writing this thesis.

Thank you to the members of staff at the University of Birmingham. In particular, the analytical staff for their efforts in creating solutions for data collection that could not otherwise have been obtained from standard walk-up services, Dr Louise Male for her time and patience in training me in single crystal X-ray diffraction, and Dr Cecile Le Duff for the chats and her expertise in NMR spectroscopy.

Lastly, I thank my family for their encouragement and love. Dad, thank you for inspiring me to follow your aspirations no matter what age. Mum, thank you for your endless words of encouragement and for teaching me ‘she thought she could, so she did’. And Phil, my husband and my everything, thank you for being my biggest cheerleader, for believing in me when I didn’t, and for being by my side every step of the way.

## TABLE OF CONTENTS

## LIST OF ABBREVIATIONS

| | |
|---|---|
| A | Anthracene |
| Ar | Aryl |
| ASAP | Atmospheric Solids Analysis Probe |
| BINOP-F | Bis(pentafluorophenyl)-phosphine |
| BQ | Benzoquinone |
| BSD | Bis(trimethylsilyl)diazene |
| Bu | Butyl |
| Cp | Cyclopentadiene |
| Cp* | Pentamethylcyclopentadiene |
| Cy | Cyclohexyl |
| DABCO | 1,4-diazabicyclo[2.2.2]octane |
| DCM | Dichloromethane |
| $D_e$ | Dissociation energy |
| DFT | Density Functional Theory |
| DMAP | 4-Dimethylaminopyridine |
| DMF | Dimethylformamide |
| DMPO | 3,4-dihydro-2,3-dimethyl-2H-pyrrole 1-oxide |
| DMS | Dimethylsulfide |
| EPR | Electron Paramagnetic Resonance |
| ESI | Electrospray Ionisation |
| Et | Ethyl |
| FLP | Frustrated Lewis Pair |
| FTIR | Fourier Transform Infrared |
| GC-MS | Gas Chromatography Mass Spectrometry |
| HH | Head-to-head |
| HT | Head-to-tail |
| HOMO | Highest Occupied Molecular Orbital |
| IPA | Isopropanol |
| $^{i}$Pr | Isopropyl |

| | |
|---|---|
| IR | Infrared |
| LKB | Ligand Knowledge Base |
| LKB-C | Ligand Knowledge Base for carbenes |
| LKB-Bid | Ligand Knowledge Base for bidentate ligands |
| LKB-P | Ligand Knowledge Base for monodentate phosphorus(III) ligands |
| LKB-PP | Ligand Knowledge Base for bidentate *P,P*- and *P,N*-donor ligands |
| LUMO | Lowest Unoccupied Molecular Orbital |
| Mbdp | 1-methylbenzimidazoediphenyl phosphine |
| Me | Methyl |
| MeCN | Acetonitrile |
| Mes | Mesityl |
| Mes* | 2,4,6-$^{t}Bu_3C_6H_2$ |
| Midp | Methylimidazolediphenyl phosphine |
| MLC | Metal Ligand Cooperation |
| NBO | Natural Bond Orbital |
| NMR | Nuclear Magnetic Resonance |
| NPA | Natural Population Analysis |
| OPiv | Pivalate |
| OTf | Triflate |
| $P(Ar^F)_3$ | Fluoroaryl phosphine |
| PCA | Principal Component Analysis |
| Ph | Phenyl |
| Py | Pyridyl |
| RT | Room temperature |
| *sec*-BuLi | *sec*-butyllithium |
| SXRD | Single Crystal X-ray Diffraction |
| TAS | Transient Absorption Spectroscopy |
| TEP | Tolman's Electronic Parameter |
| TOF | Turn Over Frequency |
| TON | Turn Over Number |
| $^{t}Bu$ | *tert*-butyl |

| | |
|---|---|
| THF | Tetrahydrofuran |
| TLC | Thin Layer Chromatography |
| UV/Vis. | Ultraviolet/Visible |
| WBI | Wiberg Bond Order Index |
| Å | Angstroms |
| $\kappa^1$ | Monodentate |
| $\kappa^2$ | Bidentate |
| μ | Bridging |

## LIST OF COMPOUNDS

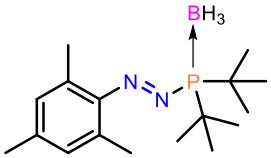

**1** $MesN_2P^tBu_2{\cdot}BH_3$

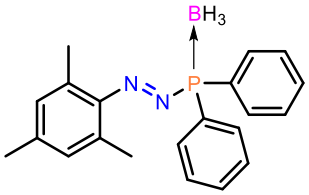

**2** $MesN_2PPh_2{\cdot}BH_3$

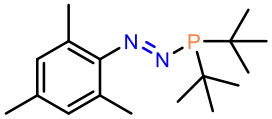

**3** $MesN_2P^tBu_2$

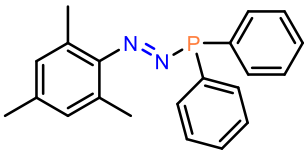

**4** $MesN_2PPh_2$

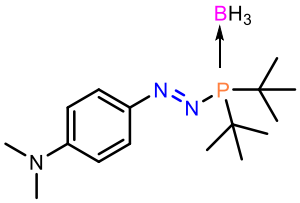

**5** $(p\text{-}NMe_2)C_6H_4N_2P^tBu_2{\cdot}BH_3$

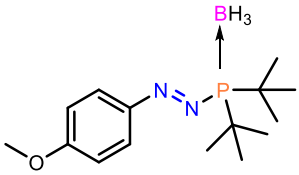

**6** $(p\text{-}OMe)C_6H_4N_2P^tBu_2{\cdot}BH_3$

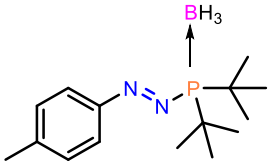

**7** $(p\text{-}Me)C_6H_4N_2P^tBu_2{\cdot}BH_3$

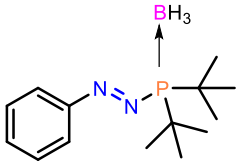

**8** $C_6H_5N_2P^tBu_2{\cdot}BH_3$

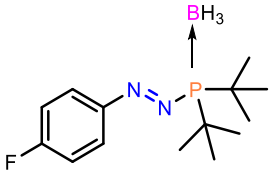

**9** $(p\text{-}F)C_6H_4N_2P^tBu_2{\cdot}BH_3$

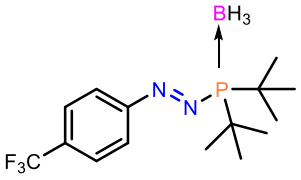

**10** $(p\text{-}CF_3)C_6H_4N_2P^tBu_2{\cdot}BH_3$

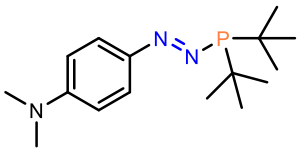

**11** $(p\text{-}NMe_2)C_6H_4N_2P^tBu_2$

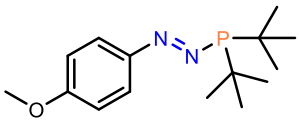

**12** $(p\text{-}OMe)C_6H_4N_2P^tBu_2$

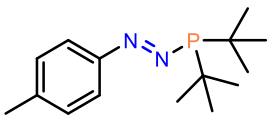

**13** $(p\text{-}Me)C_6H_4N_2P^tBu_2$

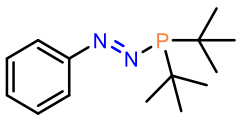

**14** $C_6H_5N_2P^tBu_2$

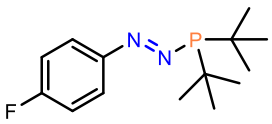

**15** $(p\text{-}F)C_6H_4N_2P^tBu_2$

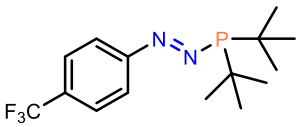

**16** ($p$-$CF_3$)$C_6H_4N_2P^tBu_2$

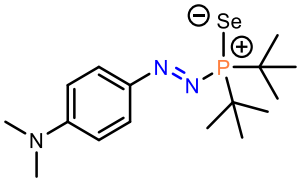

**17** ($p$-$NMe_2$)$C_6H_4N_2P(Se)^tBu_2$

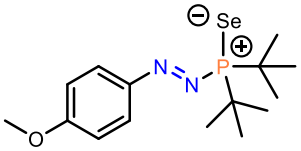

**18** ($p$-OMe)$C_6H_4N_2P(Se)^tBu_2$

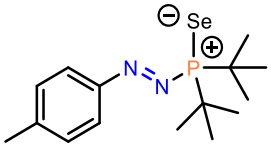

**19** ($p$-Me)$C_6H_4N_2P(Se)^tBu_2$

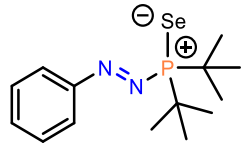

**20** $C_6H_5N_2P(Se)^tBu_2$

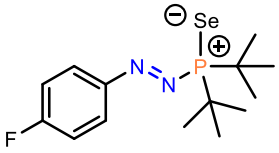

**21** ($p$-F)$C_6H_4N_2P(Se)^tBu_2$

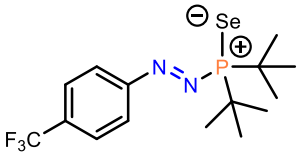

**22** ($p$-$CF_3$)$C_6H_4N_2P(Se)^tBu_2$

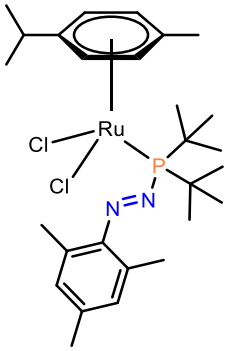

**23** Ru($p$-cymene)($\kappa^1P$-**3**)$Cl_2$

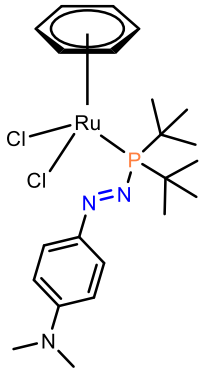

**24** Ru(benzene)($\kappa^1P$-**11**)$Cl_2$

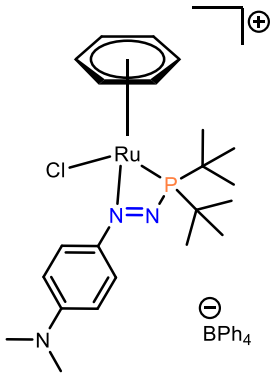

**25** [Ru(benzene)($\kappa^2P,N$-**11**)Cl][$BPh_4$]

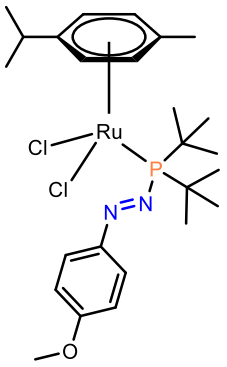

**26** Ru($p$-cymene)($\kappa^1P$-**12**)$Cl_2$

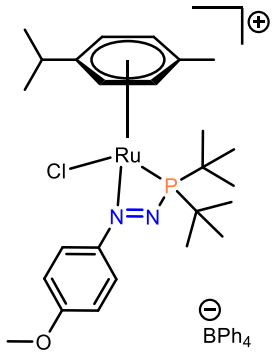

**27** [Ru($p$-cymene)($\kappa^2P,N$-**12**)Cl][$BPh_4$]

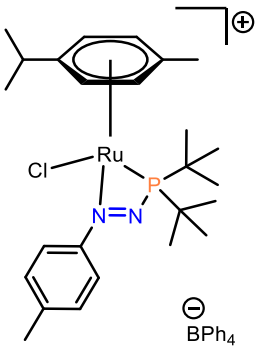


**28** [Ru(*p*-cymene)(κ²*P*,*N*-**13**)Cl][$BPh_4$]

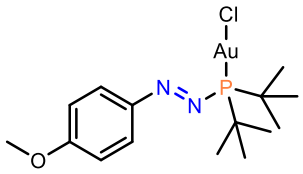


**29** Au(κ¹*P*-**12**)Cl

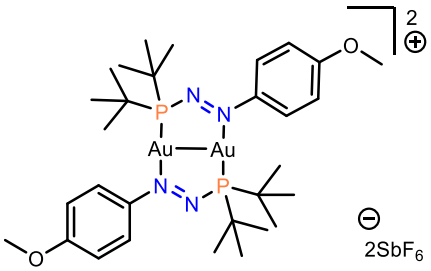


**30** [Au(μ*P*,*N*-**12**)]₂[$SbF_6$]₂

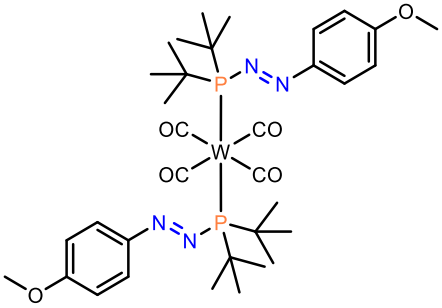


**31** *trans*-W(κ¹*P*-**3**)₂$CO_4$

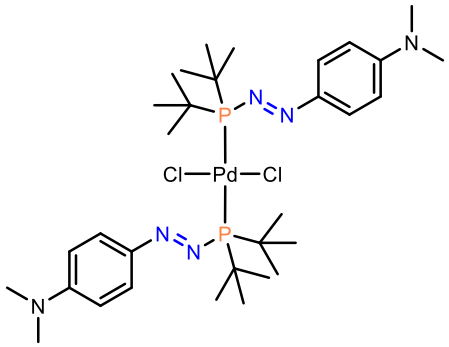


**32** *trans*-Pd(κ¹*P*-**11**)₂$Cl_2$

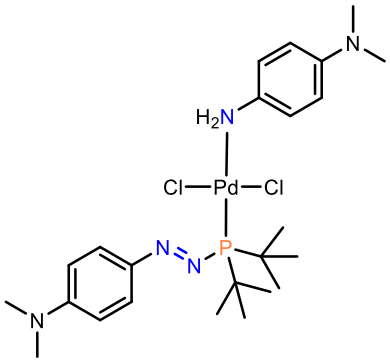


**33** Pd(κ¹*P*-**11**)(κ¹*N*-$NH_2C_6H_4$(*p*-$NMe_2$)$Cl_2$

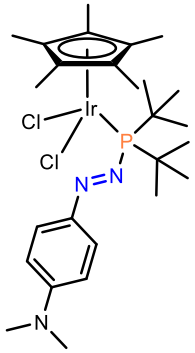


**34** Ir(Cp*)(κ¹*P*-**11**)$Cl_2$

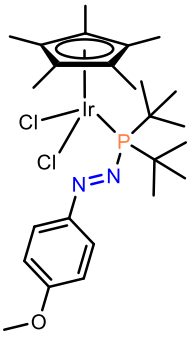


**35** Ir(Cp*)(κ¹*P*-**12**)$Cl_2$

# CHAPTER 1

# Introduction

## 1.1 Phosphorus Analogues of Common Functional Groups

Functional groups are the cornerstone of predicting and rationalising reactivity in synthetic chemistry. The conceptual replacement of 2p elements in common functional groups with heavier main-group congeners can lead to drastically different properties and reactivity. The study of phosphorus-containing analogues of nitrogen-containing moieties has grown in recent years. Low coordinate examples are those featuring P=C ($\lambda^3\sigma^2$) or P≡C ($\lambda^3\sigma^1$) bonds, such as the phosphorus-containing analogues of pyridine and the cyanate and cyanide anions (Figure 1.1A – C)[1–8] Tri-coordinate examples featuring P–C ($\lambda^3\sigma^3$) bonds are the phosphorus-containing analogues of urea and *N,N*-dimethylformamide (DMF) (Figure 1.1D and E).[9,10] The synthesis of new phosphorus-containing architectures and their applications is a theme of research continued in the Jupp group.[8–11]

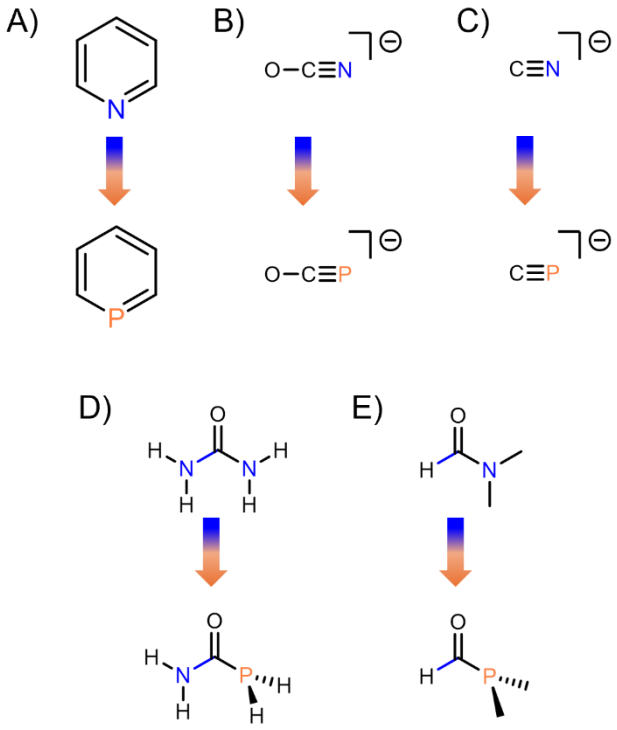


**Figure 1.1.** Phosphorus-containing analogues of (A) pyridine, (B) cyanate, (C) cyanide, (D) urea and (E) DMF.

### 1.1.1 Low Coordinate Phosphorus

Weak overlap between the 3s and 3p orbitals means heavier elements such as phosphorus have difficulty achieving hybridisation. An intriguing aspect of this field of research is that low coordinate phosphorus compounds are rarely comparable with classical phosphines. When phosphorus is in a low-coordinate environment, it has been shown that it is more similar to carbon than to nitrogen, principally due to the isolobal nature of P and C and their similar electronegativities, resulting in phosphorus being dubbed the carbon copy.[12] This is a manifestation of the so-called diagonal relationship where trends in chemical reactivity of one element can more closely parallel that of an adjacent group and neighbouring period. An excellent example of this is a comparison of dinitrogen (N≡N) with its heavier congener diphosphorus (P≡P) where $N_2$ is an extremely unreactive, essentially inert, molecule and $P_2$ is a highly unstable and reactive species.[13–15] Experimental and theoretical studies have shown that the chemical and electronic structural properties of $P_2$ instead more closely resembles those of acetylene (HC≡CH) as the reactivities of both, although not of the same magnitude, are governed by high-energy π bonds which lie above the corresponding σ-bonding interaction.[16–19] Nitrogen is more electronegative than carbon and phosphorus and so, by contrast, its π-bonding interactions fall below the energy of the σ-bond.[18,20] As illustrated in Figure 1.2, a comparison of the triple bond dissociation energy ($D_e$) reveals P≡P ($D_e$ = 117 kcal mol$^{-1}$) is much weaker than that of HC≡CH ($D_e$ = 230 kcal mol$^{-1}$) and N≡N ($D_e$ = 226 kcal mol$^{-1}$).[21] A comparison of the gap between the highest occupied molecular orbital (HOMO) and the lowest unoccupied molecular orbital (LUMO) reveals that of $P_2$ (3.65 eV) is much smaller than that of $N_2$ (8.33 eV).[22]

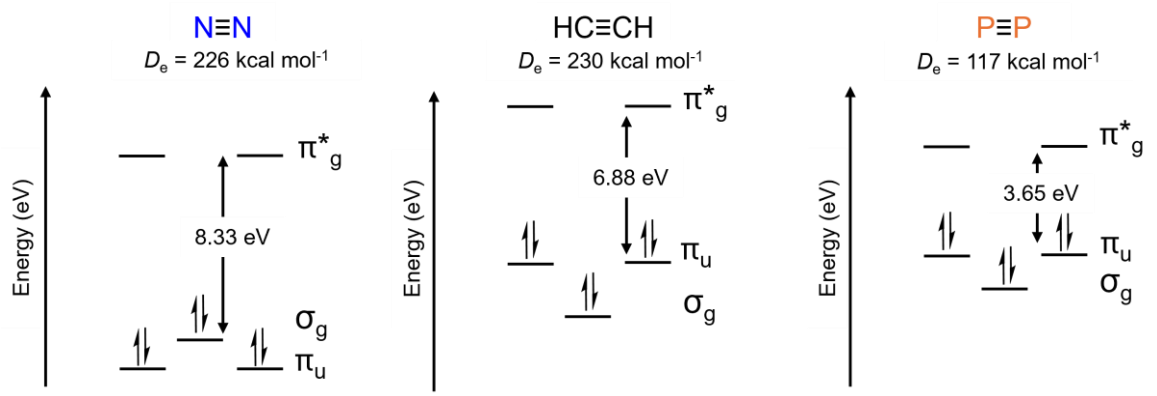


**Figure 1.2.** Partial molecular orbital diagrams for dinitrogen (N≡N), acetylene (HC≡CH), and diphosphorus (P≡P) showing the relative energies of the frontier σ- and π-symmetry orbitals of the triple bonds. Figure adapted, and molecular orbital energy gaps obtained, from Figueroa and co-workers.[22]

The coordination chemistry of mono-, di- and tri-phosphinines (Figure 1.1A) has long been known,[1,2] and phosphaalkynes (P≡CR) are well established to bind mononuclear transition metals in a side-on configuration.[23] Analogous to the side-on coordinative configurations of acetylene, the side-on coordination of $P_2$ has recently been demonstrated.[22] Similarly, far from simply being laboratory curiosities, phosphaethynolate ($PCO^-$) and cyaphide ($C{\equiv}P^-$) anions as P-containing functional groups of cyanate and cyanide, respectively (Figure 1.1B and C), have been demonstrated to serve as ligands[7,24–26] and, in the case of $PCO^-$, as a catalyst.[27]

### 1.1.2 Tri-coordinate Phosphorus

For tri-coordinate phosphorus, the presence of the lone pair means that there are obvious parallels with analogous nitrogen compounds, although there is a significantly reduced propensity for delocalisation of this lone pair in the former. In their study of phosphinecarboxamide as a P-containing analogue of urea (Figure 1.1D), Goicoechea and co-workers found the spectroscopic properties, bond metric data and computed electronic structure all suggested that the P lone pair is reasonably isolated from the

amide functional group. Most pertinent is that the HOMO was computed to have considerable P lone pair character.[29] Similarly, Stephan and co-workers obtained spectroscopic data that showed for *P,P*-dimethylformylphosphine, the P-containing analogue of DMF (Figure 1.1E), the P-bound methyl groups are equivalent, consistent with free rotation about the P–C(O) bond.[10] For DMF, the N-bound methyl groups are inequivalent due to significant C–N double bond character which restricts rotation about the N–C(O) bond. The authors corroborated these data computationally calculating a low barrier to P–C(O) bond rotation and that the resonance structure arising from delocalisation of the P lone pair into the C=O π* orbital contributed only 4.0% to the overall structure (Figure 1.3). The major resonance contribution of P–C single bond and C=O double bond was computed to be 82.3% similar to that of pivaldehyde (C–C(O)) (83.8%) and is consistent with the notion that phosphorus is the 'carbon copy'.

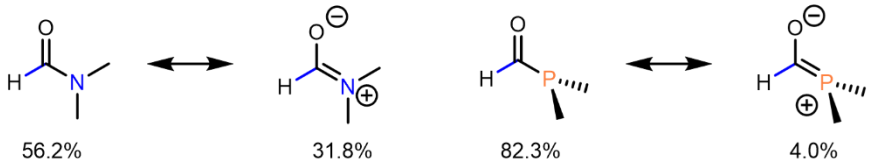


**Figure 1.3.** Delocalisation of the nitrogen and phosphorus lone pair in DMF and its P-containing analogue. Percentages represent the contribution of that resonance structure to the overall structure reported by Stephan and co-workers.[10]

The ramifications of the reduced propensity of the P lone pair for delocalisation is seen in the pyramidal geometry at phosphorus for phosphinecarboxamide and *P,P*-dimethylformylphosphine, in contrast to the planar geometry at nitrogen for urea and DMF (Figure 1.4). Coordination of phosphinecarboxamide to tungsten and molybdenum and *P,P*-dimethylformylphosphine to ruthenium occurred *via* the phosphorus atom.[10,29] In the former, an assessment of ligand basicity using

experimental and theoretical studies found the phosphine demonstrated average σ-donor and π-acceptor properties, comparable to that of $PH_3$ and trialkylphosphites.[29]

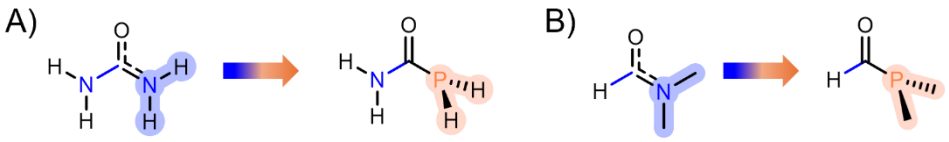


**Figure 1.4.** Planar geometry at nitrogen and pyramidal geometry at phosphorus in (A) urea and phosphinecarboxamide, and (B) DMF and *P,P*-dimethylformylphosphine.

Phosphines are one of the most important L-type ligands in organometallic chemistry (discussed in Section 1.4). Based on the precedent for reduced propensity of the P lone pair for delocalisation, it is prudent to consider phosphorus-analogues of common functional groups in the design of new ligands. One such candidate is triazene which will first be introduced in Section 1.2 before considering its P-containing analogues.

## 1.2 Triazenes

Triazenes ($RN{=}N{-}NR'_2$) are a common functional group in organic chemistry, and can be found in dyes and pharmaceuticals, such as anti-cancer medications *Temozolomide* and *Dacarbazine* (Figure 1.5).[30–32]

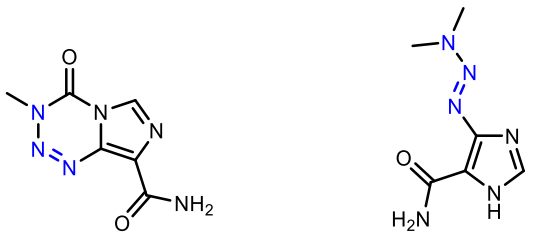

Temozolomide Dacarbazine

**Figure 1.5.** Structures of triazene-containing pharmaceuticals, *Temozolomide* and *Dacarbazine*.

They are also versatile tools in organic synthesis, where the triazene moiety can act as a robust protecting group for amines, or as a precursor in numerous synthetic transformations.[33–35] The N=N–N moiety is labilised and can be selectively decomposed after treatment with the appropriate reagent. For example, acid-induced decomposition generates a diazonium and ammonium species, from which each can be further utilised. In this sense, the versatility of triazenes lies in their eventual decomposition. Charge delocalisation over the N–N–N π-system results in triazenes adopting a planar geometry in which the sum of the angles around the amino nitrogen has been reported to be very close to 360° (Figure 1.6).[36,37] As a result, the coordination chemistry of triazenes is dominated by the triazenide anion (RN=N–N$^-$) and will be further discussed in Chapter 4.

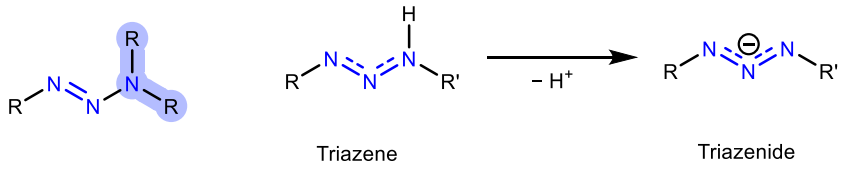


**Figure 1.6.** Planar geometry at the amino nitrogen of triazenes, and charge delocalisation in triazenes and triazenides.

Returning to the concept of phosphorus-containing analogues of common functional groups that was introduced in Section 1.1, the conceptual replacement of one or more nitrogen atoms in triazenes with phosphorus yields multiple different connectivities (Figure 1.7).

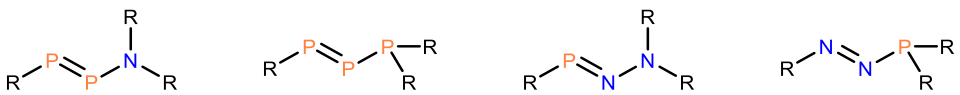

**Figure 1.7.** Conceptual replacement of nitrogen in triazene with phosphorus. Examples include P=P–N, P=P–P, P=N–N and N=N–P connectivities.

Since Yoshifuji isolated the first diphosphene Mes*P=PMes* (Mes*, 2,4,6-$^{t}$Bu$_3$C$_6$H$_2$) in 1981,[38,39] a number of RP=PR compounds, and heavier congeners with different substituents at the P=P core, are known.[38–40] The presence of a primary amino substituent gave the *Z*-configured RN(H)–P=PMes* and single crystal X-ray analysis of an imidazolyl–P=P–N($^{i}$Pr)$_2$ aminodiphosphene revealed partial PN multiple bonding from the planarity of the tri-coordinate N-atom (Figure 1.8A and B).[40]

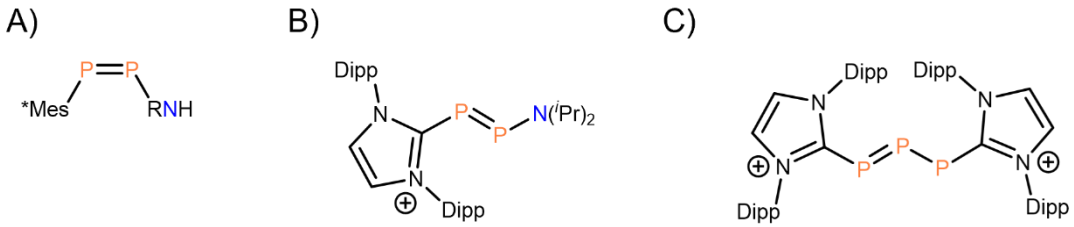


**Figure 1.8.** Structures of (A) *Z*-RN(H)P$_2$Mes*; (B) imidazolyl-P$_2$N($^{i}$Pr)$_2$; (C) symmetrical imidazolyl-triphosphene.

Bulky phosphino groups also provide stability to the P=P bonds.[39] Single crystal X-ray analysis of an imidazolyl–P=P–P–imidazolyl triphosphene revealed P–P bond distances between the values of single and double bonds due to delocalisation of the π-electrons (Figure 1.8C).[41] Beyond just the relative synthetic accessibilities, by replacing the tri-coordinate nitrogen in triazenes with phosphorus (N=N–P), the coordinating ability of a tri-coordinate soft phosphine would be combined with a hard sp$^2$ N-donor atom. If the precedent for localisation of the P lone pair extends to this situation, it could potentially yield a sophisticated hybrid ligand. By maintaining the N=N azo group, similarities in structure are drawn with the well-established photoswitch azobenzene (further discussed in Section 1.5).

## 1.3 Azophosphines

The conceptual replacement of the tri-coordinate nitrogen centre in triazenes with a phosphorus atom yields azophosphines: RN=N–PR'$_2$ (Figure 1.9A).

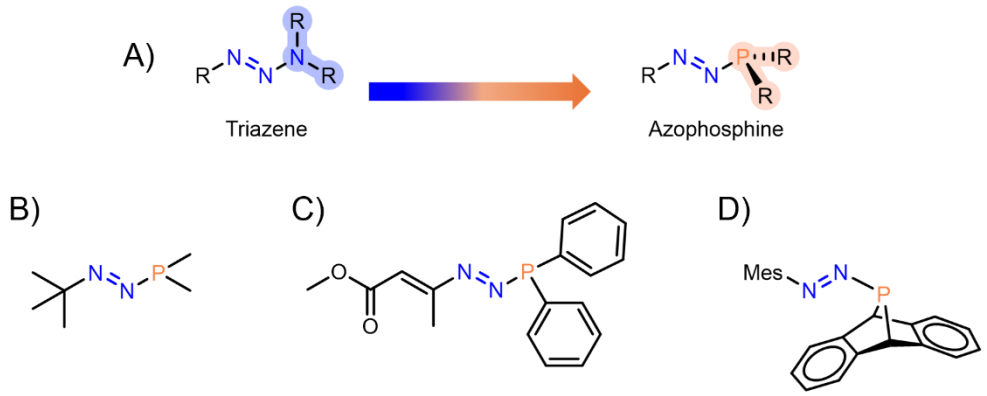


**Figure 1.9.** (A) Azophosphines as P-containing analogues of triazenes; examples of azophosphines synthesised by: (B) Wiberg and co-workers;[42] (C) Attanasi and co-workers;[43] (D) Cummins and co-workers.[44]

Azophosphines were first synthesised in the late 1970s by Wiberg and co-workers by the reaction of silyldiazenes and chlorophosphines,[42,45] and alkenyl-substituted variants were subsequently prepared in the late 1980s by Attanasi and co-workers (Figure 1.9B and C, Scheme 1.1A and B).[43] These first reports were limited in their study of azophosphines; the publication by Wiberg[45] briefly refers to the synthesis of *phosphanylorganyldiazenes*[42] to support an assumption that formation of a silylated-phosphine $Me_3Si–PR_2$ occurred *via* decomposition of $Me_3Si–N=N–PR_2$[46], and the publication by Attanasi and co-workers is restricted to a synthetic methodology and subsequent characterisation by only $^1$H NMR spectroscopy and IR spectroscopy.[43]

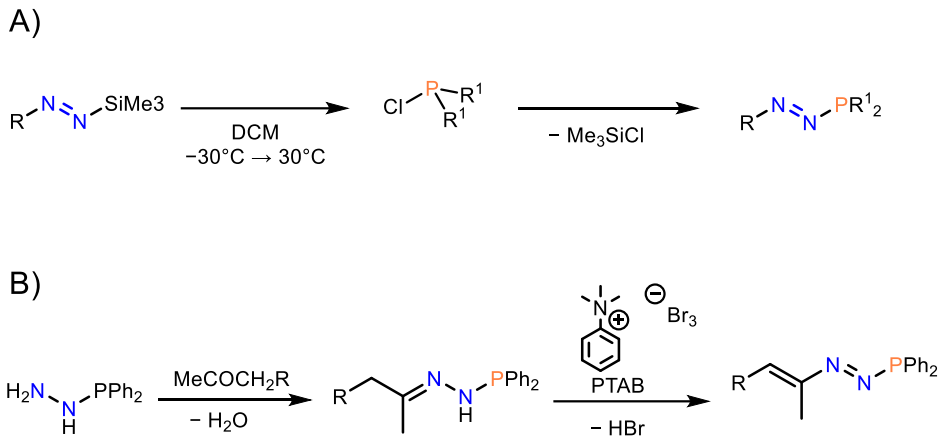


**Scheme 1.1.** (A) Wiberg synthesis of azophosphines by reaction of silyldiazenes and chlorophosphines; (B) Attanasi synthesis of alkenyl-substituted variants of azophosphines. Bu, butyl; Et, ethyl. These syntheses are discussed in further detail in Chapter 2.

In 2020, at the time of beginning the research discussed in this thesis – in particular, chapter 2 – the publications by Wiberg and co-workers and Attanasi and co-workers encapsulated the research in azophosphines that was available in the literature. In 2021 Cummins and co-workers synthesised and crystallographically characterised $MesN_2P$**A** (Mes, mesityl; **A**, anthracene) (Figure 1.9D), which was utilised as a synthetic equivalent of mesitylphosphaazide ($MesN_2P$) in a range of cycloaddition reactions on account of the labile anthracene moiety (Scheme 1.2A).[44]

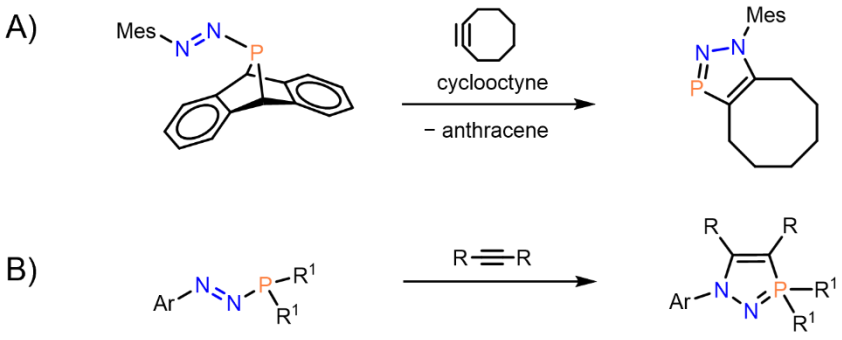


**Scheme 1.2.** 1,3-Dipolar cycloadditions of azophosphines and alkynes by Cummins and co-workers (A) Transfer of mesitylphosphaazide from $MesN_2P$**A** to cyclooctyne; (B) General synthesis of an N-heterocyclic iminophosphorane. Schemes adapted from references [44] and [47].

Study of the frontier molecular orbitals using density functional theory suggested $MesN_2P$**A** could behave as a 1,3-dipole on account of the HOMO being the phosphorus lone pair and the LUMO the N=N π* orbital. This was followed by a subsequent publication by the Cummins group in which a wider range of azophosphines were synthesised and their reactivity explored with alkynes to afford N-heterocyclic iminophosphoranes (Scheme 1.2B).[47]

As a result of the work that will be discussed in this thesis, the synthesis and exploration of the key properties of azophosphines has recently been reported by the Jupp group.[48,49] This research will be discussed in further detail, along with the syntheses of azophosphines that were introduced in this section, in Chapter 2. An analysis of their properties is provided in Chapter 3.

## 1.4 Coordination Chemistry

### 1.4.1 Phosphine Ligands

Phosphines ($PR_3$) are most often spectator ligands, meaning that they do not participate in reactions, yet much of homogeneous transition metal catalysis is underpinned by metal-phosphine coordination complexes, including Wilkinson's,[50] Crabtree's,[51] and Grubbs' catalysts,[52] and Vaska's complex (Figure 1.10A – D).[53] Here, good catalytic activity is typically governed by the phosphine being both electron-rich and sufficiently sterically-encumbered. The ubiquity of phosphines across metal coordination chemistry can be attributed to a ready tuneability in which a high degree of control over these electronic and steric properties is enabled.[54]

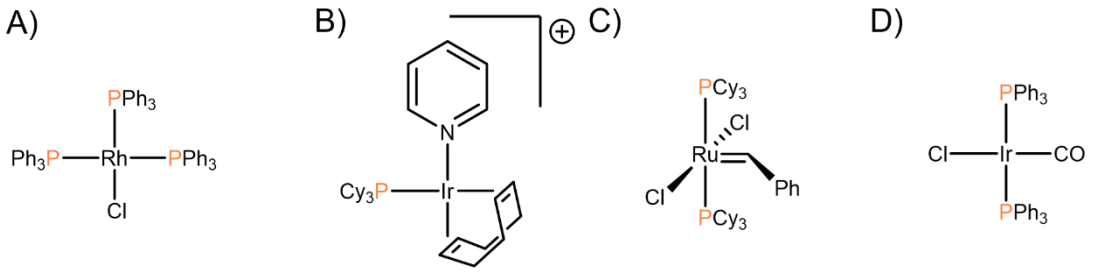


**Figure 1.10.** Structures of seminal metal-phosphine catalysts (A) Wilkinson's (B) Crabbtree's (C) Grubb's catalysts, and (D) Vaska's complex.

Phosphines are dative ligands, in which coordination to a metal centre involves the lone pair of electrons on the phosphorus interacting with an empty metal d orbital to form a σ bond. The electronic nature of the R groups influences the electron-donating ability of the phosphorus atom, in which *P*-alkyl phosphines tend to be better electron donors than *P*-aryl phosphines on account of the lower electronegativity of $sp^3$ hybrid orbitals relative to $sp^2$ orbitals.. Phosphines also participate in π-backbonding, resulting in the transfer of electron density from the metal to the phosphine, thus relieving negative charge from the metal centre. This phenomenon is rationalised by a metal d-orbital interacting with the antibonding σ* P–R orbitals (Figure 1.11).[55]

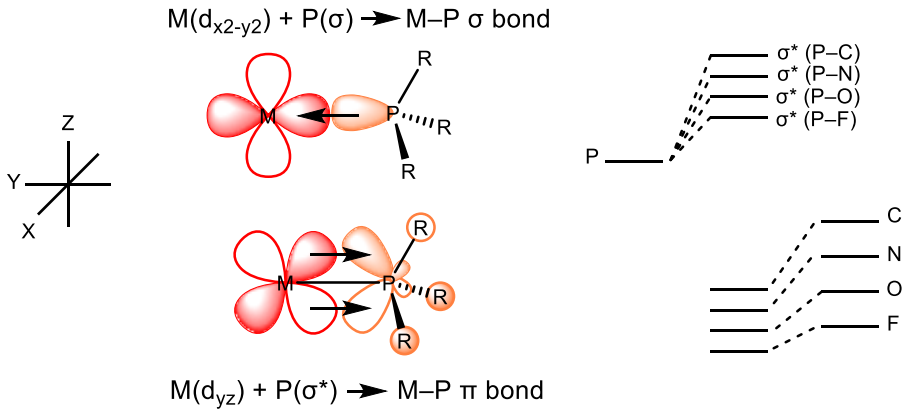


**Figure 1.11.** Schematic representation of backbonding resulting in the transfer of electron density from the metal (M) d-orbital to the phosphine σ* orbital.

Strongly electron-withdrawing R groups can drastically lower the energy of the σ* orbital, in turn increasing the π-acceptor ability of the phosphine. This implies that the σ* orbital of the P–R bond becomes more accessible for back donation in the order R = C < N < O < F.

Chelating bidentate phosphine ligands are common and their excellent ligating properties have encouraged extensive study of other polydentate phosphines.[56] An important characteristic of chelating phosphines is the P–M–P bite angle formed upon chelation to a metal in which a compromise is made between the preferred bite angle of the ligand and the one preferred by the metal centre. It has long been observed that the correlation between the P–M–P bite angle and catalytic activity of the complex is linked and is a useful parameter in explaining rates, selectivities and efficiencies in catalytic reactions.[57,58] It is therefore an important consideration in the design of new ligands for application in catalysis.

Another important consideration is the steric effect of phosphine ligands on their coordination chemistry and performance as catalysts. Since Tolman introduced the concept of the cone angle – the apex angle of a cone formed with its origin at the metal centre with edges along the van der Waals spheres of the atoms in the R groups – it has been a widely accepted parameter for measuring the steric properties of monodentate phosphine ligands (Figure 1.12A).[59] By incorporating Tolman's Electronic Parameter (TEP) – that is, the CO stretching frequency of mixed phosphine-carbonyl complexes – Tolman's map of phosphine ligands illustrates their relative steric and electronic properties.[59] Tolman's cone angle can, however, be inaccurate as smaller ligands can coordinate more closely to a metal centre, overestimating the size of its cone angle, and for larger ligands which coordinate further from the metal centre, an

underestimation of its cone angle can occur. Tolman's method also assumes the ligand is folded up to make the smallest possible cone, which may not be representative of the lowest energy conformation adopted in the metal complex. Nolan and Cavallo proposed the 'percent buried volume' – defined as the percent of the total volume of a sphere occupied by a ligand – as an alternate model to measure steric bulk (Figure 1.12B).[60,61]

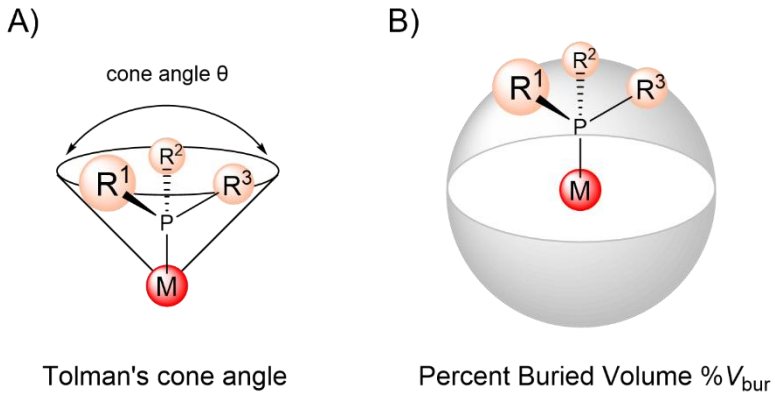


**Figure 1.12.** Schematic representation of established steric parameters: (A) Tolman's cone angle and (B) Percent Buried Volume in which the volume of the sphere around the metal occupied by the ligand is the buried volume.

Percent buried volume removes the inaccuracies of cone angle and considers the spatial volume occupied by the ligand in all dimensions, although this is not paired to an electronic parameter. The difficulty in finding an unambiguous measure of the electronic properties of a phosphine lies in the so-called σ/π controversy where participation of σ-donor and π-acceptor orbitals can give rise to complementary effects.[62–64] Nevertheless, TEP can provide insight for interpreting net effects in concepts such as *trans*-influence.

### 1.4.2 Metal-Ligand Cooperativity of P,N Hybrid Ligands

By including different donor atoms more sophisticated, hybrid ligands can be designed. Hybrid ligands are bi- or polydentate ligands that feature at least two different donor sites capable of binding to metal centres.[65,66] Of these, P,N based hybrid ligands are the most abundant[65] and can show large differences in the binding affinity of the soft P and hard N donors for a particular metal. The backbone of P,N ligands can be based on simple P–N–P or P–C–N connectivity to more elaborate bicyclic and P–$(C)_n$–N–$(C)_n$–P connectivity.[67] Hemilability can be demonstrated where one coordinating atom is easily displaced from the metal centre while the other atom remains firmly bound thus transitioning between monodentate ($\kappa^1$) and bidentate ($\kappa^2$) coordination modes (Figure 1.13A).

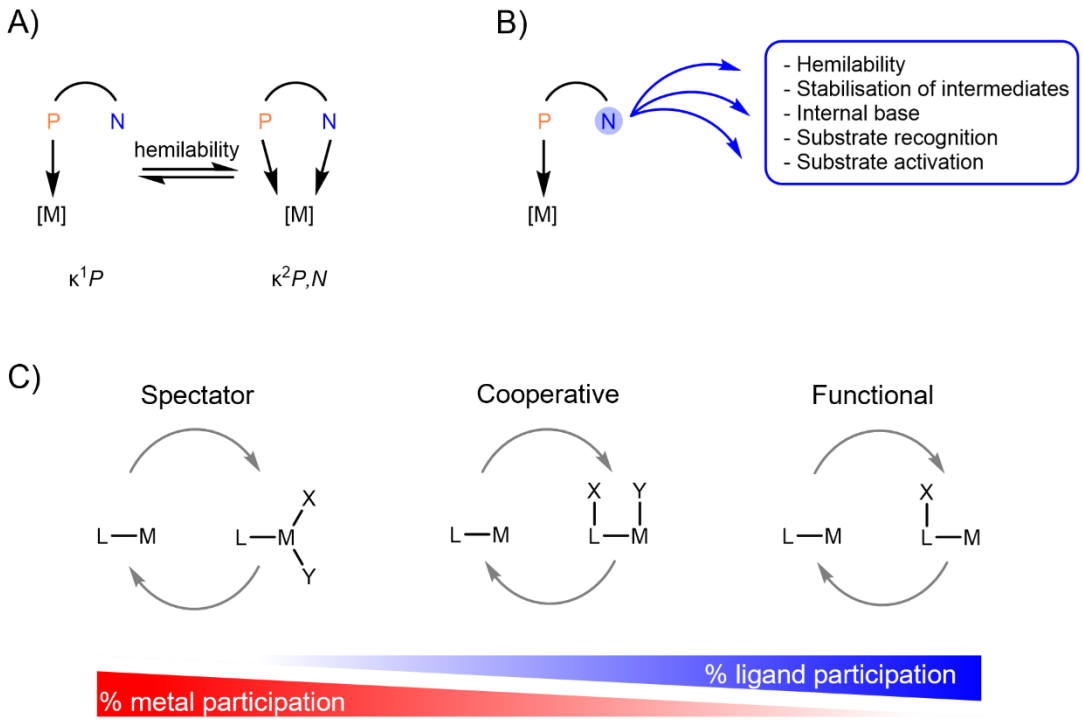


**Figure 1.13.** (A) Hemilability and (B) Cooperative effects as properties of P,N ligands; (C) Ligand participation in reactivity in transition metal catalysis. L, ligand; M, metal; X Y, reactive substituents. Adapted from Radosevich and co-workers.[68]

The distinctive bonding preferences of different donor atoms in hybrid ligands give control of the coordination chemistry and allow for cooperative effects such as proton shuttling, stabilisation of intermediates, and substrate recognition and activation to be pursued in catalysis (Figure 1.13B). In contrast to 'classical' transition metal catalysis where the ligand acts as a spectator while all key transformations occur at the metal centre, metal-ligand cooperation (MLC) is a concept where both the metal and the ligand actively participates in bond activation processes.[69] At the far extreme of the spectrum of reactivity is a 'functional' class of ligands where, in a role reversal, bond making and breaking processes are localised on the ligand in conjunction with a spectator metal (Figure 1.13C).[68,70–72]

The role of MLC in enabling effective catalysis was comprehensively reviewed by Khusnutdinova and Milstein in which the most studied systems were found to be based on N-donor ligands and MLC reactivity involving $H_2$ or HX activation was most common.[73] Khusnutdinova and Milstein note that metal-mediated reactivity and MLC pathways are not always easily distinguishable, requiring detailed experimental and theoretical studies to elucidate the role of the ligand. Parallels between MLC and frustrated Lewis pairs (FLP) chemistry have been drawn by Slootweg and co-workers in that both involve the cooperative action of a Lewis acid and a Lewis base.[74] As a rapidly growing field since its conception in 2006 by Stephan,[75,76] the authors assert that principles and reactions from main-group FLPs can be used to broaden the scope of MLC reactivity and highlights the contributions this could make to understanding MLC pathways.

### 1.4.3 1,3-P,N Ligands

1,3-P,N ligands are a subclass of P,N ligands with a P–X–N connectivity where typically X = C. Extensive study of this class of compounds has demonstrated that they can bind selectively through the hard N atom ($\kappa^1N$), the soft P atom ($\kappa^1P$), or both ($\kappa^2P,N$) and can bind to one or multiple metal centres ($\mu P,N$) (Figure 1.14A).[77,78] 1,3-P,N ligands are typified by 2-pyridyldiphenylphosphine $PyPPh_2$ since its introduction as a ligand in 1972,[79–81] and were soon followed by 2-imidazolyl-, amino and iminophosphines (Figure 1.14B).[67,77,78]

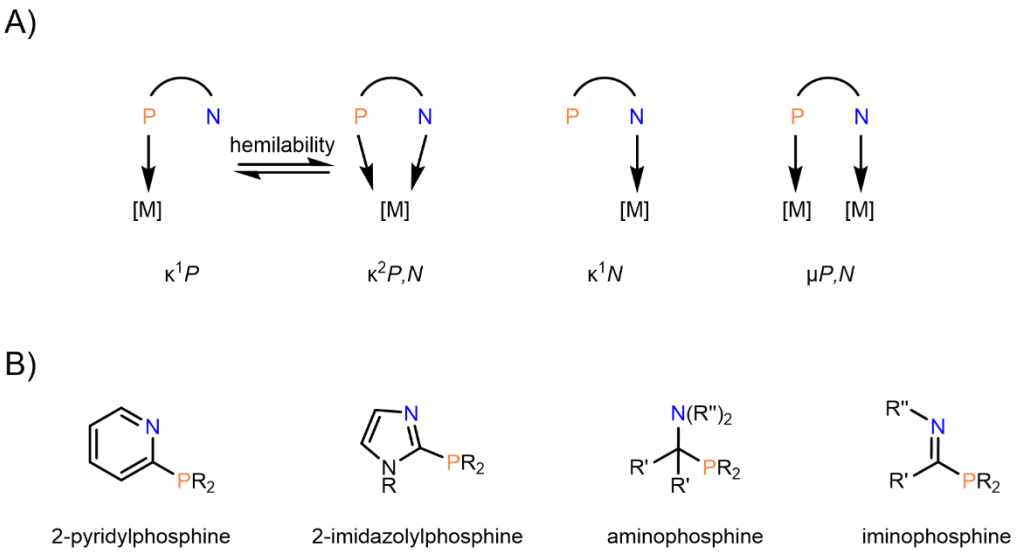


**Figure 1.14.** (A) Coordination modes of 1,3-P,N ligands; (B) Structures of typical 1,3-P,N ligands

Of these, 1,3-P,N complexes mostly feature pyridyl- and imidazolyl-based ligands. The pyridyl-based ligands, in particular, have been used in a plethora of catalytic transformations.[77] Given these important applications it is unfortunate that both have structural limitations that are inherent to their syntheses and lack easy tuneability.[82] Selective access to 6-substituted $PyPPh_2$ *via* general synthetic methodologies has been developed by Hintermann and co-workers (Scheme 1.3A);[83] however, in general,

the direct and selective functionalisation of the pyridine ring remains a challenge which attracts considerable attention.[84] Highly tuneable iminophosphines and their tautomers phosphaamidines can be independently substituted on the P, C, and N atoms.[85–87] They can be obtained *via* nitrilium triflate precursors as dynamic E/Z isomer mixtures (Scheme 1.3B); however, equilibrium shifts to the desired Z conformer on coordination to metals.[85,88–91]

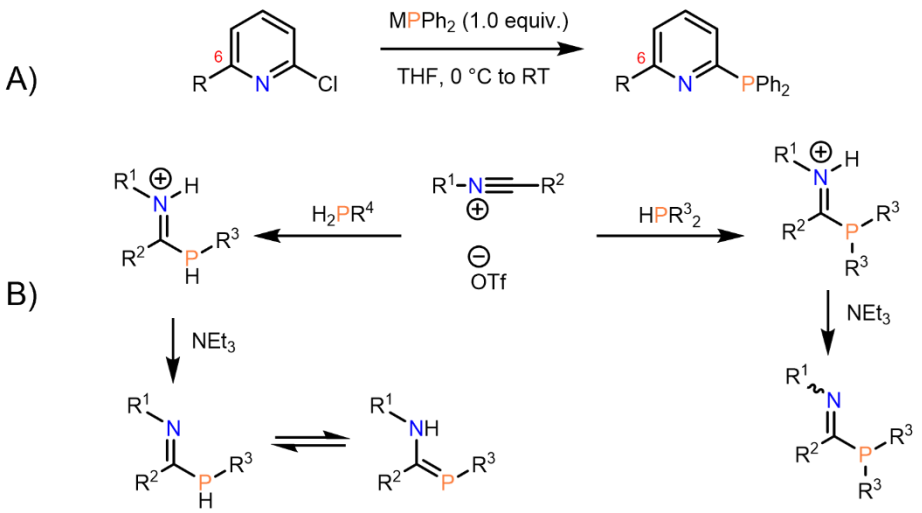


**Scheme 1.3.** (A) Synthesis of 6-substituted $PyPh_2$ from halogenated precursors; (B) Synthesis of iminophosphines and their tautomers phosphaamidines.

### *κ¹P and κ²P,N Coordination*

1,3-P,N ligands display κ¹*P* and κ²*P,N* coordination to a range of metal centres. κ¹*N* coordination is rare; it has been reported and crystallographically resolved for $PyPPh_2$ coordinated to Fe(II) and Zn(II) metal centres.[92,93] As first-row transition metals, the relatively high charge density of Fe(II) and, in particular, Zn(II) facilitates κ¹*N* coordination. Spectroscopic evidence of rapid interchange between κ¹*P* and κ¹*N* coordination has been obtained for $PPh_2$-substituted cyclic imines coordinated to Rh (Scheme 1.4).[94] Here, the aryl groups of phosphorus reduce the donating property of

the phosphine whilst the cyclic alkyl chain enhances the donating properties of the imine.

Ruthenium(II), a borderline metal in hard-soft acid-base theory, is one of the most common partners in complexes featuring 1,3-P,N ligands. The literature on this coordination chemistry will be discussed in further detail in Chapter 4 (Section 4.1.2). Here, therefore, the effect of ligand substituents on $\kappa^1$*P* and $\kappa^2$*P,N* coordination of 1,3-P,N ligands will be considered.

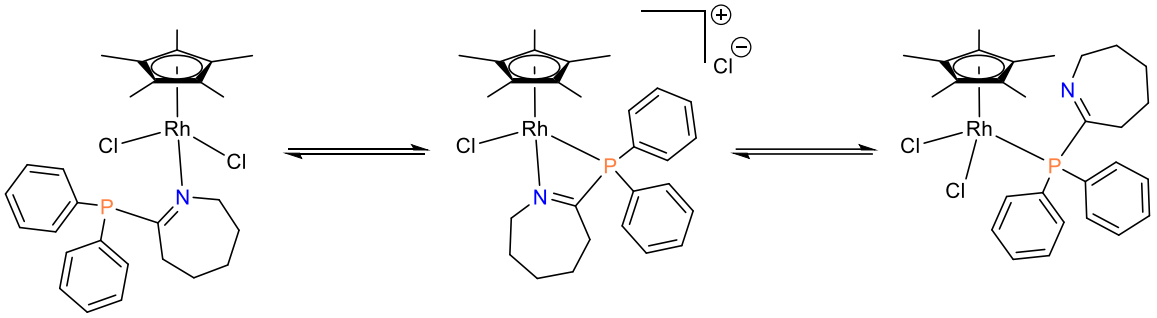


**Scheme 1.4.** Rapid interchange between $\kappa^1$*N* and $\kappa^1$*P* proposed by Lammertsma and co-workers.[94]

Due to having only one spacer, a carbon, bridging the P and N donor atoms, 1,3-P,N ligands upon chelation to a metal centre form a strained, four-membered ring prone to opening by a competing ligand. By incorporating a bulky $^t$Bu group in the *ortho*-position to the imidazolyl and pyridyl N atoms (Figure 1.15), Grotjahn and co-workers demonstrated far superior catalyst performance in the anti-Markovnikov hydration of terminal alkynes to aldehydes.[95,96]

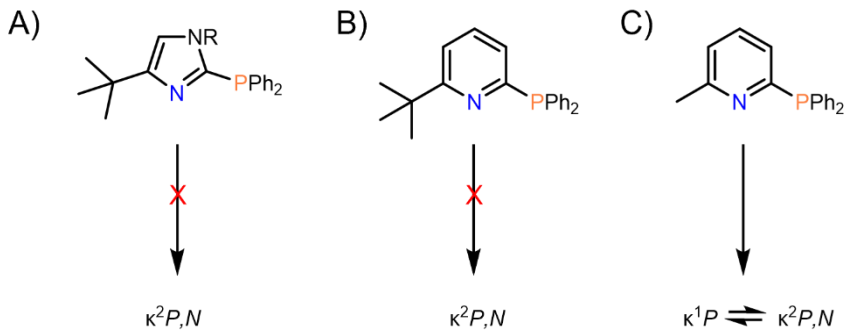


**Figure 1.15.** Steric shielding by *ortho*-substitution on (A) imidazolyl- and (B) pyridyl-based 1,3-P,N ligands; (C) Decreasing the steric bulk to methyl promoted hemilability.

The effect on catalysis of this crucial ligand modification was ascribed to the steric shielding of the N-donor lone pair by the sterically demanding $^{t}$Bu group preventing $\kappa^2$*P,N* coordination (Figure 1.15A and B).[97,98] This has since paved the way for the design of other highly active catalysts *via* incorporation of a sterically demanding group in the *ortho*-position to the imidazolyl and pyridyl N atoms which prevents $\kappa^2$*P,N* chelation.[82,83,99] Incorporating a methyl group as the steric bulk in 6-MePyPPh$_2$ did not prevent $\kappa^2$*P,N* chelation and instead promoted hemilability of the pyridyl N atom in Pt and Pd complexes (Figure 1.15C).[100] In the case of the more tuneable imino-based 1,3-P,N ligands, ring-opening of $\kappa^2$*P,N* coordination to $\kappa^1$*P* coordination in Rh complexes correlated with the electronic properties of the ligands and the basicity of the nitrogen donor from modulating the N and C substituents (Scheme 1.5).[85,91]

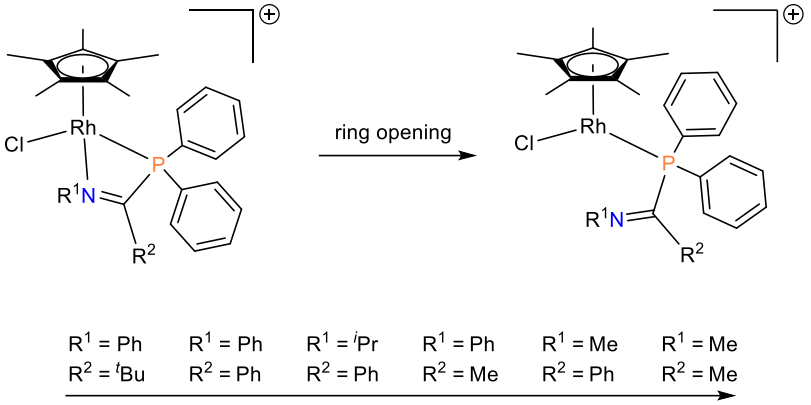


**Scheme 1.5.** Influence of the imine and C substituents on the N-donor capacity. A computational investigation by Lammertsma, Slootweg and co-workers.[85]

*μP,N Coordination*

1,3-P,N ligands bridging two metal centres can assume a head-to-tail configuration (*HT*) or a head-to-head configuration (*HH*). In homobimetallic systems, there is a propensity for *HT* configurations (Figure 1.16A). When monitoring the comproportionation reactions of Pd and Pt complexes, mixtures of *HH* and *HT* isomers were detected before isomerisation of the *HH* isomers to the corresponding *HT* configuration.[101,102] This spontaneous isomerisation from the kinetically favoured *HH* isomer to the thermodynamically favoured *HT* isomer can likely be attributed to internal strain due to the distortion from the ideal square planar geometry around the metal centre. An exception to the tendency for *HT* configuration is when the two metal centres have different oxidation states – for example, M and $M^+$ – and can be rationalised by the soft P and the hard N preferably binding to M and $M^+$, respectively, to form the *HH*-isomer (Figure 1.16B).

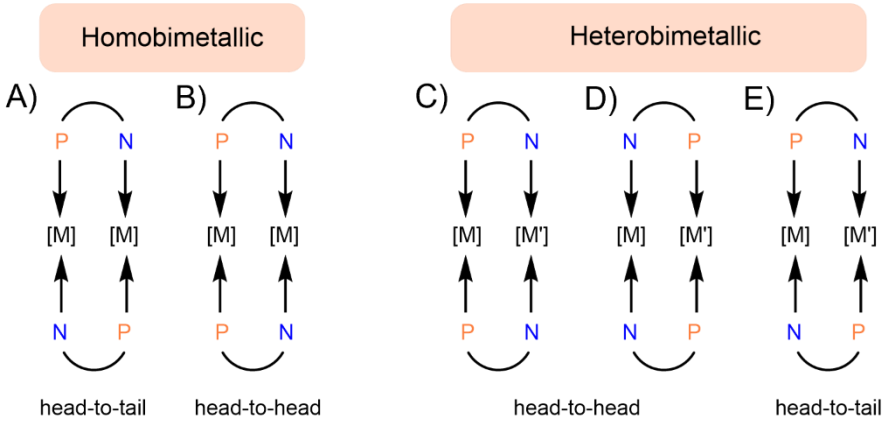


**Figure 1.16.** Binding configurations that can be observed with μ*PN* coordination of a 1,3-P,N ligand. (A) head-to-tail and (B) head-to-head configurations in homobimetallic complexes; (C) and (D) the different head-to-head configurations and (E) head-to-tail configuration of heterobimetallic complexes.

For heterobimetallic systems, two *HH* configurations can exist depending on P and N coordination to M and M′, respectively, or *vice versa* (Figure 1.14C and D). The relative hardness/softness of M and M′ influence the ratios of *HH* isomers and *HT* isomers; if one metal is much harder the *HH* isomer predominates and if the metals are very similar the *HT* isomer is dominant (Figure 1.14E). The rigidity of the pyridyl- and imidazolyl-based backbones are suited to μ*P,N* coordination as they do not allow a large metal···metal separation. In contrast, there are a limited number of bimetallic complexes obtained with the non-rigid aminophosphine ligands and can be explained by the nearly planar configuration of the free amino N-donor which precludes coordination to a metal centre.

### 1.4.4 Azophosphines as Ligands

All previous examples of 1,3-P,N ligands feature C as the bridging element between the P and N donors. The combination of a soft phosphorus and hard nitrogen donor classify azophosphines as 1,3-P,N ligands; however, their coordination chemistry had remained unexplored (Figure 1.17A). The work by Cummins and co-workers had

focussed instead on the onward reactivity of azophosphines in cycloaddition reactions (Figure 1.17B).[44,47] Indeed, the Jupp group has very recently reported five- and seven-membered phosphorus-based heterocycles that can be derived from cycloaddition reactions of azophosphines (Figure 1.17C and D).[103]

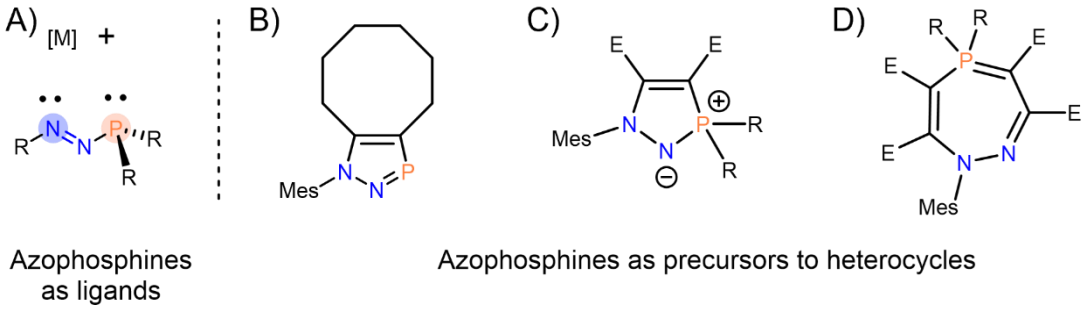


**Figure 1.17.** Applications of azophosphines as (A) ligands; (B) as precursors to P- and N-based heterocycles by Cummins and co-workers;[44,47] and (C and D) by Jupp and co-workers.[103] M, metal; Mes, mesityl; E, $CO_2Et$ (Et, ethyl).

The only prior example of a coordinated azophosphine was the unexpected reaction of a $PF_3$ ligand in $[RhCl(PF_3)(PPh_3)_2]$ with a silyldiazene, which generated the *P,P*-difluoroazophosphine $PhN{=}N{-}PF_2$ bound to Rh; this product was only characterised by NMR spectroscopy and elemental analysis, but the results were consistent with P coordination of the ligand.[104] Our work in the Jupp group has demonstrated that azophosphines can act as 1,3-P,N ligands in ruthenium complexes.[48,49] This research will be presented in Chapter 4.

## 1.5 Photo-switchable N=N Bond

Molecular switches are a type of artificial molecular machine which uses various stimuli to switch between two metastable states. Much of the contemporary research is focussed around molecular photoswitches, attributable to the low toxicity and ease of implementation of light. Classic examples of photoswitches include photo-induced

cycloadditions, heterolytic cleavage of σ-bonds, or *trans*- to *cis*-isomerisation of π-bonds.[105] Of the latter, those based on isomerisation due to the N=N bond have particular success due, in part, to their convenient isomerisation induced by light in the visible or near-UV range and a facile synthesis which enables control over substituents thus providing excellent tuneability.[106]

### 1.5.1 Azobenzene

Azobenzene is a well-studied N=N photoswitch (Figure 1.18A).[105–108] Since Hartley discovered the *cis*-isomer of azobenzene in 1937,[109,110] additional studies soon concluded that the *trans*-isomer is more stable than the *cis*-isomer, with an energy barrier to the photoexcited state of ~20-25 kcal $mol^{-1}$ meaning, at room temperature, the *trans*-isomer prevails over the *cis*-isomer in the dark.[111] The former is converted to the latter by irradiation with wavelengths of 300-350 nm; the reverse process occurs thermally and by irradiation at 400-450 nm.[108] Representative UV/Vis spectra of *trans*- and *cis*-azobenzene are shown in Figure 1.18B, where the main absorption peak of the *trans*-isomer between 300-350 nm corresponds to π-π* transitions, and the smaller absorption peak between 400-450 nm corresponds to n-π* transitions. Incomplete switching due to overlapping absorptions are a significant disadvantage,[112] and thermal isomerisation of the *cis*-isomer back to the more favourable *trans*-isomer can occur within milliseconds or days, dependent on substituents and conditions.[111]

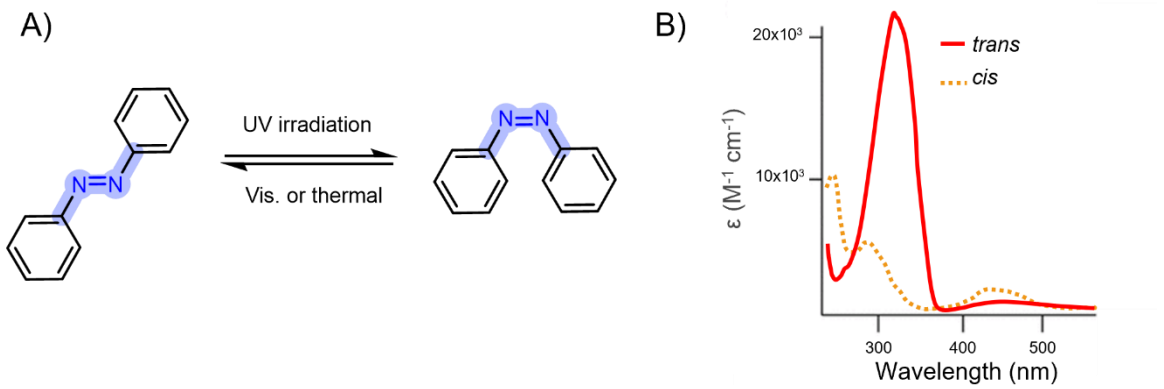


**Figure 1.18.** (A) *trans*- to *cis*- isomerism of azobenzene; (B) schematic UV/Vis spectra of *trans*- and *cis*-isomers of azobenzene. Figure adapted from Luboch and Wagner-Wysiecka.[108]

The mechanisms of N=N bond isomerisation are debated and can depend on the substituents at the N=N bond, in addition to solvent and pressure; however, the most common for *trans*- to *cis*-isomerisation are inversion and rotation.[113] Weakly allowed n–π* electronic transitions, from the $S_0$ to $S_1$ state, are predicted to facilitate inversion at the nitrogen atom, whilst more intense symmetry allowed π-π* transitions, from the $S_0$ to $S_2$ state, are predicted to facilitate rotation (Scheme 1.6A and B, respectively).[114] Common to both is the excitation of electrons into the π* orbital, thus weakening the N=N bond sufficiently for inversion or rotation to occur. Photo-induced push-pull resonance and tautomerism are other possible mechanisms photoswitches following these mechanisms have fewer applications due to the relatively free rotation limiting their control.[113]

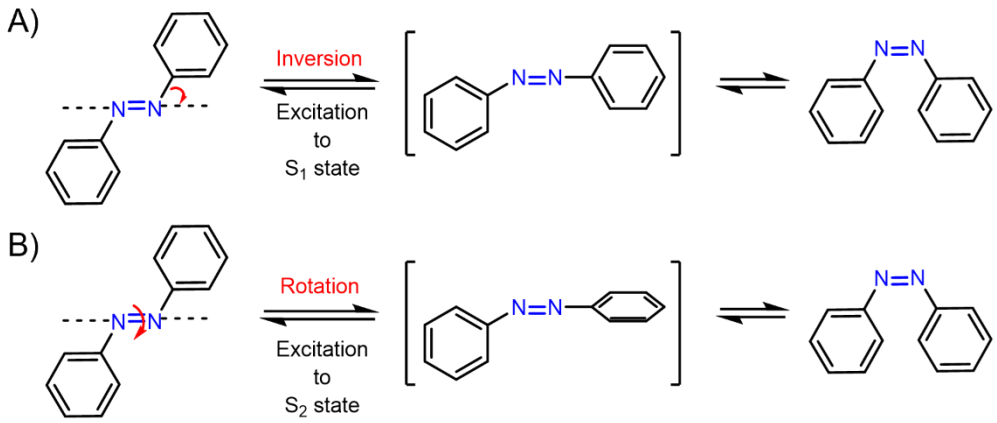


**Scheme 1.6.** Photoisomerisation of N=N bond *via* mechanisms of (A) inversion and (B) rotation.

In recent years, azo-based compounds have seen increased medical applications, where they are used to modulate biological processes.[115,116] Light of at least 600 nm wavelength is long enough to penetrate deeper into human tissue, thus enabling a photoswitch to localise activation of a prodrug and/or modulate biological processes with light. An azo-$BF_2$ based photoswitch has been synthesised with a longer activation wavelength for this purpose.[117] Photoswitchable catalysis, however, has received the most development.[118]

### 1.5.2 Phosphines as Photoswitches

As discussed in Section 1.4, phosphines are common ligands in organometallic catalysts. The strong σ-donating ability of the phosphorus lone pair, combined with π-acidity, variable steric properties, and wide range of possible bite angles enable phosphines to facilitate a range of catalytic processes.[119] Most commonly, their use as photoswitchable catalysts has been in combination with azo compounds, thus combining the advantages of N=N photoswitches with the coordinating ability of phosphines.[120–122] Although these molecules contain azo groups and phosphine groups, they are not directly bonded to each other (Figure 1.19).

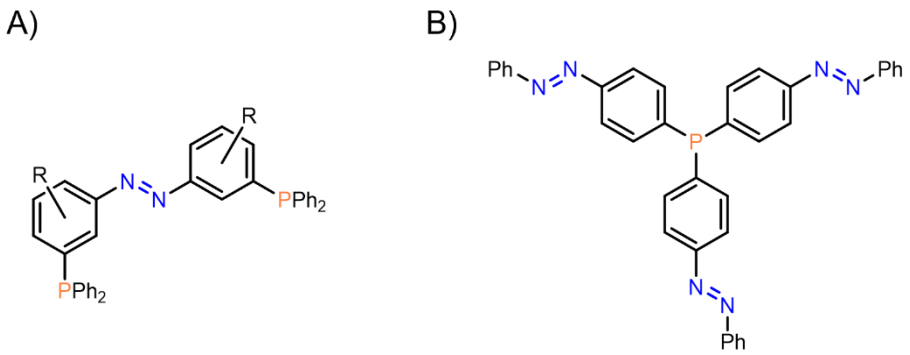


**Figure 1.19.** *Trans*-isomers of phosphine ligands based on an azobenzene backbone reported by (A) Marinetti and co-workers[121] and (B) Freixa and co-workers.[122]

Coordination of the diphosphine (Figure 1.19A) to independent Au(I) centres and photoisomerization of the N=N bond to the *cis*-isomer resulted in significantly enhanced catalytic activity compared to the *trans*-isomer.[121] The authors proposed a cooperative effect is enabled between the two Au(I) atoms in the *cis*-isomer which is not possible within the *trans*-isomer. The *trans*- to *cis*-isomerisation of an azobenzene-appended phosphine ligand (Figure 1.19B) was found to remain efficient when $\kappa^1$*P* coordinated to a Ru(II)(*p*-cymene) framework, whereas for the analogous coordination of azobenzene-appended pyridine it was strongly inhibited.[122] When tested as a precatalyst, the authors cite proof-of-concept for light-controlled hydrogen generation. The development of these ligands as photoswitchable catalysts when coordinated to a metal centre has been hindered due to the mechanisms of catalysis being poorly understood.

### 1.5.3 Azophosphines as Photoswitches

The presence of the N=N azo group in azophosphines begs the question of their potential photoswitching properties (Scheme 1.7).

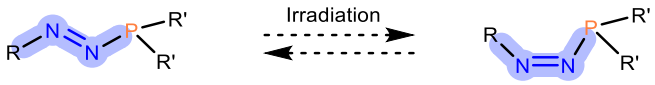


**Scheme 1.7.** Hypothesised *trans*- to *cis*-photoisomerisation of azophosphines.

No research into the viability of this application of azophosphines has yet been published. Research towards answering this question runs through this thesis as subsections within Chapters 2 – 4.

## 1.6 Project Aims

This thesis is concerned with exploring azophosphines as heavier analogues of triazenes - specifically, their synthesis, coordination chemistry and catalytic applications (Figure 1.20).

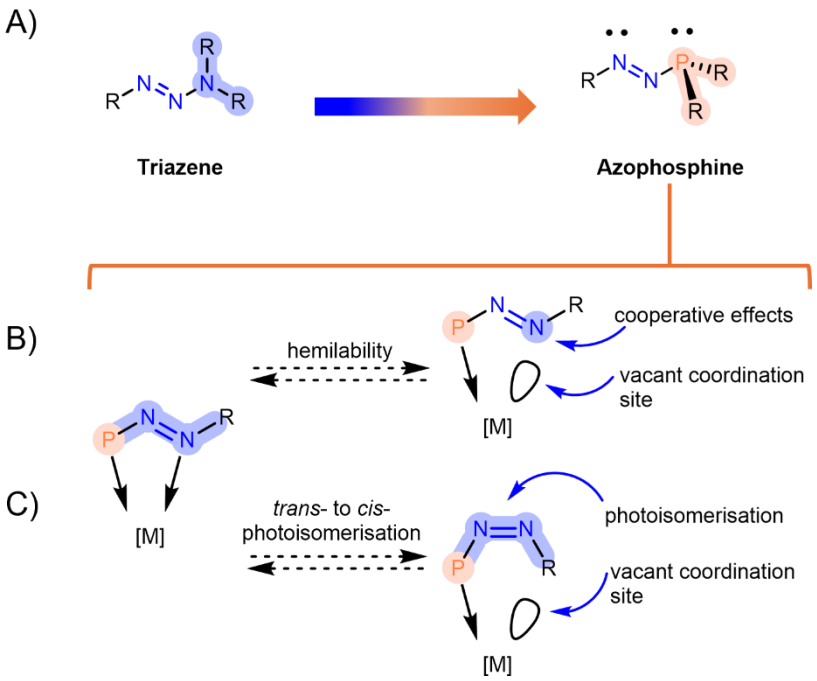


**Figure 1.20.** (A) Potential localisation of P lone pair in azophosphines relative to triazenes; (B) Viable application of azophosphines as 1,3-P,N hybrid ligands; (C) Hypothesised photoisomerisation of N=N bond in azophosphines.

At the time of starting this research, the study of azophosphines was limited to only two publications in the 1970s and 80s in which analyses of their key properties were not pursued.[43,45] By possessing the N=N–P moiety, azophosphines hold a wealth of chemistry to be explored. The reduced propensity of the P lone pair for delocalisation in other phosphorus-containing analogues of nitrogen-containing moieties suggest azophosphines could serve as P- and N-donor ligands (Figure 1.20A). The rich coordination chemistry of hybrid ligands opens viable applications of azophosphines in organometallic catalysis (Figure 1.20B). Direct bonding of the phosphorus to an N=N azo group suggests that an investigation of the photoswitching capability of azophosphines, in which fundamental chemistry beyond the immediate implications of a photoswitchable ligand, could be explored (Figure 1.20C).

Broadly, the aims of this research can be categorised as follows:

1) To develop a simple and general synthetic method to azophosphines that tolerates tuning of sterics and electronics (Chapter 2).
2) To understand the fundamental properties of azophosphines and introduce systematic modulations from which trends in azophosphines can be identified (Chapters 2 and 3).
3) To determine whether azophosphines are competent ligands and explore their coordination chemistry (Chapter 4).
4) To investigate the application of azophosphines in organometallic catalysis (Chapter 5).
5) To elucidate whether the presence of the N=N azo group in azophosphines yields photoswitchable properties similar to azobenzene, whether as a free ligand (Chapters 2 and 3) or when coordinated to a metal centre (Chapter 4).

## References


1 P. Le Floch, *Coord. Chem. Rev.*, 2006, **250**, 627–681.

2 N. T. Coles, A. Sofie Abels, J. Leitl, R. Wolf, H. Grützmacher and C. Müller, *Coord. Chem. Rev.*, 2021, **433**, 213729.

3 A. J. Ashe, *J. Am. Chem. Soc.*, 1971, **93**, 3293–3295.

4 J. M. Goicoechea and H. Grützmacher, *Angew. Chem. Int. Ed.*, 2018, **57**, 16968–16994.

5 M. Regitz, *Chem. Rev.*, 1990, **90**, 191–213.

6 J. G. Cordaro, D. Stein, H. Rüegger, H. Grützmacher, J. G. Cordaro, D. Stein, H. Rüegger and H. Grützmacher, *Angew. Chem. Int. Ed.*, 2006, **45**, 6159–6162.

7 D. W. N. Wilson, S. J. Urwin, E. S. Yang and J. M. Goicoechea, *J. Am. Chem. Soc.*, 2021, **143**, 10367–10373.

8 A. R. Jupp and J. M. Goicoechea, *Angew. Chem. Int.Ed.*, 2013, **52**, 10064–10067.

9 A. R. Jupp and J. M. Goicoechea, *J. Am. Chem. Soc.*, 2013, **135**, 19131–19134.

10 K. M. Szkop, A. R. Jupp and D. W. Stephan, *J. Am. Chem. Soc.*, 2018, **140**, 12751–12755.

11 B. Lu, J. Jiang, L. Wang, A. R. Jupp, J. M. Goicoechea, S. Liu, Z. Li, M. Zhou and X. Zeng, *J. Am. Chem. Soc.*, 2024, **146**, 18699–18705.

12 K. B. Dillon, F. Mathey and J. F. Nixon, *Phosphorus: The Carbon Copy: From Organophosphorus to Phospha-organic Chemistry*, John Wiley & Sons, Ltd, 1998.

13 H. W. Melville and S. C. Gray, *Trans. Faraday Soc.*, 1936, **32**, 271–285.

14 D. P. Stevenson and D. M. Yost, *J. Chem. Phys.*, 1941, **9**, 403–408.

15 N. A. Piro, J. S. Figueroa, J. T. McKellar and C. C. Cummins, *Science*, 2006, **313**, 1276–1279.

16 N. A. Piro and C. C. Cummins, *J. Am. Chem. Soc.*, 2008, **130**, 9524–9535.

17 D. Tofan and C. C. Cummins, *Angew. Chem. Int. Ed.*, 2010, **49**, 7516–7518.

18 W. Kutzelnigg, *Angew. Chem. Int. Ed.,*1984, **23**, 272–295.

19 L. T. Xu and T. H. Dunning, *J. Chem. Theory Comput.*, 2015, **11**, 2496–2507.

20 K. I. Goldberg, D. M. Hoffman and R. Hoffmann, *Inorg. Chem.*, 1982, **21**, 3863–3868.

21 S. W. Benson, *J. Chem. Educ.*, 1965, **42**, 502–515.

22 S. Wang, J. D. Sears, C. E. Moore, A. L. Rheingold, M. L. Niedig and J. S. Figueroa, *Science*, 2022, **375**, 1393–1397.

23 J. F. Nixon, *Coord. Chem. Rev.*, 1995, **145**, 201–258.

24 C. Camp, N. Settineri, J. Lefèvre, A. R. Jupp, J. M. Goicoechea, L. Maron and J. Arnold, *Chem. Sci.*, 2015, **6**, 6379–6384.

25 A. R. Jupp, M. B. Geeson, J. E. McGrady and J. M. Goicoechea, *Eur. J. Inorg. Chem.*, 2016, **2016**, 639–648.

26 S. Basappa, R. Bhawar, D. H. Nagaraju and S. K. Bose, *Dalton Trans.*, 2022, **51**, 3778–3806.

27 D. Heift, Z. Benko, H. Grützmacher, A. R. Jupp and J. M. Goicoechea, *Chem. Sci.*, 2015, **6**, 4017–4024.

28 S. V. F. Beddoe, S. D. Cosham, A. N. Kulak, A. R. Jupp, J. M. Goicoechea and G. Hyett, *Dalton Trans.*, 2018, **47**, 9221–9225.

29 M. B. Geeson, A. R. Jupp, J. E. McGrady and J. M. Goicoechea, *Chem. Commun.*, 2014, **50**, 12281–12284.

30 S. Akocak, N. Lolak, S. Bua and C. T. Supuran, *J. Enzyme Inhib. Med. Chem.*, 2018, **33**, 1575–1580.

31 N. Lolak, S. Akocak, S. Bua, M. Koca and C. T. Supuran, *Bioorg. Chem.*, 2018, **77**, 542–547.

32 A. Khazaei, M. Kazem-Rostami, A. Zare, A. R. Moosavi-Zare, M. Sadeghpour and A. Afkhami, *J. Appl. Polym. Sci.*, 2013, **129**, 3439–3446.

33 A. A. Suleymanov and K. Severin, *Angew. Chem. Int. Ed.*, 2021, **60**, 6879–6889.

34 D. B. Kimball and M. M. Haley, *Angew. Chem. Int. Ed.*, 2002, **41**, 3338–3351.

35 R. Lazny, J. Poplawski, J. Kobberling, D. Enders and S. Brase, *Synlett*, 1999, **1999**, 1304–1306.

36 F. R. Fronczek, C. Hansch and S. F. Watkins, *Acta Crystallogr. C Struct. Chem.*, 1988, **44**, 1651–1653.

37 G. Albertin, S. Antonlutti, M. Bedin, J. Castro and S. Garcia-Fontán, *Inorg. Chem.*, 2006, **45**, 3816–3825.

38 M. Yoshifuji, *Eur. J. Inorg. Chem.*, 2016, **2016**, 607–615.

39 L. Weber, F. Ebeler and R. S. Ghadwal, *Coord. Chem. Rev.*, 2022, **461**, 214499.

40 L. Weber, *Chem. Rev.*, 1992, **92**, 1839–1906.

41 A. M. Tondreau, Z. Zolt´, Z. Benk}, J. R. Harmer, H. Hansj¨, H. Grützmacher and G. Grützmacher, *Chem. Sci.*, 2014, **5**, 1545–1554.

42 W. Schneid, Zur Darstellung und Reactivität Silylierter, Germylierter und Stannylierter Mono(Organyl)Diimine, Ludwig Maximilians-Universitat Munchen, 1977.

43 O. A. Attanasi, P. Filippone, P. Guerra and F. Serra-Zanetti, *Synth. Commun.*, 1987, **17**, 555–561.

44 M. L. Y. Riu, W. J. Transue, J. M. Rall and C. C. Cummins, *J. Am. Chem. Soc.*, 2021, **143**, 7635–7640.

45 N. Wiberg, *Adv. Organomet. Chem.*, 1984, **23**, 131–191.

46 G. Schwenk, Zur Reaktivität von Bis(Trimethylsilyl)-Diimine, Ludwig Maximilians-Universitat Munchen, 1971.

47 K. Tanaka, M.-L. Y. Riu, B. Valladares and C. C. Cummins, *Inorg. Chem.*, 2022, **61**, 13662–13666.

48 E. J. Jordan, E. D. E. Calder, H. V. Adcock, L. Male, M. Nieger, J. C. Slootweg and A. R. Jupp, *Chem. – Eur. J.*, 2024, **30**, 35, e202401358.

49 E. J. Jordan, E. D. E. Calder, B. L. Greene, H. V. Adcock, L. Male, P. W. Davies and A. R. Jupp, *Organometallics*, 2024, **43**, 2674–2685.

50 J. F. Young, J. A. Osborn, F. H. Jardine and G. Wilkinson, *Chem. Commun. (London)*, 1965, 131–132.

51 N. Aresta, M. Rossi, A. Sacco, ; A Bennett, D. A. Milner, ; P Meakin, J. P. Jesson and C. A. Tolman, *Acc. Chem. Res.*, 1979, **12**, 331–337.

52 T. M. Trnka and R. H. Grubbs, *Acc. Chem. Res.*, 2001, **34**, 18–29.

53 L. Vaska and J. W. DiLuzio, *J. Am. Chem. Soc.*, 1961, **83**, 2784–2785.

54 C. A. Tolman, *J. Am. Chem. Soc.*, 1970, **92**, 2953–2956.

55 D. G. Gilheany, *Chem. Rev.*, 1994, **94**, 1339–1374.

56 A. Pascariu, S. Iliescu, A. Popa and G. Ilia, *J. Organomet. Chem.*, 2009, **694**, 3982–4000.

57 P. Dierkes and P. W. N. M. Van Leeuwen*, Dalton Trans.*, 1999, 1519–1530.

58 S. M. Mansell, *Dalton Trans.*, 2017, **46**, 15157–15174.

59 C. A. Tolman, *Chem. Rev.*, 1977, **77**, 313–348.

60 A. C. Hillier, W. J. Sommer, B. S. Yong, J. L. Petersen, L. Cavallo and S. P. Nolan, *Organometallics*, 2003, **22**, 4322–4326.

61 H. Clavier and S. P. Nolan, *Chem. Commun.*, 2010, **46**, 841–861.

62 P. B. Dias, M. E. M. de Piedade and J. A. M. Simões, *Coord. Chem. Rev.*, 1994, **135–136**, 737–807.

63 E. C. Alyea and S. Song, *Comments on Inorganic Chemistry*, 1996, **18**, 189–221.

64 S. Song and E. C. Alyea, *Comments on Inorganic Chemistry*, 1996, **18**, 145–164.

65 W. H. Zhang, S. W. Chien and T. S. A. Hor, *Coord. Chem. Rev.*, 2011, **255**, 1991–2024.

66 A. Bader and E. Lindner, *Coord. Chem. Rev.*, 1991, **108**, 27–110.

67 M. B. Smith, *Molecules,* 2022, **27**, 6293.

68 Q. J. Bruch, A. Tanushi, P. Müller and A. T. Radosevich, *J. Am. Chem. Soc.*, 2022, **144**, 21443–21447.

69 J. I. Van Der Vlugt, *Eur. J. Inorg. Chem.*, 2012, **2012**, 363–375.

70 V. T. Annibale, D. A. Dalessandro and D. Song, *J. Am. Chem. Soc.*, 2013, **135**, 16175–16183.

71 K. Lee, C. M. Donahue and S. R. Daly, *Dalton Trans.*, 2017, **46**, 9394–9406.

72 M. Skaria, J. D. Culpepper and S. R. Daly, *Chem. – Eur. J.*, 2022, **28**, e202201791.

73 J. R. Khusnutdinova, D. Milstein, D. Milstein and J. R. Khusnutdinova, *Angew. Chem. Int. Ed.*, 2015, **54**, 12236–12273.

74 E. R. M. Habraken, A. R. Jupp, M. B. Brands, M. Nieger, A. W. Ehlers and J. C. Slootweg, *Eur. J. Inorg. Chem.*, 2019, **2019**, 2436–2442.

75 G. C. Welch, R. R. San Juan, J. D. Masuda and D. W. Stephan, *Science*, 2006, **314**, 1124–1126.

76 D. W. Stephan, *J. Am. Chem. Soc.*, 2015, **137**, 10018–10032.

77 M. K. Rong, F. Holtrop, J. C. Slootweg and K. Lammertsma, *Coord. Chem. Rev.*, 2019, **380**, 1–16.

78 M. K. Rong, F. Holtrop, J. C. Slootweg and K. Lammertsma, *Coord. Chem. Rev.*, 2019, **382**, 57–68.

79 G. R. Newkome, *Chem. Rev.*, 1993, **93**, 2067–2089.

80 Z. Z. Zhang and H. Cheng, *Coord. Chem. Rev.*, 1996, **147**, 1–39.

81 H. G. Ang, W. E. Kow and K. F. Mok, *Inorg. Nucl. Chem. Letters*, 1972, **8**, 829–832.

82 P. C. Kunz, I. Thiel, A. L. Noffke, G. J. Reiß, F. Mohr and B. Spingler, *J. Organomet. Chem.*, 2012, **697**, 33–40.

83 L. Hintermann, T. T. Dang, A. Labonne, T. Kribber, L. Xiao and P. Naumov, *Chem. – Eur. J.*, 2009, **15**, 7167–7179.

84 S. Maity, A. Bera, A. Bhattacharjya and P. Maity, *Org. Biomol. Chem.*, 2023, **21**, 5671–5690.

85 T. Vandijk, S. Burck, A. J. Rosenthal, M. Nieger, A. W. Ehlers, J. C. Slootweg and K. Lammertsma, *Chem. – Eur. J.*, 2015, **21**, 9328–9331.

86 J. E. Radcliffe, A. S. Batsanov, D. M. Smith, J. A. Scott, P. W. Dyer and M. J. Hanton, *ACS Catal.*, 2015, **5**, 7095–7098.

87 M. Fischer, H. Steinert, M. Schmidtmann and R. Beckhaus, *Dalton Trans.*, 2019, **48**, 1936–1940.

88 T. Van Dijk, S. Burck, M. K. Rong, A. J. Rosenthal, M. Nieger, J. C. Slootweg and K. Lammertsma, *Angew. Chem. Int. Ed.*, 2014, **53**, 9068–9071.

89 T. Van Dijk, M. S. Bakker, F. Holtrop, M. Nieger, J. C. Slootweg and K. Lammertsma, *Org. Lett.*, 2015, **17**, 1461–1464.

90 T. Van Dijk, M. K. Rong, J. E. Borger, M. Nieger, J. C. Slootweg and K. Lammertsma, *Organometallics*, 2016, **35**, 827–835.

91 M. K. Rong, K. Van Duin, T. Van Dijk, J. J. M. De Pater, B. J. Deelman, M. Nieger, A. W. Ehlers, J. C. Slootweg and K. Lammertsma, *Organometallics*, 2017, **36**, 1079–1090.

92 E. S. Donovan, B. M. Barry, C. A. Larsen, M. N. Wirtz, W. E. Geiger and R. A. Kemp, *Chem. Commun.*, 2016, **52**, 1685–1688.

93 E. C. Carson and S. J. Lippard, *J. Am. Chem. Soc.*, 2004, **126**, 3412–3413.

94 M. K. Rong, F. Holtrop, E. O. Bobylev, M. Nieger, A. W. Ehlers, J. C. Slootweg and K. Lammertsma, *Chem. – Eur. J.*, 2021, **27**, 14007–14016.

95 D. B. Grotjahn and D. A. Lev, *J. Am. Chem. Soc.*, 2004, **26**, 12232–12233.

96 D. B. Grotjahn, C. D. Incarvito and A. L. Rheingold, *Angew. Chem. Int. Ed.*, 2001, **40**, 3884–3887.

97 D. B. Grotjahn, Y. Gong, L. Zakharov, J. A. Golen and A. L. Rheingold, *J. Am. Chem. Soc*, 2006, **128**, 438–453.

98 D. B. Grotjahn, *Chem. – Eur. J.*, 2005, **11**, 7146–7153.

99 A. Labonne, T. Kribber and L. Hintermann, *Org. Lett.*, 2006, **8**, 5853–5856.

100 K. Q. Almeida Leñero, Y. Guari, P. C. J. Kamer, P. W. N. M. Van Leeuwen, B. Donnadieu, S. Sabo-Etienne, B. Chaudret, M. Lutz and A. L. Spek, *Dalton Trans.*, 2013, **42**, 6495–6512.

101 M. Rashidi, M. C. Jennings and R. J. Puddephatt, *Organometallics*, 2003, **22**, 2612–2618.

102 L. Párkányi, G. Szalontai and G. Besenyei, *Inorganica Chim. Acta*, 2006, **359**, 2933–2941.

103 E. D. E. Calder, L. Male and A. R. Jupp, *Dalton Trans.*, 2024, **53**, 15032–15039.

104 J. F. Nixon and M. Kooti, *J. Organomet. Chem.*, 1978, **149**, 71–79.

105 J. D. Harris, M. J. Moran and I. Aprahamian, *Proc. Natl Acad. Sci. U S A*, 2018, **115**, 9414–9422.

106 S. Crespi, N. A. Simeth and B. König, *Nat. Rev. Chem.,* 2019, **3**, 133–146.

107 A. Tavassoli, A. D. Hamilton, D. R. Spring, A. A. Beharry and G. A. Woolley, *Chem. Soc. Rev.*, 2011, **40**, 4422–4437.

108 E. Wagner-Wysiecka, N. Łukasik, J. F. Biernat and E. Luboch, *J. Incl. Phenom. Macrocycl. Chem.*, 2018, **90**, 189–257.

109 G. S. Hartley, *Nature,* 1937, **140**, 281–281.

110 G. S. Hartley, *J. Chem. Soc. (Resumed)*, 1938, 633–642.

111 E. V. Brown and G. R. Granneman, *J. Am. Chem. Soc.*, 1975, **97**, 621–627.

112 C. E. Weston, R. D. Richardson, P. R. Haycock, A. J. P. White and M. J. Fuchter, *J. Am. Chem. Soc.*, 2014, **136**, 11878–11881.

113 J. Dokić, M. Gothe, J. Wirth, M. V. Peters, J. Schwarz, S. Hecht and P. Saalfrank, *J. Phys. Chem. A*, 2009, **113**, 6763–6773.

114 C. R. Crecca and A. E. Roitberg, *J. Phys. Chem. A*, 2006, **110**, 8188–8203.115

115 D. Prasad Mishra, P. Kumar Sahu, B. Acharya, S. Prasad Mishra and S. Bhati, *Results Chem.*, 2024, **10**, 101712.

116 P. Kobauri, F. J. Dekker, W. Szymanski and B. L. Feringa, *Angew. Chem. Int. Ed.*, 2023,**62**, e202300681.

117 Y. Yang, R. P. Hughes and I. Aprahamian, *J. Am. Chem. Soc.*, 2014, **136**, 13190–13193.

118 R. Dorel and B. L. Feringa, *Chem. Commun.*, 2019, **55**, 6477–6486.

119 P. Rojo, A. Riera and X. Verdaguer, *Coord. Chem. Rev.*, 2023, **489**, 215192.

120 H. Bricout, E. Banaszak, C. Len, F. Hapiot and E. Monflier, *Chem. Commun.*, 2010, **46**, 7813–7815.

121 T. Arif, C. Cazorla, N. Bogliotti, N. Saleh, F. Blanchard, V. Gandon, R. Métivier, J. Xie, A. Voituriez and A. Marinetti, *Catal. Sci. Technol.*, 2018, **8**, 710–715.

122 A. Telleria, P. W. N. M. Van Leeuwen and Z. Freixa, *Dalton Trans.*, 2017, **46**, 3569–3578.

# CHAPTER 2

# Synthesis of Azophosphines and Key Properties

## 2.1 Introduction and Objectives

### 2.1.1 Existing Syntheses of Azophosphines

Azophosphines (N=N–P) are a phosphorus-containing analogue of triazene (N=N–N), where the trivalent nitrogen atom has been replaced by a phosphorus atom. Azophosphines were first synthesised in the 1970s by Wiberg and co-workers by reaction of silyldiazenes and chlorophosphines, obtaining yields ranging between 20 – 90% (Scheme 2.1A).[1,2] As discussed in the doctorate thesis of Werner Schneid (Wiberg group, 1977), low yielding reactions were a result of thermal decay or polymerisation, particularly suffering when R = $R^1$ = Me or Ph (Me, methyl; Ph, phenyl).[2] The stimulus for the research described in this thesis was provided by prior research within the Wiberg group in which a silyl-azophosphine ($Me_3Si$–N=N–P) was postulated to be an intermediate in a reaction of bis(trimethylsilyl)diazene (BSD) with chlorophosphines, ultimately decomposing and reacting further with starting material to produce a diphosphine.[3]

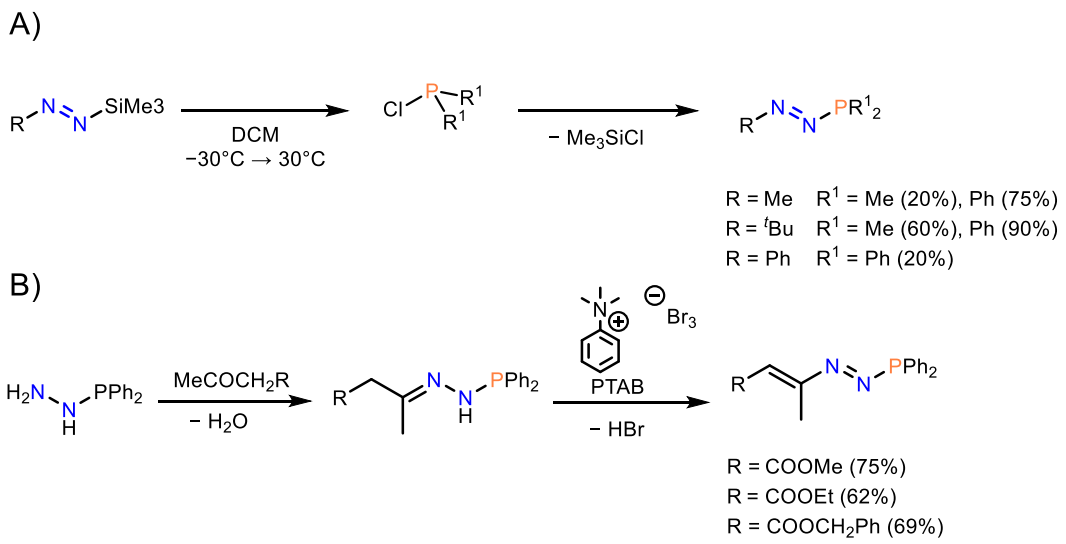


**Scheme 2.1.** (A) Wiberg synthesis of azophosphines by reaction of silyldiazenes and chlorophosphines; (B) Attanasi synthesis of alkenyl-substituted variants of azophosphines. Bu, butyl; Et, ethyl.

The next report of azophosphines came in the late 1980s when alkenyl-substituted variants were prepared by Attanasi and co-workers, obtaining yields of 62 – 75% (Scheme 2.1B).[4] The oily violet products were stored at −20 °C without appreciable decomposition for some weeks. It was over 30 years later, in 2021, that azophospines were revisited, when Cummins and co-workers synthesised and crystallographically characterised $MesN_2P$**A** (Mes = mesityl, **A** = anthracene, Scheme 2.2A).[5] This molecule was prepared in 14% yield and was thermally unstable due to the loss of the labile anthracene moiety, which enabled the molecule to act as a synthetic equivalent of mesitylphosphaazide ($MesN_2P$) in a range of cycloaddition reactions.

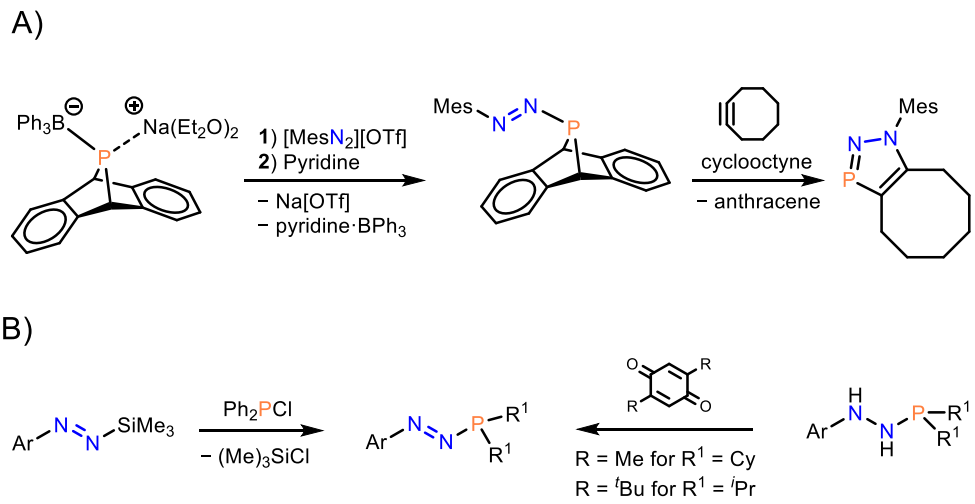


**Scheme 2.2.** Previous syntheses of azophosphines by the Cummins group. (A) Synthesis of $MesN_2P$**A**; (B) using silyldiazenes and chlorophosphines (left to right), and oxidation of a phosphinohydrazine (right to left). Pr, propyl; Cy, cyclohexyl.

The Cummins group also recently published the synthesis of a wider family of azophosphines, and explored their reactivity with alkynes to afford N-heterocyclic iminophosphoranes.[6] The azophosphines were synthesised in two different ways. The first method was analogous to Wiberg's approach[1] involving the reaction of silyldiazenes and chlorophosphines such as $^{i}Pr_2PCl$. The second approach involved

the oxidation of phosphinohydrazines with benzoquinones (BQ) and could tolerate the larger P-substituents $^{i}$Pr and Cy, although the size of the BQ had to be tailored to the steric profile of the azophosphine (Scheme 2.2B). At the time of starting the research discussed in this chapter, publications [5] and [6] by Cummins and co-workers had not been published; however, following their publication a general synthetic route to azophosphines that tolerates bulky groups is still missing.

Azophosphonium cations, $[Ar–N=N–PR_3]^+$, have recently been synthesised and are readily accessible by simple addition of a tertiary phosphine ($PR_3$) to an arenediazonium salt.[7,8,9] Unpublished research by the Jupp group found the analogous reactivity of a secondary phosphine ($HPR_2$) with arenediazonium cations (for subsequent deprotonation to the neutral azophosphine) led to uncontrolled reactivity and decomposition (Scheme 2.3A). Similarly unsuccessful results were observed for direct reactions of phosphide anions ($[PR_2]^-$) with diazonium salts, which was postulated to be due to single-electron transfer processes and subsequent decomposition of the neutral diazenyl radical (Scheme 2.3B).

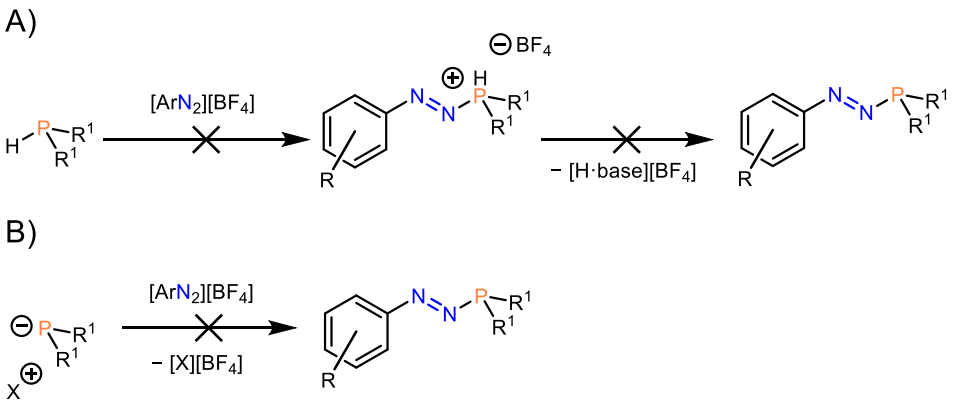


**Scheme 2.3.** Unsuccessful syntheses of azophosphines *via* arenediazonium salts and (A) secondary phosphines; (B) phosphide anions. Syntheses attempted by Dr Andrew Jupp.

### 2.1.2 Chapter Outline

This chapter will discuss the development of a general synthetic procedure for azophosphines. Using diazonium salts and secondary phosphine-boranes as starting materials, the synthesis follows a protection/deprotection strategy by first synthesising the borane-capped azophosphine which can be later deprotected to the corresponding azophosphine (Scheme 2.4). This synthetic strategy tempers the reactivity of the phosphorus lone pair and conveniently provides air-stable precursors to the target azophosphines.

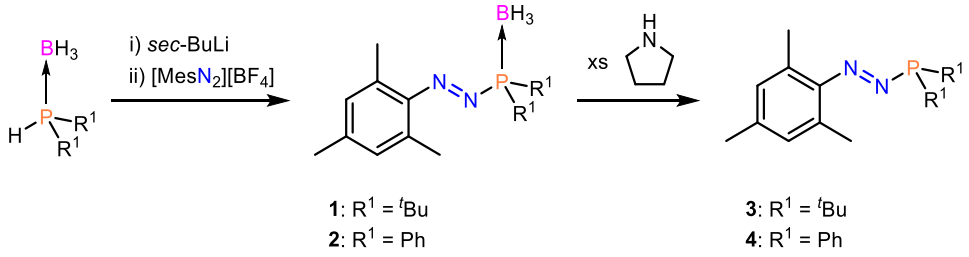


**Scheme 2.4.** General synthesis of azophosphine-boranes, and subsequent deprotection to the corresponding azophosphine.

For the exploratory syntheses, $R^1$ was maintained as *tert*-butyl ($^t$Bu) and the *N*-aryl group was, predominantly, maintained as mesityl (Mes) to target $MesN_2P^tBu_2{\cdot}BH_3$ (**1**). To establish that the bulky, alkyl $^t$Bu groups on phosphorus were not a prerequisite for the formation of azophosphine-boranes, the analogous $MesN_2PPh_2{\cdot}BH_3$ (**2**) azophosphine-borane was also synthesised. The stabilities of the deprotected azophosphines $MesN_2P^tBu_2$ (**3**) and $MesN_2PPh_2$ (**4**) will be discussed along with evidence for decomposition pathways, as provided by Electron Paramagnetic Resonance (EPR) spectroscopy. This chapter concludes with an investigation of the potential photo-switching properties of **1** – **4**, using UV/Vis and Transient Absorption spectroscopy measurements, and computational chemistry methods.

### 2.1.3 Acknowledgements

The EPR spectroscopy measurements discussed in this chapter were carried out by Callum Rosenberg (PhD student, Champness group, University of Birmingham), who ran all prepared samples and processed the corresponding data. Transient Absorption Spectroscopy (TAS) was carried out in collaboration with the University of Amsterdam. The TAS data were collected and processed by Maximilian Paradiz Dominguez (PhD student, Brouwer group, University of Amsterdam) on provided samples of **1** and **2**. The computational study discussed in Section 2.6.3 - a collaborative project with Dr Basile Curchod, University of Bristol - is titled 'Exploring the Photochemical Properties of a new Azobenzene Derivative, Azophosphine' by Pablo Rudolf Graf Rubia (MSci student, Curchod group, University of Bristol) in partial fulfilment of the requirements for the Honours Degree of MSci at the University of Bristol.[10]

### 2.1.4 Published Research

This chapter (Sections 2.3 and 2.4) contains research published in *Chemistry A European Journal*.[11] The remainder of the chapter is currently unpublished research.

## 2.2 Arenediazonium Salt Synthesis

Arenediazonium tetrafluoroborate salts ([$ArN_2$][$BF_4$]) were synthesised from known literature procedures.[9,12] The $[BF_4]^-$ salts were specifically targeted as they are known to be more stable than the commonly encountered chloride analogues.[13] Analogous arenediazonium triflate salts ([$ArN_2$][$OSO_2CF_3$]) were also synthesised due to the greater stability of the $[OSO_2CF_3]^-$ anion relative to the $[BF_4]^-$ anion. This is discussed in Section 2.3.1.

## 2.3 Azophosphine-Borane Synthesis[11]

### 2.3.1 Synthesis of $MesN_2P^tBu_2{\cdot}BH_3$ and $MesN_2PPh_2{\cdot}BH_3$

A 0.25 M solution of borane di(*t*Bu)phosphine ($H^tBu_2P{\cdot}BH_3$) in tetrahydrofuran (THF) was added to a stirred suspension of mesitylenediazonium tetrafluoroborate ([$MesN_2$][$BF_4$]) and the reaction monitored by $^{31}P\{^1H\}$ NMR spectroscopy (Scheme 2.5).

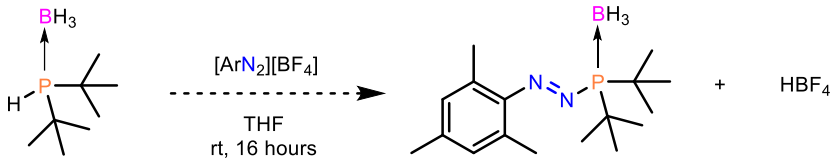


**Scheme 2.5.** Attempted synthesis of **1**. rt = room temperature.

To mitigate potential deprotection of $H^tBu_2P{\cdot}BH_3$ and premature deprotection of the borane azophosphine target, no base was added to capture the 1 equiv. of $HBF_4$ that would be generated. However, mostly unreacted $H^tBu_2P{\cdot}BH_3$ was observed in the $^{31}P\{^1H\}$ NMR spectrum identifiable by its quartet signal at 47.8 ppm, consistent with literature values. To circumvent any possible thermal or photochemical decomposition of the diazonium salt due to its slow reaction with the phosphine, *p*-

fluorobenzenediazonium tetrafluoroborate (*p*-(F)$C_6H_4N_2$][$BF_4$]), which is more reactive than its Mes analogue on account of its electron-withdrawing *p*-F substituent, was used as the arenediazonium salt. Addition of H$^t$Bu$_2$P·$BH_3$ to a stirred suspension of [*p*-(F)$C_6H_4N_2$][$BF_4$] gave an immediate pink colour; however, aliquots of the reaction solution showed several peaks in the $^{31}P\{^1H\}$ and $^{19}F\{^1H\}$ NMR spectra. Furthermore, the $^{11}B\{^1H\}$ spectrum showed additional peaks to those assigned to $BH_3$ and $[BF_4]^-$. It was concluded that generation of $HBF_4$ and subsequent decomposition of the $[BF_4]^-$ anion during the reaction was leading to a complex product mixture, thus preventing isolation of the target azophosphine-borane in the absence of base. To minimise the undesirable deprotection of H$^t$Bu$_2$P·$BH_3$ to H$^t$Bu$_2$P as a side reaction, 1 equiv. of triethylamine ($NEt_3$) base was added to a reaction mixture of [$MesN_2$][$BF_4$] and H$^t$Bu$_2$P·$BH_3$ in THF (Scheme 2.6) to serve as a proton scavenger.

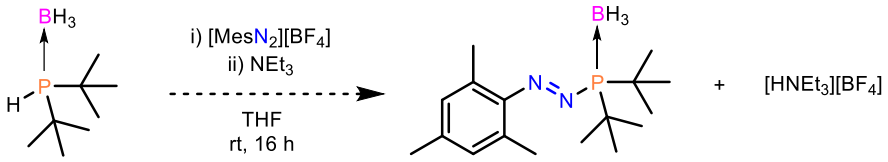


**Scheme 2.6.** Attempted synthesis of **1** using $NEt_3$ as base.

After stirring the mixture overnight, the $^{31}P\{^1H\}$ NMR spectrum showed only conversion of H$^t$Bu$_2$P·$BH_3$ to H$^t$Bu$_2$P, evidenced by the singlet at 19.6 ppm, in agreement with literature values of 20.0 ppm. The corresponding $^{31}P$ spectrum showed a doublet of multiplets due to $^1J_{P–H}$ coupling of the P–H and $^3J_{P–H}$ coupling of P to the 18 protons of the $^t$Bu groups.

To simultaneously evade addition of base to the reaction mixture to quench $HBF_4$ and acid-catalysed decomposition of the $[BF_4]^-$ anion, the diazonium salt was substituted

for its triflate analogue, chosen for the strong stability of the $[OSO_2CF_3]^-$ anion. However, addition of $H^tBu_2P{\cdot}BH_3$ to $[p\text{-}(F)C_6H_4N_2][OSO_2CF_3]$ in THF gave a solidified gel, likely due to acid-catalysed polymerisation of THF. Previously, the generated acid had reacted with the $[BF_4]^-$ anion, thus avoiding polymerisation of THF.

To circumvent the production of acid in the reaction mixture, use of an anionic base was considered to deprotonate the phosphine-borane prior to its addition to the diazonium salt (Scheme 2.7).

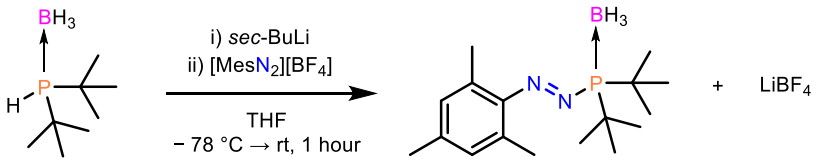


**Scheme 2.7.** Synthesis of **1** using *sec*-BuLi.

$H^tBu_2P{\cdot}BH_3$ was first deprotonated using 1 equiv. of *sec*-butyllithium (*sec*-BuLi) at −78 °C. The lithium phosphide-borane salt was added dropwise to a stirred cloudy suspension of $[MesN_2][BF_4]$ in THF at −78 °C to give an immediate purple colour and the formation of the target azophosphine-borane complex **1**. A broad quartet signal was observed at 108.5 ppm by $^{31}P\{^1H\}$ NMR spectroscopy, consistent with the P–B coupling expected for the product. A broad singlet signal was observed in the $^{31}P$ NMR spectrum, showing no presence of a P–H bond, as expected for the product. The borane group renders **1** air-stable enough to be purified by column chromatography and the product was isolated as an intensely coloured purple powder in 55 – 65% yield.

To assess whether this synthetic procedure would tolerate modulation of the phosphorus substituents, the analogous reaction of $HPPh_2{\cdot}BH_3$ with $[MesN_2][BF_4]$ was attempted, and gratifyingly gave **2** as an intensely coloured purple powder after work up in 42% yield.

The two azophosphine-borane complexes were characterised by single crystal X-ray diffraction (Figure 2.1); selected bond distances (Å) and angles (°) are tabulated in Table 2.1. The UV/Vis. spectra of **1** and **2** are discussed in Section 2.6.1. Full characterisation data for **1** and **2** are provided in the experimental section at the end of this chapter.

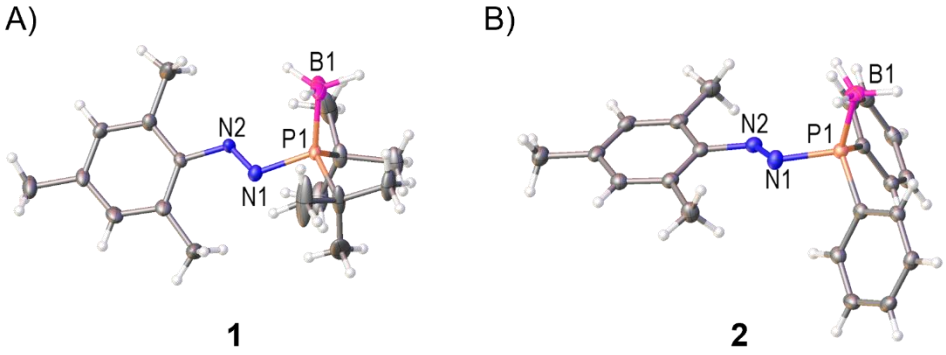


**1** **2**

**Figure 2.1.** Single crystal structures of **1** (A) and **2** (B). Selected bond distances (Å) and angles (°) are tabulated in Table 2.1. Thermal ellipsoids were drawn at the 50% probability level.[14]

### 2.3.2 Bond Metrics of $MesN_2P^tBu_2{\cdot}BH_3$ and $MesN_2PPh_2{\cdot}BH_3$

Comparison of the P1–N1 bond length of **1** (1.769(5) Å) and **2** (1.7565(10) Å) revealed no significant difference suggesting that, when pacified by the borane, there is minimal delocalisation of the phosphorus lone pair into the N=N π* orbital. The N=N bond length of **1** (1.226(6) Å) is shorter than that of **2** (1.2504(14) Å) and, due to the steric bulk of the $^t$Bu groups, the P1–$C_{tBu}$ bond lengths of **1** (1.862(6) Å, 1.844(6) Å) are slightly longer than the corresponding P1–$C_{Ar}$ bond lengths of **2** (1.7997(11) Å, 1.8021(11) Å). The P1–B1 bond length of **1** (1.925(10) Å) and **2** (1.9160(13) Å) showed no significant difference between bond length.

**Table 2.1.** Selected bond distances (Å) and bond angles (°) of crystallographically characterised azophosphine-boranes **1** and **2**.

| Structure | P1–$C_R$[a] | N1–N2 | P1–N1 | P1–N1–N2 |
|---|---|---|---|---|
| **1** | 1.862(6) | 1.226(6) | 1.769(5) | 113.5(4) |
| | 1.844(6) | | | |
| **2** | 1.7997(11) | 1.2504(14) | 1.7565(10) | 115.00(8) |
| | 1.8021(11) | | | |

[a] **1** R = $^t$Bu; **2** R = Ph.

## 2.4 Azophosphine Synthesis[11]

### 2.4.1 Synthesis of $MesN_2P^tBu_2$ and $MesN_2PPh_2$

The azophosphine-boranes are air-stable and easily-handled; however, the target is the deprotected azophosphine. Commonly, an amine is employed as a competing Lewis base to generate the deprotected phosphine and corresponding $R_3N{\cdot}BH_3$ species. Based on a study by Lloyd-Jones and Taylor,[15] which explored optimising the amine, diethylamine was first tested as the deprotecting base (Scheme 2.8).

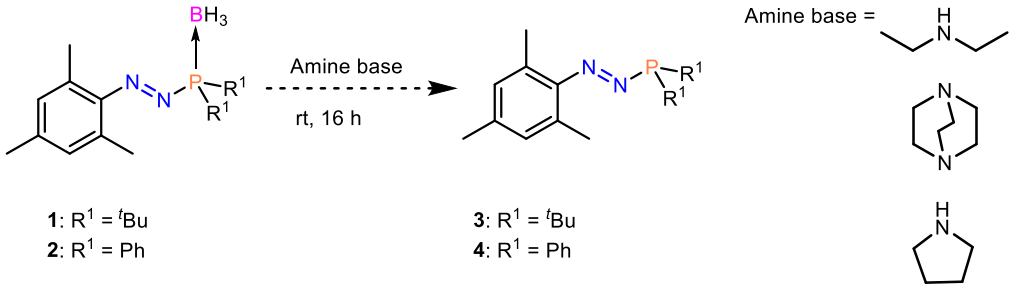


**Scheme 2.8.** Hypothesised deprotection of azophosphine-borane to azophosphine using an amine base. Amine bases tested (from top to bottom) = diethylamine, DABCO, pyrrolidine.

Advantageously, when used in excess, diethylamine could also act as solvent and be removed *in vacuo*, along with its borane adduct ($Et_2HN{\cdot}BH_3$), to leave the target deprotected azophosphine. Overnight (16 h) stirring of **1** and **2** in diethylamine failed to fully convert the azophosphine-boranes to their corresponding azophosphines, as

monitored by $^{31}P\{^{1}H\}$ NMR spectroscopy. Treatment of **1** with DABCO (1,4-diazabicyclo[2.2.2]octane), a highly nucleophilic base, resulted in a shift in the $^{31}P\{^{1}H\}$ NMR spectrum from 108.5 ppm to 118.3 ppm ($\Delta\delta$ = 9.8). The change of the broad quartet signal of **1** to a sharp singlet was indicative of loss of the quadrupolar boron centre. An additional peak in the $^{31}P\{^{1}H\}$ NMR spectrum at 20.1 ppm, however, was consistent with formation of $HP^{t}Bu_2$ as a side product, likely due to hydride transfer from DABCO·$BH_3$ to $MesN_2P^{t}Bu_2$.

The basicity of pyrrolidine sits in-between that of diethylamine and DABCO. Stirring a toluene solution of **1** with pyrrolidine (10 equiv.) overnight at room temperature gave full and clean conversion in the $^{31}P\{^{1}H\}$ NMR spectrum from the broad quartet signal of **1** to a sharp singlet at 118.3 ppm. Removal of excess pyrrolidine *in vacuo* followed by filtration through a silica plug to remove pyrrolidine·$BH_3$ afforded $MesN_2P^{t}Bu_2$ (**3**) as a purple oil in 82% yield. The analogous deprotection of **2** afforded $MesN_2PPh_2$ (**4**) as a purple oil in 66% yield and was accompanied by loss of the broad quartet signal of **2** to a sharp singlet with a smaller change in the $^{31}P\{^{1}H\}$ NMR chemical shift ($\Delta\delta$ = 1.2 ppm). The UV/Vis spectra of **3** and **4** are discussed in Section 2.6.1. Full characterisation data for **3** and **4** are provided in the experimental section at the end of this chapter.

## 2.5 Stability

During the syntheses of **1** – **4** it was noted that the synthesis of **2** resulted in more side product formation relative to **1**, and deprotection of **2** to **4** was lower yielding than **1** to **3** following filtrations through a silica plug. To ascertain the stability of azophosphines,

toluene solutions of **3** and **4**, prepared in J. Young NMR tubes, were monitored over eight weeks in ambient light (Figure 2.2, **3**_Light and **4**_Light).

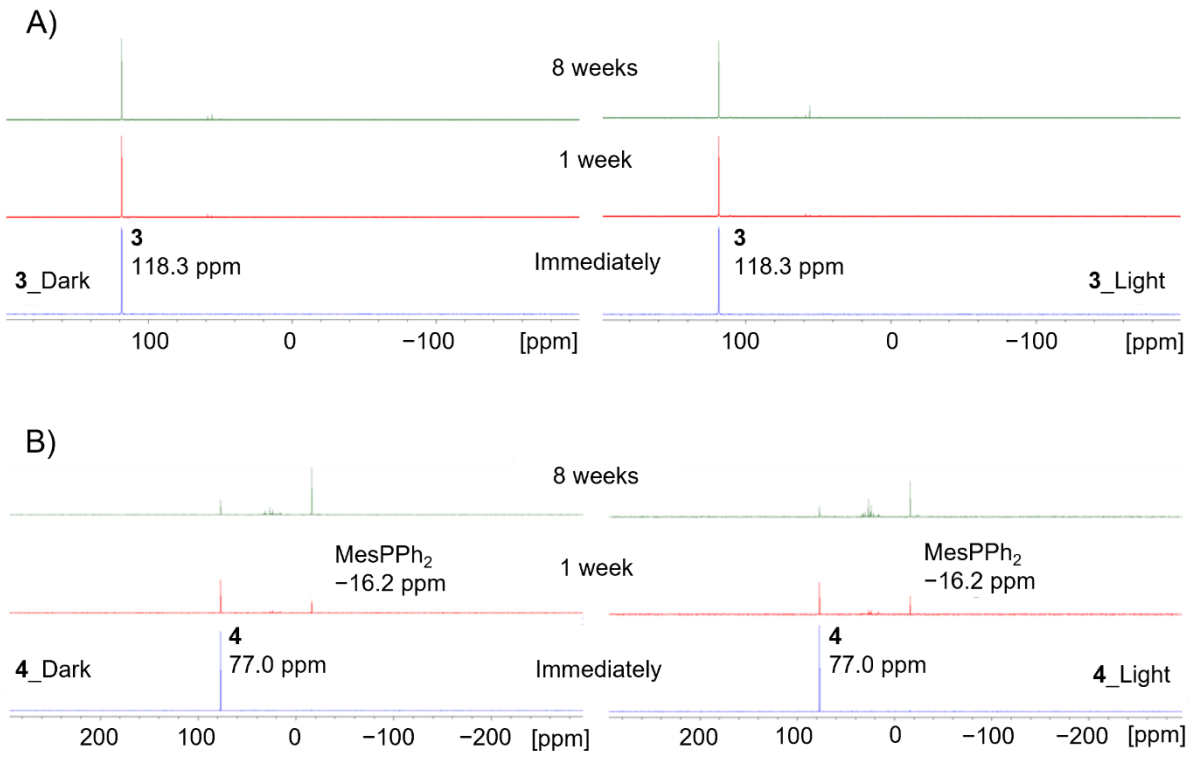


**Figure 2.2.** (A) Stacked $^{31}P\{^{1}H\}$ NMR spectra of **3** in toluene-$d_8$, monitored in the dark (**3**_Dark) and light (**3**_Light) over eight weeks. (B) Stacked $^{31}P\{^{1}H\}$ NMR spectra of **4** in toluene-$d_8$, monitored in the dark (**4**_Dark) and light (**4**_Light) over eight weeks.

Interestingly, the *P*-aryl azophosphine **4** was significantly less stable in toluene solution than the *P*-alkyl analogue **3**. Azophosphine **3** was stable in the absence of air in toluene for several weeks with minimal decomposition, whereas **4** started degrading within 24 h, and ultimately rearranged with loss of $N_2$ to afford $MesPPh_2$ as the major product, as confirmed by NMR spectroscopy and mass spectrometry. To investigate whether the observed degradation was occurring photolytically, toluene solutions of **3** and **4**, prepared in J. Young NMR tubes, were then monitored in the dark over eight weeks (Figure 2.2, **3**_Dark and **4**_Dark). Comparison of **3**_Dark and **4**_Dark with **3**_Light and

**4**_Light, respectively, showed that the exclusion of light had no significant effect on the rate of decomposition of **3** and **4**. The difference in stability between **3** and **4** can be rationalised by considering the potential mechanism of decomposition; homolytic cleavage of the P–N bond in **4** would generate a diphenylphosphinyl radical in which the electron would be delocalised into the phenyl rings, thus stabilising radical formation (Scheme 2.9), whereas in **3,** the analogous di-*tert*-butylphosphinyl radical would be destabilised by the $^{t}$Bu groups, thus disfavouring radical formation.

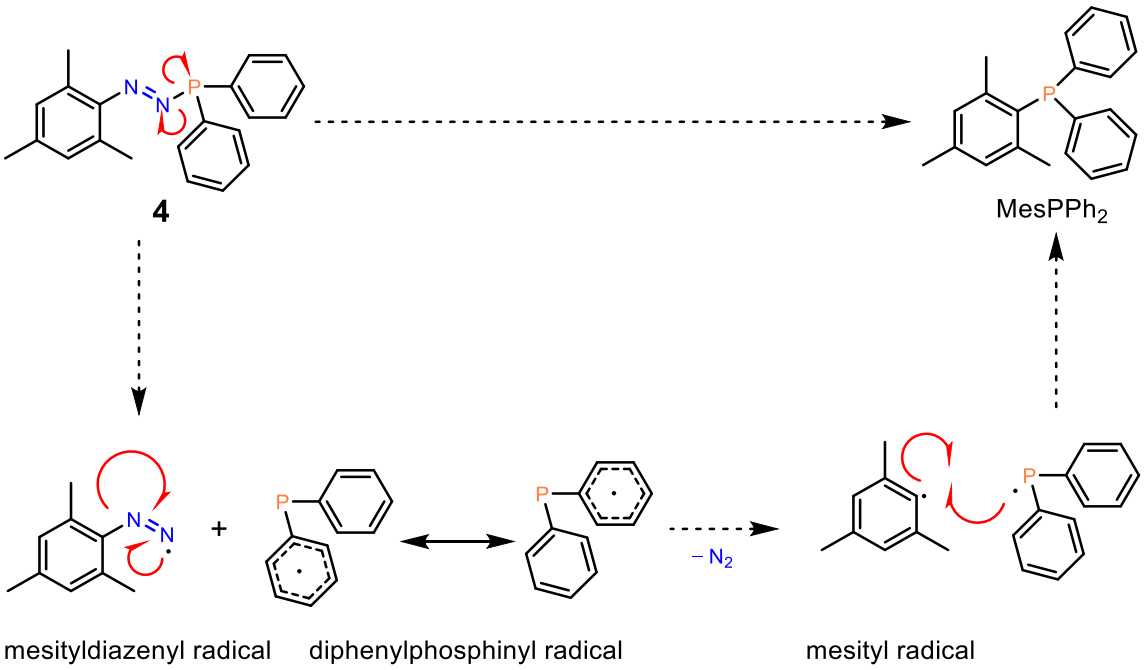


**Scheme 2.9.** Hypothesised decomposition of **4** via homolytic cleavage of the P–N bond.

The simultaneous generation of the mesityldiazenyl radical would be expected to be a short-lived intermediate on account of its highly unstable nature.[16] Thus, its decomposition to the mesityl radical, following loss of $N_2$, and subsequent quenching with the diphenylphosphinyl radical would provide a rational pathway to formation of $MesPPh_2$ (Scheme 2.9).

### 2.5.1 Mechanism of Decomposition

EPR spectroscopy was used to probe whether decomposition of **4** to $MesPPh_2$ occurred *via* a radical mechanism, in which homolytic cleavage of the P–N bond would generate the diphenylphosphinyl and mesityl radicals following loss of $N_2$.

A concentrated toluene solution of **4** at room temperature, prepared in a J. Young EPR tube, showed a signal with complex hyperfine splitting in the EPR spectrum consistent with the mesityldiazenyl radical. (Figure 2.3A).

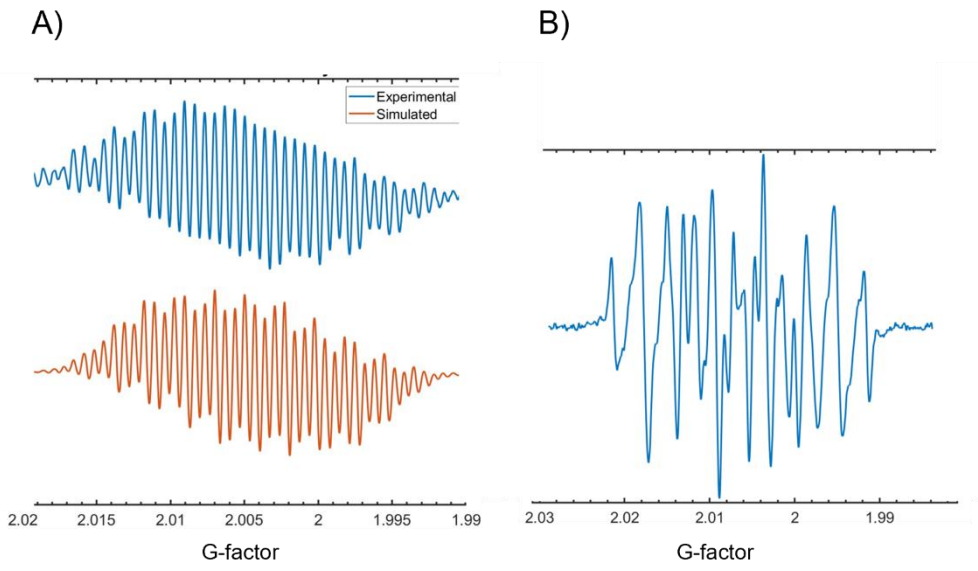


**Figure 2.3.** (A) (Top spectrum) Signal with hyper-fine splitting observed in the EPR spectrum of **4** in toluene, collected at room temperature. (Bottom spectrum) Simulated EPR spectrum of the mesityldiazenyl ($MesN_2$) radical. (B) EPR spectrum of **4** in toluene following addition of DMPO as a spin trap.

These experimental and simulated spectra are consistent with homolytic cleavage of the P–N bond as depicted in Scheme 2.9 and likely occurs in equilibrium with subsequent quenching of the mesityldiazenyl and diphenylphosphinyl radicals at room temperature, with eventual loss of $N_2$ and formation of $MesPPh_2$ (Scheme 2.10).

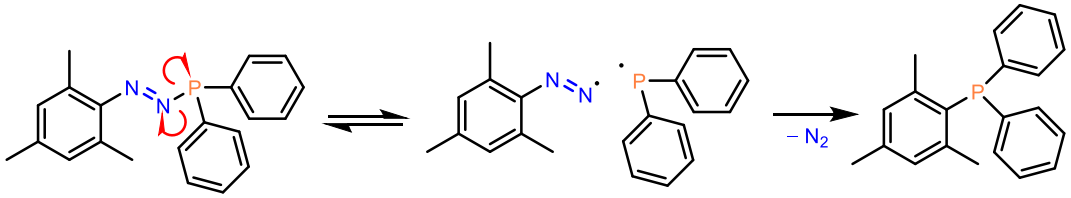


**4**

**Scheme 2.10**. Compound **4** in equilibrium with mesityldiazenyl and diphenylphosphinyl radicals, with eventual loss of $N_2$ to form $MesPPh_2$.

The diphenylphosphinyl radical is known to be undetectable in the EPR spectrum at room temperature which accounts for the absence of the doublet splitting pattern characteristic of a P-radical;[17] however, running the sample as a glass at 100 K resulted in a broad signal in the EPR spectrum. Detection of trace radicals in a solution of **4** necessitated a highly concentrated EPR sample, which, when frozen and run at 100 K, may have caused some precipitation of **4** so quenching the hyperfine coupling observed at room temperature. DMPO (5,5-dimethyl-1-pyrroline N-oxide) is a popular spin trap that undergoes coupling on the $sp^2$ carbon with P- and C-centred radicals (amongst others) forming stable adducts that can be further studied. This enables detection and/or characterisation of short-lived or hard-to-detect radicals. Addition of DMPO (2 equiv.) to a concentrated toluene solution of **4** altered the hyper-fine splitting pattern observed in the EPR spectrum (Figure 2.3B), trapping the mesityl and diphenylphosphinyl radicals as their respective DMPO adducts (Scheme 2.11), as confirmed by mass spectrometry. In comparison, a concentrated toluene solution of **3** showed no signal in the EPR spectrum at room temperature but when the sample was irradiated with white light for 10 minutes a small signal was observed which was lost with cessation of irradiation (Figure 2.4). The use of DMPO to trap, what would be expected to be, the analogous di-*tert*-butylphosphinyl and mesityl radicals was not

possible due to photoionisation of DMPO to its cation radical, $DMPO^{+}$, with UV irradiation.[18]

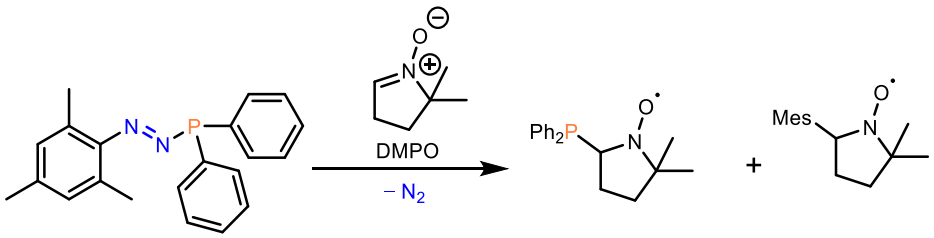


**Scheme 2.11.** Formation of adducts DMPO–$PPh_2$ and DMPO–Mes following decomposition of **4**.

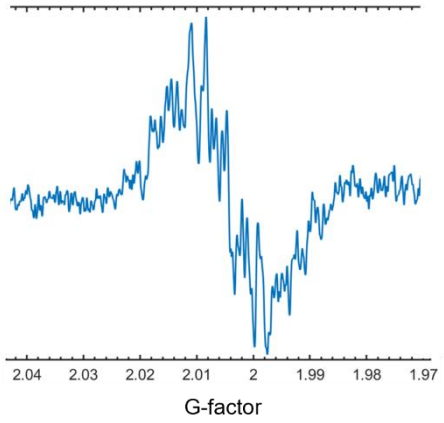


**Figure 2.4.** Trace signal observed in the EPR spectrum of **3** in toluene when irradiated with white light, collected at room temperature.

These EPR spectra corroborate the NMR spectra of **3** and **4** in toluene, in which **4** was found to be significantly less stable than **3** and provide evidence that this difference in stability can be assigned to the decomposition of **4** proceeding *via* a radical mechanism which is stabilised in **4** but destabilised in **3**. Unlike **4**, no signals in the EPR spectra were observed for **3** at room temperature and only a trace baseline signal was observed when **3** was irradiated with white light, thus supporting the corresponding NMR spectra in which no significant difference in stability was observed for **3** in the light and dark.

## 2.6 Photo-switching Properties of Azophosphines

As discussed in Chapter 1 (Section 1.5), azophosphines can be considered a phosphorus-containing derivative of azobenzene on account of the azo group in the N=N–P motif. Section 2.5 found that light had a negligible effect on the stabilities of **3** and **4** in a toluene solution and, as a result, this warranted exploration of the potential photo-switching properties of azophosphines.

### 2.6.1 UV/Vis. Spectroscopy

The UV/Vis spectra of **1** – **4** show a strong absorbance band in the UV region between 315 – 340 nm, and a much weaker absorbance band between 498 – 522 nm that is responsible for the colour of the compounds (Figure 2.5A). These absorptions are comparable to the characteristic absorptions observed in a UV/Vis spectrum of ground state *trans*-azobenzene (Figure 2.5B).[19]

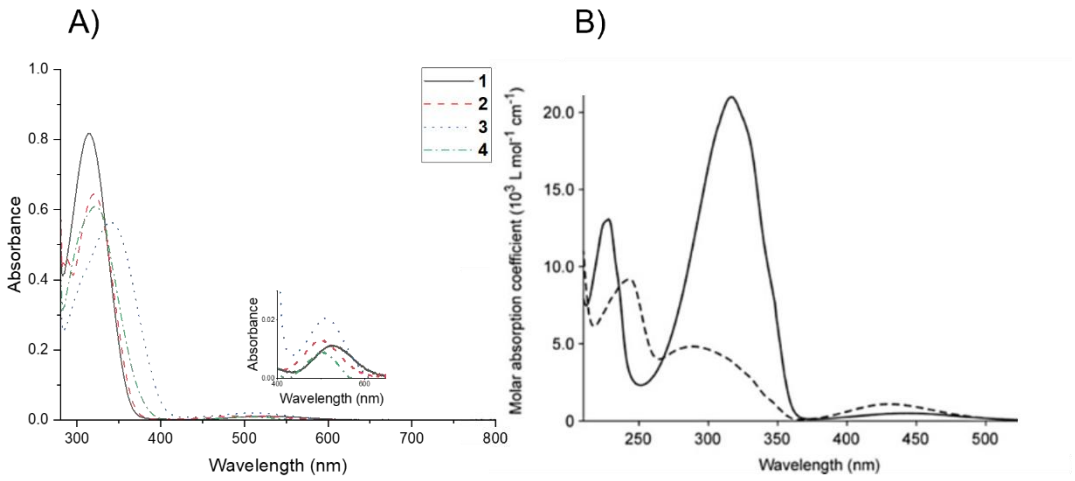


**Figure 2.5.** UV/Vis spectra of (A) **1** – **4**; (B) *E*-azobenzene (full line) and *Z*-azobenzene (dashed line), adapted from reference [18].

Irradiation of *trans*-azobenzenes with the wavelength of light corresponding to $\lambda_{max}$ of the ca.300 nm absorption band leads to photoisomerization to the corresponding *cis*-isomer, with its own distinct absorption spectrum.[20] Therefore, the analogous

absorption band for **1** – **4** was targeted in preliminary photo-switching investigations. A 400 W medium pressure mercury lamp, fitted with a 330 nm filter, was used to irradiate a toluene solution of **1** placed within a foil-wrapped enclosure with a cut-out aperture of approximately 10 x 10 mm. Irradiation of **1** with 330 nm for up to 30 min resulted in no changes between UV/Vis spectra prior and post irradiation. To ensure a significant portion of UV light was channelled towards the sample, **1** – **4** were placed within a photochemical reactor which provided a self-contained UV light source of 254 or 350 nm. Following irradiation of toluene solutions of **1** – **4** at 350 nm for 30 min, no changes between UV/Vis spectra prior and post irradiation were observed.

The half-life of *cis*-azobenzenes range from seconds to days.[21] The time delay between irradiation and spectra collection (≈ 60 s) may provide ample time for fast thermal relaxation of excited state **1** – **4**. It is known that *cis*-azobenzenes react with ketenes at room temperature, the *trans*-isomer being inert, thus enabling the photo-generated *cis*-isomer to be trapped *in-situ* following irradiation.[22] However, translation of this method for detection of the *cis*-isomer of **1** – **4** is not possible as it has been shown that azophosphines can undergo cycloaddition reactions with unsaturated substrates to form P,N heterocycles.[5,6,23]

### 2.6.2 Transient Absorption Spectroscopy

TAS is a pump/probe technique that can be used to measure changes in the excited-state absorption energies of a photogenerated process, such as isomerisation, that occur on a nano- to femto-second timeframe. Before excitation of a sample, the intensity of the ground state absorption spectrum is collected. The sample is then promoted to an electronically excited state by an excitation, or ‘pump’, pulse. A probe pulse is then sent through the sample with a ns – fs time delay. A change in absorption

spectrum can be calculated from the absorption spectrum of the excited sample minus the absorption spectrum of the sample in the ground state (ΔA). Recording a ΔA spectrum at each time delay enables a ΔA profile against time to be obtained.[24]

Samples of azophosphine-boranes **1** and **2** were sent to the University of Amsterdam for analysis by fsTAS. The transient absorption spectra for pure toluene and toluene solutions of **1** and **2** measured with a 320 nm pump pulse are shown in Figure 2.6A, B, C, respectively. Toluene produces its own small transient absorption signal (Figure 2.6A); however, no difference in absorption spectra were observed when **1** and **2** (Figure 2.6B and C, respectively) were added to the solution. The TA spectra of **1** and **2** were also measured using a 520 nm pump pulse. The power of the pulse was set to a high value in an attempt to detect a potentially weak signal. Again, no additional signal was observed compared to pure toluene. To mitigate decomposition of azophosphines **3** and **4** in transit, **1** and **2** were deprotected to the corresponding azophosphine at the University of Amsterdam. Similarly, fsTAS experiments on **3** and **4** found no difference in TA spectra to that of pure toluene when excited with either 320 or 520 nm.

In conclusion, fsTAS experiments provided no evidence of photoisomerization in toluene solutions of **1** – **4**. However, in azobenzenes, efficient N=N *trans* → *cis* photoisomerization has been found to have solvent dependence in which intermolecular forces can prevent or retard the photoisomerization process.[25] Additionally, the polarity and aromaticity of the solvent can affect the spectral broadening of the TA spectrum.[26] Future work would therefore be to explore these systems in other solvents to establish the effects of solvent type and polarity on the potential isomerisation process and TA spectra.

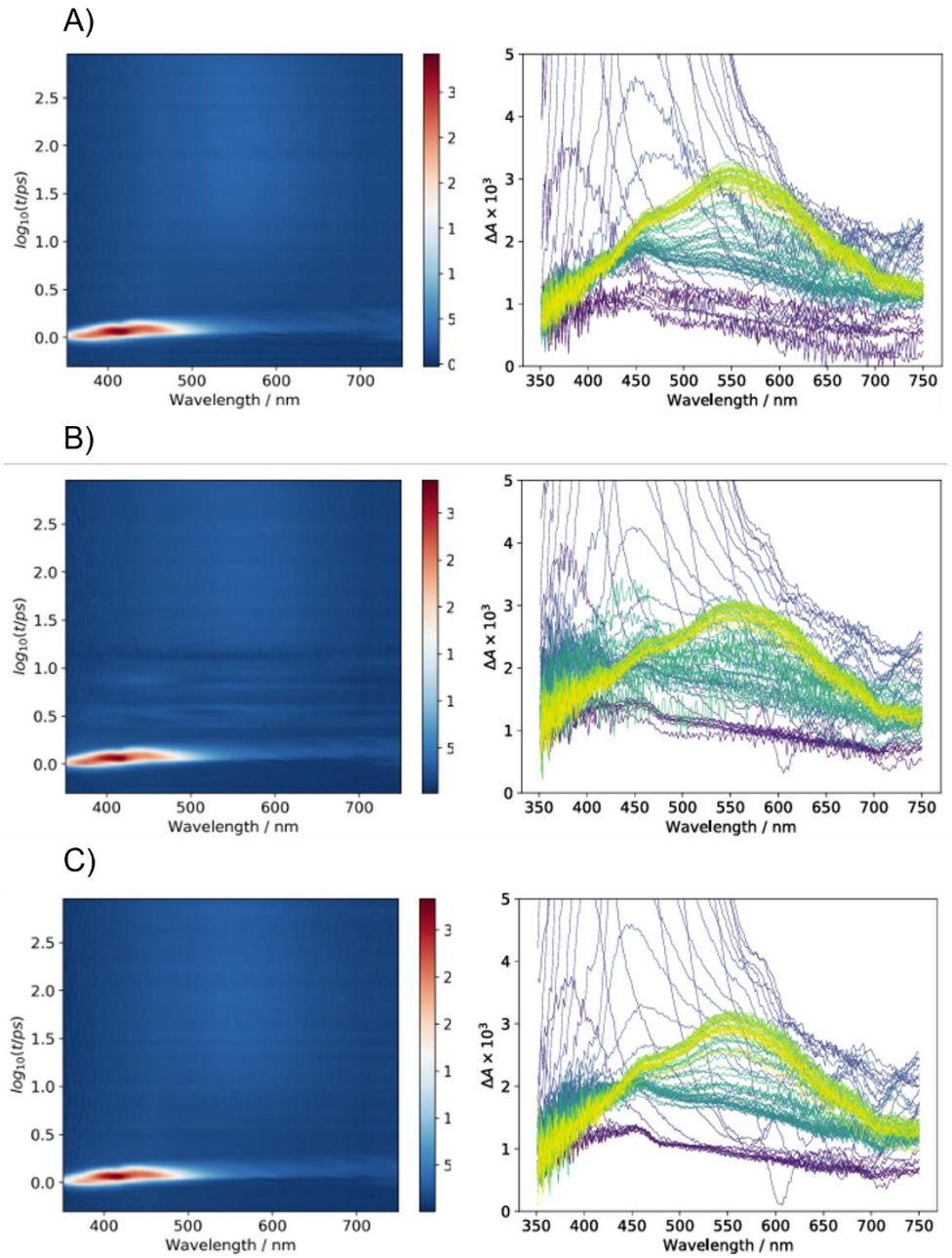


**Figure 2.6.** Time-resolved absorption spectrum measured with a 320 nm pump pulse of (A) pure toluene; (B) **1** in toluene; (C) **2** in toluene.

### 2.6.3 Computational Chemistry[10]

Experimental UV/Vis. spectra and crystallographic data provided to the University of Bristol initiated a collaborative project with Dr Basile Curchod in which the photochemical behaviour of azophosphines was explored using computational quantum chemistry methods. This project was undertaken by MSci student Pablo Rudolf Graf Rubia, supervised by the Curchod group at the University of Bristol. Here, the project's most pertinent results, summarised from the project's thesis, are provided. For complete discussion of methodology and results the reader is referred to reference [10].

To minimise the computational cost, calculations were performed at the ωB97xD/def2-SVP level of theory on the simplified theoretical azophosphine $PhN_2PMe_2$ (Figure 2.7A) in which steric bulk was minimised by substituting the sterically demanding mesityl and $^tBu_2$ groups of **3** (Figure 2.7B) with phenyl and methyl groups, respectively. Experimental crystallographic data and UV-Vis. spectra of derivatives of **3**, $PhN_2P^tBu_2$ and *p*-$(NMe_2)C_6H_4N_2P^tBu_2$ (Figure 2.7C), provided to the University of Bristol served as a model for optimising the geometry of *trans*-$PhN_2PMe_2$ and validated the suitability of ωB97xD/def2-SVP as the level of theory used in calculations.

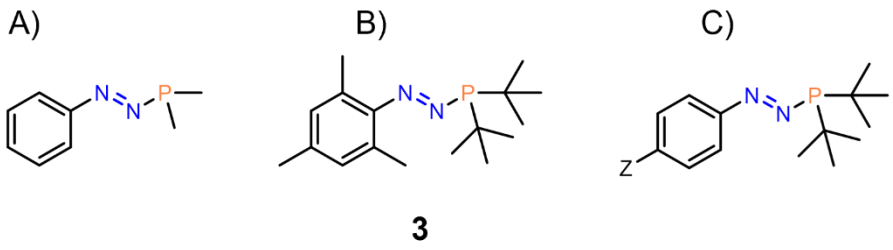


**3**

**Figure 2.7.** (A) $PhN_2PMe_2$; (B) **3**; (C) derivatives of **3** (Z = $NMe_2$, H).

Implicit consideration of solvent was found to have negligible effects on the computed data. Note, azophosphine derivatives $PhN_2P^tBu_2$ and *p*-$(NMe_2)C_6H_4N_2P^tBu_2$ will be formally introduced and discussed in more detail in Chapter 3. A conformer search found *trans* and *cis* isomers as the only significant species of $PhN_2PMe_2$. Characterisation of the orbital transitions of *trans*-azobenzene correctly predicted the nature of the $S_1$ (n–π*) and $S_2$ (π–π*) bands. In comparison, the orbital transitions of *trans*-$PhN_2PMe_2$ exhibited n–π* character, with contributions from both the nitrogen and phosphorus lone pairs of electrons in both $S_1$ and $S_2$ excitations, indicating that the photochemical properties of azophosphines are different from that of azobenzene. An examination of the critical species on the excited states of $PhN_2PMe_2$ revealed a rotation about the P–N bond, aligning the P and N lone pairs and reducing the C–N=N bond angle from 120° to 90°. This approach of the phosphorus atom to the nitrogen atoms ultimately lead to destabilisation of the phosphorus lone pair of electrons. Finally, the potential energy landscape showed that photoexcitation from *trans*-$PhN_2PMe_2$ to the $S_2$ state led to a decay back to ground-state *trans*-$PhN_2PMe_2$ and photoexcitation to the $S_1$ state decayed into a shallow minimum. Ultimately, the Curchod group found no viable pathway for the photo-isomerisation of *trans*-$PhN_2PMe_2$ to *cis*-$PhN_2PMe_2$.

## 2.7 Conclusion

This chapter has reported the development of a general synthetic route to azophosphines, *via* the corresponding azophosphine-borane, and probed the stability and fundamental structure of these underexplored compounds. Azophosphine **3** was found to be stable in the absence of air in toluene for several weeks with minimal decomposition whereas azophosphine **4** degraded within 24 h (in the light and dark), ultimately losing $N_2$ to form $MesPPh_2$ as the major product. This was corroborated by

EPR spectroscopy studies which provided evidence that homolytic cleavage of the P–N bond results in **4** existing in an equilibrium with the mesityldiazenyl and diphenylphosphinyl radicals, with eventual loss of $N_2$ to form $MesPPh_2$.

UV/Vis. spectroscopy, TA spectroscopy (in collaboration with the University of Amsterdam) and computational chemistry methods (in collaboration with the University of Bristol) were employed to investigate the photo-switching properties of **1** – **4**. Although no evidence of *trans* → *cis* photoisomerisation was observed further work remains to better understand this process in azophosphines. The synthesis of azophosphines developed in this chapter enables modulation of sterics and electronics to create a library of azophosphines for further exploration.

## 2.8 Experimental

Except as otherwise noted, the syntheses of **1 - 4** were performed using standard Schlenk line technique under a flow of dry, oxygen-free nitrogen, or an MBraun ECO glovebox under an atmosphere of dry, oxygen-free nitrogen with water and oxygen levels maintained at <0.1 ppm.

Room temperature (RT) refers to reactions where no thermostatic control was applied and the temperature was recorded as 16–25 °C. Unless otherwise stated, overnight reactions refer to a period of 16 h. Thin layer chromatography (TLC) analysis was performed using Machery-Nagel aluminium-backed silica plates. Spots were visualised by the quenching of ultraviolet light. All flash column chromatography was performed using Fluorochem 60. silica gel (particle size 40–63 μm) with a column of appropriate size. All glassware and Teflon-coated stirrer bars were dried in a 80 °C oven overnight prior to use. All molecular sieves are 3 Å and purchased from VWR chemicals and were activated by heating at 400 °C under vacuum prior to use. Unless otherwise stated, degassing refers to three freeze-pump-thaw cycles.

Commercial reagents were purchased, suitably stored as specified by the supplier, and used as received, unless otherwise stated, from Sigma-Aldrich (*sec*-butyllithium, 1.42 M in cyclohexane; borane-di(*tert*-butyl)phosphine complex, 94%; pyrrolidine, anhydrous, > 99.5%, stored in an air-tight ampoule), Acros Organics (borane-diphenylphosphine complex, 94%) or Alfa Aesar (2,4,6-trimethylaniline, 98%; sodium nitrite, 97%; tetrafluoroboric acid, ca. 50% w/w aq. sol.). Solvents were purchased and used as received, unless otherwise stated, from Sigma-Aldrich (hexane, puriss, p.a., ACS reagent, reag. Ph. Eur., 99+ (GC), degassed and stored in air-tight ampoules over

3 Å molecular sieves; diethyl ether, ACS reagent, 99.8%; acetonitrile, suitable for HPLC, gradient grade, 99.9%; acetonitrile-$d_3$, 99.8 atom % D, contains 0.03% (v/v) TMS; chloroform-*d*, 99.8 atom % D, dried by overnight reaction with $CaH_2$, degassed and stored in an air-tight ampoule over 3 Å molecular sieves; toluene-$d_8$, 99.6 atom % D, dried by overnight reaction with $CaH_2$, degassed and stored in an air-tight ampoule over 3 Å molecular sieves) or Fisher Scientific (*iso*-octane, laboratory reagent grade; dichloromethane (DCM), 99.8%, HPLC grade). Toluene was obtained from the laboratory solvent purification system, degassed, and stored in air-tight ampoules over 3 Å molecular sieves. THF was obtained from the laboratory solvent purification system, degassed, dried over Na/benzophenone, distilled and stored in air-tight ampoules over 3 Å molecular sieves. Deionised water was obtained from an Elga DV35 Purelab. For recrystallisations and as eluent for column chromatography, hexane was used as received.

All NMR spectra were collected on a Bruker 500 MHz AV_NEO Avance NMR Spectrometer or a Bruker 400 MHz AV_NEO Avance NMR Spectrometer. Chemical shifts are reported in ppm, coupling constants (*J*) are reported in Hz. $^{1}H$ and $^{13}C\{^{1}H\}$ NMR spectra were referenced internally to the most up-field solvent peak; $^{31}P$ and $^{31}P\{^{1}H\}$ NMR spectra are externally referenced to 85% $H_3PO_4$; $^{11}B\{^{1}H\}$ NMR spectra are externally referenced to $BF_3.OEt_2$.

All EPR spectra were collected on a Bruker EMX Plus instrument operating at X-Band at room temperature. Standard field calibration off-set was measured with reference to a BDPA standard (g = 2.0003). Spectra acquisition was at 2.00 mW using a modulation frequency of 100 kHz and modulation amplitude of 1.0000 G.

All UV/Vis absorption spectra were collected on a Cary50 UV/Vis Spectrometer. The samples were prepared as 50 mM solutions in toluene to a volume of 3 mL and irradiated in a quartz glass High Precision Cell cuvette (10 x 10 mm) from Hellma Analytics. Air-sensitive UV-Vis samples were collected using a sealable cuvette, with solutions made up in the glovebox.

All IR spectra were collected on a Perkin Elmer Spectrum Two FT-IR spectrometer using attenuated total reflection (ATR) sampling technique.

All mass spectra were collected on a Waters Xevo G2-XS TOF mass spectrometer using electrospray ionisation (ESI) positive ion mode or atmospheric solids analysis probe (ASAP) with atmospheric pressure ionisation positive ion mode. Using ESI, samples were dissolved in dry acetonitrile and directly injected into the ESI ionisation chamber via a 250 µL glass syringe. Using ASAP, samples were run neat by dipping a glass capillary into the sample vial, before insertion into the ASAP source.

Single-crystal X-ray diffraction data of **1** were collected at 100 K on an Agilent SuperNova A diffractometer using an Atlas detector, using Cu-Kα radiation (λ = 1.54184). The data collections were driven and processed, and absorption corrections were applied using CrysalisPro.[27] Using OLEX2[28] the structures were solved using SHELXT[29] and were refined by a full-matrix least-squares procedure on $F^2$ in SHELXL.[30] All non-hydrogen atoms were refined with anisotropic displacement parameters.

Single-crystal X-ray diffraction data of **2** was carried out on a Bruker D8 Venture diffractometer with PhotonII CPAD detector at 123(2) K using Cu-Kα radiation (λ =

1.54178 Å). The data collections were driven and processed, and absorption corrections were applied as above.

### 2.8.1 General Procedure for the Synthesis of Arenediazonium Tetrafluoroborates (GP1)

Arenediazonium tetrafluoroborates were prepared following a standard literature procedure.[9,12] To the substituted aniline (2.0 mmol, 1.0 equiv.) in water (1.0 mL), 50 wt.% aq. $HBF_4$ (0.68 mL) was added. The mixture was cooled in an ice-water bath and a solution of $NaNO_2$ (2.0 mmol, 1.0 equiv.) in water (0.4 mL) was added dropwise. The mixture was stirred for 45 min at 0 °C after which the precipitate was collected by Buchner filtration, washed with diethyl ether (3 x 20 mL) and dried *in vacuo* to obtain the crude arenediazonium tetrafluoroborate $[ArN_2][BF_4]$. The crude arenediazonium tetrafluoroborate was dissolved in minimal acetonitrile, filtered if necessary, and recrystallised by addition to excess diethyl ether (approx. 70 mL) with addition of further diethyl ether until no more precipitate formed. The precipitate was collected by Buchner filtration, washed with diethyl ether (3 x 20 mL) and dried *in vacuo* to obtain the purified arenediazonium tetrafluoroborate $[ArN_2][BF_4]$. The salts were transferred to foil-wrapped vials and stored in the freezer at −35 °C.

**Mesitylenediazonium tetrafluoroborate $[MesN_2][BF_4]$**

$[MesN_2][BF_4]$ was synthesised from 2,4,6-trimethylaniline (8.0 mmol, 1.1 g) according to GP1 and isolated as a white solid (1.1 g, 60%). $^1H$ (400.1 MHz, $CD_3CN$, 298 K): δ 7.41 (s, 2H; $H_{Ar}$), 2.65 (s, 6H; *o*-C$H_3$ (Mes)), 2.51 (s, 3H; *p*-C$H_3$ (Mes)). $^{19}F\{^1H\}$ (376.5 MHz, $CD_3CN$, 298 K): δ -152.0 (s; $^{11}BF_4$), -151.9 (s; $^{10}BF_4$). This is consistent with literature values.[9,12]

***p*-fluorobenzenediazonium tetrafluoroborate [*p*-(F)$C_6H_4N_2$][$BF_4$]**

[*p*-(F)$C_6H_4N_2$][$BF_4$] was synthesised from *p*-fluoroaniline (4.0 mmol, 0.38 mL) according to GP1 and isolated as a white solid (370 mg, 43%). $^1$H (400.1 MHz, $CD_3CN$, 298 K): δ 8.61-8.58 (m, 2H; $H_{Ar}$), 7.69-7.64 (m, 2H; $H_{Ar}$). $^{19}$F{$^1$H} (376.5 MHz, $CD_3CN$, 298 K): δ −84.76 (s; *p*-*F*), −151.41 (s; $^{11}BF_4$), −151.47 (s; $^{10}BF_4$). This is consistent with literature values.[9,12]

### 2.8.2 General Procedure for the Synthesis of Arenediazonium Triflates (GP2)

Arenediazonium triflates were prepared following a standard literature procedure.[31] A precooled (10 – 15 °C) solution of substituted aniline (1.0 mmol, 1.0 equiv.) and *tert*-butyl nitrite (1.2 mmol, 1.2 equiv.) in glacial acetic acid (4.0 mL) was added dropwise to a precooled (10 – 15 °C) solution of triflic acid (1.2 mmol, 1.2 equiv.) in glacial acetic acid (6.0 mL). The reaction mixture was stirred for 25 min, and the progress of the reaction monitored by the consumption of the substituted aniline using TLC (ethyl acetate/hexane, 2:3). Addition of diethyl ether (100 – 140 mL) precipitated the diazonium salt. The crude salt was dissolved in minimal acetonitrile and pipetted into diethyl ether (approx. 100 mL). The precipitate was filtered, washed with diethyl ether (3 x 20 mL) and dried *in vacuo* to obtain the purified diazonium salt.

***p*-fluorobenzenediazonium trifluoromethanesulfonate [*p*-(F)$C_6H_4N_2$][$OSOCF_3$]**

[*p*-(F)$C_6H_4N_2$][$OSOCF_3$] was synthesised from *p*-fluoroaniline (1 mmol, 0.09 mL) according to GP2 and isolated as a pale yellow solid (240 mg, 90%). $^1$H NMR (400.1 MHz, $CD_3CN$, 298 K): δ 8.64-8.59 (m, 2H; $H_{Ar}$), 7.70-7.64 (m, 2H, $H_{Ar}$). $^{19}$F{$^1$H} NMR (376.5 MHz, $CD_3CN$, 298 K): δ -79.3 (s; $OSO_2CF_3$), -84.7 (s; *p*-$F_{Ar}$). This is consistent with literature values.[31]

### 2.8.3 General Procedure for the Synthesis of Azophosphine-Borane Adducts (GP3)

A 25 mL Schlenk flask was charged with a 0.25 M THF solution of $HR_2P.BH_3$ (1.0 equiv.) and cooled to –78 °C. A 1.42 M cyclohexane solution of *sec*-butyllithium (1.0 equiv.) was added dropwise, resulting in a colour change from colourless to pale yellow when R = $^t$Bu or from colourless to orange when R = Ph. The solution was allowed to warm to room temperature over 2 h, and then stirred for a further 30 min at room temperature. This solution was added dropwise from a syringe purged with $N_2$ to a separate Schlenk flask containing a slurry of arenediazonium tetrafluoroborate salt (1.0 equiv.) in THF at –78 °C, resulting in an immediate colour change. The reaction was left to warm slowly to room temperature and stirred for 1 h. The volatiles were removed *in vacuo*, and the product isolated by column chromatography. Removal of the volatiles *in vacuo* yielded the product as an intensely coloured solid. The air-stable, solid products were stored in vials, away from direct light, in the freezer.

**$MesN_2P(^tBu)_2.BH_3$ (1)**

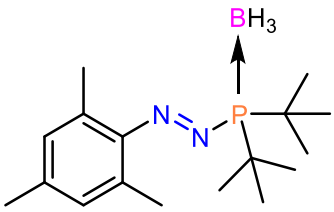


Borane azophosphine **1** was synthesised from precursor $[MesN_2][BF_4]$ (0.67 mmol, 160 mg, 1.0 equiv.) according to GP3. Purification by column chromatography (eluent = 0 → 5% diethyl ether in hexane) obtained **1** as a purple powder (110 mg, 55%). Single crystals of **1** suitable for single-crystal X-ray diffraction were grown by slow evaporation of an *iso*-octane solution of the product at room temperature. $^1$H (500.1 MHz, $CDCl_3$, 298 K): δ 6.96 (s, 2H; $H_{Ar}$ (Mes)), 2.47 (s, 6H; *o*-C$H_3$ (Mes)), 2.34 (s, 3H; *p*-C$H_3$ (Mes)),

1.41 (d, $^{3}J_{H-P}$ = 12 Hz, 18H; $^{t}$Bu), 0.56 (br. quart., 3H; B$H_3$). $^{13}C\{^{1}H\}$ (125.8 MHz, $CDCl_3$): δ 150.3 (d, $^{3}J_{C-P}$ = 35 Hz; *i*-$C_{Ar}$ (Mes)), 142.3 (s; *p*-$C_{Ar}$ (Mes)), 133.7 (s; *o*-$C_{Ar}$ (Mes)), 130.7 (s; *m*-$C_{Ar}$ (Mes)), 34.6 (d, $^{1}J_{C-P}$ = 24 Hz; $C(CH_3)_3$), 27.9 (s; $C(CH_3)_3$), 21.5 (s; *p*-$CH_3$ (Mes)), 20.7 (s; *o*-$CH_3$ (Mes)). $^{31}P\{^{1}H\}$ (202.4 MHz, $CDCl_3$): δ 108.5 (br. quart.). $^{31}P$ (162.0 MHz, $CDCl_3$): δ 108.5 (br. s). $^{11}B\{^{1}H\}$ (160.4 MHz, $CDCl_3$): δ -42.5 (d, $^{1}J_{11B-P}$ = 51 Hz). UV-Vis (toluene, nm) $\lambda_{max}$: 315 (s); 522 (w). ESI-HRMS m/z for $C_{17}H_{31}N_2PB$ [*M* – H]$^{+}$: calcd (found) 305.2321 (305.2339), 306.2351 (306.2371). IR: $\nu_{max}$ ($cm^{-1}$) 3734.0 (w), 3709.3 (w), 3634 (w), 3604 (w), 2989 (w), 2968 (w), 2921 (w), 2870 (w), 2369.0 (m) (B–H), 1607.1 (m) (N=N).

**$MesN_2PPh_2.BH_3$ (2)**

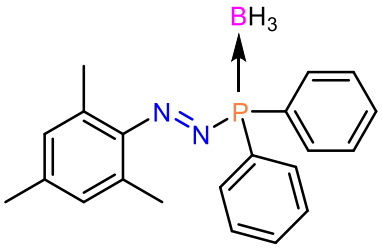


Borane azophosphine **2** was synthesised from precursor $[MesN_2][BF_4]$ (1.9 mmol, 420 mg, 1.0 equiv.) according to GP3. Purification by column chromatography (eluent = 0 → 5% diethyl ether in hexane) obtained **2** as a pink powder (260 mg, 42%). Single crystals of **2** suitable for single-crystal X-ray diffraction were grown by slow evaporation of a hexane solution of the product at room temperature. $^{1}H$ (500.1 MHz, $CDCl_3$, 298 K): δ 7.81 (m, 4H; *o*-$H_{Ar}$ (Ph)), 7.53 (m, 6H; *p*-$H_{Ar}$ *m*-$H_{Ar}$ (Ph)), 6.91 (s, 2H; *m*-$H_{Ar}$ (Mes)), 2.31 (s, 3H, *p*-$CH_3$ (Mes)), 2.30 (s, 6H, *o*-$CH_3$ (Mes)), 1.19 (br. quart., 3H; B$H_3$). $^{13}C\{^{1}H\}$ (125.8 MHz, $CDCl_3$): δ 150.3 (d, $^{3}J_{C-P}$ = 38 Hz; *i*-$C_{Ar}$ (Mes)), 142.3 (s; *p*-$C_{Ar}$ (Mes)), 133.6 (d; $^{4}J_{C-P}$ = 2 Hz; *o*-$C_{Ar}$ (Mes)), 133.5 (d; $^{2}J_{C-P}$ = 9 Hz; *o*-$C_{Ar}$ (Ph)), 132.1 (d; $^{4}J_{C-P}$ = 2 Hz; *p*-$C_{Ar}$ (Ph)), 130.5 (d; $^{5}J_{C-P}$ = 1 Hz; *m*-$C_{Ar}$ (Mes)), 128.8 (d; $^{3}J_{C-P}$ = 10 Hz, *m*-

$C_{Ar}$ (Ph)), 128.5 (d; $^{1}J_{C-P}$ = 57 Hz; *i*-$C_{Ar}$ (Ph)), 21.5 (s; *p*-$CH_3$ (Mes)), 20.0 (s; *o*-$CH_3$ (Mes)). $^{31}P\{^{1}H\}$ (202.4 MHz, $CDCl_3$): δ 75.8 (br. quart.). $^{31}P$ (202.4 MHz, $CDCl_3$): δ 75.8 (br. s). $^{11}B\{^{1}H\}$ (160.4 MHz, $CDCl_3$): δ -38.8 (br. doublet). UV-Vis (toluene, nm) $\lambda_{max}$: 320 (s); 508 (w). ESI-HRMS m/z for $C_{12}H_{23}N_2PB$ $[M - H]^+$: calcd (found) 345.1696 (345.1691), 346.1726 (346.1756). IR: $\nu_{max}$ ($cm^{-1}$) 3726 (w), 3699 (w), 3623 (w), 3598 (w), 2962 (w), 2924 (w), 2377 (m) (B–H), 1606 (m) (N=N).

### 2.8.4 General Procedure for the Synthesis of Azophosphines (GP4)

$MesN_2PR_2.BH_3$ (1.0 equiv.) was added to a 25 mL Schlenk ampoule and dissolved in toluene. To this, pyrrolidine was added (10 equiv.), and the mixture stirred at room temperature overnight (16 h), which gave 100% conversion to $MesN_2PR_2$ by crude $^{31}P\{^{1}H\}$ NMR spectroscopy. Excess pyrrolidine was removed *in vacuo* and the resulting oil filtered through a silica plug (eluent = 10% diethyl ether in hexane) to remove the pyrrolidine.$BH_3$ adduct. Removal of the eluent *in vacuo* obtained the target deprotected $MesN_2PR_2$ product as a dark-coloured solid or oil. The air-sensitive products were stored in vials in the glovebox freezer.

**$MesN_2P(^tBu)_2$ (3)**

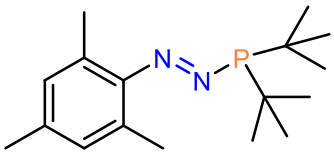


Azophosphine **3** was synthesised from azophosphine borane **1** (0.049 mmol, 15 mg, 1.0 equiv.) according to GP4. The reaction was stirred at room temperature overnight (16 h) to obtain 100% conversion of **1** to **3**, and isolated as a purple oil (12 mg, 82%). The flask was then rinsed with toluene-$d_8$ to prepare an NMR sample. $^{1}H$ 500.1 MHz, tol-$d_8$, 298 K): δ 6.71 (m, 2H; *m*-$H_{Ar}$ (Mes)), 2.38 (s, 6H; *o*-C$H_3$ (Mes)), 2.10 (s, 3H; *p*-

C$H_3$ (Mes)), 1.32 (d, $^3J_{H–P}$ = 11 Hz, 18H; $^t$Bu). $^{13}C\{^1H\}$ (125.8 MHz, tol-$d_8$): δ 152.2 (d, $^3J_{C–P}$ = 21 Hz; *i*-$C_{Ar}$ (Mes)), 138.1 (s: *p*-$C_{Ar}$ (Mes)), 130.7 (d, $^4J_{C–P}$ = 2 Hz; *o*-$C_{Ar}$ (Mes)), 130.5 (s; *m*-$C_{Ar}$ (Mes)), 35.8 (d, $^1J_{C–P}$ = 27 Hz; $C(CH_3)_3$), 29.2 (d, $^2J_{C–P}$ = 12 Hz; $C(CH_3)_3$), 20.9 (s; *p*-$CH_3$ (Mes)), 20.2 (s; *o*-$CH_3$ (Mes)). $^{31}P\{^1H\}$ (202.4 MHz, tol-$d_8$): δ 118.3 (s). $^{31}P$ (162.0 MHz, tol-$d_8$): δ 118.3 (br. m). UV-Vis (toluene, nm) $\lambda_{max}$: 340 (s); 508 (w). ASAP-HRMS m/z for $C_{17}H_{30}N_2P$ [*M* + H]$^+$: calcd (found) 293.2147 (293.2155). IR: $\nu_{max}$ ($cm^{-1}$) 2983 (m), 2941 (m), 2894 (m), 2859 (m), 1606 (m) (N=N).

**Mes$N_2$P$Ph_2$ (4)**

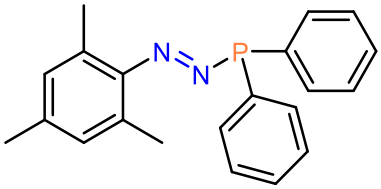


Azophosphine **4** was synthesised from azophosphine borane **2** (0.29 mmol, 100 mg, 1.0 equiv.) according to GP4. The reaction was stirred at room temperature overnight (16 h) to obtain 100% conversion of **2** to **4**, and isolated as a purple oil (63 mg, 66%). The flask was then rinsed with toluene-$d_8$ to prepare an NMR sample. $^1H$ (500.1 MHz, tol-$d_8$, 298 K): δ 7.60 (m, 4H; *o*-$H_{Ar}$ (Ph)), 7.12 (m, 6H; *p*-$H_{Ar}$ and *m*-$H_{Ar}$ (Ph)), 6.64 (s, 2H; *m*-$H_{Ar}$ (Mes)), 2.22 (s, 6H, *o*-C$H_3$ (Mes)), 2.06 (s, 3H, *p*-C$H_3$ (Mes)). $^{13}C\{^1H\}$ (125.8 MHz, tol-$d_8$): δ 151.6 (d, $^3J_{C–P}$ = 25 Hz; *i*-$C_{Ar}$ (Mes)), 138.8 (d, $^6J_{C–P}$ = 1 Hz; *p*-$C_{Ar}$ (Mes)), 138.0 (d; $^1J_{C–P}$ = 15 Hz; *i*-$C_{Ar}$ (Ph)), 133.8 (d; $^2J_{C–P}$ = 19 Hz; *o*-$C_{Ar}$ (Ph)), 131.2 (d; $^4J_{C–P}$ = 1 Hz; *o*-$C_{Ar}$ (Mes)), 130.3 (s; *m*-$C_{Ar}$ (Mes)), 129.6 (s; *p*-$C_{Ar}$ (Ph)), 128.6 (d; $^3J_{C–P}$ = 7 Hz; *m*-$C_{Ar}$ (Ph)), 21.0 (s; *p*-$CH_3$ (Mes)), 19.4 (s; *o*-$CH_3$ (Mes)). $^{31}P\{^1H\}$ (162.0 MHz, tol-$d_8$): δ 77.0 (s). $^{31}P$ (162.0 MHz, tol-$d_8$): δ 77.0 (s). UV-Vis (toluene, nm) $\lambda_{max}$: 322 (s); 498 (w). ASAP-HRMS m/z for $C_{21}H_{22}N_2P$ [*M* – H]$^+$: calcd (found) 333.1521 (333.1522). IR: $\nu_{max}$ ($cm^{-1}$) 3054 (w), 2961 (w), 2918 (w), 1607 N=N).

### 2.8.5 Stability Study using NMR Spectroscopy

Duplicate NMR spectroscopy samples of **3** (10 mg) in toluene-$d_8$ (0.5 mL) were prepared in J. Young NMR tubes. The first sample (**3**_Dark) was wrapped in foil to prevent light exposure, and the second sample (**3**_Light) was left exposed to light. This was repeated with **4** (**4**_Dark, **4**_Light) to give four samples overall. All samples were monitored by $^{31}P\{^1H\}$ NMR spectroscopy over the course of eight weeks. All samples were stored in the back of the fume cupboard. The $^{31}P\{^1H\}$ NMR spectra for **4**_Light and **4**_Dark show decomposition to predominately a peak at -16.2 ppm, consistent with literature values for $MesPPh_2$, following loss of $N_2$ from **4**. The presence of $MesPPh_2$ in **4**_Light and **4**_Dark was confirmed with mass spectrometry. ESI-HRMS m/z for $C_{21}H_{22}P$ $[M + H]^+$: calcd. (found) 305.1459 (305.1459).

### 2.8.6 Stability Study using EPR Spectroscopy

EPR spectroscopy samples of **3** and **4** (19 μmol) in toluene (250 μL) were prepared in J. Young EPR tubes. EPR spectra were collected at room temperature.

DMPO as spin trap: To a solution of **4** (3 mg) in toluene (2 mL) DMPO (2 mg, 2 equiv.) was added and the mixture stirred for 2 min. 250 μL was transferred to a J. Young EPR tube and an EPR spectrum collected at room temperature. The presence of DMPO–$PPh_2$ and DMPO–Mes adducts was confirmed with mass spectrometry. ASAP-HRMS m/z for $C_{18}H_{21}NOP$ (DMPO–$PPh_2$) $[M]^+$: calcd (found) 298.1361 (298.1370). ASAP-HRMS m/z for $C_{15}H_{22}NO$ (DMPO–Mes) $[M]^+$: calcd (found) 232.1701 (232.1706).

### 2.8.7. Transient Absorption Spectroscopy

Experimental details provided by Maximilian Paradiz Dominguez.

**320 nm pump**

The 320 nm pump beam was generated using the optical parametric amplifier (OPA). The 800 nm beam is split into signal (1280 nm) and idler (2133 nm). The remaining 800 nm pump was filtered out. The 1280 nm was doubled to make a 640 nm beam using a type II BBO. The 640 nm was doubled again using a type II BBO to make the 320 nm beam. Two 300 nm mirrors were used to selectively reflect the 320 nm pump beam and get rid of the remaining 640 nm, 800 nm, and 1280 nm input beams. For these experiments, the power of the pump was set to 940 nJ per pulse. The spot had an approximate diameter of 730 μm at the sample position. This gave a radiant exposure of 0.22 mJ $cm^{-2}$ per pulse. The probe light had a power of 660 nJ per pulse. The spot diameter was of approximately 700 μm at the sample position. The radiant exposure was then 0.17 mJ $cm^{-2}$ per pulse. A polarizer was used to set the relative polarizations of the pump and probe breams at the magic angle of 54.7°.

**520 nm pump**

To make the 520 nm pump, the 800 nm pump beam is first split into a signal (1486 nm) and idler (1733 nm). The 800 nm pump and the 1486 nm are then combined via sum-frequency mixing to make the 520 nm pump. The pump power was controlled using a pinhole. The power was set to 8 muJ/pulse, and the spot had a diameter of 780 μm. The radiant exposure was of 1.7 mJ $cm^{-2}$.

### 2.8.7. Computational Chemistry

All computational details can be found in the experimental section of reference [10].

## References


1 N. Wiberg, *Adv. Organomet. Chem.*, 1984, **23**, 131–191.

2 W. Schneid, Zur Darstellung und Reactivität Silylierter, Germylierter und Stannylierter Mono(Organyl)Diimine, Ludwig Maximilians-Universitat Munchen, 1977.

3 G. Schwenk, Zur Reaktivität von Bis(Trimethylsilyl)-Diimine, Ludwig Maximilians-Universitat Munchen, 1971.

4 O. A. Attanasi, P. Filippone, P. Guerra and F. Serra-Zanetti, *Synth. Commun.*, 1987, **17**, 555–561.

5 M. L. Y. Riu, W. J. Transue, J. M. Rall and C. C. Cummins, *J. Am. Chem. Soc.*, 2021, **143**, 7635–7640.

6 K. Tanaka, M.-L. Y. Riu, B. Valladares and C. C. Cummins, *Inorg. Chem.*, 2022, **61**, 13662–13666.

7 A. E. Waked, R. Ostadshariff Memar and D. W. Stephan, *Angew. Chem. Int. Ed.*, 2018, **57**, 11934–11938.

8 E. R. M. Habraken, L. J. C. van der Zee, K. N. A. van de Vrande, A. R. Jupp, M. Nieger, A. W. Ehlers and J. C. Slootweg, *Eur. J. Inorg. Chem.*, 2019, **2019**, 1594–1603.

9 E. R. M. Habraken, N. P. van Leest, P. Hooijschuur, B. de Bruin, A. W. Ehlers, M. Lutz and J. C. Slootweg, *Angew. Chemie Int. Ed.*, 2018, **57**, 11929–11933.

10 P. R. Graf Rubia, Exploring the Photochemical Properties of a new Azobenzene Derivative, Azophosphine, University of Bristol, 2024.

11 E. J. Jordan, E. D. E. Calder, H. V Adcock, L. Male, M. Nieger, J. C. Slootweg and A. R. Jupp, *Chem. – A Eur. J.*, 2024, 30, 35, e202401358.

12 E. R. M. Habraken, L. J. C. van der Zee, K. N. A. van de Vrande, A. R. Jupp, M. Nieger, A. W. Ehlers and J. C. Slootweg, *Eur. J. Inorg. Chem.*, 2019, **2019**, 1594–1603.

13 J. D. Firth and I. J. S. Fairlamb, *Org. Lett.*, 2020, **22**, 7057–7059.

14 Deposition numbers 2334072 (for **1**) and 2190921 (for **2**) contain the supplementary crystallographic data for this chapter. These data are provided free of charge by the joint Cambridge Crystallographic Data Centre and Fachinformationszentrum Karlsruhe Access Structures service

15 G. C. Lloyd-Jones and N. P. Taylor, *Chem. – A Eur. J.*, 2015, **21**, 5423–5428.

16 L. Pichereau, L. Fillaud, N. Kostopoulos, E. Maisonhaute, T. Cauchy, M. Allain, J. M. Noël, C. Gautier and T. Breton, *J. Phys. Chem. Lett.*, 2022, **13**, 11866–11871.

17 Y. Sueishi and Y. Nishihara, *J. Chem. Res.*, 2001, 84–86.

18 C. F. Chignell, A. G. Motten, R. H. Sik, C. E. Parker and K. Reszka, *Photochem. Photobiol.*, 1994, **59**, 5–11.

19 M. Baroncini, J. Groppi, S. Corra, S. Silvi and A. Credi, *Adv. Opt. Mater.*, 2019, **7**, 1900392.

20 H. M. D. Bandara and S. C. Burdette, *Chem. Soc. Rev.*, 2012, **41**, 1809–1825.

21 D. Das, M. K. Yadav, L. Singla, A. Kumar, M. Karanam, S. Dev and A. R. Choudhury, *ChemistrySelect*, 2020, **5**, 13957–13962.

22 R. C. Kerber and T. J. Ryan, *Tetrahedron Lett.*, 1970, **11**, 703–706.

23 E. D. E. Calder, L. Male and A. R. Jupp, *Dalton Trans.*, 2024, **53**, 15032-15039.

24 R. Berera, A. E. Rienk, G. Ae and J. T. M. Kennis, *Photosynth Res.*, 2009, **101**, 105-118.

25 H. Nakagawa, A. Matsumoto, A. Daicho, Y. Ozaki, C. Ota and Y. Nagasawa, *J. Photochem. Photobiol. A Chem.*, 2018, **358**, 308–314.

26 R. Zheng, M. Cheng, R. Ma, D. Schipper, K. Pichugin and G. Sciaini, *Phys. Chem. Chem. Phys.*, 2024, **26**, 1039–1045.

27 CrysAlisPro, Rigaku Oxford Diffraction, 2021.

28 O. V Dolomanov, L. J. Bourhis, R. J. Gildea, J. A. K. Howard and H. Puschmann, *J. Appl. Crystallogr.*, 2009, **42**, 339–341.

29 G. M. Sheldrick, *Acta Crystallogr.*, 2015, **A71**, 3–8.

30 G. M. Sheldrick, *Acta Crystallogr.*, 2015, **C71**, 3–8.

31 V. D. Filimonov, E. A. Krasnokutskaya, A. Z. Kassanova, V. A. Fedorova, K. S. Stankevich, N. G. Naumov, A. A. Bondarev and V. A. Kataeva, *Eur. J. Org. Chem.*, 2019, **2019**, 665–674.

# CHAPTER 3

# Broadening the Synthetic Scope and Identifying Trends in Azophosphines

## 3.1 Introduction and Objectives

### 3.1.1 Trends in the Literature

Azophosphines are a relatively underexplored group of compounds represented by only a small number of publications in the literature.[1–4]

The first report of azophosphines by Wiberg was set within the much broader discussion of silyl, germyl and stannyl derivatives of azenes, and, as a result, were not a topic of analysis.[1] Although a more in-depth study of these azophosphines is found in the corresponding doctorate thesis of Schneid this is limited to the collection of $^{31}$P NMR and UV/Vis. spectroscopic data (Table 3.1).[5]

**Table 3.1.** Spectroscopic data collected for a range of azophosphines by Schneid.[5]

| RN=N–PR$^1_2$ | $^{31}$P Chemical Shift (ppm)[a] | $\lambda_{max}$ (nm)[b] |
|---|---|---|
| 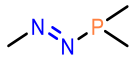 | Not Available | 419.3 |
| 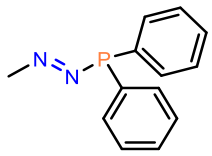 | 71.2 | 426.8 |
| 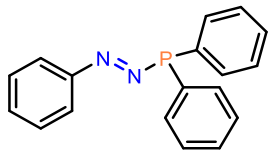 | 75.0 | 481.9 |
| 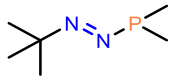 | 61.5 | 424.4 |
| 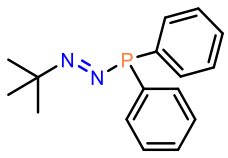 | Could not be collected due to thermolabillity | 434.2 |

[a] Collected at 24.3 MHz, solvent identity not provided; [b] Collected in DCM.

Of the five azophosphines isolated, there is no systematic modulation of electronics of R and $R^1$, preventing analysis of any trends in these spectroscopic data. It could be said that when $R^1$ = Ph, R increases in steric bulk in the order Me < Ph < $^t$Bu; however, an effect on the spectroscopic data would not be expected and is not seen.

Attanasi and co-workers synthesised a small range of three azophosphines, in which only R was modulated; however, only $^1$H NMR and IR spectroscopic data were collected (Table 3.2). Minimal deviations are seen within these data; the synthesis of a larger range of azophosphines is required for reliable analysis.

**Table 3.2.** Spectroscopic data collected for a range of azophosphines by Attanasi and co-workers.[2]

| **RN=N–PPh$_2$** | **$^1$H Chemical Shift (ppm)[a]** **P*Ph$_2$*** | **$\nu_{max}$ (cm$^{-1}$)** |
|---|---|---|
| 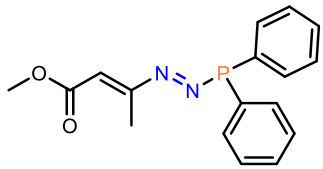 | 7.30 – 8.27 | 1720, 1645, 1590, 1435, 1215, 1125, 1030 |
| 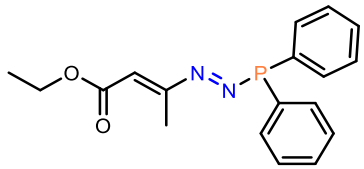 | 7.38 – 8.30 | 1720, 1645, 1590, 1435, 1210, 1125, 1040 |
| 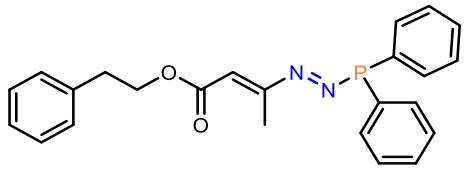 | 7.21 – 8.23 | 1725, 1645, 1590, 1440, 1220, 1125, 1025 |

[a] Collected in $CDCl_3$ at 60 Hz

Cummins and co-workers have published two studies of azophosphines in which the 1,3-dipolar cycloaddition reactions with alkynes were investigated.[3,4] Here, it was the onward reactivity of the azophosphines that was explored rather than the elucidation

of structural or spectroscopic trends. Only $^{31}P\{^{1}H\}$ NMR spectroscopic data are available for this analysis (Table 3.3).

**Table 3.3.** $^{31}P\{^{1}H\}$ NMR chemical shifts for a range of azophosphines synthesised by Cummins and co-workers.[3,4]

| **RN=N–PR$^{1}_{2}$** | **$^{31}P\{^{1}H\}$ Chemical Shift (ppm)[a]** |
|---|---|
| 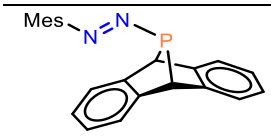 | 207.8 |
| 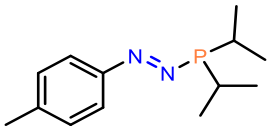 | 104.73 |
| 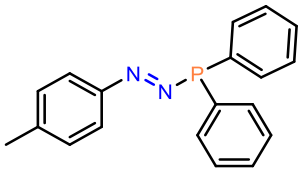 | 74.67 |
| 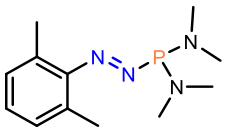 | 116.49 |
| Could not be purified | |
| 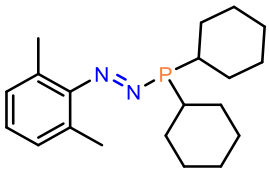 | 102.56 |
| 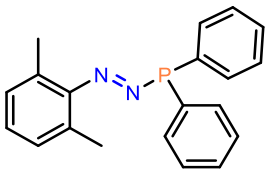 | 78.22 |
| Could not be purified | |

[a] Collected in $C_6D_6$ at 202 Hz

When $R^1$ = Ph the $^{31}P$ chemical shift is downfield (≈ 70 ppm) relative to when $R^1$ = alkyl (≈ 100 ppm) and can be rationalised by some delocalisation of the P lone pair into the

two phenyl substituents deshielding the P centre. When R = *o*-xylyl, $R^1$ = $NMe_2$, Cy and Ph, and the $^{31}P$ chemical shift increases in the order Ph (78.22 ppm) < Cy (102.56) < $NMe_2$ (116.49). The up-field shift in ppm for $R^1$ = $NMe_2$ can be attributed to mesomeric donation of the N lone pair shielding the P centre relative to when $R^1$ = Cy.

It is not possible to make comparisons between the studies discussed here as each focus on different parameters, highlighting the scarcity of research in azophosphines. The fundamental structure of azophosphines and the effect of systematically modulating their electronics remains to be explored and is the objective of this chapter.

### 3.1.2 Chapter Outline

The research discussed in Chapter 2 found that the *P*-alkyl azophosphine $MesN_2P^tBu_2$ (**3**) was significantly more stable in toluene solution than the *P*-aryl analogue $MesN_2PPh_2$ (**4**). In this chapter, a broader library of azophosphines (*p*-(Z)$C_6H_4N_2P^tBu_2$) is synthesised, maintaining $^t$Bu as the P substituent and introducing variety at the *N*-aryl substituent which spans the electron-donating to electron-withdrawing range. To gain insight into the effect of varying the electronics, only the *para*-position on the terminal nitrogen's aryl ring is modulated. Discussion will begin with the synthesis and characterisation of the library of azophosphines. The structural and spectroscopic trends observed due to systematically varying Z are explored by single crystal X-ray diffraction and Density Functional Theory (DFT) studies, and $^{31}P\{^1H\}$ NMR and UV/Vis spectroscopy, respectively. The effect of Z on the donor strength of the phosphorus centre is analysed *via* the $^1J_{P-Se}$ coupling constant of the corresponding azophosphine-selenides (*p*-(Z)$C_6H_4N_2P(Se)^tBu_2$), and their values compared against established phosphines. The chapter concludes with a brief exploration of whether the changes in

electronics by varying Z has an effect on the ability of azophosphines to act as photo-switches.

### 3.1.3 Acknowledgements

The computational calculations discussed in this chapter were performed by Ethan Calder (PhD student, Jupp group, University of Birmingham).

### 3.1.4 Published Research

The research in this chapter (Sections 3.2 – 3.5) has been published in *Organometallics*[6] and *Chemistry A European Journal*.[7] Section 3.6 is currently unpublished research.

## 3.2 Synthesis of Azophosphine Library[6,7]

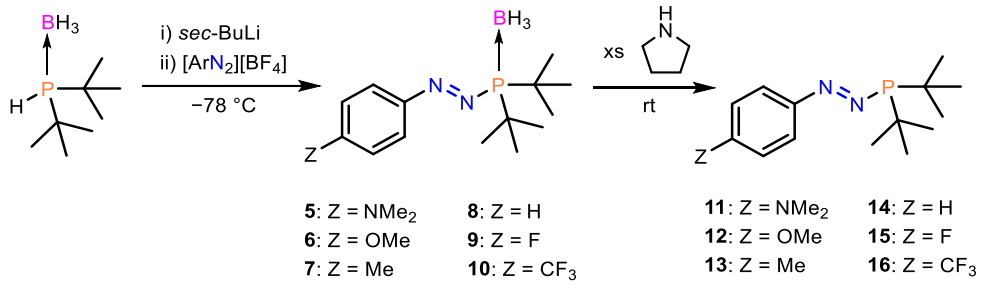


**Scheme 3.1.** Synthesis of azophosphines **11-16** via the corresponding azophosphine-boranes **5-10**.

Using our general synthetic route to azophosphines (Scheme 3.1), azophosphine-boranes Z = $NMe_2$ (**5**), OMe (**6**), Me (**7**), H (**8**), F (**9**) and $CF_3$ (**10**) were obtained as brightly coloured pink/red solids (isolated yields = 46 – 84%) with subtle differences in colour. In general, the yield decreased as Z moved from electron-donating (Z = $NMe_2$ 84%) to electron-withdrawing (Z = $CF_3$ 46%) in nature. **5** – **10** were fully deprotected to the corresponding azophosphines Z = $NMe_2$ (**11**), OMe (**12**), Me (**13**), H (**14**), F (**15**), $CF_3$ (**16**) as darker coloured solids or oils (isolated yields = 50 – 76%). Interestingly, only **11** and **12** could be obtained as solids. Azophosphine-boranes **5** – **10** and azophosphines **11** and **12** were characterised by single crystal X-ray diffraction (Figure 3.1); selected bond distances, bond angles and torsion angles are tabulated in Table 3.4 and Table 3.5, respectively, and are discussed in Section 3.3.1. Spectroscopic trends in **11** – **16** are discussed in Section 3.4. Full characterisation data for azophosphine-boranes **5** – **10** and azophosphines **11** – **16** are provided in the experimental section at the end of this chapter.

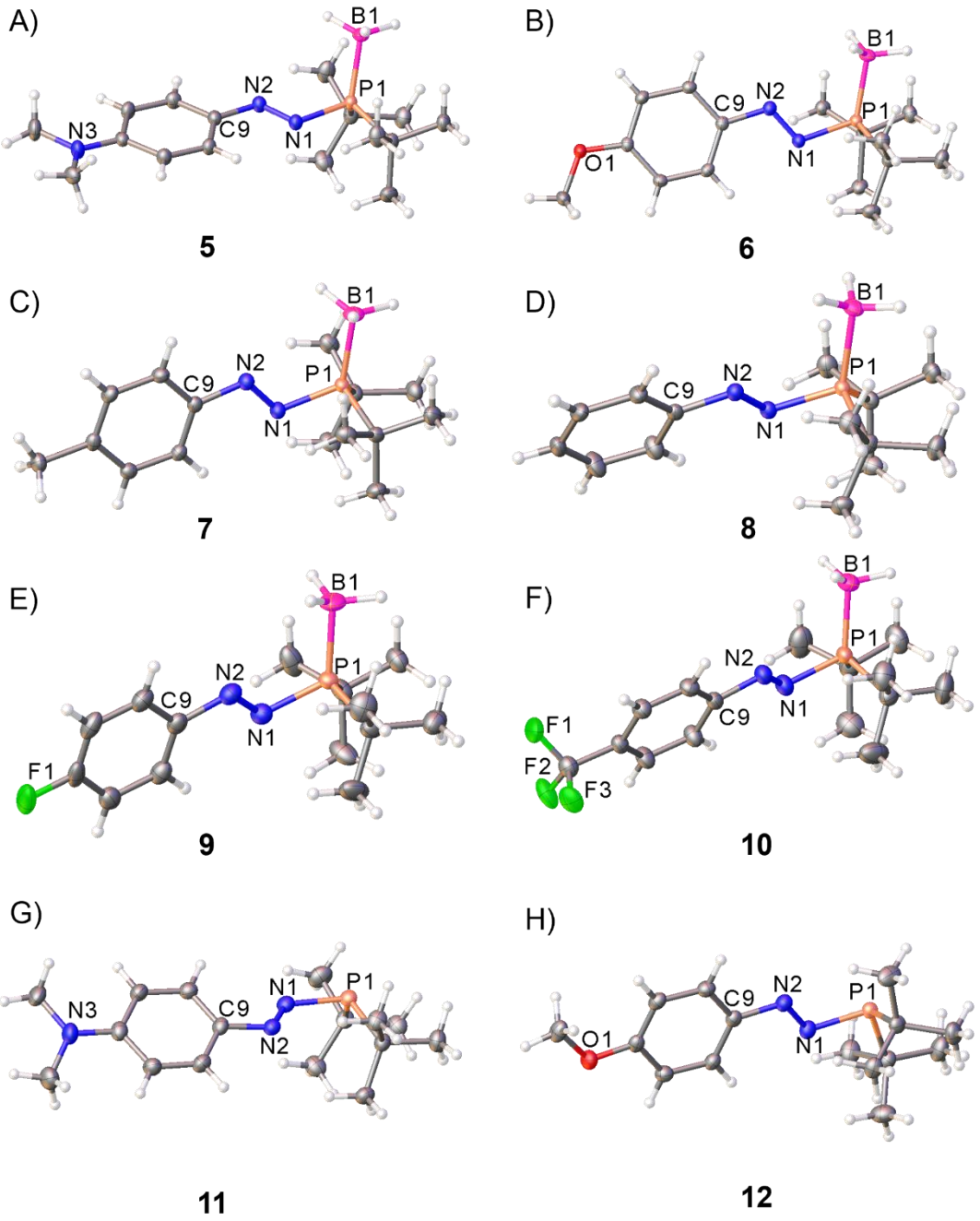


**Figure 3.1.** Single crystal structures of azophosphine-boranes **5** – **10** (A – F, respectively) and azophosphines **11** and **12** (G, H, respectively). *N*-aryl *para*-substituent = $NMe_2$ (A, G); OMe (B, H); Me (C); H (D), F (E); $CF_3$ (F). The structures of **5**, **10** and **11** contain two crystallographically independent molecules. The structure of **9** contains four crystallographically independent molecules. Only one molecule is shown for clarity. Single crystals of **8** were grown by Ethan Calder during his MSci project with supervision by the author. Thermal ellipsoids were drawn at the 50% probability level.[8]

## 3.3 Structural Trends[6,7]

### 3.3.1 X-ray Analysis

Selected bond distances, bond angles and torsion angles for crystallographically characterised azophosphine-boranes **5** – **10** are tabulated in Table 3.4.

**Table 3.4.** Selected bond distances (Å), bond angles (°) and torsion angles (°) of crystallographically characterised azophosphine-boranes **5** – **10**.

| Structure | C9–N2 | N1–N2 | N1–P1 |
|---|---|---|---|
| **5**[a] | 1.4047(18) | 1.2681(17) | 1.7380(12) |
| **6** | 1.4237(15) | 1.2561(14) | 1.7574(10) |
| **7** | 1.4318(17) | 1.2475(16) | 1.7519(12) |
| **8** | 1.4329(14) | 1.2514(14) | 1.7575(10) |
| **9**[a] | 1.442(4) | 1.233(4) | 1.762(3) |
| **10**[a] | 1.443(2) | 1.235(2) | 1.7552(17) |

| Structure | P1–N1–N2 | C10–C9–N1–N2 |
|---|---|---|
| **5**[a] | 114.33(10) | 4.3(2) |
| | | 0.3(2) |
| **6** | 113.38(8) | 6.23(16) |
| **7** | 114.28(9) | 3.79(19) |
| **8** | 113.05(8) | 1.31(16) |
| **9**[a] | 113.4(3) | 4.4(5) |
| **10**[a] | 115.20(14) | 1.9(3) |
| | | 12.7(3) |

[a] Structure contains >1 crystallographically independent molecule. One representative value is provided if there is no statistically significant difference (3σ); values for each molecule are provided if there is a statistical difference.

The single crystal structures of all six azophosphine-boranes **5** – **10** were obtained, so enabling assessment of systematic trends as the electronic properties of the Z group are varied. In general, the N1–N2 bond distance increases and the C9–N2 bond distance decreases as the Z group becomes more electron-donating, as expected with

the increased donation of electron density from the N-aryl substituent into the N=N π* orbital. This effect can be seen most clearly by comparing the two extreme azophosphine-boranes in terms of electronic properties, **5** (C9–N2: 1.4047(18) Å; N1–N2: 1.2681(17) Å) and **10** (C9–N2: 1.443(2) Å; N1–N2: 1.235(2) Å). The percentage change in the P–N bond distances is much smaller across the series and not in a rational order, which is understandable because the phosphine lone pair is forming a dative bond to the borane moiety and therefore cannot have a significant interaction with the neighbouring N=N π* orbital. The P1–N1–N2 bond angles also do not sequentially increase/decrease moving through the library, although there is a small degree of variation. The most significant differences in torsion angle within the series of azophosphine-boranes are observed within **5** and **10**, which contain more than one crystallographically independent molecule; thus these differences can likely be assigned to crystal packing effects.

As tabulated in Table 3.5, the pyramidal structure at phosphorus is reflected in the single crystal structures of azophosphines **11** and **12**, in which the sum of the angles around P1 is 313° and 308°, respectively, with N1–N2 and N1–P1 bond lengths of 1.258(3) and 1.17494(18) Å (**11**) and 1.2560(17) and 1.7660(13) Å (**12**), respectively. By contrast, the sum of the angles around the analogous nitrogen centre in related triazenes has been reported to be very close to 360°, with N=N bond lengths of 1.270(1) Å, 1.281(7) Å, and 1.288(6) Å,[9] highlighting the increased planarization in these species.

**Table 3.5.** Selected bond distances (Å), bond angles (°) and torsion angles (°) of crystallographically characterised azophosphines **11** – **12**.

| Structure | C9–N2 | N1–N2 | N1–P1 |
|---|---|---|---|
| **11**[a] | 1.424(3) | 1.258(3) | 1.7494(18) |
| | | | 1.7655(19) |
| **12** | 1.4333(19) | 1.2560(17) | 1.7660(13) |

| Structure | P1–N1–N2 | C10–C9–N1–N2 |
|---|---|---|
| **11**[a] | 119.34(14) | 22.9(3) |
| | 115.16(15) | 15.9(2) |
| **12** | 113.81(11) | 3.4(2) |

[a] Structure contains >1 crystallographically independent molecule. One representative value is provided if there is no statistically significant difference (3σ); values for each molecule are provided if there is a statistical difference.

### 3.3.2 Computational Analysis[6,7]

To probe the differences between azophosphine **11** and its N-containing analogue, triazene **A** (Table 3.6), DFT calculations and Natural Bond Orbital (NBO) analyses were carried out at the M06-2X-D3(Toluene)/def2-TZVPP level of theory. The computed bond metric data show **11** has a shorter N=N bond (1.239 Å) than **A** (1.247 Å); this is corroborated by a Wiberg Bond Index (WBI) of 1.84 for the N=N bond of **11**, and 1.67 for **A**. Both metrics are consistent with reduced donation from the pnictogen lone pair into the N=N π* orbital for **11** compared to **A**. This was further supported by the examination of the donor/acceptor interactions of the pnictogen lone pair into the N=N π* orbital; the value of 4.73 kcal $mol^{-1}$ for **11** is significantly smaller than 79.58 kcal $mol^{-1}$ for **A**. Additionally, the sum of the angles around the phosphorus centre in **11** (307.3°) is significantly lower than the angles around the nitrogen centre in **A** (357.6°), indicative of a pyramidal structure around the phosphorus centre, compared to the

highly planarized triazene. This is consistent with the crystal structure of **11** and **12** discussed above.

Given the diagonal relationship between phosphorus and carbon,[10] **11** was also compared to carbon analogue **B** (Table 3.6). The computed N=N bond length (1.232 Å) and WBI (1.86) for **B** places **11** in between **A** and **B** for both. These values are consistent with **B** possessing significant N=N double bond character and NC(H) single bond character (computed bond length of 1.465 Å). By contrast, the N=N bonds of **11** and **A** are both longer than the additive covalent radii for an N=N double bond, and the N–P/N–N bonds shorter, indicative of the increased delocalisation in these structures. These data underline that the structure of **11** exists somewhere between that of triazene **A** and the carbon equivalent **B**.

**Table 3.6.** Key computational parameters for the comparison of 11 with N and C(H) analogues. Table reproduced from reference [2].

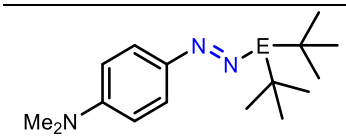


**E** = P (**11**)
N (**A**)
C(H) (**B**)

| | **3** | **A** | **B** |
|---|---|---|---|
| WBI for N=N bond | 1.84 | 1.67 | 1.86 |
| N=N bond length (Å) | 1.239 | 1.247 | 1.232 |
| E lone pair to N=N π* donation from NBO calculations (kcal mol$^{-1}$) | 4.73 | 79.58 | - |
| Sum of angles around E | 307.3 | 357.6 | - |

To explore the electronic structure of azophosphines **11** – **16** in more detail, DFT calculations and NBO analyses were carried out at the M06-2X-D3(Toluene)/def2-

TZVPP level of theory. The N–N bond distances in this series are all in a narrow range of 1.236 – 1.239 Å, which implies there is an approximately equal degree of delocalisation of electron density into the N=N π* orbital across the series. However, the source of this donated electron density varies as a function of the nature of the N-aryl *para* group, as shown by the two resonance structures **α** and **β** (Figure 3.2).

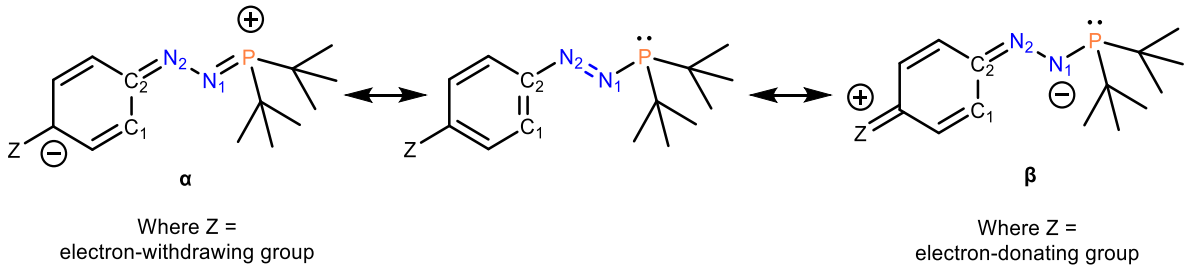


**Figure 3.2.** Key resonance structures of azophosphines, where the *para*-substituent is varied from electron-withdrawing to electron-donating group.

Natural population analysis (NPA) shows an increasingly electron-poor phosphorus centre as more electron-withdrawing substituents are used. This is consistent with a higher contribution from resonance canonical **α** as the phosphorus lone pair is increasingly delocalised into the N=N π* orbital and extended π-system. Conversely, with more electron-donating substituents, the NPA value for N1 becomes more negative, consistent with a higher contribution from resonance canonical **β** as more electron density resides on the formally anionic N1 centre. The NPA values are further supported by examination of the donor/acceptor interactions, which show larger donations from the neighbouring aryl π orbital into the N=N π* orbital with electron-donating substituents and increasing donation of the phosphorus lone pair into the N=N π* orbital with electron-withdrawing substituents. The similarity of the lengths of the N=N bonds across the series is reflective of both resonance canonicals **α** and **β** imparting similar effects on the bond. These data underline the effects of both

competing resonances on azophosphines and suggest that control over substituent may have an important role on the applications of azophosphines as ligands, with electron-donating substituents yielding a more electron-rich phosphorus centre.

## 3.4 Spectroscopic Trends[6]

The electronic effect of modulating Z can be seen spectroscopically in the $^{31}P\{^{1}H\}$ NMR spectra and UV/Vis spectra of azophosphines **11** – **16**. The $^{31}P$ chemical shift becomes gradually more deshielded as the Z group becomes more electron-withdrawing (107.8 – 119.7 ppm, Figure 3.3A), which demonstrates that although the Z group is far away from the phosphorus centre it does still influence its properties. This trend is evident in a plot of the $^{31}P$ NMR chemical shifts of **11** – **16** against the corresponding σ-*para* Hammett constants of Z, which shows a positive linear trend with an $R^2$ value of close to unity (Figure 3.3B). The colours of **11** – **16** are various shades of orange and red. The UV/Vis spectra of each azophosphine shows a strong absorbance band in the UV region between 350 and 388 nm, and a much weaker absorbance band between 500 and 521 nm that is responsible for the colour of the compounds. This weak absorbance band is red-shifted relative to the $\lambda_{max}$ values reported by Schneid (419 – 434 nm) in which yellow-coloured azophosphines were reported when the terminal nitrogen substituent was alkyl and can be rationalised by considering the effect of conjugation in the azophosphines. As conjugation increases, the energy difference between the highest occupied molecular orbital (HOMO) and the lowest occupied molecular orbital (LUMO) decreases meaning less energy is required to excite an electron, thus the wavelength of radiation that is absorbed is longer. For the one example where the N-substituent is aromatic ($PhN_2PPh_2$), similarly to **11** – **16**, the azophosphine is red and $\lambda_{max}$ is 482 nm.[5] The blue-shift of this value compared to **14** (Z = H, 512 nm) can be

attributed to the $PPh_2$ substituents of Schneid's $PhN_2PPh_2$ compared to the $P^tBu_2$ substituents of **14**. The UV/Vis spectra of **11** – **16** show only minor differences in absorption as the Z group is varied. Overall, absorbance is red-shifted moving from Z = $NMe_2$ to Z = $CF_3$; however, Z = F is blue-shifted relative to Z = H due to the mesomeric effect of F. This is summarised in the plot of UV/Vis absorbance of **11** – **16** against the corresponding σ-*para* Hammett constants of Z (Figure 3.3C), which shows an overall linear trend with an $R^2$ of 0.82727.

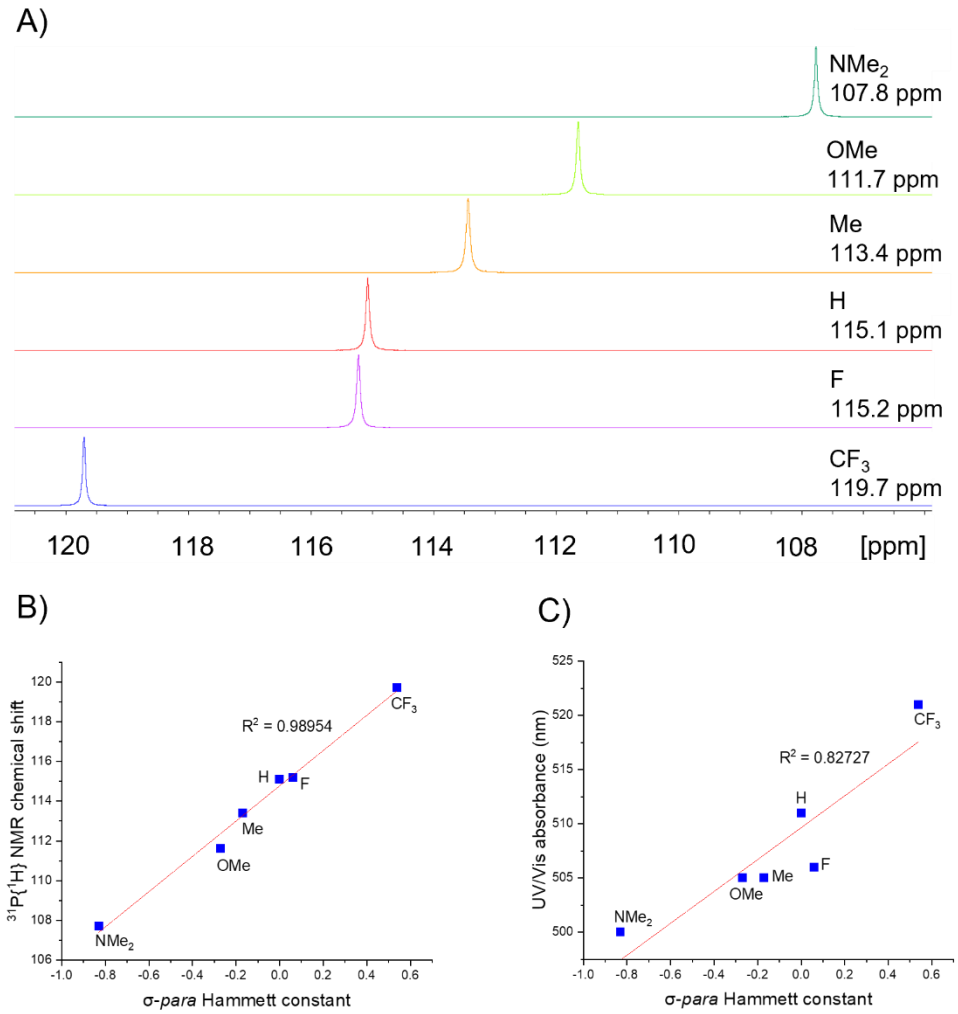


**Figure 3.3.** (A) Stacked $^{31}P\{^1H\}$ NMR spectra of **11** – **16** in toluene-$d_8$. (B) Plot of $^{31}P\{^1H\}$ NMR chemical shift (δ) against σ-para Hammett constant for **11** – **16**. (C) Plot of $\lambda_{max}$ (nm) of UV/Vis absorbance between 500 – 521 nm against σ-para Hammett constant for **11** – **16**.

## 3.5 Azophosphine-selenides[6]

To gain more insight into how varying the electronics of the *N*-aryl group affect the σ-donor character of the phosphorus centre of the azophosphine ligands, we investigated the $^{31}P–^{77}Se$ spin-spin coupling constants ($^{1}J_{P–Se}$) of the corresponding azophosphine selenides (**17** – **22**; Scheme 3.2) by $^{31}P\{^{1}H\}$ NMR spectroscopy ($^{77}Se$: 7.6% abundant, $I$ = ½). This approach is well-established in the literature[11–14] as an alternative to the more traditional measurement of the Tolman electronic parameter.[13,15,16] Providing the steric bulk surrounding the phosphorus atom remains similar,[11] the value of the $^{1}J_{P–Se}$ coupling constant is dependent on the electronic nature of the substituents at P and, as governed by Bent's rule and the Fermi-contact interactions of the s-orbitals of P and Se, increases with increasingly electron-withdrawing substituents. The magnitude of $^{1}J_{P–Se}$ therefore inversely corresponds to the relative σ-donor capability of a homologous series of P-based ligands.

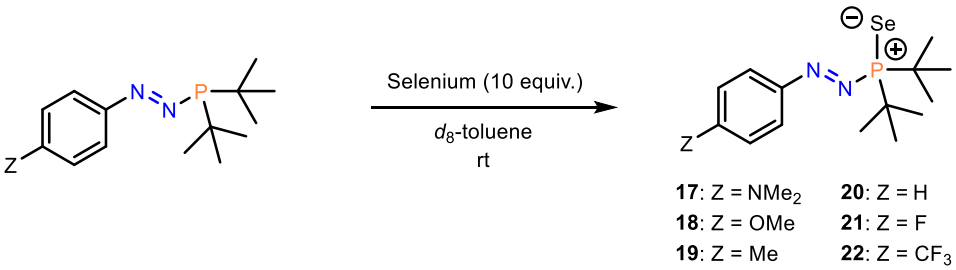


**Scheme 3.2**. Synthesis of azophosphine-selenides **17** – **22**.

The azophosphine-selenides were prepared by reaction of a toluene solution of the azophosphine **11** – **16** with excess grey selenium (Scheme 3.2). Full conversion to the azophosphine-selenide was confirmed by $^{31}P\{^{1}H\}$ NMR spectroscopy. A similar trend in the $^{31}P$ chemical shift to that of **11** – **16** is observed for the azophosphine-selenides, increasing in ppm from **17** to **22** (Table 3.7). The value of the $^{1}J_{P–Se}$ coupling constant

increases from **17** to **22**, which demonstrates that the phosphorus centres in the azophosphine ligands **11** – **16** become a poorer σ donor as Z gets increasingly electron-withdrawing, as expected.

**Table 3.7.** Chemical shifts (ppm) of **11** – **16** and **17** – **22**, and $^{1}J_{P-Se}$ coupling constants (Hz) of **17** – **22**, determined by $^{31}P\{^{1}H\}$ NMR spectroscopy in $d_8$-toluene.

| Z | δ / ppm (**11 – 16**) | δ / ppm (**17** – **22**) | $^{1}J_{P-Se}$ / Hz (**17** – **22**) |
|---|---|---|---|
| $NMe_2$ | 107.8 | 108.8 | 794 |
| OMe | 111.7 | 112.0 | 801 |
| Me | 113.4 | 113.3 | 804 |
| H | 115.1 | 114.1 | 806 |
| F | 115.2 | 114.4 | 806 |
| $CF_3$ | 119.7 | 116.4 | 810 |

To put these values in perspective against established phosphines that have a similar steric profile around the phosphorus centre, the $^{1}J_{P-Se}$ values of the selenides of P$^t$Bu$_3$ (709 Hz in $C_6D_6$ or 686 Hz in $CDCl_3$) and JohnPhos (a ligand used with high success in Pd-catalysed cross-coupling reactions; 735 Hz in $CDCl_3$) (Figure 3.4) are significantly lower than those of azophosphines **11** – **16**, and the azophosphines are therefore much poorer donors.[13,14,17]

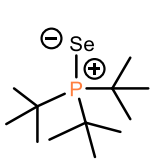


P$^t$Bu$_3$–selenide

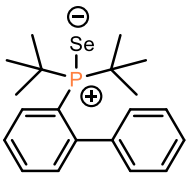


JohnPhos–selenide

**Figure 3.4.** Structures of the selenides of P$^t$Bu$_3$ and JohnPhos

The influence of the electronegative azo group on the donor ability of azophosphine-selenides **17** – **22** can be seen by comparing **20** (806 Hz) and **22** (810 Hz) with the

selenides of the analogous PhP$^t$Bu$_2$ (708 Hz in $CDCl_3$) and *p*-($CF_3$)$C_6H_4$P$^t$Bu$_2$ (720 Hz in $CDCl_3$), respectively.[14] **20** and **22** are both approximately 100 Hz greater in $^1J_{P–Se}$ value than their non-azo analogues. These data show that in general azophosphines are relatively weak phosphine donors, and that within this chemical space it is possible to fine-tune the donor properties by varying the Z group.

## 3.6 Photo-switching

The changes in electronics of azophosphines **11** – **16**, due to systematically varying the *N*-aryl substituent, provide clear trends in the NMR and UV/Vis spectroscopic measurements. A minor effect on the structure of azophosphine-boranes **5** – **10** and azophosphines **11** – **16** was also observed, as explored by single crystal X-ray diffraction and DFT studies, respectively. With this in mind and considering the photo-switching investigations discussed in Chapter 2 were restricted to **1** – **4**, the potential effect of varying the *N*-aryl substituent on the ability of the azophosphines to act as photo-switches was explored (Scheme 3.3).

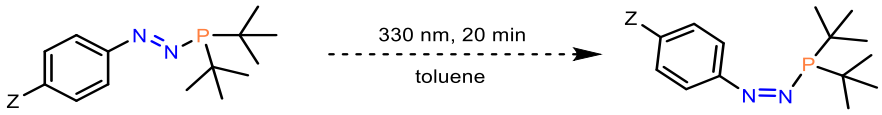


**Scheme 3 3.** Hypothesised *E* to *Z* isomerisation of azophosphines with UV irradiation.

Irradiation for 20 min at 330 nm of 50 mM solutions of **11** (Z = $NMe_2$) and **16** (Z = $CF_3$) in toluene produced no observable difference in UV/Vis spectra prior and post irradiation. When an analogous solution of azophosphine **12** (Z = OMe) was irradiated at 330 nm, after 20 min a subtle decrease in absorption was observed, albeit with no difference in $\lambda_{max}$ for either absorption band (Figure 3.5A). When repeated with the corresponding azophosphine-borane **6** these differences in absorption between

spectra prior and post irradiation were not observed (Figure 3.5B). The azophosphines are known to be unstable with heating beyond 30 °C thus preventing extended irradiation beyond 20 min.

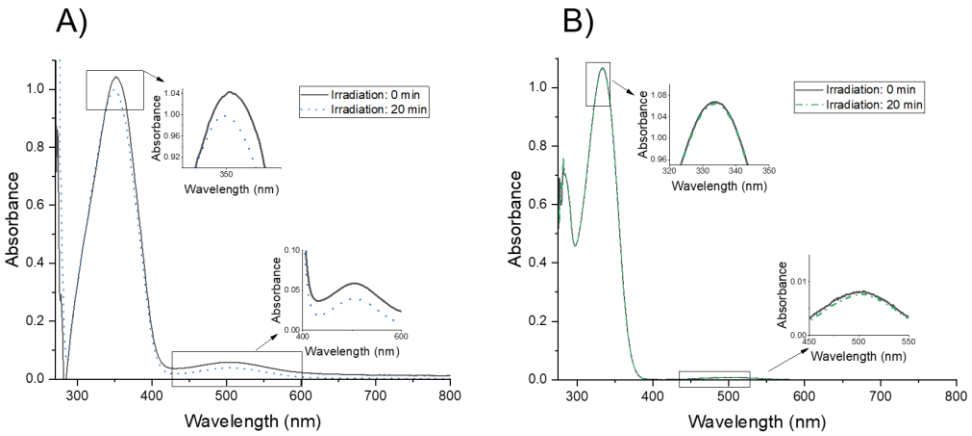


**Figure 3.5.** (A) UV/Vis spectrum of **12** after 0 and 20 min of irradiation at 330 nm. (B) UV/Vis spectrum of **6** after 0 and 20 min of irradiation at 330 nm. Prepared as 50 mM solutions in toluene.

The difference in absorption for **12** prior and post irradiation is minimal; however, it does suggest that these differences could be due to changes in the electronics of the azophosphine. Although no difference in absorption is observed for **6**, in which the phosphorus lone pair is coordinated to the borane, once coordinated to a metal centre the electronics would be sufficiently different to that of **6** to warrant further investigation of the photo-switching ability of a metal-azophosphine complex (discussed in Chapter 4).

## 3.7 Conclusion

This chapter discussed the synthesis of a library of azophosphines of general formula *p*-(Z)$C_6H_4N_2P^tBu_2$, in which Z was systematically modulated to span the electron-donating to electron-withdrawing range (Z = $NMe_2$, OMe, Me, H, F, $CF_3$), using the general synthetic route reported in Chapter 2. Structural trends were observed in

azophosphine-boranes **5** – **10** and azophosphines **11** – **16** from analysis of X-ray diffraction data and computational methods, respectively. The effect of modulating Z was further observed in spectroscopic trends from analysis of NMR and UV/Vis. spectra of **11** – **16**. The pyramidal structure at phosphorus, determined by X-ray diffraction of single crystals of **11** and **12**, was consistent with computational data and highlighted the availability of the phosphorus lone pair and the viable application of azophosphines as ligands. Analysis of the $^{1}J_{P-Se}$ coupling constants, by $^{31}P\{^{1}H\}$ NMR spectroscopy, of the corresponding azophosphine-selenides of **11** – **16** found varying the electronics of Z affected the σ-donor character of the phosphorus centre of the azophosphine ligands, with electron-donating Z substituents yielding a more electron-rich phosphorus centre. When compared to established phosphines with a similar steric profile around phosphorus, in general, azophosphines were relatively weak phosphine donors. Differences in UV/Vis. absorption for azophosphine **12** prior and post irradiation at 330 nm, albeit minimal, could potentially be assigned to changes in electronics of the azophosphine, thus encouraging investigation of the photo-switching ability of a metal-azophosphine complex.

## 3.8 Experimental

Except as otherwise noted, the syntheses of **5 - 22** were performed using standard Schlenk line technique under a flow of dry, oxygen-free nitrogen, or an MBraun ECO glovebox under an atmosphere of dry, oxygen-free nitrogen with water and oxygen levels maintained at <0.1 ppm.

Room temperature (RT) refers to reactions where no thermostatic control was applied and the temperature was recorded as 16–25 °C. Unless otherwise stated, overnight reactions refer to a period of 16 h. Thin layer chromatography (TLC) analysis was performed using Machery-Nagel aluminium-backed silica plates. Spots were visualised by the quenching of ultraviolet light. All flash column chromatography was performed using Fluorochem 60. silica gel (particle size 40–63 μm) with a column of appropriate size. All glassware and Teflon-coated stirrer bars were dried in a 80 °C oven overnight prior to use, unless otherwise stated. All molecular sieves are 3 Å and purchased from VWR chemicals and were activated by heating at 400 °C under vacuum prior to use. Unless otherwise stated, degassing refers to three freeze-pump-thaw cycles.

Commercial reagents were purchased, suitably stored as specified by the supplier, and used as received, unless otherwise stated, from Sigma-Aldrich (*p*-anisidine, 99%; aniline, 99.5%; *p*-(trifluoromethyl) aniline, 99%; *sec*-butyllithium, 1.42 M in cyclohexane; borane-di(*tert*-butyl)phosphine complex, 94%; pyrrolidine, anhydrous, > 99.5%, stored in an air-tight ampoule), Acros Organics (*N*,*N*-dimethyl-*p*-phenylenediamine, 97%) or Alfa Aesar (*p*-toluidine, 99+%; *p*-fluoroaniline, 99%; sodium nitrite, 97%; tetrafluoroboric acid, ca. 50% w/w aq. sol.) Solvents were purchased and used as received, unless otherwise stated, from Sigma-Aldrich

(hexane, puriss, p.a., ACS reagent, reag. Ph. Eur., 99+ (GC), degassed and stored in air-tight ampoules over 3 Å molecular sieves; diethyl ether, ACS reagent, 99.8%; acetonitrile, suitable for HPLC, gradient grade, 99.9%; acetonitrile-$d_3$, 99.8 atom % D, contains 0.03% (v/v) TMS; chloroform-*d*, 99.8 atom % D, dried by overnight reaction with $CaH_2$, degassed and stored in an air-tight ampoule over 3 Å molecular sieves; toluene-$d_8$, 99.6 atom % D, dried by overnight reaction with $CaH_2$, degassed and stored in an air-tight ampoule over 3 Å molecular sieves) or Fisher Scientific (*iso*-octane, laboratory reagent grade; dichloromethane (DCM), 99.8%, HPLC grade). Toluene was obtained from the laboratory solvent purification system, degassed, and stored in air-tight ampoules over 3 Å molecular sieves. THF was obtained from the laboratory solvent purification system, degassed, dried over Na/benzophenone, and stored in air-tight ampoules over 3 Å molecular sieves. Deionised water was obtained from an Elga DV35 Purelab. For recrystallisations and as eluent for column chromatography, hexane was used as received.

All NMR spectra were collected on a Bruker 500 MHz AV_NEO Avance NMR Spectrometer or a Bruker 400 MHz AV_NEO Avance NMR Spectrometer. Chemical shifts are reported in ppm, coupling constants (*J*) are reported in Hz. $^{1}H$ and $^{13}C$ NMR spectra were referenced internally to the most up-field solvent peak; $^{31}P$ and $^{31}P\{^{1}H\}$ NMR spectra are externally referenced to 85% $H_3PO_4$; $^{11}B\{^{1}H\}$ NMR spectra are externally referenced to $BF_3.OEt_2$; $^{19}F\{^{1}H\}$ NMR spectra are externally referenced to $CFCl_3$.

All UV/Vis absorption spectra were collected on a Cary50 UV/Vis Spectrometer. The samples were prepared as 50 mM solutions in toluene to a volume of 3 mL and irradiated in a quartz glass High Precision Cell cuvette (10 x 10 mm) from Hellma

Analytics. Air-sensitive UV-Vis samples were collected using a sealable cuvette, with solutions made up in the glovebox.

All IR spectra were collected on a Perkin Elmer Spectrum Two FT-IR spectrometer using attenuated total reflection (ATR) sampling technique.

All mass spectra were collected on a Waters Xevo G2-XS TOF mass spectrometer using electrospray ionisation (ESI) positive ion mode or atmospheric solids analysis probe (ASAP) with atmospheric pressure ionisation positive ion mode. Using ESI, samples were dissolved in dry acetonitrile and directly injected into the ESI ionisation chamber via a 250 µL glass syringe. Using ASAP, samples were run neat by dipping a glass capillary into the sample vial, before insertion into the ASAP source.

Single-crystal X-ray diffraction data were collected at either 100 or 120 K on an Agilent SuperNova A diffractometer using an Atlas detector, using Cu-Kα radiation (λ = 1.54184). The data collections were driven and processed, and absorption corrections were applied using CrysalisPro.[18] Using OLEX2[19] the structures were solved using SHELXT[20] and were refined by a full-matrix least-squares procedure on $F^2$ in SHELXL.[21] All non-hydrogen atoms were refined with anisotropic displacement parameters.

All computational details are provided in the supporting information of references [6] and [7].

### 3.8.1 General Procedure for the Synthesis of Arenediazonium Tetrafluoroborates (GP5).

Arenediazonium tetrafluoroborates were prepared following a standard literature procedure.[22,23] To the substituted aniline (2.0 mmol, 1.0 equiv.) in water (1 mL), 50 wt.%

aq. $HBF_4$ (0.68 mL) was added. The mixture was cooled in an ice-water bath and a solution of $NaNO_2$ (2.0 mmol, 1.0 equiv.) in water (0.4 mL) was added dropwise. The mixture was stirred for 45 min at 0 °C after which the precipitate was collected by Buchner filtration, washed with diethyl ether (3 x 20 mL) and dried *in vacuo* to obtain the crude arenediazonium tetrafluoroborate $[ArN_2][BF_4]$. The crude arenediazonium tetrafluoroborate was dissolved in minimal acetonitrile, filtered if necessary, and recrystallised by addition to excess diethyl ether (approx. 70 mL) with addition of further diethyl ether until no more precipitate formed. The precipitate was collected by Buchner filtration, washed with diethyl ether (3 x 20 mL) and dried *in vacuo* to obtain the purified arenediazonium tetrafluoroborate $[ArN_2][BF_4]$. The salts were transferred to foil-wrapped vials and stored in the freezer at −35 °C.

**_p_-dimethylaminobenzenediazonium tetrafluoroborate [_p_-(NMe$_2$)C$_6$H$_4$N$_2$][BF$_4$]**

[*p*-(NMe$_2$)C$_6$H$_4$N$_2$][BF$_4$] was synthesised from *N*,*N*-dimethylphenylenediamine (4.0 mmol, 540 mg) according to GP5 and isolated as a dark grey solid (240 mg, 53%). $^1$H (400.1 MHz, $CD_3CN$, 298 K): δ 8.00 (d, $^3J_{H\text{-}H}$ = 10 Hz, 2H; $H_{Ar}$), 6.93 (d, $^3J_{H\text{-}H}$ = 10 Hz, 2H; $H_{Ar}$), 3.26 (s, 6H; N(C$H_3$)$_2$). $^{19}$F{$^1$H} (376.5 MHz, $CD_3CN$, 298 K): δ −152.0 (s; $^{11}BF_4$), −151.9 (s; $^{10}BF_4$). This is consistent with literature values.[22,23]

**_p_-anisyldiazonium tetrafluoroborate [_p_-(OMe)C$_6$H$_4$N$_2$][BF$_4$]**

[*p*-(OCH$_3$)C$_6$H$_4$N$_2$][BF$_4$] was synthesised from *p*-anisidine (8.0 mmol, 0.92 mL) according to GP5 and isolated as a white solid (1.1 g, 65%). $^1$H (400.1 MHz, $CD_3CN$, 298 K): δ 8.43-8.39 (m, 2H; $H_{Ar}$), 7.36-7.32 (m, 2H; $H_{Ar}$), 4.06 (s; 3H, *p*-OC$H_3$). $^{19}$F{$^1$H} (376.5 MHz, $CD_3CN$, 298 K): δ −151.6 (s; $^{11}BF_4$), −151.6 (s; $^{10}BF_4$). This is consistent with literature values.[22,23]

**_p_-tolyldiazonium tetrafluoroborate [_p_-(Me)$C_6H_4N_2$][$BF_4$]**

[_p_-($CH_3$)$C_6H_4N_2$][$BF_4$] was synthesised from _p_-toluidine (2.0 mmol, 0.22 mL) according to GP5 and isolated as a white solid (160 mg, 38%). $^1$H (400.1 MHz, $CD_3CN$, 298 K): δ 8.36 (d, $^3J_{H\text{-}H}$ = 9 Hz, 2H; $H_{Ar}$), 7.73 (d, $^3J_{H\text{-}H}$ = 9 Hz, 2H; $H_{Ar}$), 2.61 (s; 3H, _p_-C$H_3$). $^{19}$F{$^1$H} (376.5 MHz, $CD_3CN$, 298 K): δ −151.6 (s; $^{11}$B$F_4$), −151.7 (s; $^{10}$B$F_4$). This is consistent with literature values.[22,23]

**Benzenediazonium tetrafluoroborate [$C_6H_4N_2$][$BF_4$]**

[$C_6H_4N_2$][$BF_4$] was synthesised from aniline (2.0 mmol, 0.18 mL) according to GP5 and isolated as an off-white solid (120mg, 31%). $^1$H (400.1 MHz, $CD_3CN$, 298 K): δ 7.90-7.94 (m, 2H; $H_{Ar}$), 8.25 tt, $^3J_{H\text{-}H}$ = 8 Hz, $^4J_{H\text{-}H}$ = 1 Hz, 1H; $H_{Ar}$), 8.49-8.51 (m, 2H; $H_{Ar}$). $^{19}$F{$^1$H} (376.5 MHz, $CD_3CN$, 298 K): δ −150.3 (s; B$F_4$). This is consistent with literature values.[22,23]

**_p_-fluorobenzenediazonium tetrafluoroborate [_p_-(F)$C_6H_4N_2$][$BF_4$]**

[_p_-(F)$C_6H_4N_2$][$BF_4$] was synthesised from _p_-fluoroaniline (4.0 mmol, 0.38 mL) according to GP5 and isolated as a white solid (370 mg, 43%). $^1$H (400.1 MHz, $CD_3CN$, 298 K): δ 8.61-8.58 (m, 2H; $H_{Ar}$), 7.69-7.64 (m, 2H; $H_{Ar}$). $^{19}$F{$^1$H} (376.5 MHz, $CD_3CN$, 298 K): δ −84.8 (s; _p-F_), −151.4 (s; $^{11}$B$F_4$), −151.5 (s; $^{10}$B$F_4$). This is consistent with literature values.[22,23]

**_p_-(trifluoromethyl)benzenediazonium tetrafluoroborate [_p_-($CF_3$)$C_6H_4N_2$][$BF_4$]**

[_p_-($CF_3$)$C_6H_4N_2$][$BF_4$] was synthesised from _p_-(trifluoromethyl)aniline (7.4 mmol, 0.78 mL) according to GP5 and isolated as a pale yellow solid (860 mg, 45%). $^1$H (400.1 MHz, $CD_3CN$, 298 K): δ 8.74-8.68 (m, 2H; $H_{Ar}$), 8.34-8.16 (m, 2H; $H_{Ar}$). $^{19}$F{$^1$H} (376.5 MHz, $CD_3CN$, 298 K): δ −64.8 (s; _p_-C$F_3$), −151.1 (s; B$F_4$). This is consistent with literature values.[22,23]

### 3.8.2 General Procedure for the Synthesis of Azophosphine-Borane Adducts (GP6)

A 25 mL Schlenk flask was charged with a 0.25 M THF solution of H$^t$Bu$_2$P·BH$_3$ (1.0 equiv.) and cooled to –78 °C. A 1.42 M cyclohexane solution of *sec*-butyllithium (1.0 equiv.) was added dropwise, resulting in a colour change from colourless to pale yellow. The solution was allowed to warm to room temperature over 2 h, and then stirred for a further 30 min at room temperature. This solution was added dropwise to a separate Schlenk containing a slurry of arenediazonium tetrafluoroborate salt (1.0 equiv.) in THF at –78 °C, resulting in an immediate colour change. The reaction was left to warm slowly to room temperature and stirred for 1 h. The volatiles were removed *in vacuo*, and the product isolated by column chromatography. Removal of the volatiles *in vacuo* yielded the product as an intensely coloured solid. The air-stable, solid products were stored in vials, away from direct light, in the freezer.

***p*-(NMe$_2$)C$_6$H$_4$N$_2$P$^t$Bu$_2$·BH$_3$ (5)**

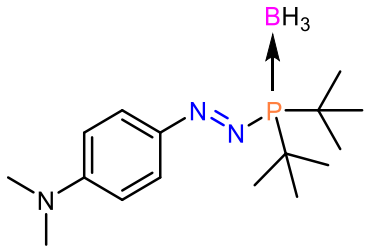


Borane azophosphine **5** was synthesised from precursor [*p*-N(CH$_3$)$_2$C$_6$H$_4$N$_2$][BF$_4$] (2.1 mmol, 490 mg, 1.0 equiv.) according to GP6. Purification by column chromatography (eluent = 0 → 10% diethyl ether in hexane) obtained **5** as a red powder (550 mg, 84%). Single crystals of **5** suitable for single-crystal X-ray diffraction were grown by slow evaporation of a hexane solution of the product at room temperature. $^1$H (400 MHz,

$CD_3CN$, 298 K): δ 7.81 – 7.68 (m, 2H; $H_{Ar}$), 6.80 – 6.73 (m, 2H; $H_{Ar}$), 3.09 (s, 6H; *p*-N($CH_3$)$_2$), 1.34 (d, $^3J_{H\text{-}P}$ = 12 Hz, 18H; $^t$Bu), 0.44 (br. quart., 3H; B$H_3$). $^{13}$C (101 MHz, $CD_3CN$, 289 K): δ 155.1 (s; N-$C_{Ar}$), 147.9 (d, $^3J_{C-P}$ = 37 Hz; *ipso*-$C_{Ar}$), 129.3 (s, *o*-$C_{Ar}$) 112.1 (s, *m*-$C_{Ar}$), 40.5 (s, *p*-N($CH_3$)$_2$), 35.5 (d, $^1J_{C-P}$ = 27 Hz, $C(CH_3)_3$), 27.8 (s; $C(CH_3)_3$). $^{31}$P{$^1$H} (202.4 MHz, CDCN): δ 99.1 (br. quart.).$^{31}$P (162.0 MHz, $CD_3CN$): δ 99.1 (br. s). $^{11}$B{$^1$H} (128.4 MHz, $CD_3CN$, 298 K): δ -42.3 (d, $^1J_{B\text{-}P}$ = 55 Hz). UV-Vis (toluene, nm) $\lambda_{max}$: 406 (s), 503 (w). ASAP+ HRMS m/z for $C_{16}H_{30}BN_3P$ [*M* – H]$^+$: calcd. (found) 305.2307 (305.2316), 306.2273 (306.2283). IR: $\nu_{max}$ (cm$^{-1}$) 2984 (w), 2952 (w), 2909 (w), 2868 (w), 2375 (m, B–H), 1606.8 (s) (N=N), 1523.3 (m).

**_p_-(OMe)$C_6H_4N_2P^tBu_2$·$BH_3$ (6)**

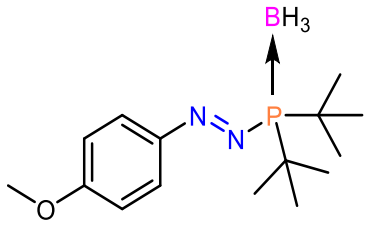


Borane azophosphine **6** was synthesised from precursor [*p*-(OMe)$C_6H_4N_2$][$BF_4$] (5.1 mmol, 1.0 g, 1.0 equiv.) according to GP6. Purification by column chromatography (eluent = 0 → 10% diethyl ether in hexane) obtained **6** as a pink powder (1.0 g, 66%). Single crystals of **6** suitable for single-crystal X-ray diffraction were grown by slow evaporation of a toluene solution of the product at room temperature. $^1$H (500.1 MHz, $CDCl_3$, 298 K): δ 7.86 (d, $^3J_{H-H}$ = 9 Hz, 2H; $H_{Ar}$), 6.99 (d, $^3J_{H-H}$ = 9 Hz, 2H; $H_{Ar}$), 3.90 (s, 3H; *p*-O$CH_3$), 1.39 (d, $^3J_{H-P}$ = 12 Hz, 18H; $^t$Bu), 0.56 (br. quart., 3H; B$H_3$). $^{13}$C{$^1$H} (125.8 MHz, $CDCl_3$): δ 163.8 (s, *p*-$C_{Ar}$), 149.9 (d; $^3J_{C-P}$ = 37 Hz; *i*-$C_{Ar}$), 124.9 (s; *o*-$C_{Ar}$), 114.3 (s; *m*-$C_{Ar}$), 55.9 (s, *p*-O$CH_3$), 35.1 (d; $^1J_{C-P}$ = 25 Hz; $C(CH_3)_3$), 27.7 (s; $C(CH_3)_3$). $^{31}$P{$^1$H} (202.4 MHz, $CDCl_3$): δ 103.9 (br. quart.). $^{31}$P (162.0 MHz, $CDCl_3$): δ 103.9 (br.

s). $^{11}B\{^1H\}$ (128.4 MHz, $CDCl_3$): δ -42.5 (d, $^1J_{B–P}$ = 51 Hz). UV-Vis (toluene, nm) $\lambda_{max}$: 334 (s), 499 (w). ESI-HRMS m/z for $C_{15}H_{27}N_2OPB$ [*M* – H]$^+$: calcd. (found) 292.1990 (292.1996), 293.1957 (293.1964). IR ($cm^{-1}$) $\nu_{max}$: 2988 (w), 2967 (w), 2868 (w), 2407 (m, B–H), 1593 (s, N=N).

***p*-(Me)$C_6H_4N_2P^tBu_2$·$BH_3$ (7)**

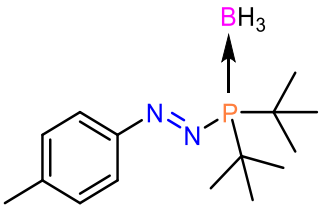


Borane azophosphine **7** was synthesised from precursor [*p*-(Me)$C_6H_4N_2$][$BF_4$] (1.6 mmol, 330 mg, 1.0 equiv.) according to GP6. Purification by column chromatography (eluent = 0 → 5% diethyl ether in hexane) obtained **7** as a pink powder (310 mg, 69%). Single crystals of **7** suitable for single-crystal X-ray diffraction were grown by slow evaporation of a toluene solution of the product at –35 °C. $^1H$ (400.1 MHz, $CD_3CN$, 298 K): δ 7.73 (d, $^3J_{H–H}$ = 8 Hz, 2H; *H*$_{Ar}$), 7.39 (d, $^3J_{H–H}$ = 8 Hz, 2H; *H*$_{Ar}$), 2.43 (s, 3H; *p*-C*H*$_3$, 1.36 (d, $^3J_{H–P}$ = 12 Hz, 18H; $^t$Bu), 0.47 (br. quart., 3H; B*H*$_3$). $^{13}C\{^1H\}$ (125.8 MHz, $CD_3CN$): δ 154.1 (d; $^3J_{C–P}$ = 36 Hz; *i*-*C*$_{Ar}$), 145.5 (s, *p*-*C*$_{Ar}$), 131.0 (s; *C*$_{Ar}$), 123.2 (s; *C*$_{Ar}$), 35.7 (d; $^1J_{C–P}$ = 25 Hz; *C*$(CH_3)_3$), 27.8 (s; *C*$(CH_3)_3$), 21.6 (s; *p*-$CH_3$). $^{31}P\{^1H\}$ (202.4 MHz, $CD_3CN$): δ 106.2 (br. quart.). $^{31}P$ (162.0 MHz, $CD_3CN$): δ 106.2 (br. s). $^{11}B\{^1H\}$ (128.4 MHz, $CD_3CN$): δ -43.0 (d, $^1J_{B–P}$ = 52 Hz). UV-Vis (toluene, nm) $\lambda_{max}$: 310 (s), 510 (w). ESI-HRMS m/z for $C_{15}H_{27}BN_2P$ [*M* – H]$^+$: calcd. (found) 276.2041 (276.2039), 277.2008 (277.2008). IR ($cm^{-1}$) $\nu_{max}$: 3727 (w), 3700 (w), 3627 (w), 3599 (w), 2983 (w), 2965 (m), 2921 (w), 2868 (w), 2414 (m), 2393 (m), 2333 (m, B–H), 1739 (w), 1598 (w, N=N), 1501 (m).

**$C_6H_5N_2P^tBu_2{\cdot}BH_3$ (8)**

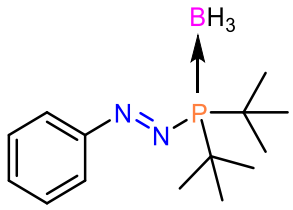


Borane azophosphine **8** was synthesised from precursor $[C_6H_4N_2][BF_4]$ (1.9 mmol, 360 mg, 1.0 equiv.) according to GP6. Purification by column chromatography (eluent = 0 → 5% diethyl ether in hexane) obtained **8** as a pink/red powder (300 mg, 60%). Single crystals of **8** suitable for single-crystal X-ray diffraction were grown by slow evaporation of a toluene solution of the product at room temperature. $^1$H (400.1 MHz, $CD_3CN$, 298 K): δ 7.84 – 7.81 (m, 2H; *H*$_{Ar}$), 7.66 – 7.57 (m, 3H; *H*$_{Ar}$), 1.38 (d, $^3J_{H-P}$ = 13 Hz, 18H; $^t$Bu), 0.48 (br. quart., 3H; B*H*$_3$). $^{13}$C{$^1$H} (101 MHz, $CD_3CN$, 289 K): δ 155.6 (d, $^3J_{C-P}$ = 35 Hz; *i*-*C*$_{Ar}$), 134.2 (s, *C*$_{Ar}$), 130.5 (s, *C*$_{Ar}$), 123.1 (s, *C*$_{Ar}$), 35.7 (d, $^1J_{C-P}$ = 25 Hz; *C*$(CH_3)_3$), 27.8 (s, C(*C*$H_3)_3$). $^{31}$P{$^1$H} (162 MHz, CDCN, 298 K): δ 107.6 (br. quart.). $^{31}$P (162.0 MHz, $CD_3CN$, 298 K): δ 107.6 (br. s). $^{11}$B{$^1$H} (128.4 MHz, $CD_3CN$, 298 K): δ -42.9 (d, $^1J_{B-P}$ = 51 Hz). UV-Vis (toluene, nm) $\lambda_{max}$: 296 (s), 509 (w). ESI-HRMS m/z for $C_{14}H_{25}BN_2P$ [*M* – H]$^+$: calcd. (found) 262.1885 (262.1882), 263.1851 (263.1855). IR (cm$^{-1}$) $\nu_{max}$: 2969 (w), 2952 (w), 2921.2 (w), 2871 (w), 2408 (m), 2372 (m, B–H), 1738 (m), 1477 (m, N=N).

***p*-(F)$C_6H_4N_2P^tBu_2{\cdot}BH_3$ (9)**

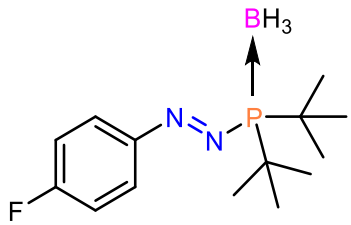

Borane azophosphine **9** was synthesised from precursor [*p*-(F)$C_6H_4N_2$][$BF_4$] (1.9 mmol, 390 mg, 1.0 equiv.) according to GP6. Purification by column chromatography (eluent = 0 → 5% diethyl ether in hexane) obtained **9** as a red solid (320 mg, 60%). Single crystals of **9** suitable for single-crystal X-ray diffraction were grown by slow evaporation of a hexane solution of the product at room temperature. $^1$H NMR (400 MHz, $CD_3CN$, 298 K): δ 7.94 – 7.84 (m, 2H; *H*$_{Ar}$), 7.37 – 7.27 (m, 2H; *H*$_{Ar}$), 1.37 (d, $^3J_{H\text{-}P}$ = 13 Hz, 18H; $^t$Bu), 0.47 (br. quart., 3H; B*H*$_3$). $^{13}$C{$^1$H} (101 MHz, $CD_3CN$, 289 K): δ 166.6 (d, $^1J_{C\text{-}F}$ = 253 Hz; *p*-*C*F), 152.5 (dd, $^3J_{C\text{-}P}$ = 36 Hz, $^4J_{C\text{-}F}$ = 3 Hz; *i*-*C*$_{Ar}$), 125.7 (dd, $^3J_{C\text{-}F}$ = 10 Hz, $^4J_{C\text{-}P}$ = 2 Hz, *o*-*C*$_{Ar}$), 117.40 (d, $^2J_{C\text{-}F}$ = 23 Hz, *m*-*C*$_{AR}$), 35.7 (d, $^1J_{C\text{-}P}$ = 25 Hz; *C*($CH_3$)$_3$), 27.8 (s, C(*C*$H_3$)$_3$). $^{31}$P{$^1$H} (162 MHz, CDCN, 298 K): δ 107.9 (br. quart.). $^{31}$P (162.0 MHz, CDCN, 298 K): δ 107.9 (br. s). $^{19}$F{$^1$H} (377 MHz, $CD_3CN$, 298 K): δ −108.0 (s). $^{11}$B{$^1$H} (128.4 MHz, $CD_3CN$, 298 K): δ -43.0 (d, $^1J_{B\text{-}P}$ = 51 Hz). UV-Vis (toluene, nm) $\lambda_{max}$: 301 (s), 510 (w). ESI-HRMS m/z for $C_{14}H_{24}BN_2FP$ [*M* – H]$^+$: calcd. (found) 280.1790 (280.1787), 281.1757 (281.1754). IR (cm$^{-1}$) $\nu_{max}$: 2983 (w), 2966 (w) 2870 (w), 2382 (m, B–H), 1589 (m, N=N), 1497 (s).

***p*-($CF_3$)$C_6H_4N_2P^tBu_2$·$BH_3$ (10)**

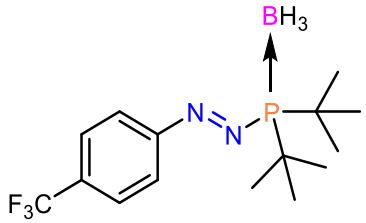


Borane azophosphine **10** was synthesised from precursor [*p*-(*C*$F_3$)$C_6H_4N_2$][$BF_4$] (1.3 mmol, 350 mg, 1.0 equiv.) according to GP6. Purification by column chromatography (eluent = 0 → 5% diethyl ether in hexane) followed by a further purification by column chromatography (eluent = 0 → 2% diethyl ether in hexane) obtained **10** as a purple

solid (160 mg, 46%). Single crystals of **10** suitable for single-crystal X-ray diffraction were grown by slow evaporation of a hexane solution of the product at −35 °C. $^{1}$H NMR (400 MHz, $CD_3CN$, 298 K): δ 7.95 (app. d, $J$ = 9 Hz, 2H; $H_{Ar}$), 7.91 (d, $J$ = 9 Hz, 2H; $H_{Ar}$), 1.40 (d, $^{3}J_{H\text{-}P}$ = 13 Hz, 18H; $^{t}$Bu), 0.49 (br. quart., 3H; B$H_3$). $^{13}$C{$^{1}$H} (101 MHz, $CD_3CN$, 289 K): δ 156.7 (d, $^{3}J_{C\text{-}P}$ = 35 Hz; *i*-$C_{Ar}$), 134.2 (q, $^{2}J_{C\text{-}F}$ = 32 Hz; *p*-$CCF_3$), 127.8 (q, $^{4}J_{C\text{-}F}$ = 4 Hz; *m*-$C_{Ar}$), 123.6 (q, $^{1}J_{C\text{-}F}$ = 272 Hz; $CF_3$); 123.6 (s, *o*-$C_{Ar}$), 35.9 (d, $^{1}J_{C\text{-}P}$ = 24 Hz; $C(CH_3)_3$), 27.8 (s, $C(CH_3)_3$). $^{31}$P{$^{1}$H} (162 MHz, $CD_3CN$, 298 K): δ 111.4 (br. quart.). $^{31}$P (162.0 MHz, $CD_3CN$, 298 K): δ 111.4 (br. s). $^{19}$F{$^{1}$H} (377 MHz, $CD_3CN$, 298 K): δ -63.3 (s). $^{11}$B{$^{1}$H} (128.4 MHz, $CD_3CN$, 298 K): δ −42.9 (d, $^{1}J_{B\text{-}P}$ = 50 Hz). UV-Vis (toluene, nm) $\lambda_{max}$: 281 (s), 523 (w). ESI-HRMS m/z for $C_{15}H_{24}BN_2F_3P$ [$M$ – H]$^{+}$: calcd. (found) 330.1758 (330.1764), 331.1725 (331.1737). IR (cm$^{-1}$) $\nu_{max}$: 2970 (w), 2925 (w), 2872 (w), 2361 (m), 2348 (m, B–H), 1738 (w) 1609 (w, N=N).

### 3.8.3 General Procedure for the Synthesis of Azophosphines (GP7)

$RN_2P^tBu_2{\cdot}BH_3$ (1.0 equiv.) was added to a 25 mL Schlenk ampoule and dissolved in toluene. To this, pyrrolidine was added (10 equiv.), and the mixture stirred at room temperature overnight (16 h), which gave 100% conversion to $RN_2P^tBu_2$ by crude $^{31}$P{$^{1}$H} NMR spectroscopy. Excess pyrrolidine was removed *in vacuo* and the resulting oil filtered through a silica plug (eluent = 10% diethyl ether in hexane) to remove the pyrrolidine·$BH_3$ adduct. Removal of the eluent *in vacuo* obtained the target deprotected $RN_2P^tBu_2$ product as a dark-coloured solid or oil. The air-sensitive products were stored in vials in the glovebox freezer.

***p*-(NMe$_2$)C$_6$H$_4$N$_2$P$^t$Bu$_2$ (11)**

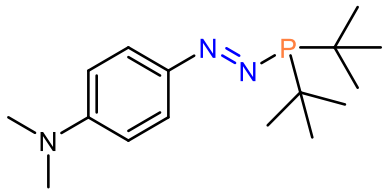

Azophosphine **11** was synthesised from azophosphine borane **5** (0.33 mmol, 100 mg, 1.0 equiv.) according to GP7. The reaction was stirred at room temperature overnight (16 h) to obtain 100% conversion of **5** to **11**, isolated as a dark red solid (130 mg, 57%). The flask was then rinsed with toluene-$d_8$ to prepare an NMR sample. Single crystals of **3** suitable for single-crystal X-ray diffraction were grown in the glovebox by slow evaporation of a hexane solution of the product at −35 °C. $^1$H (500.1 MHz, tol-$d_8$, 298 K): δ 7.77 (m, 2H; *m*-$H_{Ar}$), 6.38 (m, 2H; *o*-$H_{Ar}$), 2.44 (s, 6H; *p*-(C$H_3$)$_2$N), 1.36 (d, $^3J_{H–P}$ = 11 Hz, 18H; $^t$Bu).$^{13}$C (125.8 MHz, tol-$d_8$): δ 152.1 (s; *p*-$C_{Ar}$), 147.8 (d, $^3J_{C–P}$ = 24 Hz; *i*-$C_{Ar}$), 123.5 (s; *m*-$C_{Ar}$), 111.6 (s; *o*-$C_{Ar}$), 39.7 (s; *p*-(C$H_3$)N), 36.0 (d, $^1J_{C–P}$ = 26 Hz; *C*(CH$_3$)$_3$), 29.2 (d, $^2J_{C–P}$ = 12 Hz; C(*C*H$_3$)$_3$). $^{31}$P{$^1$H} (202.4 MHz, tol-$d_8$): δ 107.7 (s). $^{31}$P (162.0 MHz, tol-d$_8$): δ 107.7 (br. m). UV-Vis (toluene, nm) $\lambda_{max}$: 388 (s); 500 (w). ASAP-HRMS m/z for C$_{16}$H$_{29}$N$_3$P [*M* + H]$^+$: calcd (found) 294.2099 (294.2094). IR: $\nu_{max}$ (cm$^{-1}$) 2940 (m), 2895 (m), 2857 (m), 1604 (m) (N=N).

***p*-(OMe)C$_6$H$_4$N$_2$P$^t$Bu$_2$ (12)**

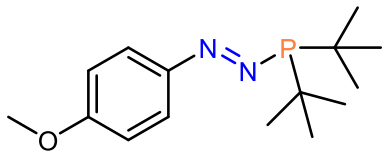

Azophosphine **12** was synthesised from azophosphine borane **6** (1.2 mmol, 340 mg, 1.0 equiv.) according to GP7. The reaction was stirred at room temperature overnight

(16 h) to obtain 100% conversion of **6** to **12**, and isolated as a dark red solid (250 mg, 76%). The flask was then rinsed with toluene-$d_8$ to prepare an NMR sample. $^{1}$H (500.1 MHz, tol-$d_8$, 298 K): δ 7.68 (m, 2H; *m*-$H_{Ar}$), 6.67 (m, 2H; *o*-$H_{Ar}$), 3.25 (s, 3H; *p*-OC$H_3$), 1.32 (d, $^{3}J_{H–P}$ = 11 Hz, 18H; $^{t}$Bu). $^{13}$C{$^{1}$H} (125.8 MHz, tol-$d_8$): δ 161.9 (s; *p*-$C_{Ar}$), 150.2 (d, $^{3}J_{C–P}$ = 22 Hz; *i*-$C_{Ar}$), 122.3 (s; *m*-$C_{Ar}$), 114.2 (s; *o*-$C_{Ar}$), 54.9 (s; *p*-O$C$H$_3$), 36.3 (d, $^{1}J_{C–P}$ = 26 Hz; $C$(CH$_3$)$_3$), 29.2 (d, $^{2}J_{C–P}$ = 12 Hz; C($C$H$_3$)$_3$). $^{31}$P{$^{1}$H} (202.4 MHz, tol-$d_8$): δ 111.6 (s). $^{31}$P (202.4 MHz, tol-$d_8$): δ 111.6 (br. m). UV-Vis (toluene, nm) $\lambda_{max}$: 354 (s), 504 (w). ASAP-HRMS m/z for $C_{15}H_{26}N_2OP$ [*M* + H]$^{+}$: calcd. (found) 281.1783 (281.1789). IR (cm$^{-1}$) $\nu_{max}$: 3070 (w), 2974 (m), 2940 (m), 2891 (m), 2860 (m), 1601 (s, N=N), 1579 (s), 1502 (s).

***p*-(Me)C$_6$H$_4$N$_2$P$^{t}$Bu$_2$ (13)**

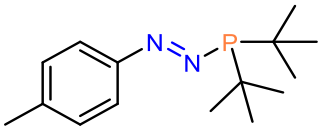


Azophosphine **13** was synthesised from azophosphine borane **7** (0.4 mmol, 100 mg, 1.0 equiv.) according to GP7. The reaction was stirred at room temperature overnight (16 h) to obtain 100% conversion of **7** to **13**, and isolated as a dark red oil (70 mg, 72%). The flask was then rinsed with toluene-$d_8$ to prepare an NMR sample. $^{1}$H (400.1 MHz, tol-$d_8$, 298 K): δ 7.62 (d, $^{3}J_{H–H}$ = 8 Hz, 2H; *m*-$H_{Ar}$), 6.94 (d, $^{3}J_{H–H}$ = 8 Hz, 2H; *o*-$H_{Ar}$), 2.05 (s, 3H; *p*-C$H_3$), 1.31 (d, $^{3}J_{H–P}$ = 11 Hz, 18H; $^{t}$Bu). $^{13}$C{$^{1}$H} (100.6 MHz, tol-$d_8$): δ 153.6 (d, $^{3}J_{C–P}$ = 22 Hz; *i*-$C_{Ar}$), 140.4 (s; *p*-$C_{Ar}$), 129.8 (s; *m*-$C_{Ar}$), 121.6 (s; *o*-$C_{Ar}$), 36.4 (d, $^{1}J_{C–P}$ = 26 Hz; $C$(CH$_3$)$_3$), 29.2 (d, $^{2}J_{C–P}$ = 12 Hz; C($C$H$_3$)$_3$), 21.1 (s; *p*-$C$H$_3$). $^{31}$P{$^{1}$H} (202.4 MHz, tol-$d_8$): δ 113.4 (s). $^{31}$P (202.4 MHz, tol-$d_8$): δ 113.4 (br. m). UV-Vis (toluene, nm) $\lambda_{max}$: 353 (s), 504 (w). ASAP-HRMS m/z for $C_{15}H_{26}N_2P$ [*M* + H]$^{+}$: calcd.

(found) 265.1833 (265.1833). IR ($cm^{-1}$) $\nu_{max}$: 2979 (w), 2940 (w), 2893 (w), 2862 (w), 1602 (w, N=N).

**$C_6H_5N_2P^tBu_2$ (14)**

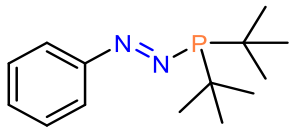

Azophosphine **14** was synthesised from azophosphine borane **8** (0.4 mmol, 100 mg, 1.0 equiv.) according to GP7. The reaction was stirred at room temperature overnight (16 h) to obtain 100% conversion of **8** to **14**, and isolated as a dark red oil (53 mg, 56%). The flask was then rinsed with toluene-$d_8$ to prepare an NMR sample. $^1$H (500.1 MHz, tol-$d_8$, 298 K): δ 7.66-7.64 (m, 2H; $H_{Ar}$), 7.15-7.11 (m, 2H; $H_{Ar}$), 7.06-7.03 (m, 1H; *p*-$H_{Ar}$), 1.30 (d, $^3J_{H-P}$ = 11 Hz, 18H; $^t$Bu). $^{13}$C{$^1$H} (125.7 MHz, tol-$d_8$): δ 155.0 (d, $^3J_{C-P}$ = 21 Hz; *i*-$C_{Ar}$), 130.3 (s; *p*-$C_{Ar}$), 129.1 (s; *m*-$C_{Ar}$), 121.6 (s; *o*-$C_{Ar}$), 36.5 (d, $^1J_{C-P}$ = 26 Hz; $C(CH_3)_3$), 29.2 (d, $^2J_{C-P}$ = 12 Hz; $C(CH_3)_3$). $^{31}$P{$^1$H} (202.4 MHz, tol-$d_8$): δ 115.1 (s). $^{31}$P (202.4 MHz, tol-$d_8$): δ 115.1 (br. m). UV-Vis (toluene, nm) $\lambda_{max}$: 350 (s), 512 (w). ASAP-HRMS m/z for $C_{14}H_{24}N_2P$ [*M* + H]$^+$: calcd. (found) 251.1677 (251.1682). IR ($cm^{-1}$) $\nu_{max}$: 2978 (w), 2941 (w), 2894 (w), 2861 (w), 1593 (w, N=N).

***p*-(F)$C_6H_4N_2P^tBu_2$ (15)**

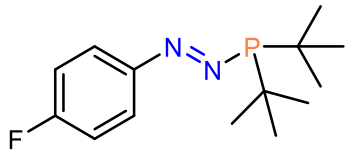

Azophosphine **15** was synthesised from azophosphine borane **9** (0.4 mmol, 100 mg, 1.0 equiv.) according to GP7. The reaction was stirred at room temperature overnight (16 h) to obtain 100% conversion of **9** to **15**, and isolated as a dark red oil (63 mg,

63%). The flask was then rinsed with toluene-$d_8$ to prepare an NMR sample. $^{1}$H (500.1 MHz, tol-$d_8$, 298 K): δ 7.48-7.44 (m, 2H; $H_{Ar}$), 6.75-71 (m, 2H; $H_{Ar}$), 1.28 (d, $^{3}J_{H-P}$ = 11 Hz, 18H; $^{t}$Bu). $^{13}$C{$^{1}$H} (125.7 MHz, tol-$d_8$): δ 164.3 (dd; *p*-$C_{Ar}$), 151.6 (dd; *i*-$C_{Ar}$), 123.3 (d, $^{3}J_{C-P}$ = 9 Hz; *m*-$C_{Ar}$), 115.9 (d, $^{2}J_{C-F}$ = 26 Hz; *o*-$C_{Ar}$), 36.5 (d, $^{1}J_{C-P}$ = 26 Hz; $C(CH_3)_3$), 29.2 (d, $^{2}J_{C-P}$ = 12 Hz; $C(CH_3)_3$). $^{31}$P{$^{1}$H} (162.0 MHz, tol-$d_8$): δ 115.2 (s). $^{31}$P (162.0 MHz, tol-$d_8$): δ 115.2 (br. m). $^{19}$F{$^{1}$H} (470.5 MHz, tol-$d_8$): δ −111.0 (br. m). UV-Vis (toluene, nm) $\lambda_{max}$: 353 (s), 506 (w). ASAP-HRMS m/z for $C_{14}H_{23}FN_2P$ [*M* + H]$^{+}$: calcd. (found) 269.1583 (269.1586). IR (cm$^{-1}$) $\nu_{max}$: 3055 (w), 2970 (m), 2944 (m), 2897 (w), 2862 (m), 1591 (m, N=N).

***p*-($CF_3$)$C_6H_4N_2P^tBu_2$ (16)**

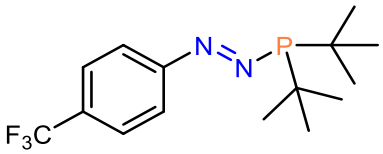


Azophosphine **16** was synthesised from azophosphine borane **10** (0.3 mmol, 92 mg, 1.0 equiv.) according to GP7. The reaction was stirred at room temperature overnight (16 h) to obtain 100% conversion of **10** to **16**, and isolated as a dark red oil (44 mg, 50%). The flask was then rinsed with toluene-$d_8$ to prepare an NMR sample. $^{1}$H (500.1 MHz, tol-$d_8$, 298 K): δ 7.41-7.39 (m, 2H; $H_{Ar}$), 7.31-7.29 (m, 2H; $H_{Ar}$), 1.29 (d, $^{3}J_{H-P}$ = 11 Hz, 18H; $^{t}$Bu). $^{13}$C{$^{1}$H} (125.7 MHz, tol-$d_8$): δ 155.7 (dd; *p*-$C_{Ar}$), 131.8-131.0 (m; *p*-$C_{Ar}$), 126.5-126.4 (m; *m*-$C_{Ar}$), 121.5 (s, *o*-$C_{Ar}$), 37.0 (d, $^{1}J_{C-P}$ = 27 Hz; $C(CH_3)_3$), 29.2 (d, $^{2}J_{C-P}$ = 12 Hz; $C(CH_3)_3$). $^{31}$P{$^{1}$H} (202.4 MHz, tol-$d_8$): δ 119.7 (s). $^{31}$P (202.4 MHz, tol-$d_8$): δ 119.7 (br. m). $^{19}$F{$^{1}$H} (470.5 MHz, tol-$d_8$): δ −62.3 (s). UV-Vis (toluene, nm) $\lambda_{max}$: 361 (s), 519 (w). ASAP-HRMS m/z for $C_{15}H_{23}F_3N_2P$ [*M* + H]$^{+}$: calcd. (found) 319.1551 (319.1559). IR (cm$^{-1}$) $\nu_{max}$: 2980 (w), 2944 (w), 2897 (w), 2864 (w) 1611 (w, N=N).

### 3.8.4 General Procedure for the Synthesis of Azophosphine-Selenides (GP8)

$RN_2P^tBu_2$ (1.0 equiv.) was added to a vial and dissolved in toluene-$d_8$ (1.0 mL). To this, grey selenium was added (10 equiv.) and the mixture left to stir at room temperature for 30 min. After this time, an aliquot was transferred to a J. Young's NMR tube and conversion from $RN_2P^tBu_2$ to $RN_2P(Se)^tBu_2$ monitored by crude $^{31}P\{^1H\}$ NMR spectroscopy.

***p*-(NMe$_2$)C$_6$H$_4$N$_2$P(Se)$^t$Bu$_2$ (17)**

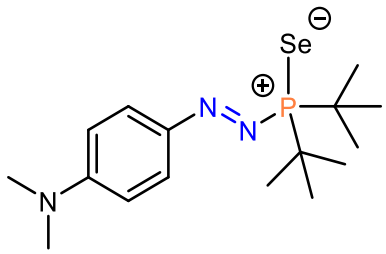


Azophosphine-selenide **17** was synthesised from azophosphine **5** (0.02 mmol, 6 mg, 1 equiv.) according to GP8 to obtain 100% conversion of **5** to **17**. $^{31}P\{^1H\}$ (202.4 MHz, tol-$d_8$): δ 108.8 (d, $^1J_{P–Se}$ = 794 Hz).

***p*-(OMe)C$_6$H$_4$N$_2$P(Se)$^t$Bu$_2$ (18)**

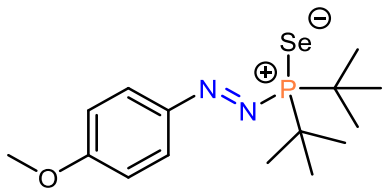


Azophosphine-selenide **18** was synthesised from azophosphine **6** (0.02 mmol, 6 mg, 1 equiv.) according to GP8 to obtain 100% conversion of **6** to **18**. $^{31}P\{^1H\}$ (202.4 MHz, tol-$d_8$): δ 112.1 (d, $^1J_{P–Se}$ = 801 Hz).

***p*-(Me)$C_6H_4N_2P(Se)^tBu_2$ (19)**

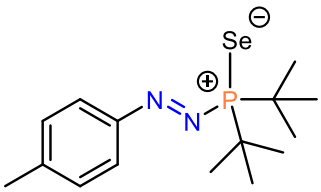

Azophosphine-selenide **19** was synthesised from azophosphine **7** (0.02 mmol, 6 mg, 1 equiv.) according to GP8 to obtain 100% conversion of **7** to **19**. $^{31}P\{^1H\}$ (202.4 MHz, tol-$d_8$): δ 113.3 (d, $^1J_{P-Se}$ = 804 Hz).

**$C_6H_5N_2P(Se)^tBu_2$ (20)**

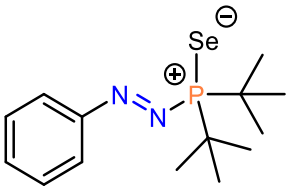

Azophosphine-selenide **20** was synthesised from azophosphine **8** (0.02 mmol, 6 mg, 1 equiv.) according to GP8 to obtain 100% conversion of **8** to **20**. $^{31}P\{^1H\}$ (202.4 MHz, tol-$d_8$): δ 114.1 (d, $^1J_{P-Se}$ = 806 Hz).

***p*-(F)$C_6H_4N_2P(Se)^tBu_2$ (21)**

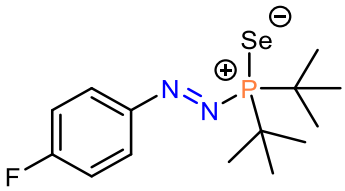

Azophosphine-selenide **21** was synthesised from azophosphine **9** (0.02 mmol, 6 mg, 1 equiv.) according to GP8 to obtain 100% conversion of **9** to **21**. $^{31}P\{^1H\}$ (202.4 MHz, tol-$d_8$): δ 114.4 (d, $^1J_{P-Se}$ = 806 Hz).

***p*-(CF$_3$)C$_6$H$_4$N$_2$P(Se)$^t$Bu$_2$ (22)**

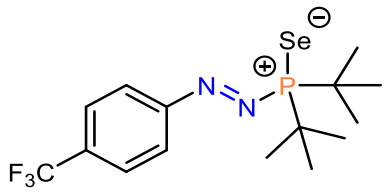


Azophosphine-selenide **22** was synthesised from azophosphine **10** (0.02 mmol, 6 mg, 1 equiv.) according to GP8 to obtain 100% conversion of **10** to **22**. $^{31}P\{^1H\}$ (202.4 MHz, tol-$d_8$): δ 116.3 (d, $^1J_{P–Se}$ = 810 Hz).

## References


1 N. Wiberg, *Adv. Organomet. Chem.*, 1984, **23**, 131–191.

2 O. A. Attanasi, P. Filippone, P. Guerra and F. Serra-Zanetti, *Synth. Commun.*, 1987, **17**, 555–561.

3 M. L. Y. Riu, W. J. Transue, J. M. Rall and C. C. Cummins, *J. Am. Chem. Soc.*, 2021, **143**, 7635–7640.

4 K. Tanaka, M.-L. Y. Riu, B. Valladares and C. C. Cummins, *Inorg. Chem.*, 2022, **61**, 13662–13666.

5 W. Schneid, Zur Darstellung und Reactivitat Silylierter, Germylierter und Stannylierter Mono(Organyl)Diimine, Ludwig Maximilians-Universitat Munchen, 1977.

6 E. J. Jordan, E. D. E. Calder, B. L. Greene, H. V. Adcock, L. Male, P. W. Davies and A. R. Jupp, *Organometallics*, 2024, **43**, 2674–2685.

7 E. J. Jordan, E. D. E. Calder, H. V Adcock, L. Male, M. Nieger, J. C. Slootweg and A. R. Jupp, *Chem. Eur. J.*, e202401358.

8 Deposition numbers 2334075 (for **5**), 2358660 (for **6**), 2358661 (for **7**), 2358659 (for **8**), 2358663 (for **9**), 2358666 (for **10**) 2334076 (for **11**), 2358664 (for **12**) contain the supplementary crystallographic data for this chapter. These data are provided free of charge by the joint Cambridge Crystallographic Data Centre and Fachinformationszentrum Karlsruhe Access Structures service.

9 F. R. Fronczek, C. Hansch and S. F. Watkins, *Acta Crystallogr. Sect. C Struct. Chem.*, 1988, **44**, 1651–1653.

10 K. B. Dillon, F. Mathey, J. F. Nixon, *Phosphorus: The Carbon Copy: From Organophosphorus to Phospha-organic Chemistry*, John Wiley & Sons, 1998.

11 U. Beckmann, D. Süslüyan and P. C. Kunz, *Phosphorus, Sulfur Silicon Relat. Elem.*, 2011, **186**, 2061–2070.

12 S. Konishi, T. Iwai and M. Sawamura, *Organometallics*, 2018, **37**, 1876–1883.

13 J. L. Lamola, A. S. Adeyinka, F. P. Malan, P. T. Moshapo, C. W. Holzapfel and M. C. Maumela, *New J. Chem.*, 2022, **46**, 4677–4686.

14 Z. L. Niemeyer, A. Milo, D. P. Hickey and M. S. Sigman, *Nat. Chem. 2016 86*, 2016, **8**, 610–617.

15 M. L. Clarke, G. L. Holliday, A. M. Z. Slawin and J. D. Woollins, *J. Chem. Soc. Dalt. Trans.*, 2002, 1093–1103.

16 O. Diebolt, G. C. Fortman, H. Clavier, A. M. Z. Slawin, E. C. Escudero-Adán, J. Benet-Buchholz and S. P. Nolan, *Organometallics*, 2011, **30**, 1668–1676.

17 C. G. Hrib, F. Ruthe, E. Seppälä, M. Bätcher, C. Druckenbrodt, C. Wismach, P. G. Jones, W. W. Du Mont, V. Lippolis, F. A. Devillanova and M. Bühl, *Eur. J. Inorg.*

*Chem.*, 2006, **2006**, 88–100.

18 CrysAlisPro, Rigaku Oxford Diffraction, 2021.

19 O. V Dolomanov, L. J. Bourhis, R. J. Gildea, J. A. K. Howard and H. Puschmann, *J. Appl. Crystallogr.*, 2009, **42**, 339–341.

20 G. M. Sheldrick, *Acta Crystallogr.*, 2015, **A71**, 3–8.

21 G. M. Sheldrick, *Acta Crystallogr.*, 2015, **C71**, 3–8.

22 E. R. M. Habraken, N. P. van Leest, P. Hooijschuur, B. de Bruin, A. W. Ehlers, M. Lutz and J. C. Slootweg, *Angew. Chem. Int. Ed.*, 2018, **57**, 11929–11933.

23 E. R. M. Habraken, L. J. C. van der Zee, K. N. A. van de Vrande, A. R. Jupp, M. Nieger, A. W. Ehlers and J. C. Slootweg, *Eur. J. Inorg. Chem.*, 2019, **2019**, 1594–1603.

# CHAPTER 4

# Coordination Chemistry of Azophosphines

## 4.1 Introduction and Objectives

### 4.1.1 Triazene Ligands

Azophosphines (RN=N–$PR_2$) are the heavier congener of triazenes (RN=N–$NR_2$) in which a trigonal planar geometry is adopted at the amino nitrogen due to delocalisation of its lone pair over the N–N–N π system. This reduced availability of the lone pair is reflected in the coordination chemistry of triazenes, on which the literature is scant. All examples feature monodentate coordination to the metal centre *via* the terminal imino nitrogen, and there are no examples of binding through the tri-coordinate amino nitrogen centre (Figure 4.1A).[1–4] *N,N'*-disubstituted triazenes are much more commonly deprotonated to afford anionic triazenides ([RNNNR]$^-$), which can then act as monodentate ($\kappa^1$), bidentate ($\kappa^2$) and bridging (μ) ligands to a wide range of metal centres (Figure 4.1B(i–iii).[5–7]

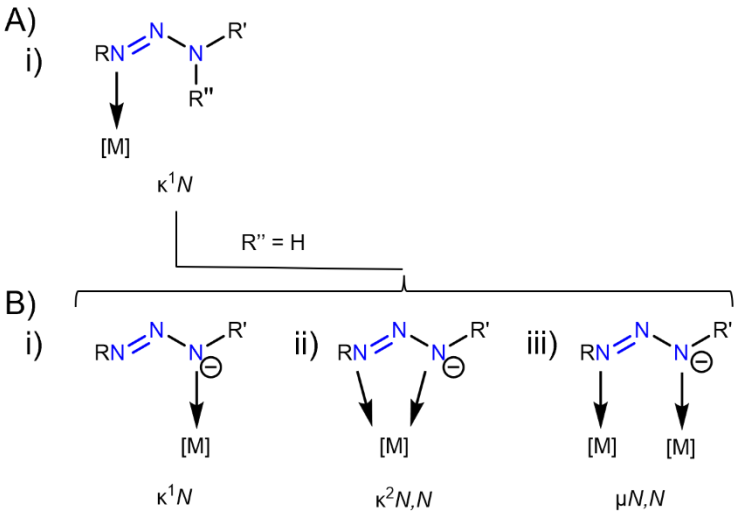


**Figure 4.1.** (A) Coordination modes of triazene: (i) $\kappa^1$*N* coordination *via* imino N only. (B) Coordination modes of triazenide: (i) $\kappa^1$*N*, (ii) $\kappa^2$*N,N* and (iii) μ*N,N*.

Triazenides are isoelectronic with amidinates ([RNC(R')NR]$^-$), but the central electronegative nitrogen in triazenides results in a reduced charge density of the

terminal nitrogen atoms relative to amidinates, which would confer an increased electrophilicity at the ligand metal centre.[8] As a result, the utilisation of triazenides tend to be overlooked in favour of the aminidate analogues.

### 4.1.2 1,3-P,N Ligands

By including different donor atoms more sophisticated ligands can be designed to enable metal-ligand cooperativity, which unlocks reactivity that is not possible at the metal centre alone. As introduced in Chapter 1, 1,3-P,N ligands are a widely studied class of compounds that display diverse coordination modes, including $\kappa^1$*N*, $\kappa^1$*P*, $\kappa^2$*P,N*, and $\mu$*P,N,* in which all examples feature C as the bridging element between the P and N donors, and are typified by pyridyl- and imidazolyl-based ligands or imino- and amino-based ligands.[9–11] In this section, the coordination chemistry of 1,3-P,N ligands to a ruthenium(II)(arene) framework and to a gold(I) centre is discussed, chosen for their diverse and interesting coordinative properties and relevance in catalysis.

*Coordination to Ru(II)(arene) Frameworks*

Ruthenium(II)(arene) complexes are often characterised as ‘half-sandwich’ or ‘piano stool’ structures on account of the $\eta^6$-coordinated arene and X, Y and Z ligands of either mono-, bi-, or tridenticity, forming a pseudo-octahedral geometry (Figure 4.2A(i)). The option to modulate each of these positions provide considerable scope for fine-tuning of sterics and electronics, thus affording an extensive repertoire of amphiphilic complexes. Typically, 1,3-P,N ligands coordinate to a ruthenium(II)(arene) framework with $\kappa^1$*P* or $\kappa^2$*P,N* coordination (Figure 4.2A(ii) and (iii), respectively), often forming as a mixture with full $\kappa^2$*P,N* coordination driven by heating or halide abstraction.[9,10,12] However, prolonged heating or refluxing with excess ligand can lead to displacement

of the arene to form a tris-bidentate coordination (Figure 4.2B).[13] When coordinating to Ru(II), a metal of intermediate softness, κ$^1$*N* coordination has been observed only as part of a dynamic mixture and could not be isolated (Figure 4.2A(iv)).[12]

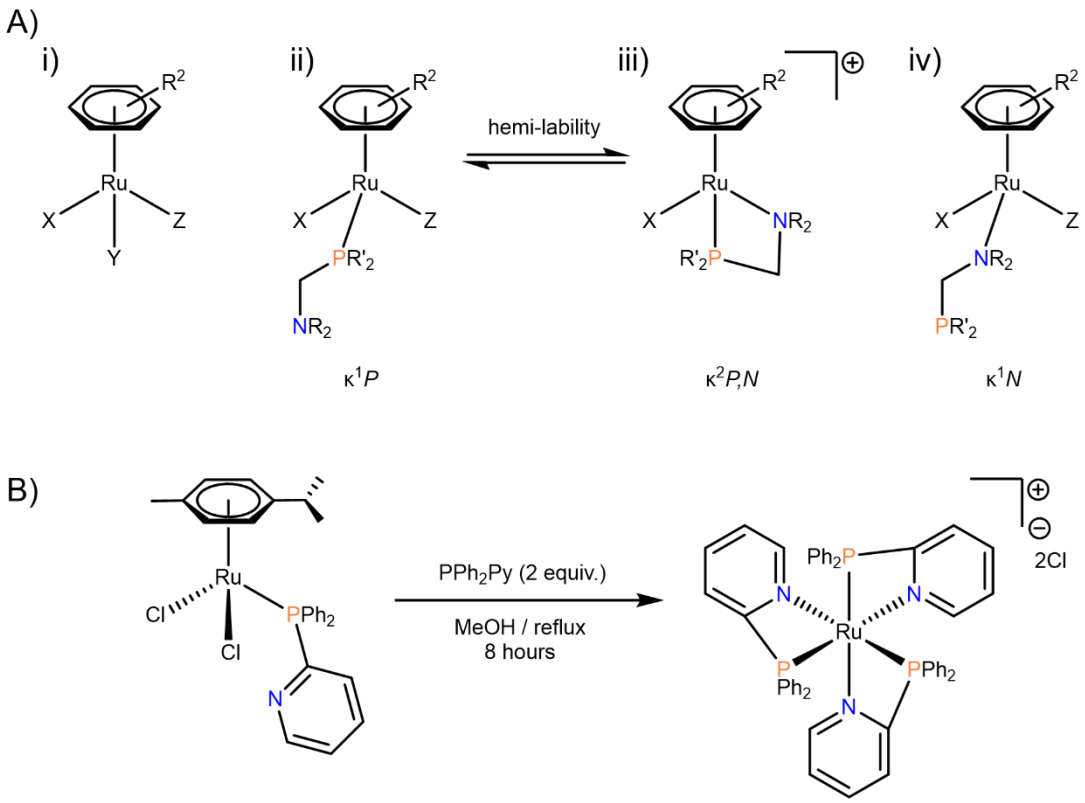


**Figure 4.2.** (A) Generic structures and coordination modes of Ru(II)(arene) complexes showing (i) piano-stool Ru(II)(arene) framework, (ii) κ$^1$*P* coordination, (iii) κ$^2$*P,N* coordination, (iv) κ$^1$*N* coordination of a 1,3-P,N ligand; (B) Reflux of Ru(*p*-cymene)Cl$_2$(κ$^1$*P*-PPh$_2$Py) with excess PPh$_2$Py leading to displacement of *p*-cymene to give the tris-bidentate coordinated complex [Ru(κ$^2$*P,N*-PPh$_2$Py)$_3$[[Cl]$_2$.

Ruthenium(II)(arene) complexes featuring 1,3-P,N ligands are predominantly based on the pyridyl- or imidazolyl-type ligand.[9] The classical diphenylphosphinopyridine (PPh$_2$Py) ligand has been κ$^1$*P* and κ$^2$*P,N* coordinated to a Ru(II)(arene) framework when the arene is *p*-cymene,[14,15] hexamethylbenzene (C$_6$Me$_6$),[16] benzene,[17] and mesitylene.[13] Although single-crystal X-ray diffraction data are available for only when the arene is *p*-cymene and C$_6$Me$_6$, no statistically relevant effect of the arene on key

bond metrics (i.e. P/N–Ru bond lengths and P–Ru–N bond angle) is observed. Introduction of an electron-donating substituent ($NMe_2$) *para* to the $PPh_2Py$ N atom favoured $\kappa^2$*P,N* coordination, with rapid and selective formation of the $\kappa^2$*P,N* complex when the arene was $C_6Me_6$ (Scheme 4.1A).[13]

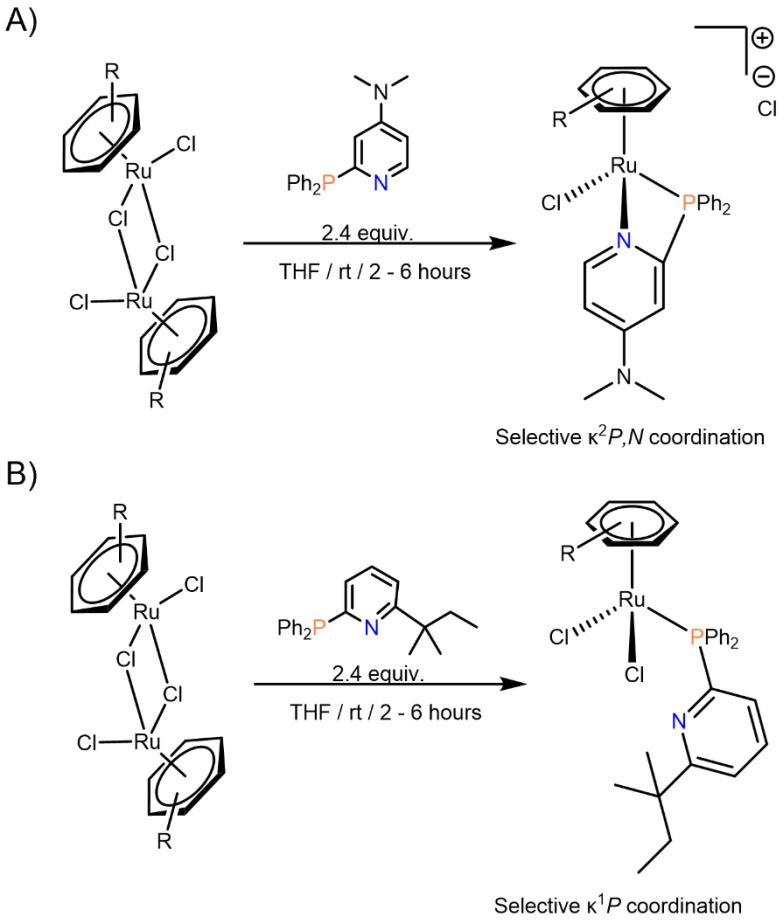


**Scheme 4.1.** (A) Selective $\kappa^2$*P,N* coordination of $PPh_2Py$ with an electron-donating group *para* to N; (B) Selective $\kappa^1$*P* coordination of $PPh_2Py$ with a bulky group *ortho* to N. R = hexamethylbenzene (A), *p*-cymene and benzene (B).

The four-membered chelate rings generated by $\kappa^2$*P,N* coordination of $PPh_2Py$ or its $NMe_2$-substituted derivative were highly stable, impervious to ring-opening by displacement of the N atom despite the hemilabile character usually associated with $PPh_2Py$ ligands.[18–21] Indeed, in a reaction medium of high polarity the $\kappa^1$*P* complexes were observed to form the corresponding $\kappa^2$*P,N* complexes, with consequences for

their intended catalytic application (discussed further in Chapter 5). In contrast, introduction of a bulky group *ortho* to the $PPh_2Py$ N atom can suppress $\kappa^2$*P,N* coordination even after addition of a halide abstracting reagent (Scheme 4.1B).[13,22]

Imidazolyl-based 1,3-P,N ligands are also well-established ligands for ruthenium(II)(arene) frameworks, forming $\kappa^1$*P* and $\kappa^2$*P,N* coordination complexes and, in some cases, bis-$\kappa^1$*P* coordination complexes. Generally, in non-coordinating solvents $\kappa^1$*P* coordination is favoured. In methanol, a good solvent for solvation of chloride, spontaneous $\kappa^2$*P,N* coordination has been achieved, otherwise, full $\kappa^2$*P,N* coordination can be forced by using a halide abstracting reagent.[23] By using $[Ru(Cp)(CH_3CN)_3][PF_6]$ as the Ru(II)(arene) starting material Grotjahn and co-workers achieved >90% pure $\kappa^2$*P,N* coordination complex by repeated co-evaporation of added acetone which liberated $CH_3CN$.[24] Similarly to pyridyl-based 1,3-P,N ligands, imidazolyl-based ligands can be substituted *ortho* to the donor imine N atom but, in addition, can also be substituted at the non-donor amino N atom (Figure 4.3A).[23]

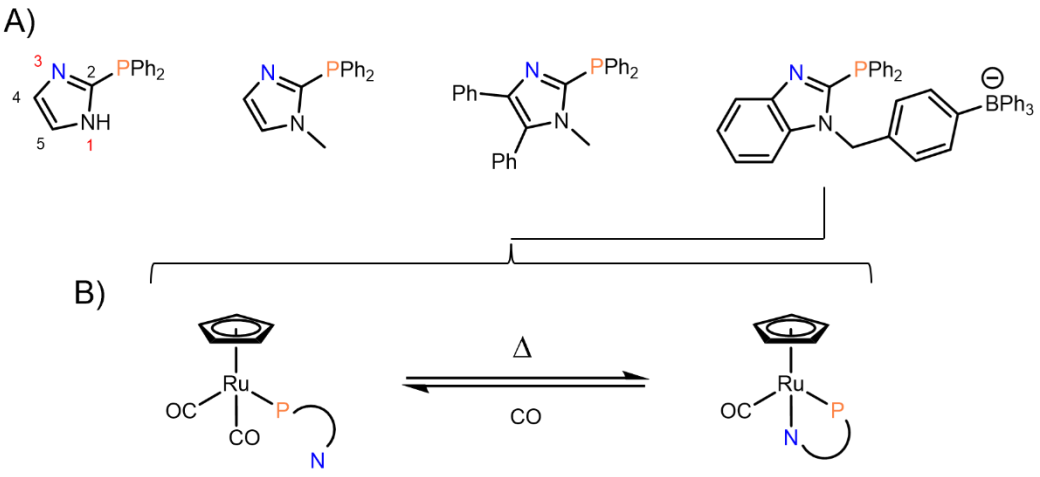


**Figure 4.3.** (A) Examples of imidazolyl-based 1,3-P,N ligands substituted at the 1-position N and/or 4- and 5-position C.[23] (B) Heat-driven hemi-lability by CO displacement and re-coordination.[25]

Modulation of this latter position enabled heat-driven $\kappa^1P \leftrightarrow \kappa^2P,N$ hemilability by CO displacement, and re-coordination under CO pressure (Figure 4.3B).[25]

Imino- and amino-based 1,3-P,N ligands are the least represented in the literature on account of their reduced rigidity relative to the pyridyl- and imidazolyl-based ligands. As discussed in Chapter 1 (Section 1.4.3), the pyridyl- and imidazolyl-based ligands are limited in their tuneability, whereas iminophosphanes (RN=C(R')–PR''$_2$) and their tautomers phosphaamidines ($R_2$N–C(R')=PR'') can be independently substituted on the P, C and N atoms (Figure 4.4A).[26–28] A dynamic *E/Z* isomer mixture is obtained that shifts to the desired *Z* conformer on coordination. Non-isomerisable cycloiminophosphanes have been developed that have a locked conformation (Figure 4.4B).[12]

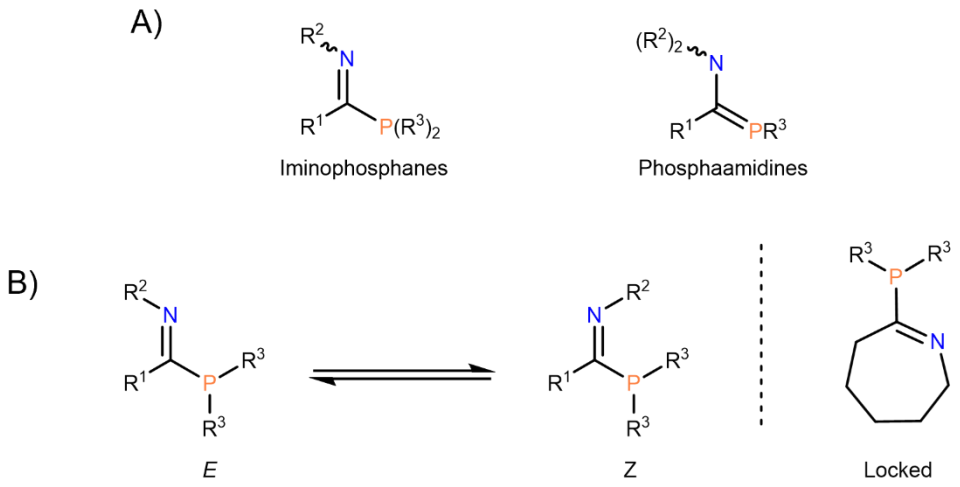


**Figure 4.4.** (A) Iminophosphanes and their tautomers phosphaamidines; (B) Dynamic *E*/*Z* isomer mixture of iminophosphanes and a non-isomerisable cycloiminophosphane.

When added to the [Ru(*p*-cymene)$Cl_2$]$_2$ dimer, the reaction mixture showed the presence of two products which the authors tentatively assigned to the $\kappa^1P$ and $\kappa^1N$ complexes. Of the isolated $\kappa^1P$ complexes, $\kappa^2P,N$ coordination was achieved by

addition of $NaBF_4$; although no characterisation data were reported for the isolated compounds. Diphenylphosphanylhydrazide ($Ph_2P–NH–NR$) ligands were found to coordinate to ruthenium *via* only the phosphorus when reacted with the [Ru(*p*-cymene)$Cl_2$]$_2$ dimer, with $\kappa^2$*P,N* coordination forced by addition of $AgBF_4$.[29] Substituting the ruthenium starting material for [Ru(Cp)($CH_3CN$)$_3$][$PF_6$] resulted in a 5:1 mixture of $\kappa^1$*P* and $\kappa^2$*P,N* coordination in which $\kappa^1$*P* coordination could be favoured by performing the reaction in the presence of 1 equivalent of $CH_3CN$.[30]

The $^{31}P\{^1H\}$ NMR spectrum can be diagnostic of coordination mode. A small downfield shift in ppm is observed when the free 1,3-P,N ligand becomes $\kappa^1$*P* coordinated and a significant upfield shift occurs when the ligand coordinates as a $\kappa^2$*P,N* chelate. This is due to an increase in shielding of the P donor atom by back-donation as the metal becomes more electron-rich with coordination of N.

*Coordination to Au(I)*

A common geometry of Au(I) complexes is two-coordinate linear in which the L–Au–X (L, ligand; X, an anion which can also act as a ligand) bond angle is close to 180° (Figure 4.5A). Depending on the nature of L and the coordinating power of X, coordination compounds of closed-shell $5d^{10}$ gold(I) can often aggregate with Au(I)···Au(I) distances ranging between 2.5 – 3.5 Å that are shorter than the sum of their van der Waals radii (3.8 Å).[31] As a result of the strong relativistic, dispersion and correlation effects possessed by gold, the less-diffuse s- and p-orbitals contract and are stabilised, whereas the more-diffuse d- and f-orbitals expand due to the enhanced shielding provided by the contracted s/p-orbitals.[32] The lowered energy difference between the filled 5d and empty 6s/6p orbitals give rise to Au···Au interactions, a phenomenon termed ‘aurophilic interactions’, with a bond energy comparable to a

strong hydrogen bond (8 – 25 kcal $mol^{-1}$).[33] This aurophilicity can be exploited by mixed donor ligands which serve as bridging ligands to hold two Au(I) ions in proximity (Figure 4.5B).

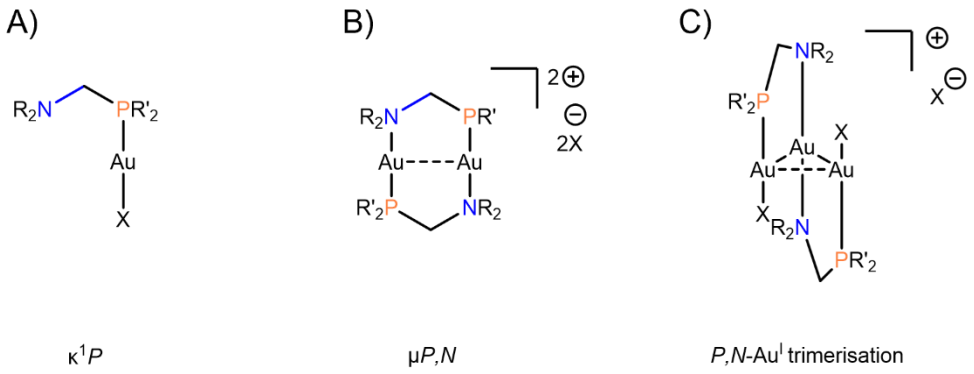


**Figure 4.5.** Au(I) complexes with 1,3-P,N ligands (A) κ$^1$*P*-Au(I) monomer; (B) μ*P,N*-Au(I) dimer; (C) μ*P,N*-Au(I) trimer.

There are limited examples of homonuclear gold(I) dimers that feature bridging 1,3-P,N ligands, and are based on the pyridyl- or imidazolyl-type ligand.[34–38] A more rigid bridging ligand would constrain the Au···Au separation so allowing for better stabilisation of the dimer, in which the N–Au–Au–N and P–Au–Au–P torsional angles would be reduced. The absence of gold(I) dimers that feature amino- or imino-based 1,3-P,N ligands can likely be attributed to the reduced rigidity of these ligands. Instead, T-shaped, three-coordinate complexes of the type $L_2$–Au–X have been obtained when L was an aminophosphine.[39] μ*P,N* coordination of a 1,3-P,N ligand is common, however, when coordinating to Au(I), typically the favoured product is a trinuclear arrangement (Figure 4.5C). When employing Au(I) complexes featuring 1,3-P,N ligands as catalysts, *P,N*-Au(I) trimerisation has been attributed to deactivation of the catalyst; this will be discussed further in Chapter 5. The metallophilic interactions facilitated by 1,3-P,N ligands also enables access to heteronuclear cluster complexes with more than four metal nuclei, in which gold is prominent.[10] Such heteronuclear

cluster complexes are not within the scope of this research and will not be further discussed.

*Photoluminescence in Au(I) Dimers*

Au(I)···Au(I) complexes are often luminescent in the solid state with emission energies spanning the visible spectrum. The heavy gold centre enhances the spin-orbit coupling of the system, facilitating access to a triplet excited state *via* intersystem crossing. Due to its $5d^{10}$ electronic configuration, d-d transitions cannot occur in gold(I) complexes. The origin of the emission is widely believed to be associated with a metal-centred 5dσ* → 6pσ transition in which an increase in aurophilic interactions would lead to a shift in emission to lower energy.[35,40,41] The formation of an exciplex, where Au–L, Au–solvent, and Au–counterion interactions play a significant role, has also been suggested.[42–44]

With respect to 1,3-P,N ligands, the photoluminescence of Au(I) dimers of only 1-methylimidazolediphenyl phosphine (midp)[35] or 1-methylbenzimidazoediphenyl phosphine (mbdp)[38], shown in Figure 4.6, have been investigated.

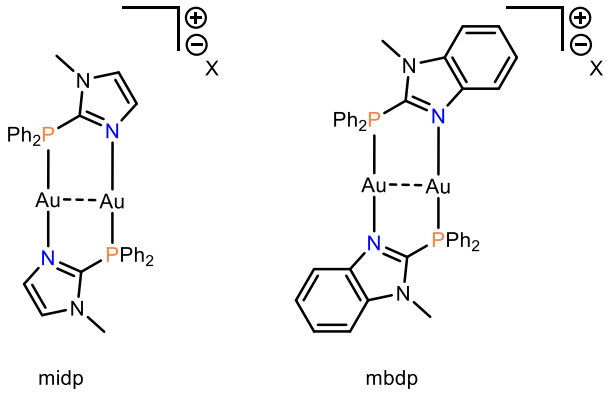


**Figure 4.6.** Au(I) dimers of midp and mbdp investigated for their photoluminescence properties. X = $ClO_4$ or $BF_4$ for midp and $BF_4$ for mbdp.

Photoluminescence was observed in $[Au(midp)]_2^{2+}$ ($\lambda_{max}$ of emission = 548 nm) and $[Au(mbdp)]_2^{2+}$ ($\lambda_{max}$ of emission = 448 nm) when the complexes were excited with a hand-held UV lamp in the solid-state. Interestingly, emissions were also observed for monomeric Au(midp)Cl ($\lambda_{max}$ of emission = 493 nm) and Au(mbdp)Cl ($\lambda_{max}$ of emission = 445 nm) in which the corresponding crystallographic data for each monomer found no Au···Au interaction. This experimental observation was supported by computational studies of Au(mbdp)Cl in which aurophilic interactions were not found to be responsible for its luminescence profile and instead were a result of ligand-centred excitation and emission.

1,3-P,N ligands display rich coordination chemistry; however, control of the target coordination mode during synthesis, and subsequent isolation of the product, can be challenging. The availability of the phosphorus lone pair, discussed in Chapter 3, highlighted the potential application of azophosphines as ligands, and the P–N=N functionality classifies them as 1,3-P,N ligands. It was hypothesised that the central nitrogen of azophosphines would reduce charge density at the terminal nitrogen and enable finer control of coordination mode, leading to an investigation of their ability to act as ligands.

### 4.1.3 Chapter Outline

In this chapter, azophosphines $MesN_2P^tBu_2$ (**3**) and *p*-$(Z)C_6H_4N_2P^tBu_2$ (**11** – **16**) (Z = $NMe_2$, OMe, Me, H, F, $CF_3$, respectively) are assessed as 1,3-P,N ligands, and their accessible coordination modes demonstrated, in ruthenium(II)(arene) complexes and gold(I) complexes. The discussion first focuses on coordination to Ru(II), including an analysis of bond metrics by single crystal X-ray diffraction. The effect of modulating the

electronics of Z on the ability of the azophosphine to act as a competent $\kappa^2$*P,N* ligand is examined using experimental and computational studies. The diversity of coordination modes accessible by azophosphines is expanded by then exploring their coordination to Au(I). The photo-switching ability of the Ru(II)- and Au(I)-azophosphine complexes is discussed within each respective subsection. The coordination chemistry of azophosphines is further, briefly explored when coordinated to a tungsten(0), palladium(II) and, finally, iridium(III) metal centre. Application of the ruthenium and gold complexes in catalysis will be discussed in Chapter 5.

### 4.1.4 Acknowledgements

The computational calculations discussed in this chapter were performed by Ethan Calder (PhD student, Jupp group, University of Birmingham). Sections 4.3 and 4.4 contain research conducted by Ellen M. Tait and Mark G. Butler, respectively, (MSci students, Jupp group, University of Birmingham), with supervision by the author, in partial fulfilment of the requirements of the Honours degree of MSci at the University of Birmingham.[45,46]

### 4.1.5 Published Research

Research in this chapter (Section 4.2) has been published in *Chemistry A European Journal*[47] and *Organometallics*.[48] The remainder of the chapter is currently unpublished research.

## 4.2 Ruthenium

### 4.2.1 Synthesis of κ¹*P* and κ²*P,N* Complexes

Azophosphines **3** and **11** – **16** were prepared according to the synthetic methods outlined in Chapter 2 (Sections 2.8.3 and 2.8.4) and Chapter 3 (Sections 3.8.2 and 3.8.3), respectively. Reaction of azophosphine **3** with half an equivalent of the [Ru(*p*-cymene)$Cl_2$]$_2$ dimer in chlorobenzene was monitored by $^{31}P\{^1H\}$ NMR spectroscopy (Scheme 4.2), and clean conversion of the free azophosphine at 118.3 ppm to a new species at 121.7 ppm was observed (Figure 4.7A).

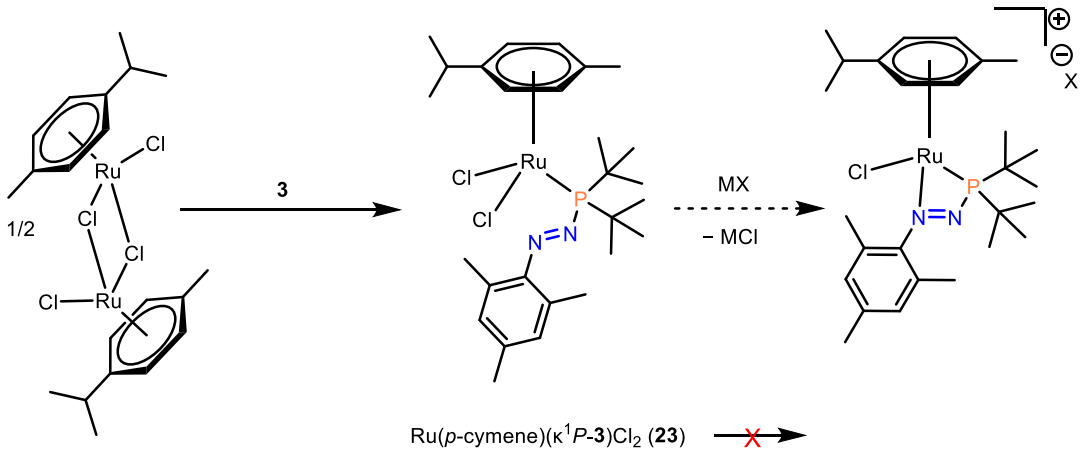


**Scheme 4.2.** Synthesis and isolation of Ru(*p*-cymene)(κ¹*P*-**3**)$Cl_2$ (**23**) and attempted synthesis of the corresponding κ²*P,N* complex by addition of halide-extraction agents (MX).

Single crystal X-ray diffraction showed that this product was the half-sandwich piano stool complex Ru(*p*-cymene)(κ¹*P*-**3**)$Cl_2$ (**23**), which featured the azophosphine coordinated to the metal centre exclusively *via* the phosphine centre (Figure 4.7B). Chlorobenzene as solvent proved to be imperative for clean coordination of **3** even amongst other polar, non-coordinating solvents.

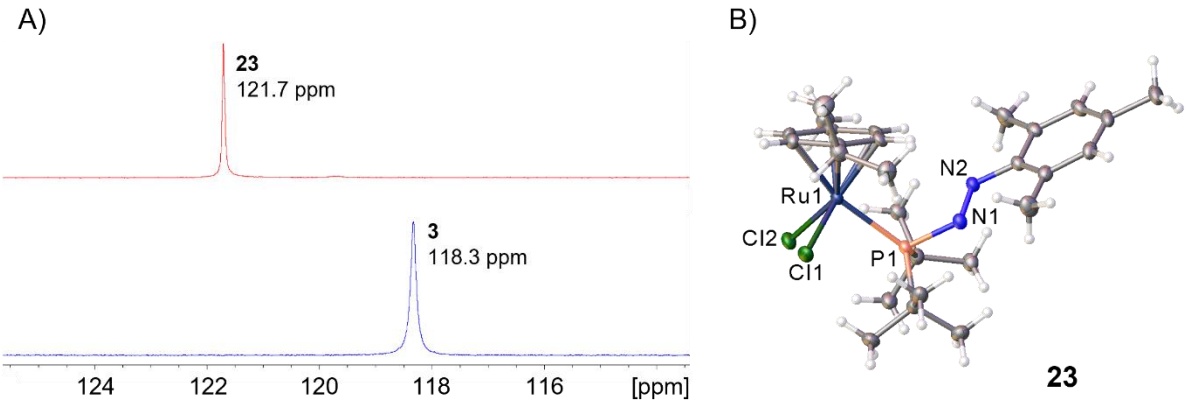


**Figure 4.7.** (A) Stacked $^{31}P\{^{1}H\}$ NMR spectra of (bottom) free azophosphine **3** and (top) $\kappa^1P$ coordination of **3** in complex **23**; (B) Single crystal structure of Ru-azophosphine complex Ru(*p*-cymene)($\kappa^1P$-**3**)$Cl_2$ (**23**). Selected bond distances (Å) and angles (°) of **23**: P1–Ru1 2.4208(7), P1–N1 1.777(2), N1–N2 1.258(3), P1–N1–N2 114.81(17). Thermal ellipsoids were drawn at the 50% probability level.[49]

The small downfield shift from 118.3 ppm (**3**) to 121.7 ppm (**23**) in the $^{31}P\{^{1}H\}$ NMR spectrum is consistent with other 1,3-P,N ligands upon $\kappa^1P$ coordination to a Ru(II)(arene) centre. The P1–Ru1 bond length of **23** (2.4208(7) Å) is longer than those of prior Ru(II)(arene) complexes with a $\kappa^1P$ coordinated 1,3-P,N ligand (range from 2.3222(12) to 2.364(2) Å),[13,15,29] presumably due to a combination of the steric bulk of **23** and the azophosphines being relatively weak P-donors, as discussed in Chapter 3 (Section 3.5). Single crystal X-ray diffraction data could not be obtained for azophosphine **3**; however, comparison of the corresponding azophosphine-borane $MesN_2P^tBu_2{\cdot}BH_3$ (**1**) (Chapter 1, Section 2.3.2) with **23** show the P1–$C_{tBu}$ bond lengths are longer when coordinated to Ru1 (1.915(3) and 1.890(3) Å) relative to B1 (1.862(6) and 1.844(6) Å) due to electron back-donation from Ru1 into the P1–$C_{tBu}$ σ* orbitals. The P1–N1 and N1–N2 bond lengths and P1–N1–N2 bond angles of **1** (1.769(5) Å, 1.226(6) Å, 113.5(4)°, respectively) and **23** (1.777(2) Å, 1.258(3) Å, 114.81(17)°, respectively) show no difference in values.

Attempts to generate a bidentate complex with **3** *via* the terminal nitrogen by changing the temperature, solvent or using halide-extraction agents were inconclusive (Figure 4.8A). It was reasoned that this was not only due to the potentially weak binding of the nitrogen, but also the flanking steric bulk from the two *ortho*-methyl groups on the mesityl substituent, which would clash with the bulky *p*-cymene ring on the ruthenium on coordination. Two peaks observed in the $^{31}P\{^{1}H\}$ NMR spectrum at approximately 57 ppm could tentatively be assigned to $\kappa^2$*P,N* coordination of **3**. If there was hindered rotation of the *p*-cymene group due to a clash with the mesityl group this would give two different products unable to interconvert.

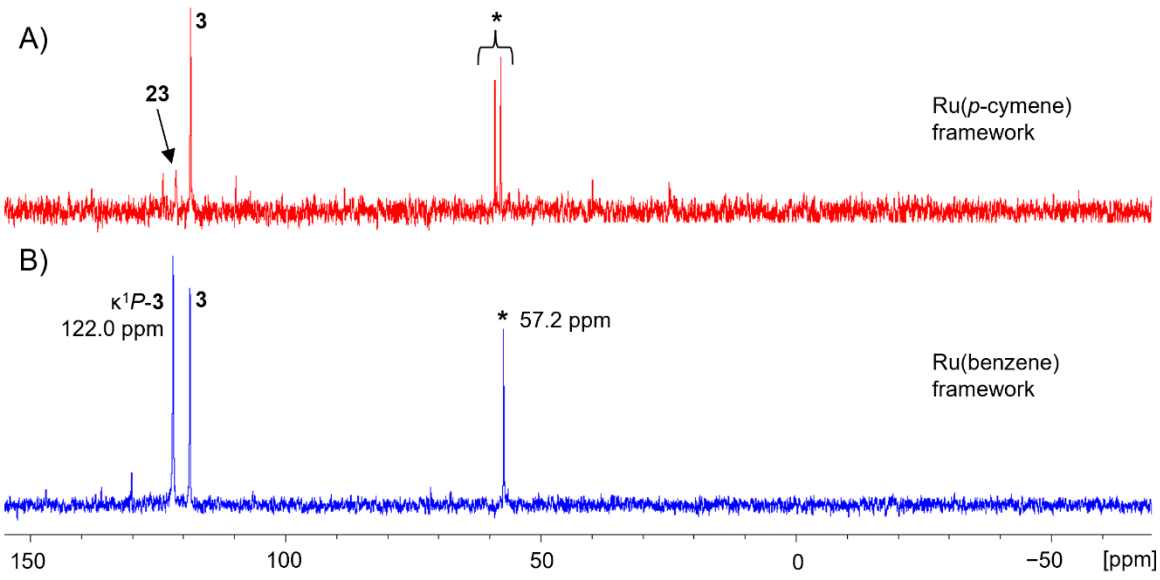


**Figure 4.8.** $^{31}P\{^{1}H\}$ NMR spectra following attempted synthesis of a bidentate complex with: (A) **3** and [Ru(*p*-cymene)$Cl_2$]$_2$ dimer; (B) **3** and [Ru(benzene)$Cl_2$]$_2$ dimer. Both reactions were performed in chlorobenzene, at room temperature, with aliquots taken for analysis after addition of $NaBPh_4$ as the halide abstracting reagent. The signal in spectra (A) and (B) marked with an asterisk is tentatively assigned to the target bidentate complex.

To circumvent this problem, the steric bulk on ruthenium was reduced by substituting the arene from *p*-cymene to benzene. Attempts to generate a bidentate complex with **3** and half an equivalent of the [Ru(benzene)$Cl_2$]$_2$ dimer were more promising in that

only one significant signal was observed in the 50-60 ppm region of the spectrum, that could be indicative of bidentate formation; however, it remained that mostly uncoordinated **3** was present in the reaction mixture, along with a new species at 122.0 ppm, consistent with a [Ru(benzene)(κ$^1$*P*-**3**)Cl$_2$] coordination complex (Figure 4.8B). Attempts to isolate the peak at 57.2 ppm were unsuccessful.

In a bid to concomitantly reduce steric bulk and increase electron density at the terminal nitrogen, **3** was substituted for azophosphine *p*-(NMe$_2$)C$_6$H$_4$N$_2$P$^t$Bu$_2$ (**11**) and the [Ru(*p*-cymene)Cl$_2$]$_2$ dimer substituted for [Ru(benzene)Cl$_2$]$_2$. To a chlorobenzene solution of **11** was added half an equivalent of [Ru(benzene)Cl$_2$]$_2$ dimer (Scheme 4.3).

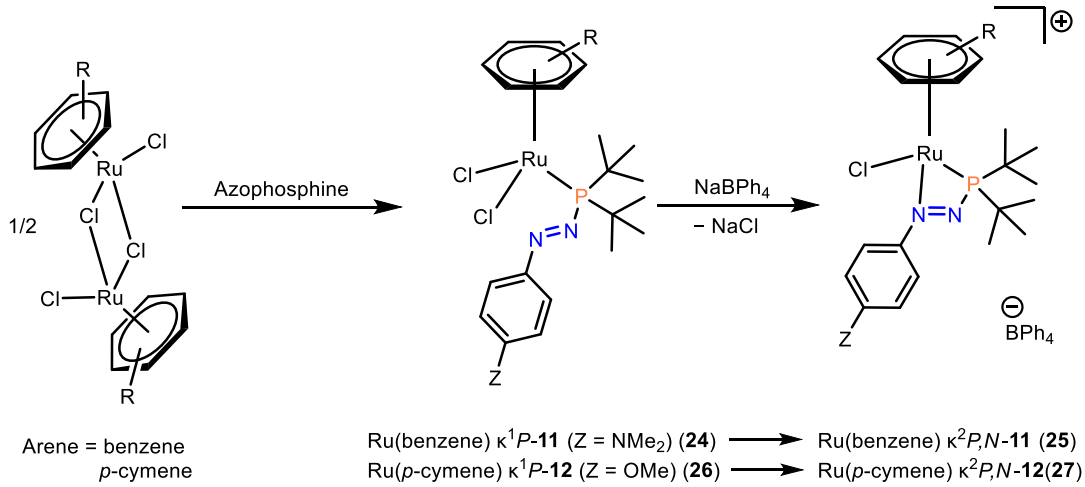


**Scheme 4.3.** General synthesis of Ru(arene)-azophosphine complexes. Isolated and fully characterised complexes: Ru(benzene)(κ$^1$*P*-**11**)Cl$_2$ (**24**); [Ru(benzene)(κ$^2$*P,N*-**11**)Cl][BPh$_4$] (**25**); Ru(*p*-cymene)(κ$^1$*P*-**12**)Cl$_2$ (**26**); [Ru(*p*-cymene)(κ$^2$*P,N*-**12**)Cl][BPh$_4$] (**27**).

Analysis by $^{31}$P{$^1$H} NMR spectroscopy revealed a similar small downfield shift (107.7 ppm (**11**) to 111.9 ppm) indicative of κ$^1$*P* coordination of the ligand. This was corroborated by single crystal X-ray diffraction and showed that the compound has the composition Ru(benzene)(κ$^1$*P*-**11**)Cl$_2$ (**24**) (Figure 4.9A). Addition of NaBPh$_4$ to the chlorobenzene solution of **24** gave a brown solid, and extraction into dichloromethane

left a white precipitate (NaCl). The $^{31}P\{^{1}H\}$ NMR spectrum showed a significant upfield shift to 58.0 ppm. Single crystals suitable for analysis confirmed the bidentate nature of the ligand in the complex [Ru(benzene)(κ$^2$*P*,*N*-**11**)Cl][$BPh_4$] (**25**) (Figure 4.9B).

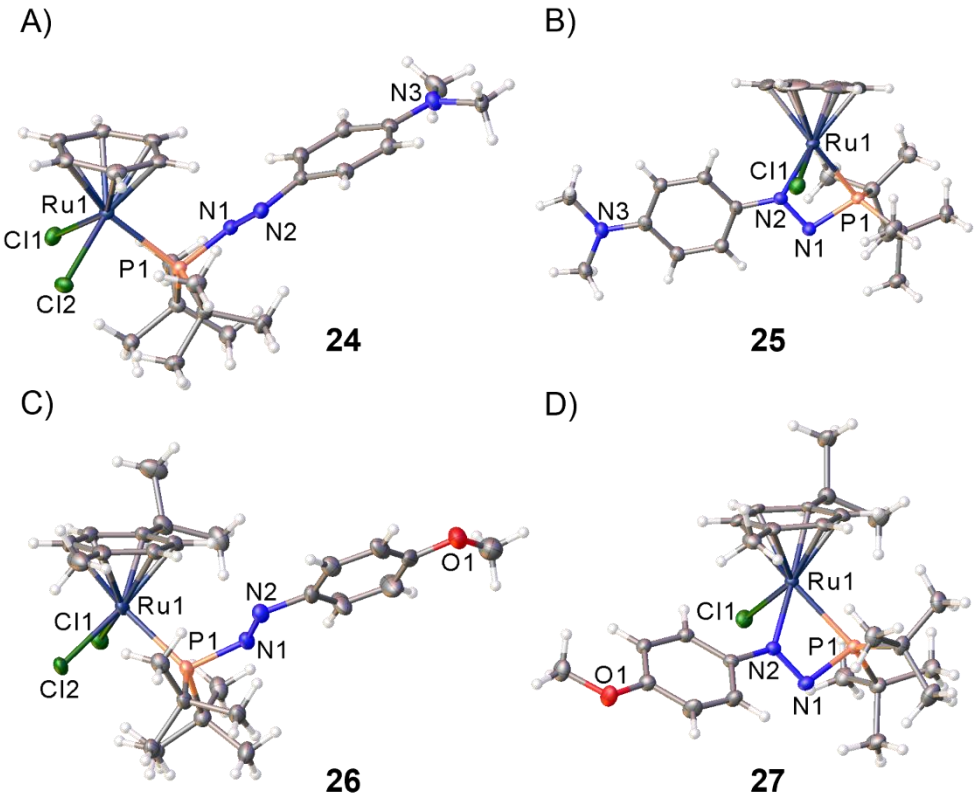


**Figure 4.9.** Single crystal structures of Ru-azophosphine complexes (A) Ru(benzene)(κ$^1$*P*-**11**)$Cl_2$ (**24**); (B) [Ru(benzene)(κ$^2$*P,N*-**11**)Cl][$BPh_4$] (**25**); (C) Ru(*p*-cymene)(κ$^1$*P*-**12**)$Cl_2$ (**26**); (D) [Ru(*p*-cymene)(κ$^2$*P,N*-**12**)Cl][$BPh_4$] (**27**). Selected bond distances and bond angles are tabulate in Table 4.3. **25** and **27**: the $[BPh_4]^-$ counter anion has been omitted for clarity. Thermal ellipsoids were drawn at the 50% probability level.[49]

To learn whether fine-tuning of their electronics, in addition to sterics, could also affect κ$^2$*P,N* coordination, reaction of **12** with half an equivalent of the [Ru(*p*-cymene)$Cl_2$]$_2$ dimer was tested, giving full conversion from 111.7 ppm (**12**) to 115.2 ppm in the $^{31}P\{^{1}H\}$ NMR spectrum, indicative of κ$^1$*P* coordination. This was corroborated by single crystal X-ray diffraction, and showed the complex has the composition Ru(*p*-cymene)(κ$^1$*P*-

**12**)$Cl_2$ (**26**) (Figure 4.9C). Addition of $NaBPh_4$ to the chlorobenzene solution of **26** gave a white precipitate (NaCl) and filtration, removal of solvent, and washing with hexane gave [Ru(*p*-cymene)(κ$^2$*P*,*N*-**12**)Cl][$BPh_4$] (**27**) as a brown solid in 71% isolated yield. The $^{31}P\{^1H\}$ NMR spectrum showed a clean, upfield shift to 67.4 ppm, indicative of κ$^2$*P*,*N* coordination. Again, this was confirmed by single crystal X-ray diffraction, which showed the bidentate nature of the ligand in the complex (Figure 4.9D). Pleasingly, this demonstrated that κ$^2$*P*,*N* coordination was compatible with the bulkier η$^6$-(*p*-cymene) on the ruthenium centre and did not require the switch to benzene.

The stacked $^{31}P\{^1H\}$ NMR spectra of **11**, **24** and **25** (Figure 4.10A), and **12**, **26** and **27** (Figure 4.10B) show the small downfield shift in ppm upon κ$^1$*P* coordination of the ligand and the significant upfield shift in ppm upon κ$^2$*P,N* coordination.

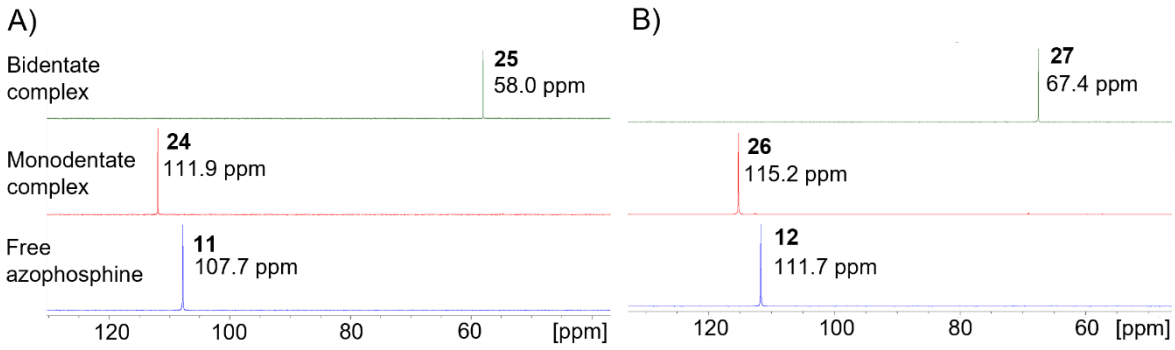


**Figure 4.10.** Stacked $^{31}P\{^1H\}$ NMR spectra of (A) azophosphine **11** (Z = $NMe_2$), Ru(benzene)(κ$^1$*P*-**11**)$Cl_2$ (**24**), and [Ru(benzene)(κ$^2$*P,N*-**11**)Cl][$BPh_4$] (**25**); (B) azophosphine **12** (Z = OMe), Ru(*p*-cymene)(κ$^1$*P*-**12**)$Cl_2$ (**26**), and [Ru(*p*-cymene)(κ$^2$*P,N*-**12**)Cl][$BPh_4$] (**27**).

Preparation of the κ$^2$*P,N* complexes using the general synthesis in Scheme 4.3 does not require prior isolation of the corresponding κ$^1$*P* complexes and can be accessed in a 'one-pot' method. Addition of [Ru(*p*-cymene)$Cl_2$]$_2$ dimer to a solution of azophosphine **13** (Z = Me) in chlorobenzene gave the characteristic downfield shift in ppm (113.4 ppm

(**13**) to 116.5 ppm) when analysed by $^{31}P\{^{1}H\}$ NMR spectroscopy (Figure 4.11A). Without isolation of [Ru(*p*-cymene)(κ$^{1}$*P*-(**13**))$Cl_2$], addition of $NaBPh_4$ to the solution gave a white precipitate (NaCl). The $^{31}P\{^{1}H\}$ NMR spectrum showed a significant upfield shift to 71.5 ppm. Single crystals suitable for analysis confirmed the bidentate nature of the ligand in the complex [Ru(*p*-cymene)(κ$^{2}$*P*,*N*-**13**)Cl][$BPh_4$] (**28**) (Figure 4.11B). X-ray analysis of the crystallographically-solved ruthenium-azophosphine complexes will be provided in Section 4.2.3.

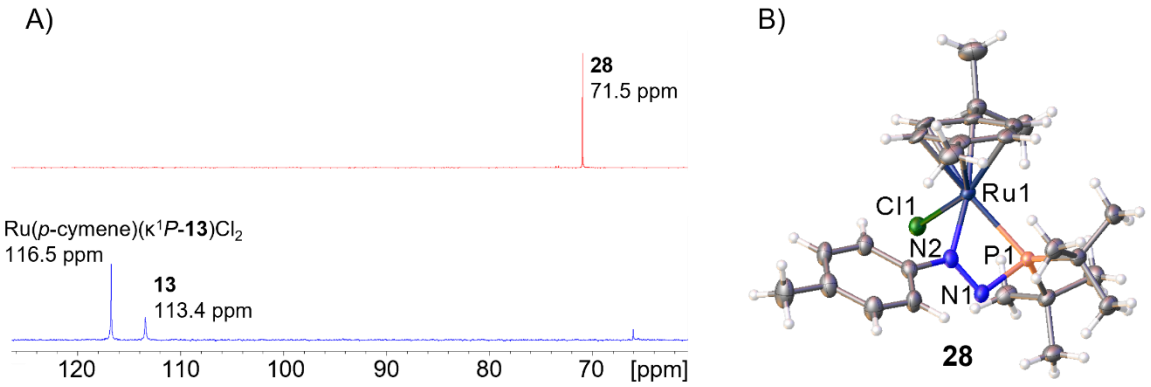


**Figure 4.11.** (A) Stacked crude$^{31}P\{^{1}H\}$ NMR spectra of aliquots of reaction mixture following (bottom) addition of [Ru(*p*-cymene)$Cl_2$]$_2$ dimer to a chlorobenzene solution of azophosphine **13** and (top) κ$^{2}$*P*,*N* coordination of 1**3** in complex **28** after addition of $NaBPh_4$; (B) Single crystal structure of Ru-azophosphine complex [Ru(*p*-cymene)(κ$^{2}$*P*,*N*-1**3**)Cl][$BPh_4$] (**28**). Selected bond distances (Å) and angles (°) of **28** are tabulated in Table 4.3. The [$BPh_4$]$^{-}$ counter anion has been omitted for clarity. Thermal ellipsoids were drawn at the 50% probability level.

### 4.2.2 Effect of Z on κ$^{2}$*P*,*N* Coordination

To test how modulating the electronics of the azophosphines affected their ability to act as competent κ$^{2}$*P*,*N* ligands, the formation of the bidentate complex was probed with the increasingly electron-poor azophosphines. To chlorobenzene solutions of azophosphines **11** – **16** was added half an equivalent of the [Ru(*p*-cymene)$Cl_2$]$_2$ dimer. Without isolation of the corresponding Ru(*p*-cymene)(κ$^{1}$*P*-(**Z**))$Cl_2$ products (Z = **11** –

**16**), $NaBPh_4$ was added to initiate $\kappa^2$*P,N* coordination to attempt to access the respective complex [Ru(*p*-cymene)($\kappa^2$*P,N*-(**Z**))Cl][$BPh_4$] salts, as assessed by $^{31}P\{^1H\}$ NMR spectroscopy without any further purification (Figure 4.12).

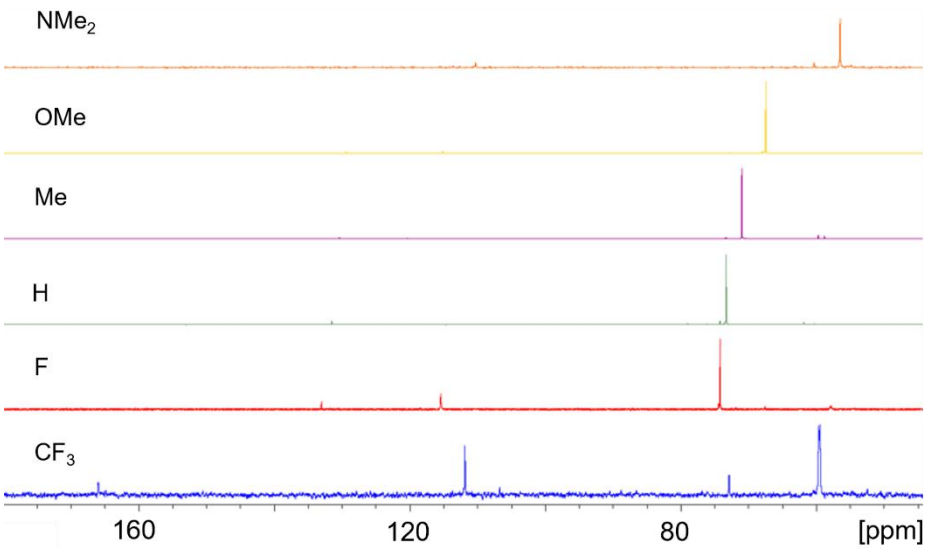


**Figure 4.12.** Crude $^{31}P\{^1H\}$ NMR spectra of products from reaction in Scheme 4.1B, in most cases showing formation of $\kappa^2$*P,N* complex.

These experiments show that the electron-rich azophosphines **11** and **12** (Z = $NMe_2$ and OMe, respectively) affords $\kappa^2$*P,N*-(**11**) and $\kappa^2$*P,N*-(**12**) coordination in quantitative yields under these conditions (as measured by $^{31}P\{^1H\}$ NMR spectroscopy). **13** (Z = Me) and **14** (Z = H) formed predominantly $\kappa^2$*P,N*-**13** (71.5 ppm) and $\kappa^2$*P,N*-**14** (73.6 ppm), respectively; however the crude spectra included trace signals for **13** (113.4 ppm) and **14** (115.1 ppm), $\kappa^1$-*P*-**13** (116.5 ppm), and a trace unknown impurity (Z = Me, 130.1 ppm; Z = H, 131.6 ppm). **15** (Z = F) also formed mostly $\kappa^2$*P,N*-**15** (74.3 ppm); however, the crude spectrum showed signals associated with **15** (115.4 ppm) and an unknown impurity (113.3 ppm) of greater intensity than when Z = Me or H. **16** (Z = $CF_3$) was shown not to be an effective ligand for this transformation. It is possible that a small amount of $\kappa^2$*P,N*-**16** was formed (tentatively assigned as 72.9 ppm), but the crude

spectrum showed two main signals at 59.8 ppm and 112.1 ppm, and a smaller signal at 165.7 ppm; none of which can be assigned to **16** (119.7 ppm) or $\kappa^1$*P*-**16** (121.6 ppm). These results show that subtle differences to the electronics of the system can have major implications on the ligand properties of azophosphines, which is supported by the relatively minor deviations of the $^1J_{P-Se}$ coupling constants of the azophosphine-selenide compounds **17** – **22** discussed in Chapter 3 (Section 3.5).

### 4.2.3 X-ray Analysis

Table 4.1 contains a non-exhaustive tabulation of P–Ru bond lengths and P–Ru–N bond angles of selected crystallographically-solved Ru(II)(arene) complexes with $\kappa^2$*P,N* coordinated 1,3-P,N ligands reported in the literature.

**Table 4.1.** P–C–N and P–Ru–N bond angles (°) and P–Ru bond length (Å) of Ru(II)(arene) complexes with $\kappa^2$*P,N* coordinated 1,3-P,N ligands.

| RN=N–PR$^1_2$ | P–X–N | P–Ru–N | P–Ru | Reference |
|---|---|---|---|---|
| 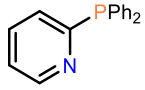 | Not available | 67.21(13) | 2.106(4) | [15] |
| 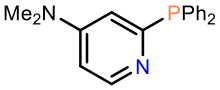 | 99.6(4)[a] | 66.3(1) | 2.332(2) | [13] |
| 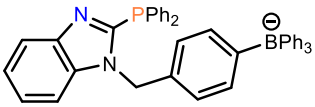 | 104.4(4)[a] | 67.6(1) | 2.342(2) | [25] |
| 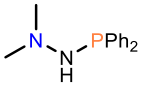 | 106.4(3)[b] | 66.79(10) | 2.3133(9) | [29] |
| 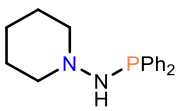 | 106.7(2)[b] | 66.75(8) | 2.3109(9) | [29] |

[a] X = C; [b] X = N

Chelation forms a strained four-membered ring in which, typically, the bite angle ranges from 66.3(1) – 67.6(1)°. The P–Ru bond length of $\kappa^2$*P,N* coordinated $PPh_2Py$ is 2.106(4) Å, otherwise, a bond length of approximately 2.3 Å is typical. The ring strain is highlighted by the decreased P–X–N bond angles (99.6(4) – 106.7(2)°) from that of the corresponding $\kappa^1$*P* complexes (116.9(2) – 117.7(2)°). The structures of **23** – **28** were solved by single-crystal X-ray diffraction; selected bond distances and bond angles are tabulated in Table 4.2.

**Table 4.2.** Selected bond distances (Å) and bond angles (°) of crystalllographically characterised Ru-azophosphine complexes **23** – **28**.

| Structure | P1–Ru1 | P1–N1 | N1–N2 |
|---|---|---|---|
| **23** | 2.4208(7) | 1.777(2) | 1.258(3) |
| **24** | 2.4041(8) | 1.744(3) | 1.272(4) |
| **25** | 2.3607(6) | 1.749(2) | 1.300(3) |
| **26** | 2.4078(13) | 1.751(4) | 1.257(6) |
| **27** | 2.3933(5) | 1.7758(16) | 1.283(2) |
| **28** | 2.4059(7) | 1.784(3) | 1.271(3) |

| Structure | P1–N1–N2 | P1–Ru1–N2 |
|---|---|---|
| **23** | 114.81(17) | – |
| **24** | 118.3(2) | – |
| **25** | 99.08(15) | 62.62(6) |
| **26** | 118.7(4) | – |
| **27** | 99.18(11) | 62.92(4) |
| **28** | 98.87(19) | 62.75(7) |

The P1–Ru1–N2 bite angles of **25** (62.62(6)°), **27** (62.92(4)°) and **28** (62.75(7)°) are significantly shorter than those in Table 4.1, presumably due to the shorter covalent radius of the central nitrogen atom compared to carbon. The P1–Ru1 bond lengths of

**25** (2.3607(6) Å) and **27** (2.3933(5) Å) are shortened relative to their $\kappa^1$*P* analogues **24** (2.4041(8) Å) and **26** (2.4078(13) Å) due to formation of the strained four-membered ring.The N1–N2 bond lengths are lengthened likely due to back-donation from Ru1 into the N–N π* orbital (**24**, **25** 1.272(4) and 1.300(3) Å, respectively; **26**, **27** 1.257(6) and 1.283(2) Å, respectively). Relative to those tabulated in Table 4.1, the P1–Ru1 bond lengths of $\kappa^2$*P,N* **25**, **27** and **28** are marginally longer presumably due to a combination of steric bulk (P–$^t$Bu$_2$ compared to P–Ph$_2$) and the azophosphines being relatively weak P-donors. The ring strain in **25** (99.08(15)°) and **27** (99.18(11)°) is highlighted by the decreased P1–N1–N2 bond angle from that of **24** (118.3(2)°) and **26** (118.7(4)°), respectively. This is also evident when compared to the P–X–N bond angles in Table 4.1 which range between 104.4(4) and 106.7(2)°, with exception to the NMe$_2$-substitued PPh$_2$Py ligand (99.6(4)°).

### 4.2.4 Computational Analysis

The effect of the Z group on the formation of the bidentate complexes was further studied by DFT calculations (see supporting information of references [47] and [48] for details). The structures of **κ$^1$*P*-*Z*** were optimised, as well as the analogous bidentate complexes [Ru(*p*-cymene)($\kappa^2$*P,N*-(**11** – **16**))Cl][Cl] labelled as **Bid-*Z*** (note these bidentate complexes studied computationally contain the Cl$^-$ counter anion instead of those accessed experimentally, which feature the BPh$_4^-$ counter anion (Figure 4.13A)). In all cases, the monodentate complex **κ$^1$*P*-*Z*** is favoured over the analogous bidentate complex **Bid-*Z*** (see reference [48] for values); this is in line with the experimental data, in which the bidentate complexes do not form spontaneously from the corresponding monodentate complex, and a halide-abstracting agent is required to promote the reaction. However, the bidentate complexes become less disfavoured when electron

donating substituents are used (Figure 4.13B), which is rationalised by the donor sites on the azophosphine becoming more electron rich. These data highlight the importance of electron-donating *para* substituents when forming bidentate complexes with azophosphines.

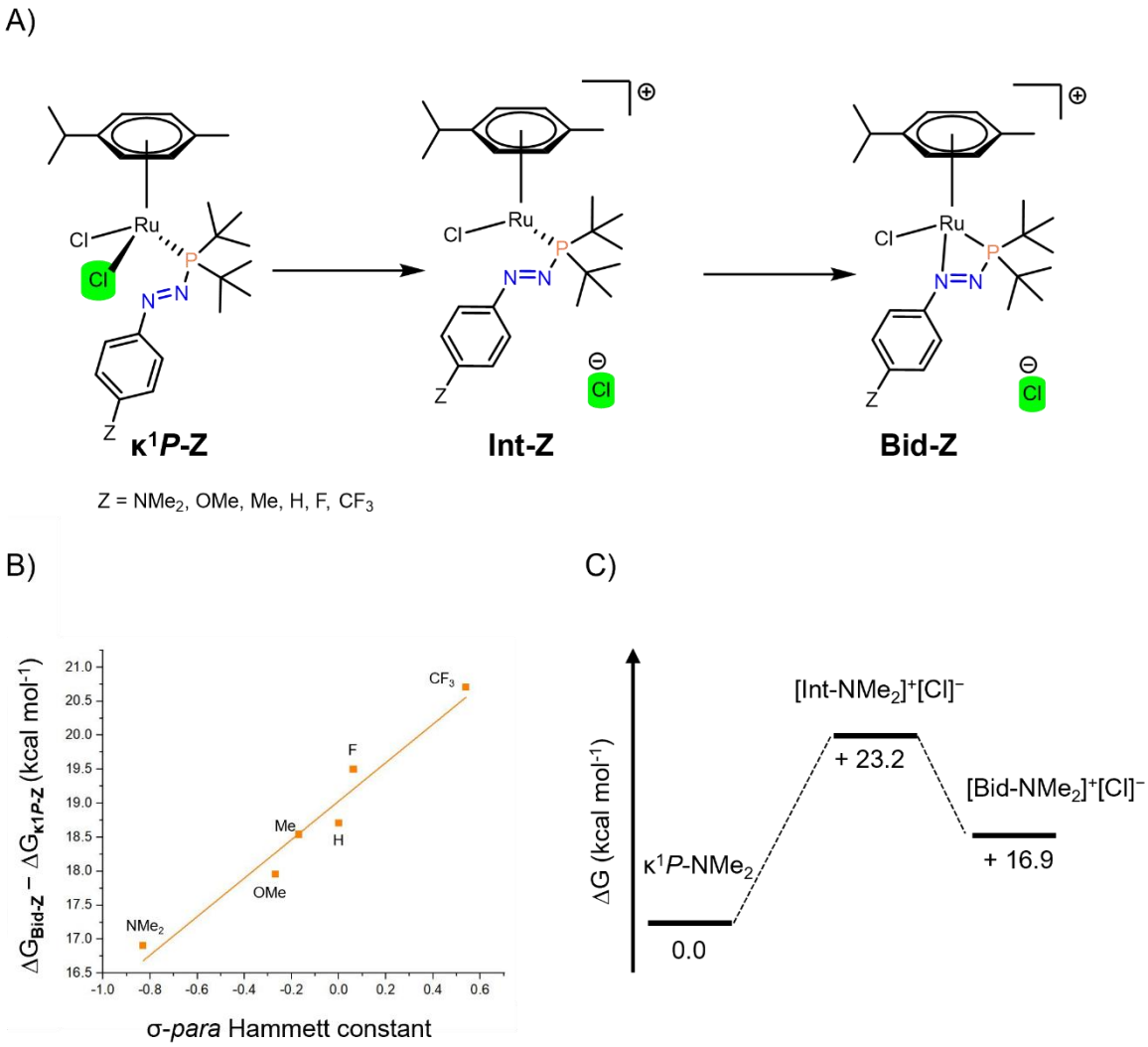


**Figure 4.13.** (A) Ru complexes analysed computationally. (B) Energy difference between **κ¹*P*-Z** and **Bid-Z** against Hammett parameter of the *para*-substituent. (C) Reaction coordinate for the conversion of **κ¹*P*-NMe₂** to **Bid-NMe₂** via **Int-NMe₂**. Optimisations performed at the ωB97XD(toluene)/def2TZVP level of theory.

Despite the formation of the bidentate complexes being thermodynamically uphill relative to the monodentate complexes, this reaction is driven by precipitation of the

corresponding NaCl salt following halide abstraction, and subsequent formation of an intermediate (**Int-Z**; Figure 4.13A) For all the Z groups explored, **Bid-Z** is more energetically favoured than the corresponding **Int-Z**; for Z = $NMe_2$ this value is −6.26 kcal $mol^{-1}$, whereas for the electron-withdrawing Z = $CF_3$ this value is only −3.38 kcal $mol^{-1}$ (see reference [48] for values; the reaction profile for the $NMe_2$-substituted compounds is shown in Figure 4.13C).

Experimentally, the complexation of azophosphine **3** showed that, although it was simple to access the $\kappa^1$*P*-**3** complex **23**, despite extensive synthetic efforts the corresponding $\kappa^2$*P,N*-**3** complex could not be synthesised. Therefore, the same computational study on azophosphine **3** was completed and found that the final bidentate product is higher in energy than the halide abstracted intermediate by 6.49 kcal $mol^{-1}$, so although halide abstraction is experimentally possible, the formation of the bidentate complex is disfavoured. This result shows that the steric profile of the *N*-aryl group on the azophosphine is key, and in the mesityl case the *ortho*-methyl substituents are bulky enough to preclude formation of the bidentate complex.

### 4.2.3 Displacement of N from Ru Centre

Azophosphines feature a soft P-atom and hard N-atom as donor sites and selectively coordinate in a $\kappa^1$*P* manner to a ruthenium(arene) centre. Addition of $NaBPh_4$ is required to free a coordination site at ruthenium to force $\kappa^2$*P,N* coordination. No $\kappa^1$*N* coordination is observed. It was therefore hypothesised that the N2 atom would demonstrate heightened hemilability and be easily displaced by a competing ligand (Scheme 4.4).

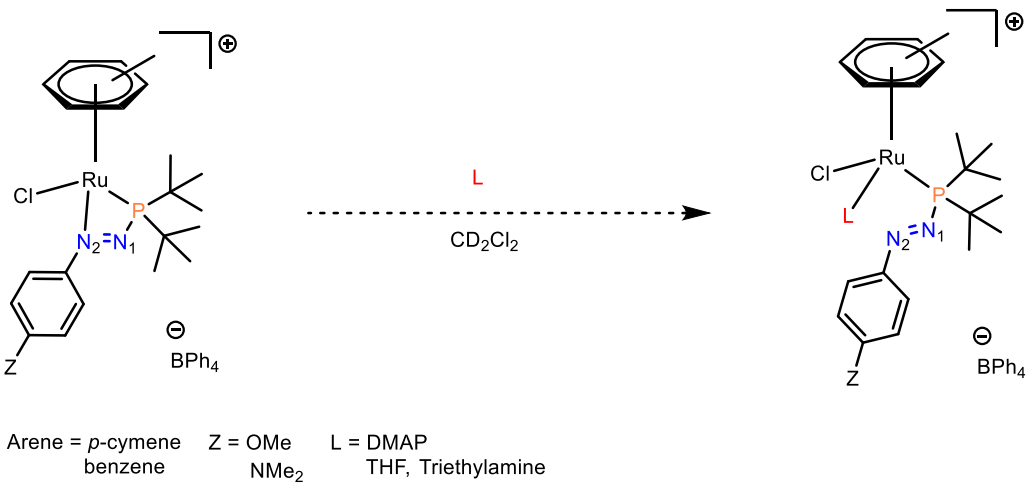


**Scheme 4.4.** Hypothesised displacement of N from Ru centre by ligand L. THF = tetrahydrofuran, DMAP = 4-dimethylaminopyridine.

Addition of 1 – 5 equivalents of THF to a solution of **28** in $CD_2Cl_2$ showed no change in the $^{31}P\{^1H\}$ NMR spectrum after 3 days. However, **28** is unstable when THF-$d_8$ is used as solvent. When triethylamine (1 equiv.) was used as the competing ligand, again, no change was observed in the $^{31}P\{^1H\}$ NMR spectrum. However, multiple signals were observed in the spectrum 1.5 days after sample preparation of which none could be assigned to **28**. Addition of 1 equiv. of DMAP (4-dimethylaminopyridine) to a solution of **26** in chlorobenzene showed one extra signal in the $^{31}P\{^1H\}$ NMR spectrum at 111.7 ppm (Figure 4.10, middle spectrum) which is associated with the free azophosphine **12**. Attempts to grow crystals from this mixture suitable for single crystal X-ray diffraction were unsuccessful. After 48 hours, a complex $^{31}P\{^1H\}$ NMR spectrum, with only trace signals of **26** and a broad, poorly resolved signal at 56 – 57 ppm was observed (Figure 4.14, top spectrum).

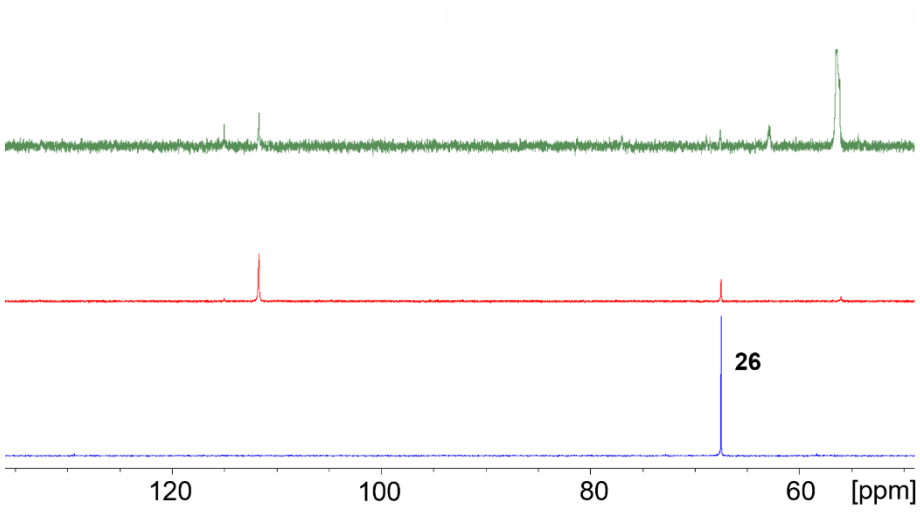


**Figure 4.14.** (Bottom) $^{31}P\{^{1}H\}$ NMR spectrum of **26** in chlorobenzene; (Middle) $^{31}P\{^{1}H\}$ NMR spectrum of **26** immediately after addition of DMAP; (Top) $^{31}P\{^{1}H\}$ NMR spectrum 48 hours after addition of DMAP.

The P–N bond and ring strain in **28** and **26** make them susceptible targets to nucleophilic attack, in addition to displacement of N2, likely to cause the complexity observed in the $^{31}P\{^{1}H\}$ NMR spectra after addition of triethylamine and DMAP, respectively, after several hours. The $^{1}J_{P-Se}$ coupling constants for the azophosphines (discussed in Chapter 3, Section 3.5) showed that, in general, azophosphines are relatively weak P donors. This too may contribute to the complexity observed. A wider range of competing ligands would need to be tested to establish the range which could give clean displacement of N2. According to a Tolman plot of electronic parameter ($\nu_{CO}$) against cone angle of common P-donor ligands, the $\nu_{CO}$ of $PCy_3$ and $P^tBu_3$ are equal differing only in the cone angle of $PCy_3$, which is approximately 10° smaller than that of $P^tBu_3$. The steric bulk of phosphine ligands can be correlated with their dissociation from a metal centre. Therefore, substituting the $^t$Bu groups on the azophosphine for cyclohexyl groups may enhance its stability towards N2 displacement by a competing ligand by introducing a small decrease in steric bulk at the phosphorus centre. For example, the $^{1}J_{P-Se}$ coupling constant of $PCy_3$ (674 Hz ($CDCl_3$) is 12 Hz smaller than

that of P$^t$Bu$_3$ (686 Hz ($CDCl_3$)).[50] As discussed in Chapter 3, Section 3.4, it was found that relatively minor deviations in $^1J_{P-Se}$ coupling constant could have major implications on the ligand properties of azophosphines. Therefore, although clean products could not be isolated, it is clear that donor ligands can perturb the bonding of the azophosphine to the ruthenium centre. This opens the possibility of using these complexes as catalysts where the substrate can bind to the metal centre and will be explored in more detail in the following chapter.

### 4.2.4 Photo-switching

The experimental studies thus far conducted on the free azophosphines failed to provide definitive evidence of photo-switching properties. Indeed, a collaborative computational project with the University of Bristol, discussed in Chapter 2, could ascertain no viable pathway for *trans*-*cis* isomerisation of the theoretical azophosphine $PhN_2PMe_2$.[51]

Azophosphines can serve as competent $\kappa^1$*P* and $\kappa^2$*P,N* ligands when coordinated to a Ru(arene) centre, and the electronic effect of coordination can be seen spectroscopically with the three individual species each having distinct UV/Vis. absorption spectra. It was therefore prudent to determine whether the influence of coordination to ruthenium(II) also extended to the photo-switching properties of the azophosphine (Scheme 4.5).

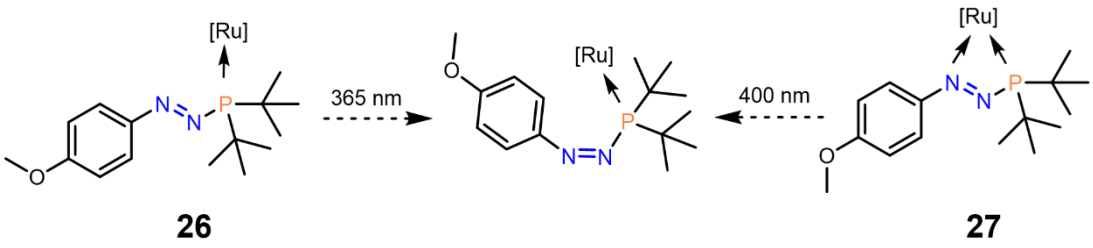


**Scheme 4.5**. Hypothesised *E* to *Z* isomerisation of Ru-azophosphine complexes **26** and **27** with UV irradiation.

Irradiation for 5 minutes with 400 nm light of a 50 μM solution of $\kappa^2$*P,N* complex **27** in chlorobenzene blue-shifted the absorbance of $\lambda_{max}$ from 392 nm to 334 nm and changed the colour of the sample from pale amber to colourless. For *cis*-azobenzene, irradiation with ca. 500 nm light results in isomerisation back to *trans*-azobenzene. However, when **27** was irradiated with 500 nm light for 10 minutes no significant change in absorption was observed in the spectrum (Figure 4.15A).

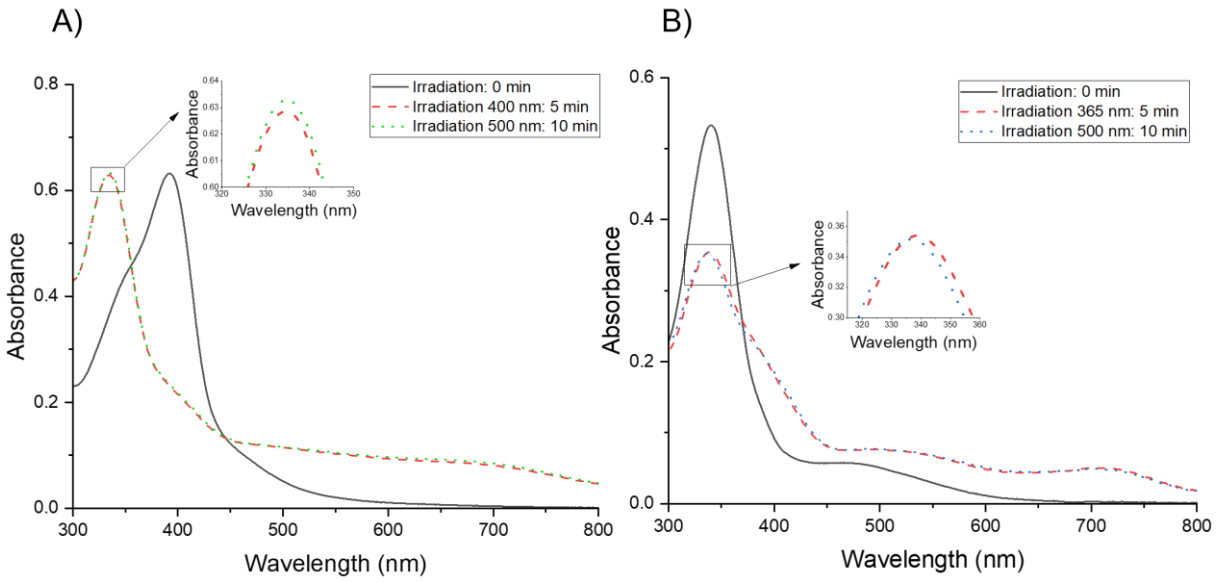


**Figure 4.15.** UV/Vis spectra of (A) **27** before irradiation and after irradiation at 400 nm (5 min) followed by irradiation at 500 nm (10 minutes), and (B) **26** before irradiation and after irradiation at 365 nm (5 min) followed by irradiation at 500 nm (10 minutes).

After 16 h at room temperature, to allow for potential thermal relaxation of **27**, still no change in absorption was observed in the spectrum. Repeating the experiment on a

more concentrated sample of **27** in chlorobenzene, to enable analysis by NMR spectroscopy post irradiation, resulted in a colour change from dark amber to black and multiple peaks in the $^{31}P\{^{1}H\}$ NMR spectrum, of which one small peak could be assigned to **27**. Irradiation of the dilute 50 μM sample of **27** blue-shifted $\lambda_{max}$ to 334 nm yielding a UV/Vis. spectrum similar to that of $\kappa^1$*P* complex **26** pre-irradiation (Figure 4.15B). It is possible that irradiation of **27** is initiating decomposition *via* de-coordination of N from $\kappa^2$*P,N* coordination to an unsaturated $\kappa^1$*P* coordination. It is known up to 5 equiv. of THF does not displace N coordination and its presence as a competing ligand during irradiation of **27** may provide evidence for this.

Irradiation for 5 minutes at 365 nm of $\kappa^1$*P* complex **26** in chlorobenzene altered the UV/Vis. spectrum, albeit with no difference in $\lambda_{max}$, and changed the colour of the sample from pale amber to colourless. Similarly to **27**, when **26** was then irradiated at 500 nm for 10 minutes, and left for 16 h with no irradiation, no change in absorption was observed in the spectra (Figure 4.15B).

Photo-switching experiments on the free azophosphines have failed to provide UV/Vis spectra that show any significant changes post irradiation. For Ru complexes **26** and **27**, differences in absorption are observed in the UV/Vis spectra post irradiation; however, the spectra do not return to their pre-irradiation profile indicating decomposition, rather than photoisomerisation, is likely to be occurring. Unfortunately, we have been unable to identify any of the decomposition products at this time.

## 4.3 Gold

Having demonstrated that azophosphines can display κ$^1$*P* and κ$^2$*P,N* coordination modes in a controlled manner to a ruthenium(arene) centre, the μ*P,N* coordination mode, also associated with 1,3-P,N ligands, was targeted (Scheme 4.4A). Coordination compounds of gold(I) often aggregate with Au(I)···Au(I) distances shorter than the sum of their van der Waals radii. This aurophilicity can be exploited by mixed donor ligands which serve as bridging ligands to hold two Au(I) ions in proximity.[52] Section 4.3 contains research by Ellen M. Tait (MSci student, Jupp group, University of Birmingham) with supervision by the author.[45]

### 4.3.1 Synthesis of κ$^1$*P* and μ*P,N* Complexes

Reaction of azophosphine **12** with an equivalent of DMSAuCl (DMS = dimethylsulfide) in DCM was monitored by $^{31}$P{$^1$H} NMR spectroscopy, and full conversion of the free azophosphine at 111.7 ppm to a new species at 124.6 ppm was observed (Scheme 4.6). Removal of volatiles *in vacuo* isolated a vibrant red powder in 86% yield.

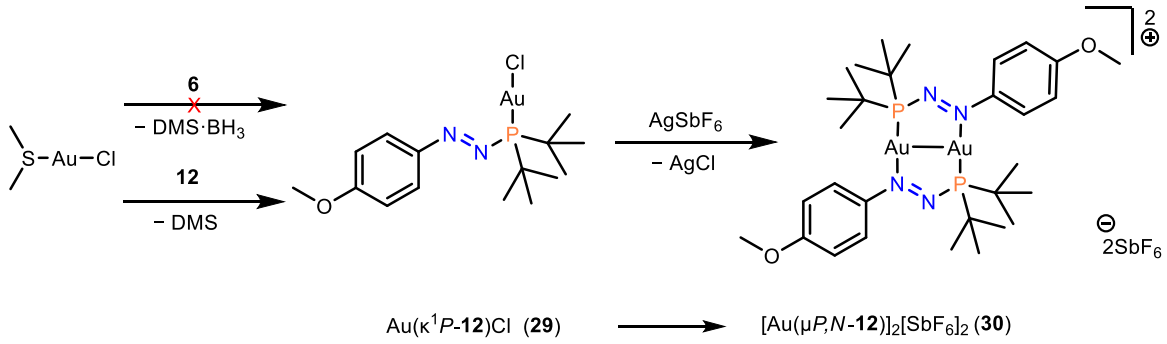


**Scheme 4.6.** General synthesis of Au-azophosphine complexes Au(κ$^1$*P*-**12**)Cl monomer (**29**) and [Au(μ*P,N*-**12**)]$_2$[SbF$_6$]$_2$ dimer (**30**).

As previously observed in the coordination of azophosphines to ruthenium, a downfield shift in the $^{31}$P{$^1$H} NMR spectrum was indicative of κ$^1$*P* coordination. This was

corroborated by single crystal X-ray diffraction, and showed that the compound had the composition Au(κ$^1$*P*-**12**)Cl (**29**) with a linear P–Au–Cl bond angle of 178.03(3)° (Figure 4.16A). Monomer **29** exhibits no intermolecular Au···Au interactions, with the closest separation being 7.279 Å in the extended crystal structure. Selected bond distances and bond angles are tabulated in Table 4.4 and will be discussed further in section 4.3.2. Due to the combination of soft Lewis acid and soft Lewis base, gold(I) has a known affinity for phosphorus. With this in mind, and to reduce the number of synthetic steps, azophosphine **12** was substituted for its azophosphine-borane analogue **6** to test whether P–Au coordination could drive displacement of DMS to DMS·$BH_3$ (Scheme 4.6). However, attempts to generate complex **29** *via* the azophosphine-borane were unsuccessful.

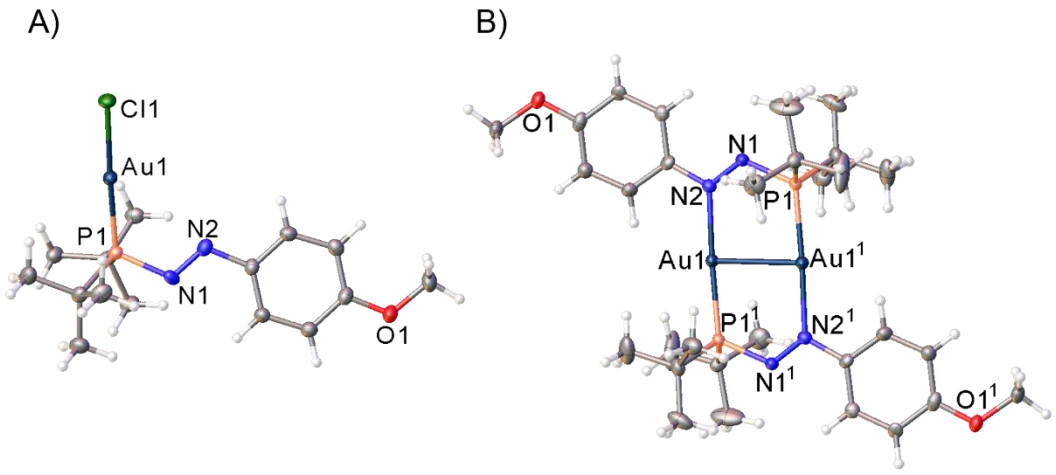


**29** **30**

**Figure 4.16.** Single crystal structures of Au-azophosphine complexes (A) Au(κ$^1$*P*-**12**)Cl (**29**); (B) ([Au(μ*P,N*-**12**)][$SbF_6$])$_2$ (**30**) (2[$SbF_6$]$^-$ counter anions removed for clarity). Selected bond distances and bond angles are tabulated in Table 4.4. Thermal ellipsoids were drawn at the 50% probability level. Single crystals of **29** and **30** grown by Ellen Tait.

A range of halide abstracting agents were tested to force formation of a dimeric Au(I) structure, in which **12** was coordinated to two gold centres in a μ*P,N* manner in which

each Au atom was coordinated to the phosphorus atom of one ligand and the terminal nitrogen atom of the second ligand. Dropwise addition of a reddish-pink solution of **29** in DCM to a colourless solution of $AgSbF_6$ in DCM gave an immediate colour change to orange and precipitation of an orange solid. Redissolution in DCM and filtration through a celite plug left an orange solution and an off-white precipitate (AgCl). Removal of volatiles isolated an orange powder in 83% yield. Analysis by $^{31}P\{^{1}H\}$ NMR spectroscopy showed an upfield shift from 124.6 ppm (**29**) to 108.1 ppm. Single crystals suitable for analysis confirmed the head-to-tail bridging nature of **12** in the dimeric complex ([Au(μ*P*,*N*-**12**)]$_2$[$SbF_6$])$_2$ (**30**) (Figure 4.16B). **30** crystallised in a monoclinic $P2_1/c$ space group with the Au–Au vector residing on a crystallographic inversion centre, making only half of the complex crystallographically unique.

### 4.3.2 X-ray Analysis

Selected bond angles (°) and Au···Au distances (Å) for previously reported μ*P,N*-Au(I) dimers featuring 1,3-P,N ligands are tabulated in Table 4.3. The Au···Au distances range between 2.776 – 2.8261 Å and the P–Au–N bond angles between 176.1 – 178.31°. The shortest Au···Au distance (2.776(1) Å) and the greatest deviation from 180° in the P–Au–N bond angle (176.1(5)°) is observed with the dimethylphosphinopyridine ($PMe_2Py$) ligand. $PMe_2Py$ has a smaller P–C–N bond angle (119.6(4)°) than that of the 1-methylbenzimidazoediphenyl phosphine (mbdp) ligand (122.6(3)°) and could be expected to contribute to the shorter Au···Au distance. However, analysis of a wider range of gold(I) complexes with 1,3-P,N bridging ligands is required to determine the effect of the pyridyl and imidazolyl ligand backbone on the bond metrics of the resultant dimer.

**Table 4.3**. P–C–N and P–Au–N bond angles (°) and Au···Au distances (Å) of μ*P,N*-Au(I) dimers with 1,3-P,N ligands.

| RN=N–PR$^1_2$ | P–C–N | P–Au–N | Au···Au | Reference |
|---|---|---|---|---|
| 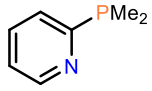 | 119.6(14) | 176.1(5) | 2.776(1) | [34] |
| 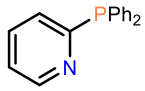 | No crystallographic data | | | [34] |
| 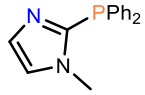 | Not available | 178.0(4)[a]<br>177.9(3)[a] | 2.8261(11)[b]<br>2.8174(10)[b] | [35] |
| 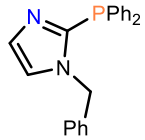 | No crystallographic data | | | [36, 37] |
| 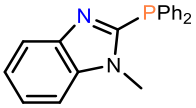 | 122.6(3) | 178.31(11) | 2.808(4) | [38] |

[a] counter ion is $ClO_4$; [b] counter ion is $BF_4$.

**Table 4.4.** Selected bond distances (Å) and bond angles (°) of crystalllographically characterised Au-azophosphine monomer **29** and dimer **30**.

| Structure | P1–Au1 | P1–N1 | N1–N2 | N2–Au1 | Au1···Au1[1] |
|---|---|---|---|---|---|
| **29** | 2.2354(10) | 1.728(3) | 1.261(4) | - | - |
| **30** | 2.2513(15) | 1.741(5) | 1.276(7) | 2.123(5) | 2.7782(5) |

| Structure | P1–N1–N2 | P1–Au1–X[a] |
|---|---|---|
| **29** | 114.1(3) | 178.03(3) |
| **30** | 121.8(4) | 176.50(14) |

[a] **29**, X = Cl1; **30**, X = N2.

Comparison of bond and angle metrics (Table 4.4) reveal the P1–Au1 bond length of monomer **29** (2.2354(10) Å) is shorter than that of dimer **30** (2.2513(15) Å), and the P1–N1–N2 bond angle of **29** (114.1(3)°) is smaller relative to **30** (121.8(4)°). A longer P1–Au1 bond length would be expected in the sterically-crowded dimer, in addition to

a wider P1–N1–N2 bond angle influenced by the limitations of the Au1···Au1$^{1}$ contact. Both **29** and **30** have a P1–Au1–X (**29**, X = Cl1; **30**, X = N2) angle of close to 180° (178.03(3)° and 176.50(14)°, respectively), with **30** having greater deviation from this value due to the rigidity imposed by its head-to-tail μ*P,N* coordination. Comparisons of **29** and **30** can be made with the respective monomer and dimer Au(I) complexes of 1,3 P,N ligands tabulated in Table 4.3. For **29** and **30**, there are no significant differences (to 3σ) between P1–Au1 bond length or P1–Au1–X bond angle. However, for the dimeric complexes the aurophilic Au1···Au1$^{1}$ interaction of **30** (2.7782(5) Å) is shorter than the imidazolyl-based ligands in Table 4.3 (2.808(4) – 2.8261(11) Å) presumably due to the shorter covalent radius of the azophosphine's central nitrogen atom compared to the imidazolyl's carbon. However, when compared with the $[Au(dmpy)]_2^{2+}$ (2.776(1) Å) there is no statistical difference in aurophilic interaction. The hexafluoroantimonate anion of **30** weakly interacts with the Au centres with the shortest Au–F separation being 3.222 Å, comparable to the shortest Au–O separation of $[Au(midp)]_2^{2+}$ and its perchlorate anion (3.22(7) Å).

Au(I)–Au(I) complexes are often luminescent. The origin of the emission is widely accepted to be associated with the metal-localised 5dσ* → 6pσ transition, with an increase in Au···Au interaction, in general, leading to a shift of emission to a lower energy.[53–55] Thus, many Au(I) complexes display luminescence in the solid state, and no detectable luminescence in solution.[55] In contrast to $[Au(midp)][ClO_4]$ and $[Au(mbdp)[BF_4]$, **30** displayed no solid-state luminescence when excited under a UV lamp. Assuming azophosphine **12** to be a weaker donor to Au(I) than dpim, the aurophilic interactions may be weakened such that the dσ* → pσ transition is higher in energy for **30** than $[Au(midp)]_2[ClO_4]_2$, and, in some cases, the coordinating ability of

the counterion has been shown to have a significant role.[56] However, this observation on the absence of luminescence of **30** is tentative and preliminary to repeated experiments in solution and on pure crystalline and ground samples, including collection of emission spectra. In Dori's seminal paper, the Au(I) complexes displayed intense luminescence at 77 K but quenching was observed at higher temperatures (>300 K).[57] Photoluminescence can be limited by dynamic behaviour in which non-emissive relaxation can result from rotation of bonds.[58] Collection of the spectra at liquid nitrogen temperatures may therefore be appropriate.

### 4.3.2 Photo-switching

For simplicity, photo-switching experiments on the Au complexes were restricted to only monomer **29** (Scheme 4.7).

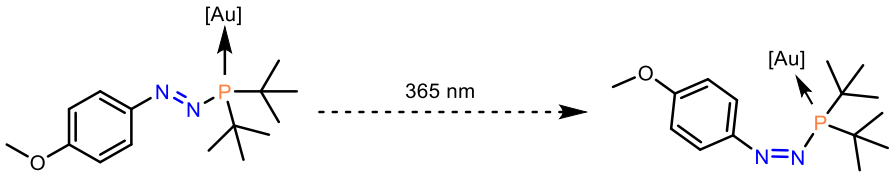


**Scheme 4.7.** Hypothesised *E* to *Z* isomerisation of **29** with UV irradiation.

Irradiation for 30 min, in two 15 min intervals, with 365 nm light of a 50 μM solution of **29** in DCM maintained the absorption of $\lambda_{max}$ at 344 nm; however, this was accompanied by a significant decrease in absorption (Figure 4.17A). For azobenzene, the strong UV band arises from the symmetry allowed π→π* transition and the much weaker band in the visible region from n→π* transitions. The π→π* transitions of *cis*-azobenzene are much weaker, and the n→π* transitions absorb more strongly, than for *trans*-azobenzene (Figure 4.17B).[59] Similarities can be seen in the corresponding π→π* transition of **29** in which absorption decreases with irradiation. However, for **29**

a decrease in absorption is also seen in the n→π* transition which is inconsistent with the changes in absorption for azobenzene. Irradiating the sample with 523 nm light, to initiate what would be expected to be *cis* → *trans* isomerisation and a reversion back to the pre-irradiation spectrum, resulted in a further decrease in absorption for the π–π* transition. After 16 h at room temperature, to allow for potential thermal relaxation of **29**, still no change in absorption was observed in the spectrum. Repeating the experiment on a more concentrated sample of **29** in DCM, to enable analysis by NMR spectroscopy post irradiation, showed no significant change in the $^{31}P\{^{1}H\}$ NMR spectrum indicating no decomposition had occurred (Figure 4.18).

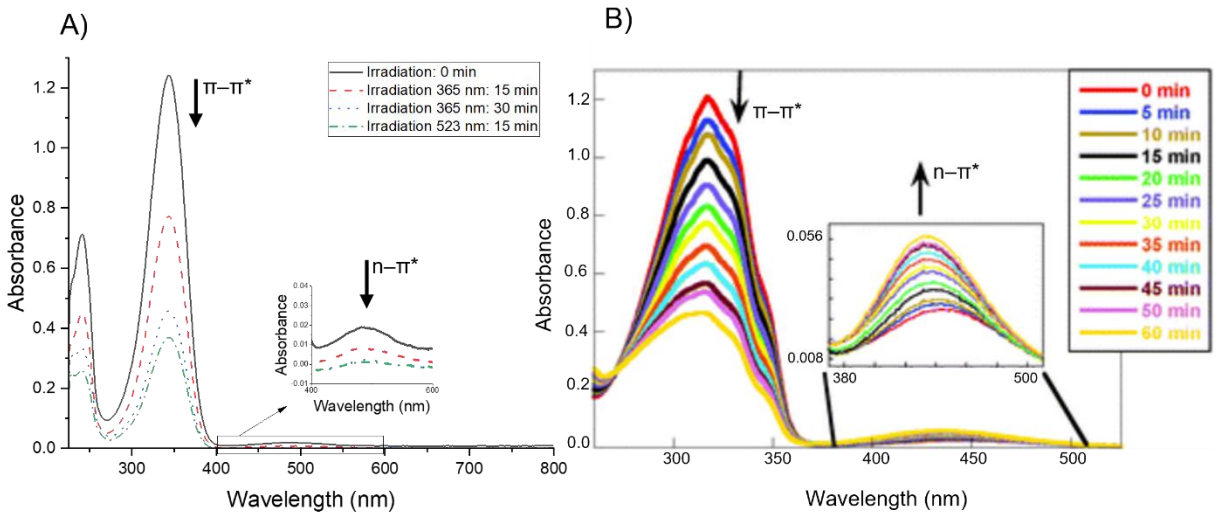


**Figure 4.17.** Changes in UV/Vis absorption spectra of (A) **29** upon irradiation with 365 nm light, followed by irradiation with 500 nm light, and (B) azobenzene upon irradiation with 316 nm light, adapted from ref [14]. The black arrows indicate an increase/decrease in absorption with irradiation.

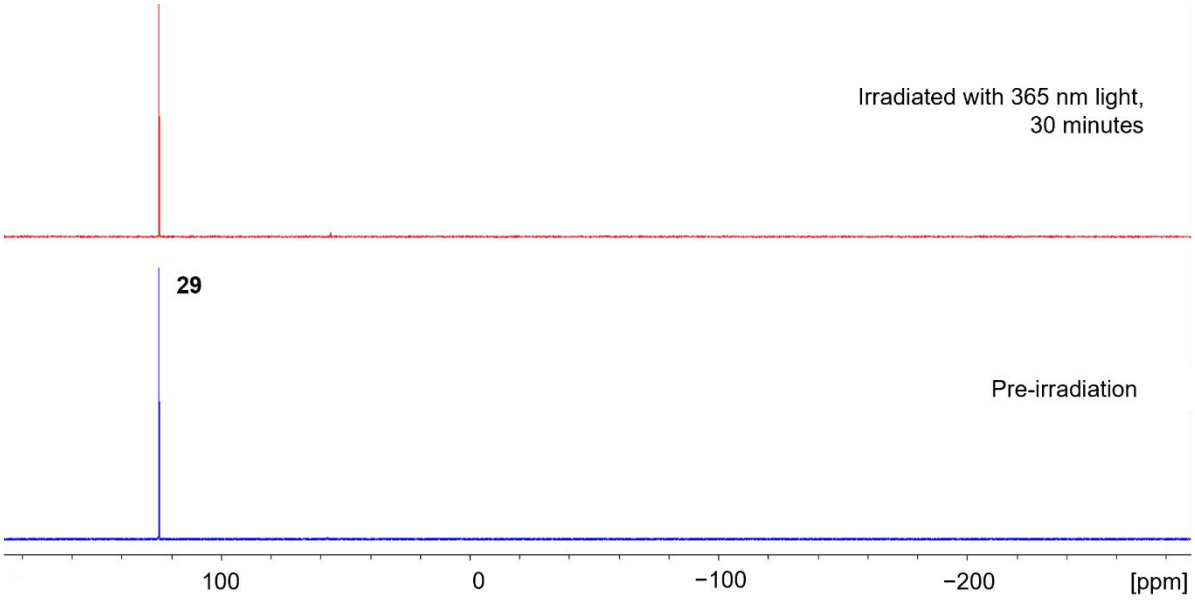


**Figure 4.18.** $^{31}P\{^{1}H\}$ NMR spectrum of (Bottom) **29** pre-irradiation and (Top) **29** after irradiation with 365 nm light for 30 min.

From these data it is not possible to conclude whether **29** displays photo-switching properties. Upon irradiation, significant changes are observed in the UV/Vis spectrum consistent with *trans* → *cis* isomerisation; however, these changes do not appear to be reversible. This would suggest decomposition of **29** has occurred; however, apart from a trace signal at approximately 60 ppm, no significant changes were observed in the $^{31}P\{^{1}H\}$ NMR spectrum post-irradiation. As the solution of **29** was more concentrated for the NMR experiment, it would be prudent to repeat this experiment with a longer irradiation time to monitor the signal at 60 ppm and test a wider spectral width for potential decomposition products. For azobenzene, small shifts in δ occur in the $^{1}H$ NMR spectrum with *trans* → *cis* isomerisation;[60] however, this is not observed in the corresponding $^{1}H$ NMR spectrum of **29**. Here, a NOESY experiment that can detect through-space interactions between nuclei may provide insight. Nevertheless, these data provide interesting results amenable to further exploration.

## 4.4 Tungsten, Iridium and Palladium

To ascertain the wider application of azophosphines as ligands, their coordination chemistry with tungsten(0), palladium(II) and iridium(III) was explored. Tungsten(0) was chosen for the structural and electronic insights coordination would provide, and palladium(II) and iridium(III) for their relevance in catalysis. Section 4.4.1 and 4.4.3 discusses research conducted by Mark G. Butler[46] and Ellen M. Tait,[45] respectively, (MSci students, Jupp group, University of Birmingham) with supervision by the author.

### 4.4.1 Tungsten

Similarly to ruthenium(II), tungsten(0) is a $d^6$ metal centre. Displacement of cyclooctadiene (COD) in $W(CO)_4COD$ by $\kappa^2$*P,N* coordination of an azophosphine would form an octahedral complex in which both *P*-coordination and *N*-coordination would be *trans* to a CO ligand (Scheme 4.8).

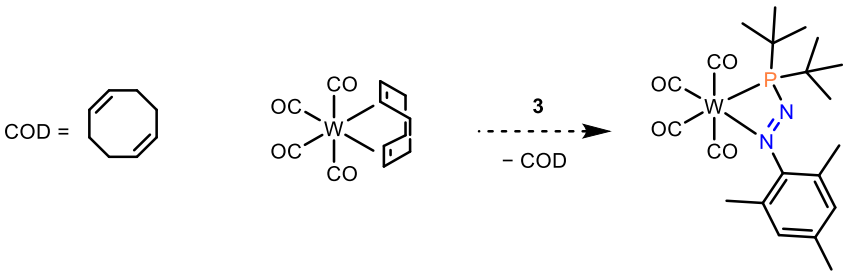


**Scheme 4.8.** Hypothesised $\kappa^2$*P,N* coordination in a $W(CO)_4$ complex by displacement of COD. COD = cyclooctadiene.

This would enable investigation of the donor abilities of P and N by measuring the Tolman electronic parameter, determined by measuring the frequency of the *trans* C–O vibrational mode (*ν*(CO)) by IR spectroscopy. A strongly electron-donating ligand increases the electron density on the metal, so weakening the C–O bond due to π back bonding and decreasing *ν*(CO).[12]

Reaction of $MesN_2P^tBu_2$ (**3**) with an equivalent of $W(CO)_4COD$ in chlorobenzene at 50 °C was very sluggish, and after 24 h there was incomplete conversion of **3** (118.3 ppm) to a signal with $^{183}W$ satellites at 139.6 ppm in the $^{31}P\{^1H\}$ NMR spectrum. Filtration through a silica plug, removal of volatiles and washing with hexane obtained a red powder. Single crystals suitable for single crystal X-ray diffraction revealed that **3** was coordinated to tungsten in a bis-monodentate fashion as $W(CO)_4(\kappa^1P\text{-}\mathbf{3})_2$ (**31**) (Figure 4.19).

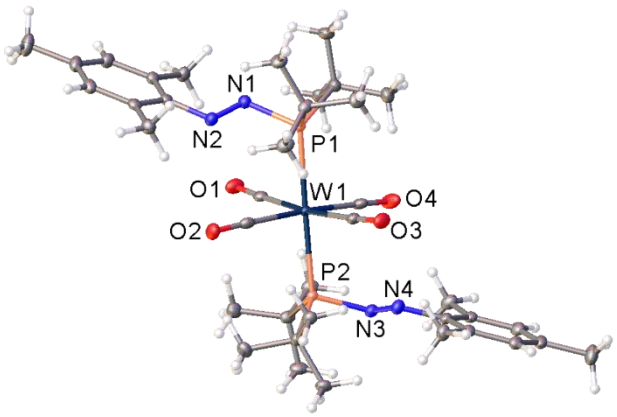


**31**

**Figure 4.19.** Single crystal of $W(CO)_4(\kappa^1P\text{-}\mathbf{3})_2$ (**31**). Selected bond distances (Å) and angles (°) are tabulated in Table 4.3. The structure contains three crystallographically-independent tungsten complexes with two being located on inversion centres, such that, for both of these complexes only half is crystallographically unique. Only one of the complexes is shown for clarity. Thermal ellipsoids were drawn at the 50% probability level. Single crystals of **31** grown by Mark Butler.

Heating the reaction for 3 days at 50 °C resulted in a second smaller signal with $^{183}W$ satellites at 139.2 ppm in the $^{31}P\{^1H\}$ NMR spectrum in addition to the signals assigned to **31** and incomplete coordination of **3**. When using a P,P type ligand, the COD ligand has been found to dissociate from tungsten stepwise by separate cleavage of each olefin bond.[61] Upon $\kappa^1P$ coordination of **3**, cleavage of the second olefin bond could be

driven by the ability of **3** to chelate by *N*-coordination, which, if slow, results in rearrangement to a *trans*-W(CO)$_4$(η$^2$-COD)(κ$^1$*P*-**3**) isomer and eventual displacement of COD by bis-monodentate coordination of **3** to give **31**. Repeating the reaction with azophosphine **12** (Z = OMe) and heating at 50 °C for 5 days obtained two new signals at 136.1 and 137.4 ppm with individual W satellites in the $^{31}$P{$^1$H} NMR spectrum. However, due to prolonged heating decomposition of **12** had also occurred which hindered isolation of the tungsten complexes in an appreciable yield to allow for further analysis.

As tabulated in Table 4.5, the bond lengths and angles within the two azophosphine ligands of bis-monodentate complex **31** show no significant difference in values.

**Table 4.5.** Selected bond distances (Å) and bond angles (°) of crystalllographically characterised W-azophosphine complex **31**

| Structure | P1–W1 | P2–W1 | P1–N1 | P2–N3 | N1–N2 | N3–N4 |
|---|---|---|---|---|---|---|
| **31**[a] | 2.4875(5) | 2.4908(5) | 1.7825(16) | 1.7821(15) | 1.249(2) | 1.250(2) |
| | 2.5019(5) | | 1.7664(16) | | | |
| | 2.5096(5) | | 1.7717(16) | | | |

| Structure | P1–N1–N2 | P2–N3–N4 |
|---|---|---|
| **31**[a] | 113.86(12) | 113.28(12) |
| | 116.53(13) | |
| | 116.07(13) | |

[a] Structure contains three crystallographically independent complexes with two being located on inversion centres, such that, for both of these complexes only half is crystallographica*l*ly unique. One representative value is provided if there is no statistically significant difference (3σ); values for each molecule are provided if there is a statistical difference.

The P1–N1–N2 bond angle differs by up to 2.67° between the three crystallographically independent complexes of **31**; however, significant deviations in torsion angle have previously been observed in structures which contain more than one

crystallographically independent molecule (Chapter 3, Section 3.3.1), thus this deviation in P1–N1–N2 bond angle can, again, likely be assigned to crystal packing effects.

Coordination of azophosphines **3** and **12** with W(0) was sluggish compared to the other metals discussed in this chapter (Ru(II), Au(I), Pd(II), Ir(III)). $W(CO)_4COD$ is a neutral complex in which the electron-withdrawing π-acidic carbonyl ligands contribute to the W(0) Lewis acidity rather than oxidation of its metal centre, thus rendering it less suitable for coordination by the weak P-donor azophosphines.

### 4.4.2 Palladium

Pd(II) compounds are often four-coordinate, square-planar complexes. 1,3-P,N ligands are known to coordinate in a $\kappa^2$*P,N* manner with ligand hemilability (*N*-release) induced by strong donors (Scheme 4.9).[62]

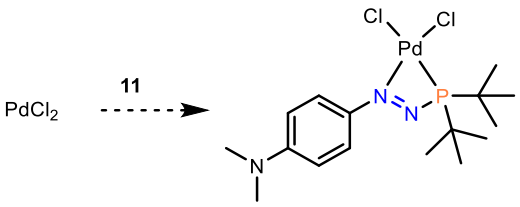


**Scheme 4.9.** Hypothesised $\kappa^2$*P,N* coordination of **11** to form a square-planar palladium complex.

Reaction of azophosphine **11** (Z = $NMe_2$) with an equivalent of $PdCl_2$ in chlorobenzene was monitored by $^{31}P\{^1H\}$ NMR spectroscopy. Full consumption of the free azophosphine (107.7 ppm) to a singlet at 90.0 ppm was observed along with several small impurities after 20 minutes of stirring at room temperature (Figure 4.20).

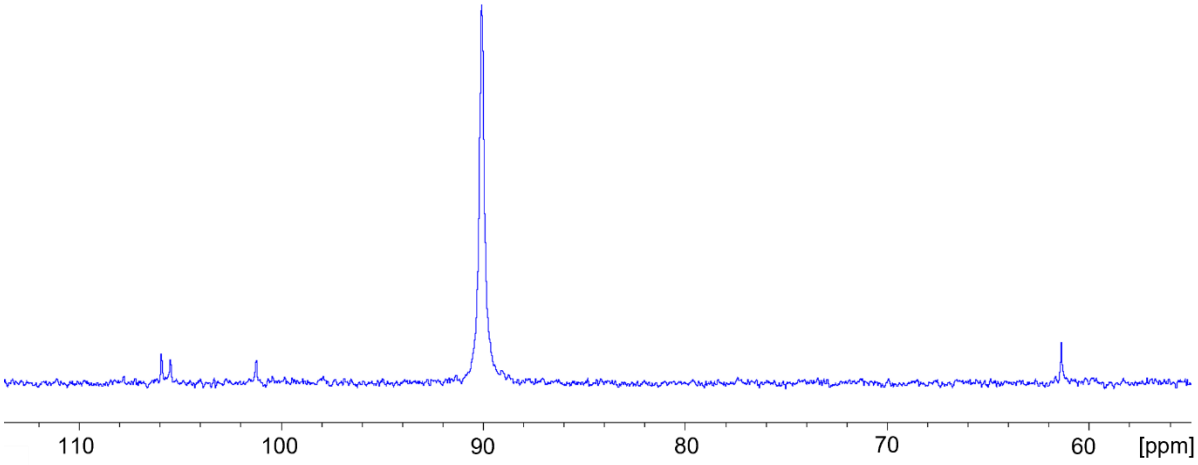


**Figure 4.20.** $^{31}P\{^{1}H\}$ NMR spectrum of an aliquot of reaction mixture following addition of **11** to $PdCl_2$ in chlorobenzene.

Without further purification, single crystals were grown by slow evaporation of chlorobenzene from the reaction mixture. Analysis by single crystal X-ray diffraction, however, revealed bis-monodentate coordination of **11** to palladium with an inversion centre in the *trans*-Pd($\kappa^1$*P*-**11**)$_2$Cl$_2$ complex (**32**) (Figure 4.21A). Multiple crystals were screened, and another unit cell was indexed. This revealed an unexpected decomposition product in which N=N cleavage had truncated one ligand **11** to (*p*-$NMe_2$)$C_6H_4NH_2$, now *N*-coordinated to palladium *via* $NH_2$ in the complex *trans*-Pd($\kappa^1$*P*-**11**)($\kappa^1$*N*-$NH_2C_6H_4$(*p*-$NMe_2$))$Cl_2$ (**33**) (Figure 4.21B). The mechanism of decomposition is unknown at this time. Further experiments to elucidate the potential role of intermediates and the presence of excess $PdCl_2$ in the reaction mixture due to the preferential bis-$\kappa^1$*P* coordination of **11** are required. No single crystals corresponding to the $\kappa^2$*P,N* coordination product of **11** were observed.

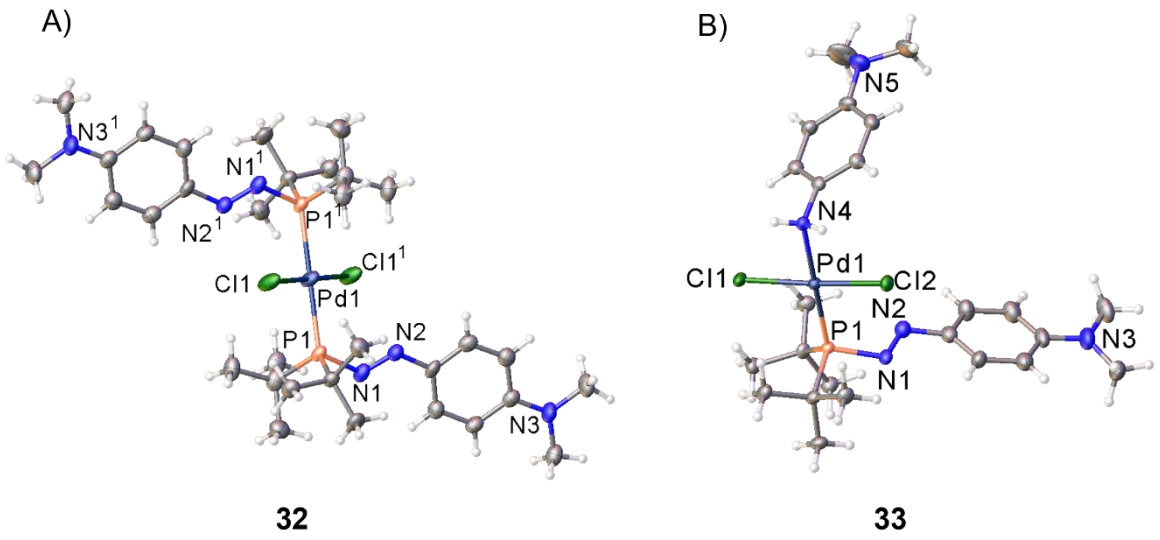


**Figure 4.21.** Single crystals of Pd-azophosphine complexes (A) Pd(κ¹*P*-**11**)₂Cl₂ (**32**); (B) Pd(κ¹*P*-**11**)(κ¹*N*-NH₂C₆H₄(*p*-NMe₂))Cl₂ (**33**). Selected bond distances (Å) and angles (°) are tabulated in Table 4.6. Thermal ellipsoids were drawn at the 50% probability level. The crystal structure of **32** contains an inversion centre at Pd1. The crystal of **33** was a two-component inversion twin with the refined ratio of the enantiomeric domains being 0.645(13):0.355(13). The hydrogen atoms bonded to N4 were located in the electron density and freely refined.

Truncated ligand (*p*-NMe₂)C₆H₄NH₂ is coordinated to Pd1 as a neutral ligand in **33** as the hydrogen atoms bonded to N4 were located in the electron density map and freely refined. Selected bond distances (Å) and angles (°) of **32** and **33** are tabulated in Table 4.6.

**Table 4.6.** Selected bond distances (Å) and bond angles (°) of crystalllographically characterised Pd-azophosphine complexes **32** and derivative **33**.

| Structure | P1–Pd1 | N4–Pd1 | P1–N1 | N1–N2 |
|---|---|---|---|---|
| **32** | 2.3551(17) | - | 1.750(6) | 1.254(9) |
| **33** | 2.2688(15) | 2.133(5) | 1.752(6) | 1.267(9) |

| Structure | P1–N1–N2 | P1–Pd1–N4 |
|---|---|---|
| **32** | 112.4(5) | - |
| **33** | 112.7(5) | 179.44(19) |

The P1–Pd1 bond length of **33** (2.2688(15) Å) is shorter than that of **32** (2.3551(17) Å) and can be assigned to the larger *trans* influence of the π-acceptor azophosphine ligand relative to the σ-only donating properties of the primary amine ligand.

No evidence of $\kappa^2$*P,N* coordination of **11** to $PdCl_2$ was found; however, it has been reported for $PPh_2Py$ ligands.[63,64] Chelation existed in a 'chelate-monodentate' mode to form the [Pd($\kappa^2$*P,N*-$PPh_2Py$)($\kappa^1$*P*-$PPh_2Py$)Cl][Cl] complex. It has been proposed that it is the *cis*-isomer of Pd($\kappa^1$*P*-$PPh_2Py)_2Cl_2$, and not the *trans*-isomer, which is involved in the chloride exchange process to form the 'chelate-monodentate' complex.[63] Interconversion between the *cis*- and *trans*-isomers were found to be temperature dependent, with the presence of the *cis*-isomer increasing with decreasing temperature. Addition of methanol to a dichloromethane suspension of *cis*-/*trans*-Pd($\kappa^1$*P*-$PPh_2Py)_2Cl_2$ at room temperature was reported to give the 'chelate-monodentate' complex in a distorted square-planar geometry. The highly strained, four-membered chelate ring had a P1–Pd1–N1 bond angle of 70.45(3)° and is a strong deviation from the ideal value of 90°. Analogous coordination of azophosphine **11** would likely give a bond angle that is shorter than this value, with stronger deviation from ideality, on account of the shorter covalent radius of the central nitrogen compared to carbon (as previously seen for the P1–Ru1–N2 bond angle in section 4.2.3). This, combined with the steric bulk of P–$^t$Bu$_2$ which may hinder *cis*-isomerisation, could preclude 'chelate-monodentate' coordination of **11** and be implicated in the formation of **33**. Variable temperature NMR experiments would be helpful to identify the presence of a *cis*-isomer of **32**, and addition of methanol, or a halide-extracting agent, to a solution of **32** could test for 'chelate-monodentate' coordination under forcing conditions.

### 4.4.3 Iridium

When coordinating to the chloro-Ru(II)(*p*-cymene) framework, exclusive $\kappa^1P$ coordination of azophosphines was observed, with $\kappa^2P,N$ coordination achieved only when using $NaBPh_4$ to abstract a chloride. Due to the higher oxidation number of iridium(III), it was considered whether spontaneous $\kappa^2P,N$ coordination could be achieved when coordinating to the chloro-Ir(III)(Cp*) framework (Cp*, pentamethylcyclopentadiene) (Scheme 4.10).

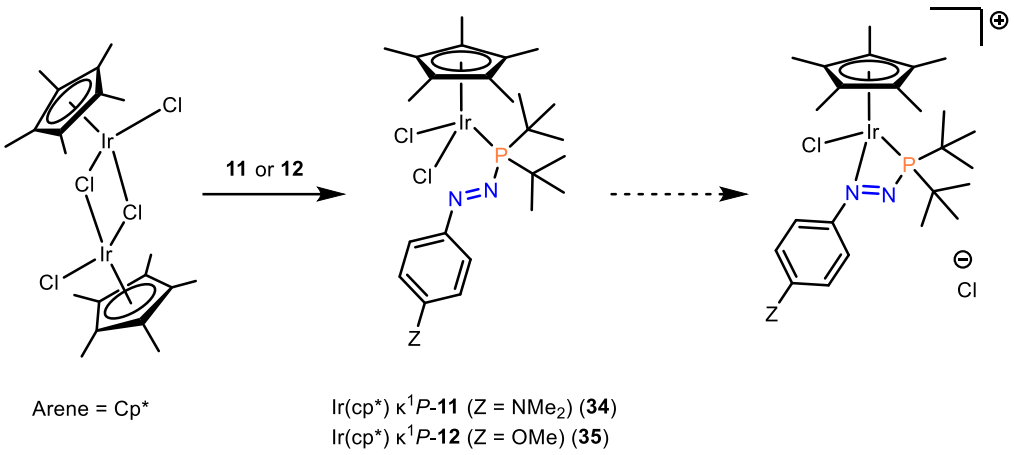


**Scheme 4.10.** Synthesis of Ir(Cp*)-azophosphine complexes Ir(Cp*)($\kappa^1P$-**11**)$Cl_2$ (**34**) and Ir(Cp*)($\kappa^1P$-**12**)$Cl_2$ (**35**) and hypothesised *N*-coordination to form $\kappa^2P,N$ complex. Cp* = pentamethylcyclopentadiene.

Reaction of azophosphine **11** (Z = $NMe_2$) with half an equivalent of the $[Ir(Cp^*)Cl_2]_2$ dimer in chlorobenzene at room temperature resulted in the immediate precipitation of a red solid. Analysis of the solution by $^{31}P\{^1H\}$ NMR spectroscopy revealed full conversion of **11** (107.7ppm) to singlets at 95.7 ppm and 85.6 ppm in a 1:2 ratio. Isolation and analysis of the red precipitate showed one peak at 85.6 ppm in the $^{31}P\{^1H\}$ NMR spectrum. Single crystals suitable for analysis by single crystal X-ray diffraction revealed this was the $\kappa^1P$ complex Ir(Cp*)($\kappa^1P$-**11**)$Cl_2$ (**34**) (Figure 4.22A). The singlet at 95.7 ppm is therefore tentatively assigned to a $\kappa^1N$ coordination complex as, similarly

to that seen with coordination to ruthenium, κ$^2$*P,N* coordination would be expected upfield to the κ$^1$*P* complex at 85.6 ppm. Heating a solution of **34** overnight (16 h) at 50 °C to encourage κ$^2$*P,N* coordination was unsuccessful, resulting in multiple peaks in the $^{31}$P{$^1$H} NMR spectrum.

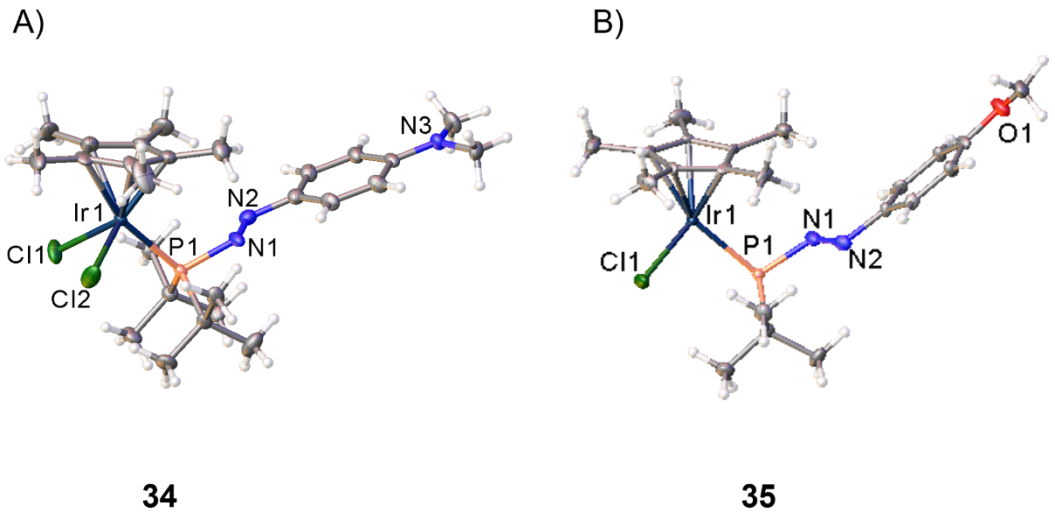


**34** **35**

**Figure 4.22.** Single crystal structures of Ir-azophosphine complexes (A) Ir(κ$^1$*P*-**11**)Cl$_2$ (**34**); (B) Ir(κ$^1$*P*-**12**)Cl$_2$ (**35**). Selected bond distances (Å) and bond angles (°) are tabulated in Table 4.7. The structure of **35** is sitting on a mirror plane running through Ir1 and P1. The Cp* and $N_2C_6H_4OCH_3$ fragments are disordered across the mirror plane at 50% occupancy by symmetry. Only one of each of the disordered fragments are shown for clarity. Thermal ellipsoids for **34** and **35** drawn at the 50% probability level. Single crystals of **35** were grown by Ellen Tait.

To promote κ$^2$*P,N* coordination, $NaBPh_4$ was added to a chlorobenzene solution of **11** and $[Ir(Cp^*)Cl_2]_2$ dimer resulting in precipitation of an off-white solid. Filtration and removal of solvent *in vacuo* obtained a reddish-pink solid which, when analysed by $^{31}$P{$^1$H} NMR spectroscopy, showed a clean, upfield shift to 43.0 ppm, indicative of κ$^2$*P,N* coordination. Repeating the synthesis with azophosphine **12** resulted in no precipitate; however, removal of solvent and analysis by $^{31}$P{$^1$H} NMR spectroscopy revealed full conversion of **12** to a singlet at 89.8 ppm, as expected for κ$^1$*P* coordination. This was again corroborated by single crystal X-ray diffraction as

Ir(Cp*)(κ$^1$*P*-**12**)Cl$_2$ (**35**) (Figure 4.22B). Surprisingly, addition of NaBPh$_4$ to chlorobenzene solutions of **12** and [Ir(Cp*)Cl$_2$]$_2$ dimer to access κ$^2$*P,N* coordination were not successful, resulting in complex $^{31}$P{$^1$H} NMR spectra. Analysis of the crystallographic data tabulated in Table 4.7 reveal no significant difference in values due to modulating Z from NMe$_2$ to OMe in **34** and **35**, respectively. This could be a result of the larger standard deviations associated with the crystallographic data of **35**; however, a rationale is also provided by the similar mesomeric effect and electron-donating properties of Z in **34** and **35**.

**Table 4.7.** Selected bond distances (Å) and bond angles (°) of crystalllographically characterised Ir-azophosphine complexes **34** and **35**.

| Structure | P1–Ir1 | P1–N1 | N1–N2 |
|---|---|---|---|
| **34** | 2.3492(10) | 1.748(4) | 1.232(6) |
| **35** | 2.353(2) | 1.749(12) | 1.259(14) |

| Structure | P1–N1–N2 |
|---|---|
| **34** | 118.2(4) |
| **35** | 120.0(8) |

## 4.5 Conclusion

This chapter discussed the application of azophosphines as ligands, encouraged by the availability of the phosphorus lone pair that was identified in Chapter 3. Selective κ$^1$*P* and controlled κ$^2$*P*,*N* coordination to Ru(II) was demonstrated (Figure 4.23A and B, respectively), in stark contrast to the triazene analogues (Figure 4.1). The P1–Ru1–N2 bite angles of the crystallographically-characterised κ$^2$*P*,*N* complexes were found to be significantly shorter than those of prior Ru complexes of 1,3-P,N ligands, highlighting a key difference between the shorter covalent radius of the central nitrogen atom compared to carbon. It was previously discussed that the donor strength of

azophosphines can be fine-tuned with the more electron-donating *N*-aryl substituents giving stronger azophosphine donors. This finding was borne out in the study on the effect of Z on κ$^2$*P*,*N* coordination, where the stronger donors afforded the bidentate [Ru(*p*-cymene)(κ$^2$*P*,*N*-(**11**–**16**))Cl][BPh$_4$] complexes more cleanly. Steric bulk in the *ortho*-positions of the *N*-aryl group of azophosphines inhibited N coordination to Ru required to form a bidentate complex. These experimental observations were corroborated by computational calculations. Selective κ$^1$*P* and controlled μ*P,N* coordination to Au(I) was demonstrated to give mononuclear and binuclear complexes, respectively (Figure 4.23A and D, respectively), and a brief exploration of the coordination chemistry of azophosphines to W(0) and Pd(II) revealed bis-κ$^1$*P* coordination (Figure 4.23C), and to Ir(III) revealed κ$^1$*P* coordination (Figure 4.23A).

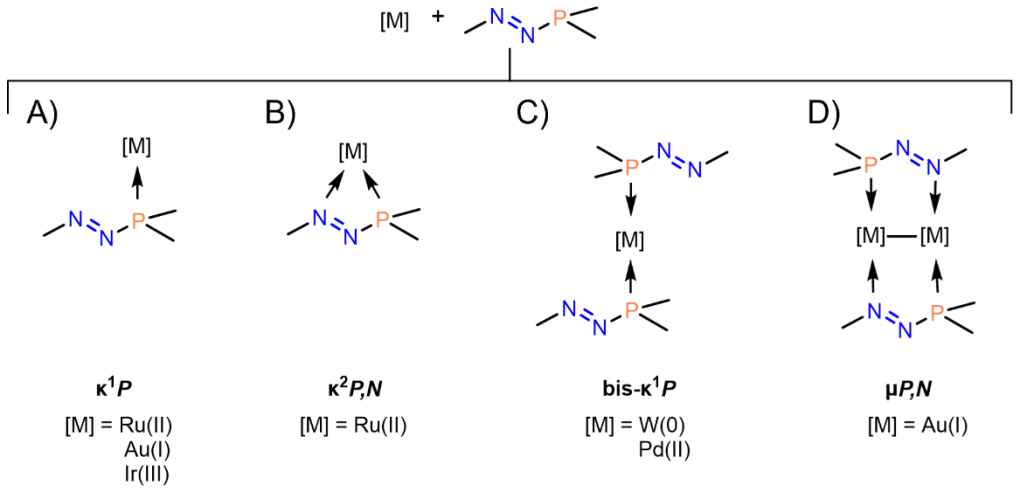


**Figure 4.23.** Coordination modes demonstrated by azophosphines (A) κ$^1$*P*; (B) κ$^2$*P,N*; (C) bis-κ$^1$*P*; (D) μ*P,N*.

Significant differences in UV/Vis absorption spectra prior and post irradiation at 365 and 400 nm for Ru complexes **26** and **27**, respectively, were observed; however, the spectra did not return to their pre-irradiation profile indicating decomposition, rather than photoisomerization, was likely to have occurred. More compelling evidence of

photo-switching was provided from irradiation of Au complex **29** at 365 nm, after which, changes in the UV/Vis spectrum were observed that were comparable to those observed in a UV/Vis spectrum of azobenzene post irradiation. Although the UV/Vis spectrum did not return to its pre-irradiation profile, unlike Ru complexes **25** and **26**, there was no evidence of decomposition of **29** following analysis by $^{31}P\{^{1}H\}$ NMR spectroscopy.

It has been shown that the replacement of the tri-coordinate nitrogen centre in triazenes with a phosphorus atom to yield azophosphines has a dramatic consequence for the ligand properties. Azophosphines can be considered a new member of the family of 1,3-P,N ligands that have a bridging N atom, rather than C atom, between the P and N sites. The application of the Ru and Au complexes in catalysis is discussed in the following chapter.

## 4.6 Experimental

Except as otherwise noted, the syntheses of **23** - **35** were performed using standard Schlenk line technique under a flow of dry, oxygen-free nitrogen, or an MBraun ECO glovebox under an atmosphere of dry, oxygen-free nitrogen with water and oxygen levels maintained at <0.1 ppm.

Room temperature (RT) refers to reactions where no thermostatic control was applied and the temperature was recorded as 16–25 °C. Unless otherwise stated, overnight reactions refer to a period of 16 h. All glassware and Teflon-coated stirrer bars were dried in an 80 °C oven overnight prior to use. All molecular sieves are 3 Å and purchased from VWR chemicals and were activated by heating at 400 °C under vacuum prior to use. Unless otherwise stated, degassing refers to three freeze-pump-thaw cycles.

Commercial reagents were purchased, suitably stored as specified by the supplier, and used as received, unless otherwise stated, from Sigma-Aldrich (sodium tetraphenylborate, ≥99.5%; di-μ-chlorobis(benzene)chlororuthenium(II), stored and handled in the glovebox; palladium(II) chloride, 99.9%, stored and handled in the glovebox; tetracarbonyl(1,5-cyclooctadiene)tungsten(0), stored and handled in the glovebox; silver hexafluoroantimonate(V), 98%, stored and handled in the glovebox), Acros Organics (di-μ-chlorobis(*p*-cymene)chlororuthenium(II), 98%, stored and handled in the glovebox; dichloro(pentamethylcyclopentadienyl)iridium(III) dimer, 99%, stored and handled in the glovebox; potassium tetrachloroaurate(III), 98%) or Alfa Aesar (dimethyl sulfide, 99+%). Solvents were purchased and used as received, unless otherwise stated, from Sigma-Aldrich (hexane, puriss, p.a., ACS reagent, reag.

Ph. Eur., 99+ (GC), degassed and stored in air-tight ampoules over 3 Å molecular sieves; chloroform-*d*, 99.8 atom % D, dried by overnight reaction with $CaH_2$, degassed and stored in an air-tight ampoule over 3 Å molecular sieves; dichloromethane-$d_2$, 99.5 atom % D, dried by overnight reaction with $CaH_2$, degassed and stored in an air-tight ampoule over 3 Å molecular sieves; bromobenzene-$d_5$, 99.5 atom % D), Fisher Scientific (dichloromethane (DCM), 99.8%, HPLC grade) or Acros Organics (chlorobenzene, 99.6%, ACS reagent, degassed and stored in an air-tight ampoule over 3 Å molecular sieves). Deionised water was obtained from an Elga DV35 Purelab.

All NMR spectra were collected on a Bruker 500 MHz AV_NEO Avance NMR Spectrometer or a Bruker 400 MHz AV_NEO Avance NMR Spectrometer. Chemical shifts are reported in ppm, coupling constants (*J*) are reported in Hz. $^{1}H$ and $^{13}C\{^{1}H\}$ NMR spectra were referenced internally to the most up-field solvent peak; $^{31}P$ and $^{31}P\{^{1}H\}$ NMR spectra are externally referenced to 85% $H_3PO_4$; $^{11}B\{^{1}H\}$ NMR spectra are externally referenced to $BF_3.OEt_2$.

All UV/Vis absorption spectra were collected on a Cary50 UV/Vis Spectrometer. The samples were prepared as 50 mM solutions in toluene to a volume of 3 mL and irradiated in a quartz glass High Precision Cell cuvette (10 x 10 mm) from Hellma Analytics. Air-sensitive UV-Vis samples were collected using a sealable cuvette, with solutions made up in the glovebox.

All IR spectra were collected on a Perkin Elmer Spectrum Two FT-IR spectrometer using attenuated total reflection (ATR) sampling technique.

All mass spectra were collected on a Waters Xevo G2-XS TOF mass spectrometer using electrospray ionisation (ESI) positive ion mode or atmospheric solids analysis

probe (ASAP) with atmospheric pressure ionisation positive ion mode. Using ESI, samples were dissolved in dry acetonitrile and directly injected into the ESI ionisation chamber via a 250 µL glass syringe. Using ASAP, samples were run neat by dipping a glass capillary into the sample vial, before insertion into the ASAP source.

Single-crystal X-ray diffraction data were collected at 100 K on an Agilent SuperNova A diffractometer using an Atlas detector, using Cu-Kα radiation (λ = 1.54184). The data collections were driven and processed, and absorption corrections were applied using CrysalisPro.[65] Using OLEX2[66] the structures were solved using SHELXT[67] and were refined by a full-matrix least-squares procedure on $F^2$ in SHELXL.[68] All non-hydrogen atoms were refined with anisotropic displacement parameters.

### 4.6.1 General Procedure for Synthesis of κ$^1$*P* Ru Coordination Complexes (GP9)

$RN_2P^tBu_2$ (1 equiv.) was added to a 25 mL round-bottomed Schlenk flask and dissolved in chlorobenzene. To this solution, $[Ru(arene)Cl_2]_2$ (0.5 equiv.) was added, and the mixture stirred at room temperature overnight (16 h). Dropwise addition to hexane gave a dark brown precipitate. This was collected by filtration, washed with further hexane, and dried *in vacuo* to exclusively obtain the κ$^1$*P* complex as a dark brown solid. The complexes were stored in vials in the glovebox freezer.

**Ru(*p*-cymene)$Cl_2$(κ$^1$*P*-3) (23)**

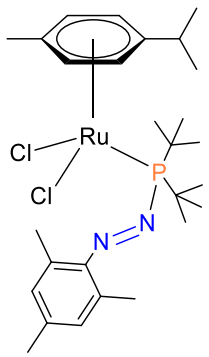

Coordination complex **23** was synthesised from azophosphine **3** (0.52 mmol, 150 mg, 2.0 equiv.) according to GP9. The reaction was stirred at room temperature overnight (16 hours) resulting in a colour change from dark red to dark reddish-brown. Isolation of **23** was achieved as a dark brown powder (0.10 mmol, 60 mg, 77%). The flask was then rinsed with $CD_2Cl_2$ to prepare an NMR sample. Single crystals of **23** suitable for single-crystal X-ray diffraction were grown by slow evaporation of a chlorobenzene solution of the product at room temperature. $^{1}H$ (500.1 MHz, $CD_2Cl_2$, 298 K): δ 7.09 (s, 2H; $H_{Ar}$ (Mes)), 5.34 (d, $^{3}J_{H–H}$ = 6 Hz, 2H; $H_{Ar}$ (*p*-cymene)), 5.10 (d, $^{3}J_{H–H}$ = 6 Hz, 2H; $H_{Ar}$ (*p*-cymene)), 2.84 (sept., $^{3}J_{H–H}$ = 7 Hz, 1H; C$H$($CH_3$)$_2$ (*p*-cymene)), 2.65 (s, 6H; *o*-$CH_3$ (Mes)), 2.39 (s, 3H; *p*-C$H_3$ (Mes)), 2.05 (s, 3H; *p*-C$H_3$ (*p*-cymene)), 1.51 (d, $^{3}J_{H–P}$ = 13 Hz, 18H; $^{t}$Bu)), 1.06 (d, $^{3}J_{H–H}$ = 7 Hz, 6H; CH(C$H_3$)$_2$ (*p*-cymene)). $^{13}C\{^{1}H\}$ (125.8 MHz): δ 148.3 (d, $^{3}J_{C–P}$ = 31 Hz; *i*-$C_{Ar}$ (Mes)), 143.4 (s; *p*-$C_{Ar}$ (Mes)), 134.5 (s; *o*-$C_{Ar}$ (Mes)), 131.8 (s; *m*-$C_{Ar}$ (Mes)), 105.9 (s; *i*-$C_{Ar}$ (*p*-cymene)), 97.4 (s; *p*-$C_{Ar}$ (*p*-cymene)), 88.0 (s; *m*-$C_{Ar}$ (*p*-cymene)), 87.7 (s; *o*-$C_{Ar}$ (*p*-cymene)), 41.5 (d, $^{1}J_{C–P}$ = 8 Hz; $C(CH_3)_3$), 30.6 (br. s; C($CH_3$)$_3$), 29.9 (s; $CH(CH_3)_2$), 22.5 (s; *o*-$CH_3$ (Mes)), 21.9 (s; CH($CH_3$)$_2$), 21.5 (s; *p*-$CH_3$ (Mes)), 17.7 (s; *p*-$CH_3$ (*p*-cymene)). $^{31}P\{^{1}H\}$ (202.4 MHz, $CD_2Cl_2$): δ 121.7 (s). $^{31}P$ (202.4 MHz, $CD_2Cl_2$): δ 121.7 (br. m). UV-Vis (DCM, nm) $\lambda_{max}$: 323 (s); 400-650 (w, br.) ESI-HRMS m/z for $C_{27}H_{43}Cl_2N_2PRu$ $[M-Cl]^+$: calcd (found) 568.1926 (568.1915), 567.1980 (567.1892), 566.1927 (566.1927), 565.1898 (565.1897), 564.1917 (564.1913), 563.1901 (563.1900), 562.1911 (562.1909), 561.1906 (561.1906), 560.1912 (560.1914), 559.1909 (559.1908), 557.1926 (557.1929). IR: $\nu_{max}$ ($cm^{-1}$) 3041 (w), 2965 (w), 2916 (w), 1607 (w) (N=N).

**Ru(benzene)$Cl_2$($\kappa^1$*P*-11) (24)**

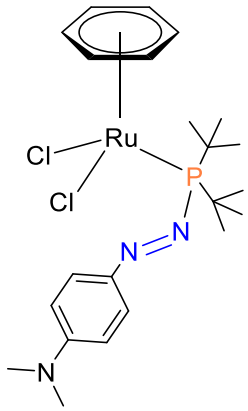


Coordination complex **24** was synthesised from azophosphine **11** (0.17 mmol, 50 mg, 1.0 equiv.) according to GP9. The reaction was stirred at room temperature for 3 hours, resulting in a colour change from dark red to dark reddish-brown. Isolation of **24** was achieved as a dark brown powder (0.12 mmol, 36 mg, 72%). The flask was then rinsed with bromobenzene-$d_5$ to prepare an NMR sample. Single crystals of **24** suitable for single-crystal X-ray diffraction were grown by slow evaporation of a DCM solution of the product at −35°C. $^1$H (400.1 MHz, bromobenzene-$d_5$, 298 K): δ 7.73 (d, $^1J_{H–H}$ = 9 Hz, 2H; $H_{Ar}$), 6.47 (d, $^1J_{H–H}$ = 9 Hz, 2H; $H_{Ar}$), 5.23 (s, 6H; $H_A$), 2.67 (s, 6H; *p*-N(C$H_3$)$_2$), 1.56 (d, $^1J_{H–P}$ = 13 Hz, 18H; $^t$Bu). $^{13}$C{$^1$H} (100.6 MHz, bromobenzene_$d_5$): δ 153.3 (s; *p*-$C_{Ar}$), 145.2 (d, $^3J_{C–P}$ = 34 Hz; *i*-$C_{Ar}$), 124.5 (s; $C_{Ar}$), 111.5 (s; $C_{Ar}$) 87.2 (d, $^2J_{C–P}$ = 3 Hz; $C_6H_6$), 42.1 (d, $^1J_{C–P}$ = 10 Hz; C($C$H$_3$)$_3$), 40.0 (s; *p*-N($C$H$_3$)$_2$), 30.5 (s; $^t$Bu). $^{31}$P{$^1$H} (162.0 MHz, bromobenzene_$d_5$): δ 111.9 (s). $^{31}$P (162.0 MHz, bromobenzene_$d_5$): δ 111.9 (m). UV-Vis (DCM, nm) $\lambda_{max}$: 425 (s), 550-650 (w, br.). ESI-HRMS m/z for $C_{22}H_{34}Cl_2N_3PRu$ $[M-Cl]^+$: calcd (found) 502.1255 (502.1255), 504.1233 (504.1229), 505.1240 (505.1245), 506.1230 (506.1234). IR: $\nu_{max}$ (cm$^{-1}$) 3067 (w), 2956 (w), 2900 (w), 2864 (w), 1598 (m) (N=N).

**Ru(*p*-cymene)$Cl_2$($\kappa^1$*P*-12) (26)**

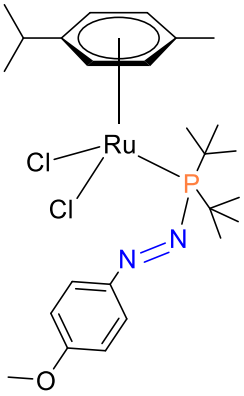


Coordination Complex **26** was synthesised from azophosphine **12** (0.14 mmol, 40 mg, 1.0 equiv.) according GP9. The reaction was stirred at room temperature for 3 h, resulting in a colour change from dark red to dark reddish-brown. Isolation of **26** was achieved as a dark brown powder (53 mg, 64%). The flask was then rinsed with $CD_2Cl_2$ to prepare an NMR sample. Single crystals of **26** suitable for single-crystal X-ray diffraction were grown from a saturated chlorobenzene solution of the product at −35 °C. $^1$H (400.1 MHz, $CD_2Cl_2$, 298 K): δ 7.92 (d, $^3J_{H–H}$ = 9 Hz, 2H; $H_{Ar}$ (*p*-anisyl)), 7.10 (d, $^3J_{H–H}$ = 9 Hz, 2H; $H_{Ar}$ (*p*-anisyl)), 5.41 (d, $^3J_{H–H}$ = 6 Hz, 2H; $H_{Ar}$ (*p*-cymene)), 5.18 (d, $^3J_{H–H}$ = 6 Hz, 2H; $H_{Ar}$ (*p*-cymene)), 3.93 (s, 3H; *p*-OC$H_3$), 2.86 (sept., $^3J_{H–H}$ = 7 Hz, 1H; C$H$($CH_3$)$_2$ (*p*-cymene)), 2.07 (s, 3H; *p*-C$H_3$ (*p*-cymene)), 1.50 (d, $^3J_{H–P}$ = 13 Hz, 18H; $^t$Bu), 1.05 (d, $^3J_{H–H}$ = 7 Hz, 6H; CH(C$H_3$)$_2$ (*p*-cymene)). $^{13}$C{$^1$H} (100.6 MHz, $CD_2Cl_2$): δ 164.0 (s; *p*-$C_{Ar}$ (*p*-anisyl)), 148.3 (d, $^3J_{C–P}$ = 33 Hz; *i*-$C_{Ar}$ (*p*-anisyl)), 124.4 (s; *m*-$C_{Ar}$ (*p*-anisyl)), 115.0 (s; *o*-$C_{Ar}$ (*p*-anisyl)), 105.7 (s; *i*-$C_{Ar}$ (*p*-cymene)), 97.7 (s; *p*-$C_{Ar}$ (*p*-cymene)), 88.0 (s; *o*-$C_{Ar}$ (*p*-cymene)), 87.6 (s; *m*-$C_{Ar}$ (*p*-cymene)), 56.2 (s; *p*-O$CH_3$), 42.1 (d, $^1J_{C–P}$ = 8 Hz; $C$($CH_3$)$_3$), 30.6 (s; C($CH_3$)$_3$), 29.6 (s; $CH$($CH_3$)$_2$), 21.8 (s; C($CH_3$)$_2$), 17.7 (s; *p*-$CH_3$ (*p*-cymene)). $^{31}$P{$^1$H} (161.7 MHz, $CD_2Cl_2$): δ 115.2 (s). $^{31}$P (161.7 MHz, $CD_2Cl_2$): δ 115.2 (br. m).: 340 (s), 400-600 (w). ESI-HRMS m/z for $C_{25}H_{39}ClN_2OPRu$

$[M-Cl]^+$: calcd (found) 556.1551 (556.1551), 555.1526 (555.1527), 554.1563 (554.1568), 553.1533 (553.1539). UV-Vis (DCM, nm) $\lambda_{max}$: 340 (s), 400-600 (w, br.). IR ($cm^{-1}$) $\nu_{max}$: 3035 (w), 2967 (w), 2838 (w), 1597 (m, N=N). Elemental Analysis: calcd (found) C% 51.19 (51.00), H% 6.70 (6.63), N% 4.78 (4.79).

### 4.6.2 General Procedure for Synthesis of κ²*P,N* Ru Coordination Complexes (GP10)

$RN_2P^tBu_2$ (1.0 equiv.) was added to a 25 mL round-bottomed Schlenk flask and dissolved in chlorobenzene. To this solution, $[Ru(arene)Cl_2]_2$ (0.5 equiv.) was added, and the mixture stirred at room temperature for 3 h. Addition of $NaBPh_4$ (1.0 equiv.) gave a dark brown precipitate, and extraction into DCM left behind a white precipitate (NaCl). Removal of DCM *in vacuo* isolated the κ²-*P,N* complex as a dark brown solid, which was stored in a vial in the glovebox freezer.

**Ru(benzene)Cl(κ²*P,N*-11) (25)**

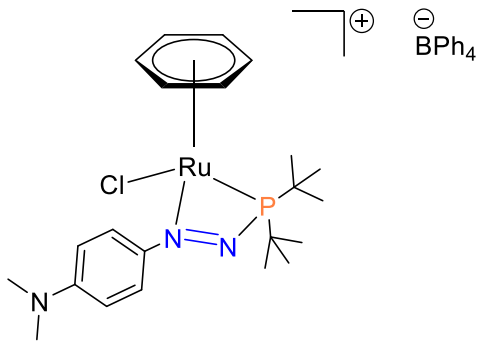


Coordination complex **25** was synthesised from azophosphine **11** (0.05 mmol, 16.0 mg, 1.0 equiv.) according to GP10. The reaction was stirred at room temperature for 3 h, resulting in a colour change from dark red to dark reddish-brown. Addition of $NaBPh_4$ (1 equiv.) gave full conversion from the κ¹-*P* complex to the corresponding κ²-*P,N* complex. Isolation of **25** was achieved as a dark brown powder (0.04 mmol, 13.0 mg,

81%). The flask was then rinsed with $CD_2Cl_2$ to prepare an NMR sample. Single crystals of **25** suitable for single-crystal X-ray diffraction were grown by slow evaporation of a chlorobenzene solution of the product at −35°C. $^1$H (400.1 MHz, $CD_2Cl_2$, 298 K): δ 7.80 (m, 2H; *m*-$H_{Ar}$ (*p*-(N(CH$_3$)$_2$)Ph), 7.37-7.23 (m; $H_{Ar}$ (BPh$_4$)), 7.01-6.97 (m, 8H; $H_{Ar}$ (BPh$_4$)), 6.87-6.83 (m, 4H; $H_{Ar}$ (BPh$_4$), 6.70 (m, 2H; *o*-$H_{Ar}$ (*p*-(N(CH$_3$)$_2$)Ph), 5.68 (s, 6H; $C_6H_6$), 3.19 (s, 6H; *p*-(N(C$H_3$)$_2$), 1.56 (d, $^3J_{H-P}$ = 16 Hz, 9H; $^t$Bu), 1.43 ($^3J_{H-P}$ = 15 Hz, 9H; $^t$Bu). $^{13}$C{$^1$H} (125.8 MHz, $CD_2Cl_2$): δ 165.0-163.8 (q, $^1J_{C-B}$ = 50 Hz; *i*-$C_{Ar}$ (BPh$_4$)), 164.4 (d, $^3J_{C-P}$ = 5 Hz; *i*-$C_{Ar}$ (*p*-(N(CH$_3$)$_2$)Ph)), 156.6 (s; *p*-$C_{Ar}$ (*p*-N(CH$_3$)$_2$Ph), 136.3 (br. s; *m*-$C_{Ar}$ (BPh$_4$)), 127.0 (s; *m*-$C_{Ar}$ (*p*-N(CH$_3$)$_2$Ph)), 126.1 (br. q; $^2J_{C-B}$ = 3 Hz; *o*-$C_{Ar}$ (BPh$_4$)), 122.2 (s; *p*-$C_{Ar}$ (BPh$_4$)), 112.2 (s; *o*-$C_{Ar}$ (*p*- N(CH$_3$)$_2$Ph)), 89.5 (d, $^2J_{C-P}$ = 2 Hz; $C_6H_6$), 43.1 (d, $^1J_{C-P}$ = 13 Hz; $C$(CH$_3$)$_3$), 41.1 (s; *p*-N(C$H_3$)$_2$)), 41.0 (s; $C$(CH$_3$)$_3$), 31.4 (d, $^2J_{C-P}$ = 4 Hz, C($C$H$_3$)$_3$), 28.7 (br. s; C($C$H$_3$)$_3$). $^{31}$P{$^1$H} (162.0 MHz, $CD_2Cl_2$): δ 58.0 (s). $^{31}$P (162.0 MHz, $CD_2Cl_2$): δ 58.0 (m). $^{11}$B{$^1$H} (128.4 MHz, $CD_2Cl_2$): δ −6.6 (s). UV/Vis (DCM, nm) $\lambda_{max}$: 509 (s). ESI-HRMS m/z for $C_{22}H_{34}ClN_3PRu$ $[M]^+$: calcd (found) 502.1255 (502.1255), 504.1233 (504.1225), 505.1240 (505.1243), 506.1230 (506.1231), 507.1234 (507.1235), 508.1225 (508.1233), 509.1236 (509.1238), 510.1222 (510.1229), 511.1252 (511.1255), 512.1214 (512.1217), 513.1238 (513.1227). ESI-HRMS m/z for $C_{24}H_{20}B$ $[M]^-$: calcd (found) 318.1694 (318.1696), 319.1662 (319.1683), 320.1694 (320.1692), 321.1727 (321.1720). IR: $\nu_{max}$ (cm$^{-1}$) 3057 (w, br), 1600 (m) (N=N).

**Ru(*p*-cymene)Cl(κ²*P,N*-12) (27)**

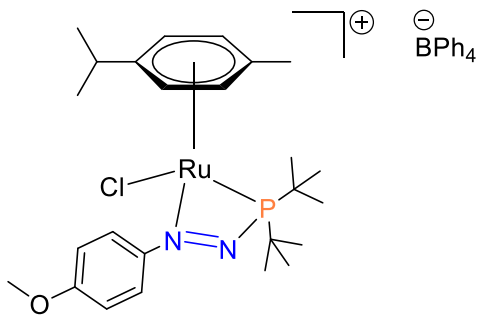


Coordination complex **27** was synthesised from azophosphine **12** (0.29 mmol, 81 mg, 1.0 equiv.) according to GP10. The reaction was stirred at room temperature for 3 h, resulting in a colour change from dark red to dark reddish-brown. Addition of $NaBPh_4$ (1 equiv.) gave full conversion from the κ¹-*P* complex to the corresponding κ²-*P,N* complex. Isolation of **27** was achieved as a dark brown powder (180 mg, 71%). The flask was then rinsed with $CD_2Cl_2$ to prepare an NMR sample. Single crystals of **27** suitable for single-crystal X-ray diffraction were grown from a saturated chlorobenzene solution of the product at −35 °C. $^1$H (400.1 MHz, $CD_2Cl_2$, 298 K): δ 7.87 (d, $^3J_{H–H}$ = 9 Hz, 2H; *m*-$H_{Ar}$ (*p*-anisyl)), 7.38-7.26 (m, 8H; $H_{Ar}$ ($BPh_4$)), 7.02 (d, 2H; *o*-C$H_3$ (*p*-anisyl)), 7.02-7.00 (m, 8H; $H_{Ar}$ ($BPh_4$)), 6.88 (t, $^3J_{H–H}$ = 7 Hz, 4H; *p*-$H_{Ar}$ ($BPh_4$)), 5.97 (d, $^3J_{H–H}$ = 6 Hz, 1H; $H_{Ar}$ (*p*-cymene)), 5.92 (d, $^3J_{H–H}$ = 6 Hz, 1H; $H_{Ar}$ (*p*-cymene)), 5.86 (d, $^3J_{H–H}$ = 6 Hz, 1H; $H_{Ar}$ (*p*-cymene)), 5.36 (d, $^3J_{H–H}$ = 6 Hz, 1H; $H_{Ar}$ (*p*-cymene)), 3.92 (s, 3H; *p*-OC$H_3$ (*p*-anisyl)), 1.80 (s, 3H; *p*-$CH_3$ (*p*-cymene)), 1.58 (d, $^3J_{H–P}$ = 16 Hz, 9H; $^t$Bu), 1.49 (d, $^3J_{H–P}$ = 15 Hz, 9H; $^t$Bu), 1.25 (d, $^3J_{H–H}$ = 7 Hz, 3H; CH(C$H_3$)$_2$ (*p*-cymene)), 1.15 (d, $^3J_{H–H}$ = 7 Hz, 3H; CH(C$H_3$)$_2$ (*p*-cymene)). $^{13}$C{$^1$H} (125.8 MHz, $CD_2Cl_2$): δ 167.0 (s; *p*-$C_{Ar}$ (*p*-anisyl)), 164.4 (q, $^1J_{C–B}$ = 50 Hz; *i*-$C_{Ar}$ ($BPh_4$)), 148.8 (d, $^3J_{C–P}$ = 23 Hz; *i*-$C_{Ar}$ (*p*-anisyl)), 136.3 (br. q, $^3J_{C–B}$ = 1 Hz; *m*-$C_{Ar}$ ($BPh_4$)), 126.7 (d, $^5J_{C–P}$ = 1 Hz; *m*-$C_{Ar}$ (*p*-anisyl)), 126.0 (q, $^2J_{C–B}$ = 3 Hz; *o*-$C_{Ar}$ ($BPh_4$)), 122.2 (s; *p*-$C_{Ar}$ ($BPh_4$)), 115.3 (s; *o*-$C_{Ar}$

(*p*-anisyl)), 107.6 (s; *i*-$C_{Ar}$ (*p*-cymene)), 102.7 (s; *p*-$C_{Ar}$ (*p*-cymene)), 98.6 (d, $^{2}J_{C-P}$ = 3 Hz, $C_{Ar}$ (*p*-cymene)), 89.9 (d, $^{2}J_{C-P}$ = 7 Hz; $C_{Ar}$ (*p*-cymene)), 89.2 (s; $C_{Ar}$ (*p*-cymene)), 86.0 (d, $^{2}J_{C-P}$ = 3 Hz; $C_{Ar}$ (*p*-cymene)), 56.9 (s; *p*-$OCH_3$ (*p*-anisyl)), 42.9 (d, $^{1}J_{C-P}$ = 4 Hz; $C(CH_3)_3$), 42.2 (d, $^{1}J_{C-P}$ = 10 Hz; $C(CH_3)_3$), 31.6 (s; $C(CH_3)_2$ (*p*-cymene)), 31.4 (d, $^{2}J_{C-P}$ = 4 Hz; $C(CH_3)_3$), 28.9 (d, $^{1}J_{C-P}$ = 3 Hz; $C(CH_3)_3$), 23.0 (s; $C(CH_3)_2$ (*p*-cymene)), 22.3 (s; $C(CH_3)_2$ (*p*-cymene)), 18.8 (s; *p*-$CH_3$ (*p*-cymene)). $^{31}P\{^{1}H\}$ (162.0 MHz, $CD_2Cl_2$): δ 67.4 (s). $^{31}P$ (202.4 MHz, $CD_2Cl_2$): δ 67.4 (m). $^{11}B\{^{1}H\}$ (128.4 MHz, $CD_2Cl_2$): δ -6.6 (s). UV-Vis (DCM, nm) $\lambda_{max}$: 392 (s), 460-650 (br. w). ESI-HRMS m/z for $C_{25}H_{39}ClN_2OPRu$ $[M]^+$: calcd (found) 556.1551 (556.1537), 555.1526 (555.1522), 554.1563 (554.1558), 553.1533 (553.1530), 552.1548 (552.1547), 551.1536 (551.1534), 550.1544 (550.1541), 549.1541 (549.1538), 548.1550 (548.1545), 547.1544 (547.1533), 545.1564 (545.1562). ESI-HRMS m/z for $C_{24}H_{20}B$ $[M]^-$: calcd (found) 321.1727 (321.1715), 320.1694 (320.1700), 319.1662 (319.1660), 318.1694 (318.1690). IR ($cm^{-1}$) $\nu_{max}$: 3054 (w), 2968 (w), 1593 (m, N=N), 1579 (m). Elemental Analysis: calcd (found) C% 67.62 (67.56), H% 6.83 (6.94), N% 3.22 (3.01).

### 4.6.3 General Procedure for Synthesis of $\kappa^1$*P* Au Coordination Complex (GP11)

DMSAuCl was synthesised from $KAuCl_4$ and DMS. To a round-bottomed flask with stirrer bar, $KAuCl_4$ was dissolved in minimal methanol and to this stirring yellow solution DMS (3.0 equiv.), dissolved in methanol, was added dropwise with immediate precipitation of an off-white solid. The reaction was stirred at room temperature for 1 hour and the solid isolated by Buchner filtration, washed with ethanol and diethyl ether, and dried *in vacuo*. Dissolution in minimal DCM followed by filtration through a celite plug and removal of volatiles obtained DMSAuCl as white crystals. ***Note***: DMS is a highly labile ligand not stable to high and prolonged vacuum.

DMSAuCl (1.0 equiv.) was added to a 25 mL Schlenk ampoule, and the headspace removed *in vacuo* (x 3) before finally backfilling with $N_2$ for transport into the glovebox. DMSAuCl was then dissolved in DCM and to this stirring, colourless solution $RN_2P^tBu_2$ (1.0 equiv.) was added with an immediate colour change to red, and the reaction stirred for 3 h. Volatiles were removed *in vacuo* to obtain the $\kappa^1$*P* complex as a red solid. The complex was stored in a vial in the glovebox freezer.

**Au- $\kappa^1$*P*-12(Cl) (29)**

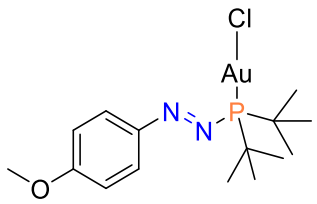


Coordination Complex **29** was synthesised from azophosphine **12** (0.36 mmol, 100 mg, 1.0 equiv.) according to GP11. The reaction was stirred at room temperature for 3 h to obtain 100% coordination of **12** to **29**, resulting in a colour change from colourless to red. Isolation of **29** was achieved as a red powder (160 mg, 86%). The flask was then rinsed with $CDCl_3$ to prepare an NMR sample. Single crystals of **29** suitable for single-crystal X-ray diffraction were grown by slow evaporation from a saturated DCM solution of the product at room temperature. $^1$H (400.1 MHz, $CDCl_3$, 298 K): δ 7.86 (d, $^3J_{H–H}$ = 9 Hz, 2H; *H*$_{Ar}$ (*p*-anisyl)), 7.01 (d, $^3J_{H–H}$ = 9 Hz, 2H; *H*$_{Ar}$ (*p*-anisyl)), 3.92 (s, 3H; *p*-OC*H*$_3$), 1.42 (d, $^3J_{H–P}$ = 15 Hz, 18H; $^t$Bu). $^{13}$C{$^1$H} (100.6 MHz, $CDCl_3$): δ 164.53 (s; *p*-*C*$_{Ar}$ (*p*-anisyl)), 149.1 (d, $^3J_{C–P}$ = 43 Hz; *i*-*C*$_{Ar}$ (*p*-anisyl)), 125.7 (s; *C*$_{Ar}$ (*p*-anisyl)), 114.6 (s; *C*$_{Ar}$ (*p*-anisyl)), 56.0 (s; *p*-O*C*H$_3$), 37.9 (d, $^1J_{C–P}$ = 27 Hz; *C*(CH$_3$)$_3$), 28.6 (d, $^2J_{C–P}$ = 4 Hz; C(*C*H$_3$)$_3$). $^{31}$P{$^1$H} (161.7 MHz, $CDCl_3$): δ 124.6 (s). $^{31}$P (161.7 MHz, $CDCl_3$): δ 124.6 (br. s). UV-Vis (DCM, nm) $\lambda_{max}$: 241 (m), 344 (s), 497 (w). ASAP-HRMS m/z for

$C_{15}H_{25}ClN_2OPAu$ $[M+H]^+$: calcd (found) 516.1140 (516.1085), 515.1111 (515.1113), 514.1168 (514.1165), 513.1137 (513.1133). IR ($cm^{-1}$) $\nu_{max}$: 2964 (w), 2922 (w), 2861 (w), 1597 (m, N=N), 1577 (m). Elemental Analysis: calcd (found) C% 35.14 (35.05), H% 4.91 (4.86), N% 5.46 (5.58).

### 4.6.4 General Procedure for Synthesis of μ*P,N* Au Coordination Complex (GP12)

A pink DCM solution of Au $\kappa^1$P-azophosphine(Cl) monomer (1.0 equiv.) was added dropwise to a stirring, colourless solution of $AgSbF_6$ (1.0 equiv.) in a 25 mL Schlenk tube with an immediate colour change to orange and precipitation of a pale orange solid. The solution was filtered through celite, and additional DCM used to dissolve the pale orange precipitate. Further dissolution of the precipitate in DCM, followed by filtration through celite left an orange solution and an off-white solid (AgCl). Volatiles were removed *in vacuo* to obtain the μ*P,N* complex as an orange solid. The complex was stored in a vial in the glovebox freezer.

**[Au-μ*P,N*-12]$_2$[$SbF_6$]$_2$ (30)**

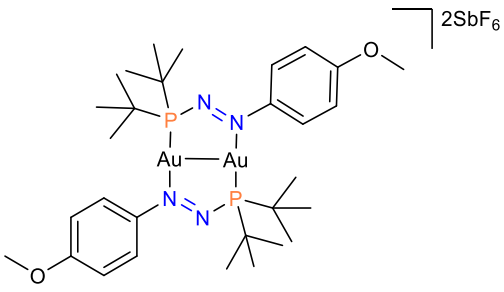


Coordination Complex **30** was synthesised from coordination complex **29** (0.04 mmol, 23 mg, 1.0 equiv.) according to GP12. 100% conversion of monomer **29** to dimer **30** was obtained, resulting in a colour change from red to orange. Isolation of **30** was achieved as an orange powder (25 mg, 83%). The flask was then rinsed with $CD_2Cl_2$

to prepare an NMR sample. Single crystals of **30** suitable for single-crystal X-ray diffraction were grown by slow evaporation from a saturated DCM solution of the product at room temperature. $^{1}$H (400.1 MHz, $CD_2Cl_2$, 298 K): δ 8.29 (d, $^{3}J_{H–H}$ = 9 Hz, 2H; $H_{Ar}$ (*p*-anisyl)), 7.28 (d, $^{3}J_{H–H}$ = 9 Hz, 2H; $H_{Ar}$ (*p*-anisyl)), 4.08 (s, 3H; *p*-OC$H_3$), 1.60 (d, $^{3}J_{H–P}$ = 18 Hz, 18H; $^{t}$Bu). $^{13}$C{$^{1}$H} (100.6 MHz, $CD_2Cl_2$): δ 170.0 (s; $C_{Ar}$ (*p*-anisyl)), 149.3 (d, $^{3}J_{C–P}$ = 26 Hz; *i*-$C_{Ar}$ (*p*-anisyl)), 139.0 (s; $C_{Ar}$ (*p*-anisyl)), 117.8 (s; $C_{Ar}$ (*p*-anisyl)), 57.7 (s; *p*-O$C$H$_3$), 41.6 (d, $^{1}J_{C–P}$ = 24 Hz; $C(CH_3)_3$), 28.6 (d, $^{2}J_{C–P}$ = 5 Hz; C($CH_3$)$_3$). $^{31}$P{$^{1}$H} (161.7 MHz, $CD_2Cl_2$): δ 108.1 (s). $^{31}$P (161.7 MHz, $CD_2Cl_2$): δ 108.1 (s). UV-Vis (DCM, nm) $\lambda_{max}$: 237 (m), 354 (s), 422 (w). ESI-HRMS m/z for $C_{30}H_{50}N_4O_2P_2Au_2$ $[M + Cl]^+$: calcd (found) 992.2436 (992.2459), 991.2414 (991.2423), 990.2460 (990.2480), 989.2429 (989.2442). ESI-HRMS m/z for $SbF_6$ $[M]^-$: calcd (found) 236.8946 (236.8949), 234.8942 (234.8944). IR ($cm^{-1}$) $\nu_{max}$: 2956 (w), 2926 (w), 2855 (w), 1601 (m, N=N), 1577 (m).

### 4.6.5 General Procedure for Synthesis of κ$^{1}$*P* W Coordination Complexes (GP13)

$RN_2P^tBu_2$ (1.0 equiv.) was added to a 25 mL round-bottomed Schlenk flask and dissolved in chlorobenzene. To this solution, $W(CO)_4COD$ (1.0 equiv.) was added, and the mixture stirred at 50 °C in a sand bath for 24 hours. Removal of solvent *in vacuo*, washing with hexane and filtration through a silica plug (eluent = toluene) obtained the bis-monodentate coordination complex as a red powder. The complexes were stored in vials in the glovebox freezer.

***trans*-W(CO)$_4$(κ$^1$*P*-3)$_2$ (31)**

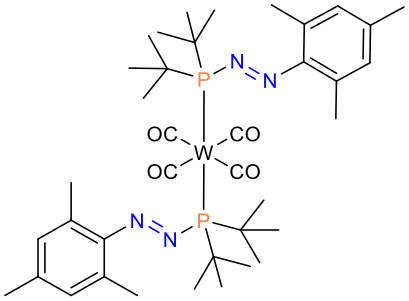

Coordination Complex **31** was synthesised from azophosphine **3** (1.0 equiv.) according to GP13. Isolation of **31** was achieved as a red powder. The flask was then rinsed with THF-$d_8$ to prepare an NMR sample. Single crystals of **31** suitable for single-crystal X-ray diffraction were grown by slow evaporation from a saturated THF-$d_8$ solution of the product at room temperature. $^1$H (400.1 MHz, THF-$d_8$, 294.9 K): δ 6.95 (s, 2H; *m*-$H_{Ar}$), 2.48 (s, 6H; *o*-C$H_3$), 2.30 (s, 3H; *p*-C$H_3$), 1.49 (d, $^3J_{H–P}$ = 12 Hz, 18H; $^t$Bu). $^{13}$C{$^1$H} (100 MHz, THF-*d*8, 295.5 K): δ 207.1 (s; *C*O), 150.1 (s; *i*-$C_{Ar}$), 141.5 (s; *p*-$C_{Ar}$), 133.8 (s; *o*-$C_{Ar}$), 131.3 (s; *m*-$C_{Ar}$), 42.1 (d, $^1J_{C–P}$ = 13 Hz; *C*(CH$_3$)$_3$), 30.3 (s; C(*C*H$_3$)$_3$), 21.5 (s; *p*-*C*H$_3$), 20.9 (s; *o*-*C*H$_3$). $^{31}$P{$^1$H} (162.0 MHz, THF-$d_8$, 298 K) δ 140.4 (s, $^1J_{P–W}$ = 268 Hz).

### 4.6.6 Procedure for Synthesis of κ$^1$*P* Pd Coordination Complexes

**11** (1.0 equiv.) was added to a vial and dissolved in chlorobenzene. To this solution, $PdCl_2$ (1.0 equiv.) was added and the dark red solution transferred to an NMR tube for monitoring by $^{31}$P{$^1$H} NMR spectroscopy.

***trans*-$PdCl_2(\kappa^1P\text{-}11)_2$ (32)**

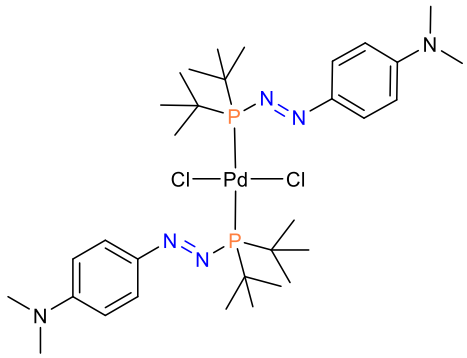

Single crystals of **32** suitable for single-crystal X-ray diffraction were grown by slow evaporation from a saturated chlorobenzene solution of the reaction mixture at room temperature.

***trans*-$PdCl_2(\kappa^1P\text{-}11)(NH_2C_6H_4(p\text{-}NMe_2))$ (33)**

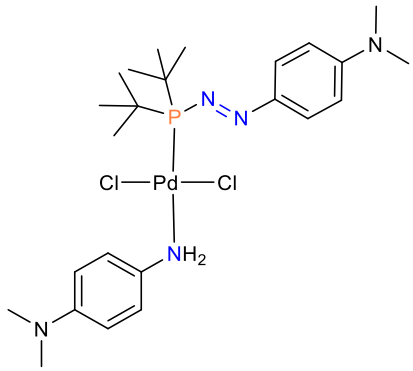

Single crystals of **33** suitable for single-crystal X-ray diffraction were grown by slow evaporation from a saturated chlorobenzene solution of the reaction mixture at room temperature.

### 4.6.7 General Procedure for Synthesis of $\kappa^1P$ Ir Coordination Complexes (GP14)

$RN_2P^tBu_2$ (1.0 equiv.) was added to a 25 mL round-bottomed Schlenk flask and dissolved in chlorobenzene. To this solution, $[Ir(cp^*)Cl_2]_2$ dimer (0.5 equiv.) was added,

and the mixture stirred at room temperature for 30 min. Isolation of a red powder obtained the κ$^1$*P* coordination complex as a red powder. The complexes were stored in vials in the glovebox freezer.

**Ir(cp*)( κ$^1$*P*-11)Cl$_2$ (34)**

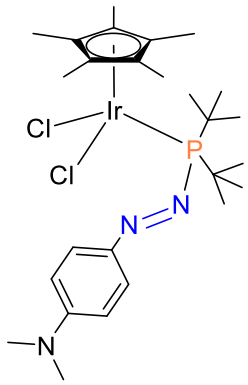


Coordination Complex **34** was synthesised from azophosphine **11** (0.02 mmol, 7 mg, 1.0 equiv.) according to GP14. The reaction was stirred at room temperature for 30 minutes with precipitation of a red solid. Filtration isolated **34** as a red powder (10 mg, 74%). The sample was then dissolved in $CDCl_3$ to prepare an NMR sample. Single crystals of **34** suitable for single-crystal X-ray diffraction were grown from a saturated $CDCl_3$ solution of the product. $^{31}P\{^1H\}$ (161.7 MHz, $CDCl_3$): δ 85.6 (s).

**Ir(cp*)(κ$^1$*P*-12)Cl$_2$ (35)**

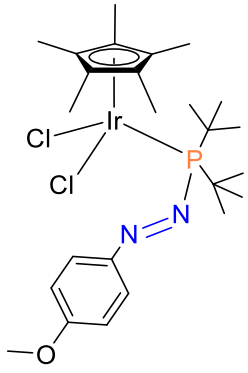

Coordination Complex **35** was synthesised from azophosphine **12** (0.04 mmol, 10 mg, 1.0 equiv.) according to GP14. The reaction was stirred at room temperature for 30 min. Removal of solvent *in vacuo* isolated **35** as a reddish-orange powder (19 mg, 75%). The sample was then dissolved in $CDCl_3$ to prepare an NMR sample. Single crystals of **35** suitable for single-crystal X-ray diffraction were grown from a saturated $CDCl_3$ solution of the product. $^{1}H$ (400.1 MHz, $CDCl_3$, 298 K): δ 7.77 (d, $^{3}J_{H–H}$ = 9 Hz, 2H; $H_{Ar}$ (*p*-anisyl)), 7.06 (d, $^{3}J_{H–H}$ = 9 Hz, 2H; $H_{Ar}$ (*p*-anisyl)), 3.92 (s, 3H; *p*-OC$H_3$), 1.54 (d, $^{3}J_{H–P}$ = 13 Hz, 18H; $^{t}$Bu), 1.41 (d, $^{4}J_{H–P}$ = 2 Hz, 15H; cp*). $^{31}P\{^{1}H\}$ (161.7 MHz, $CDCl_3$): δ 89.8 (s).

## References


1 N. G. Connelly and G. Garcia, *Dalton Trans.*, 1987, 2737-2740

2 C. J. Adams, K. M. Anderson, R. A. Baber, N. G. Connelly, M. Kandiah and A. G. Orpen, *Dalton Trans.*, 2004, 3353–3359.

3 L. Carlton, M. S. Nyoni and M. A. Fernandes, *Polyhedron*, 2016, **119**, 194–201.

4 C. Tejel, M. A. Ciriano, G. Ríos-Moreno, I. T. Dobrinovitch, F. J. Lahoz, L. A. Oro and M. Parra-Hake, *Inorg. Chem.*, 2004, **43**, 4719–4726.

5 G. Albertin, S. Antonlutti, M. Bedin, J. Castro and S. Garcia-Fontán, *Inorg. Chem.*, 2006, **45**, 3816–3825.

6 A. G. M. Barrett, M. R. Crimmin, M. S. Hill, P. B. Hitchcock, G. Kociok-Köhn and P. A. Procopiou, *Inorg. Chem.*, 2008, **47**, 7366–7376.

7 A. L. Johnson, A. M. Willcocks and S. P. Richards, *Inorg. Chem.*, 2009, **48**, 8613–8622.

8 S. O. Hauber, F. Lissner, G. B. Deacon and M. Niemeyer, *Angew. Chem., Int. Ed.*, 2005, **44**, 5871–5875.

9 M. K. Rong, F. Holtrop, J. C. Slootweg and K. Lammertsma, *Coord. Chem. Rev.*, 2019, **380**, 1–16.

10 M. K. Rong, F. Holtrop, J. C. Slootweg and K. Lammertsma, *Coord. Chem. Rev.*, 2019, **382**, 57–68.

11 S. Maggini, *Coord. Chem. Rev.*, 2009, **253**, 1793–1832.

12 M. K. Rong, F. Holtrop, E. O. Bobylev, M. Nieger, A. W. Ehlers, J. C. Slootweg and K. Lammertsma, *Chem. Eur. J.*, 2021, **27**, 14007–14016.

13 R. García-Álvarez, S. E. García-Garrido, J. Díez, P. Crochet and V. Cadierno, *Eur. J. Inorg. Chem.*, 2012, **2012**, 4218–4230.

14 R. Lalrempuia, P. J. Carroll and K. Mohan Rao, *J. Chem. Sci.*, 2004, **116**, 21–27.

15 I. Moldes, E. De La Encarnación, J. Ros, Á. Alvarez-Larena and J. F. Piniella, *J. Organomet. Chem.*, 1998, **566**, 165–174.

16 P. Govindaswamy, Y. A. Mozharivskyj and M. R. Kollipara, *Polyhedron*, 2004, **23**, 3115–3123.

17 D. Drommi, C. G. Arena, F. Nicoló, G. Bruno and F. Faraone, *J. Organomet. Chem.*, 1995, **485**, 115–121.

18 P. Espinet and K. Soulantica, *Coord. Chem. Rev.*, 1999, **193–195**, 499–556.

19 A. P. Sadimenko, *Adv. Heterocycl. Chem.*, 2011, **104**, 391–475.

20 G. R. Newkome, *Chem. Rev.*, 1993, **93**, 2067–2089.

21 Z. Z. Zhang and H. Cheng, *Coord. Chem. Rev.*, 1996, **147**, 1–39.

22 L. Hintermann, T. T. Dang, A. Labonne, T. Kribber, L. Xiao and P. Naumov, *Chem. Eur. J.*, 2009, **15**, 7167–7179.

23 P. C. Kunz, I. Thiel, A. L. Noffke, G. J. Reiß, F. Mohr and B. Spingler, *J. Organomet. Chem.*, 2012, **697**, 33–40.

24 D. B. Grotjahn, C. R. Larsen, J. L. Gustafson, R. Nair and A. Sharma, *J. Am. Chem. Soc.*, 2007, **129**, 9592–9593.

25 J. M. Walker, J. P. Tassone, H. A. Jenkins and G. J. Spivak, *J. Organomet. Chem.*, 2014, **761**, 56–63.

26 T. Van Dijk, S. Burck, M. K. Rong, A. J. Rosenthal, M. Nieger, J. C. Slootweg and K. Lammertsma, *Angew. Chem., Int. Ed.*, 2014, **53**, 9068–9071.

27 T. Vandijk, S. Burck, A. J. Rosenthal, M. Nieger, A. W. Ehlers, J. C. Slootweg and K. Lammertsma, *Chem. Eur. J.*, 2015, **21**, 9328–9331.

28 M. K. Rong, K. Van Duin, T. Van Dijk, J. J. M. De Pater, B. J. Deelman, M. Nieger, A. W. Ehlers, J. C. Slootweg and K. Lammertsma, *Organometallics*, 2017, **36**, 1079–1090.

29 A. R. Cowley, J. R. Dilworth, A. K. Nairn and A. J. Robbie, *Dalton Trans.*, 2005, 680–693.

30 S. Pavlik, F. Jantscher, G. Dazinger, K. Mereiter and K. Kirchner, *Eur. J. Inorg. Chem.*, 2006, **2006**, 1006–1021.

31 W. Wang, C. L. Ji, K. Liu, C. G. Zhao, W. Li and J. Xie, *Chem. Soc. Rev.*, 2021, **50**, 1874–1912.

32 H. Schmidbaur and A. Schier, *Chem. Soc. Rev.*, 2008, **37**, 1931–1951.

33 V. W. W. Yam and E. C. C. Cheng, *Chem. Soc. Rev.*, 2008, **37**, 1806–1813.

34 Y. Inoguchi, B. Milewski-Mahrla and H. Schmidbaur, *Chem. Ber.*, 1982, **115**, 3085–3095.

35 V. J. Catalano and S. J. Horner, *Inorg. Chem.*, 2003, **42**, 8430–8438.

36 A. Burini, B. R. Pietroni, R. Galassi, G. Valle and S. Calogero, *Inorganica Chim Acta*, 1995, **229**, 299–305.

37 F. Bachechi, A. Burini, M. Fontani, R. Galassi, A. Macchioni, B. R. Pietroni, P. Zanello and C. Zuccaccia, *Inorganica Chim Acta*, 2001, **323**, 45–54.

38 D. E. Jenkins and Z. Assefa, *J. Mol. Struct.*, 2017, **1133**, 374–383.

39 A. M. Larsonneur, R. Turpin, P. Castan and G. Bernardinelli, *Inorganica Chim Acta*, 1994, **227**, 85–90.

40 X. He and V. W. W. Yam, *Coord. Chem. Rev.*, 2011, **255**, 2111–2123.

41 Q. M. Wang, Y. A. Lee, O. Crespo, J. Deaton, C. Tang, H. J. Gysling, M. C. Gimeno, C. Larraz, M. D. Villacampa, A. Laguna and R. Eisenberg, *J. Am. Chem. Soc.*, 2004, **26**, 9488–9489.

42 W.-F. Fu, K.-C. Chan, V. M. Miskowski and C.-M. Che, *Angew. Chem., Int. Ed.,* 1999, **38**, 2638–2803.

43 K. H. Leung, D. L. Phillips, M. C. Tse, C. M. Che and V. M. Miskowski, *J. Am. Chem. Soc.*, 1999, **121**, 4799–4803.

44 K. H. Leung, D. L. Phillips, Z. Mao, C. M. Che, V. M. Miskowski and C. K. Chan, *Inorg. Chem.*, 2002, **41**, 2054–2059.

45 E. M. Tait, Exploring the Coordination and Catalytic Applications of Azophosphines, University of Birmingham, 2023.

46 M. G. Butler, Preparation and Characterisation of Azophosphine Tetracarbonyltungsten(0) Complexes, University of Birmingham, 2022.

47 E. J. Jordan, E. D. E. Calder, H. V Adcock, L. Male, M. Nieger, J. C. Slootweg and A. R. Jupp, *Chem. Eur. J.*, e202401358.

48 E. J. Jordan, E. D. E. Calder, B. L. Greene, H. V. Adcock, L. Male, P. W. Davies and A. R. Jupp, *Organometallics*, 2024, **43**, 2674–2685.

49 Deposition numbers 2334073 (for **23**), 235865 (for **25**), 2358662 (for **26**), 2334074 (for **27**), 2334077 (for **28**) contain the supplementary crystallographic data for this chapter. These data are provided free of charge by the joint Cambridge Crystallographic Data Centre and Fachinformationszentrum Karlsruhe Access Structures service.

50 W. P. Teh, D. C. Obenschain, B. M. Black and F. E. Michael, *J. Am. Chem. Soc.*, 2020, **142**, 16716–16722.

51 P. R. Graf Rubia, Exploring the Photochemical Properties of a new Azobenzene Derivative, Azophosphine, University of Bristol, 2024.

52 W. Wang, C. L. Ji, K. Liu, C. G. Zhao, W. Li and J. Xie, *Chem. Soc. Rev.*, 2021, **50**, 1874–1912.

53 X. He and V. W. W. Yam, *Coord. Chem. Rev.*, 2011, **255**, 2111–2123.

54 V. W. W. Yam and E. C. C. Cheng, *Chem. Soc. Rev.*, 2008, **37**, 1806–1813.

55 A. Barbieri, G. Accorsi and N. Armaroli, *Chem. Commun.*, 2008, 2185–2193.

56 W.-F. Fu, K.-C. Chan, V. M. Miskowski and C.-M. Che, *Angew. Chem., Int. Ed.*, 1999, **38**, 2638–2803.

57 R. F. Ziolo, S. Lipton and Z. Dori, *Chem. Commun.*, 1970, 1124–1125.

58 J. H. Jia and Q. M. Wang, *J. Am. Chem. Soc.*, 2009, **131**, 16634–16635.

59 H. M. D. Bandara and S. C. Burdette, *Chem. Soc. Rev.*, 2012, **41**, 1809–1825.

60 D. Das, M. K. Yadav, L. Singla, A. Kumar, M. Karanam, S. Dev and A. R. Choudhury, *ChemistrySelect*, 2020, **5**, 13957–13962.

61 C. Kayran, F. Kozanoglu, S. Özkar, S. Saldamli, A. Tekkaya and C. G. Kreiter, *Inorganica Chim. Acta*, 1999, **284**, 229–236.

62 M. K. Rong, F. Holtrop, J. C. Slootweg and K. Lammertsma, *Coord. Chem. Rev.*, 2019, **380**, 1–16.

63 J. Liu, C. Jacob, K. J. Sheridan, F. Al-Mosule, B. T. Heaton, J. A. Iggo, M. Matthews, J. Pelletier, R. Whyman, J. F. Bickley and A. Steiner, *Dalton Trans.*, 2010, **39**, 7921–7935.

64 T. Suzuki, M. Kita, K. Kashiwabara and J. Fujita, *Bull. Chem. Soc. Jpn.*, 1990, **63**, 3434–3442.

65 CrysAlisPro, Rigaku Oxford Diffraction, 2021

66 O. V Dolomanov, L. J. Bourhis, R. J. Gildea, J. A. K. Howard and H. Puschmann, *J. Appl. Crystallogr.*, 2009, **42**, 339–341.

67 G. M. Sheldrick, *Acta Crystallogr.*, 2015, **A71**, 3–8.

68 G. M. Sheldrick, *Acta Crystallogr.*, 2015, **C71**, 3–8.

# CHAPTER 5

# Application of Ruthenium-Azophosphine and Gold-Azophosphine Complexes in Catalysis

## 5.1 Introduction and Objectives

### 5.1.1 Ruthenium Complexes in Catalysis

Ruthenium is one of the common metal centres to which a 1,3-P,N ligand is coordinated for applications in catalysis, often investigated for catalytic activity in, but not limited to: hydration of nitriles and alkynes; transfer hydrogenation; hydroformylation; oxidation of alkenes; and [2+2] and Diels-Alder cycloaddition reactions.[3] Within the context of this thesis, it is not possible to provide a comprehensive review of the many catalytic transformations reported in the literature. Here, only the most pertinent applications of ruthenium complexes in catalysis will be discussed. Namely, the transfer hydrogenation of acetophenone and the oxidation of styrene, selected as well-established reactions with relatively mild conditions that could be used to test the catalytic activity of the Ru-azophosphine complexes.

*Transfer Hydrogenation*

Ruthenium complexes have been widely studied as catalysts for transfer hydrogenation reactions, where an organic $H_2$ surrogate is used to bypass the hazards associated with using high pressures of $H_2$ gas.[4–6] Isopropanol (IPA) has been touted as the ideal $H_2$ source, as it is inexpensive, readily available, highly solubilising, has an appropriate boiling point, and generates acetone as a by-product.[6] The Ru-catalysed transfer hydrogenation of ketones is a powerful reaction to produce alcohols, and if a chiral catalyst is used this can be done in an asymmetric manner.[5,7] The conversion of acetophenone into 1-phenylethanol using IPA as the $H_2$ source has been catalysed by a range of Ru-based catalysts,[8–15] and in all but one case an alkali metal base is required as an additive for catalysis to occur (Scheme 5.1A).

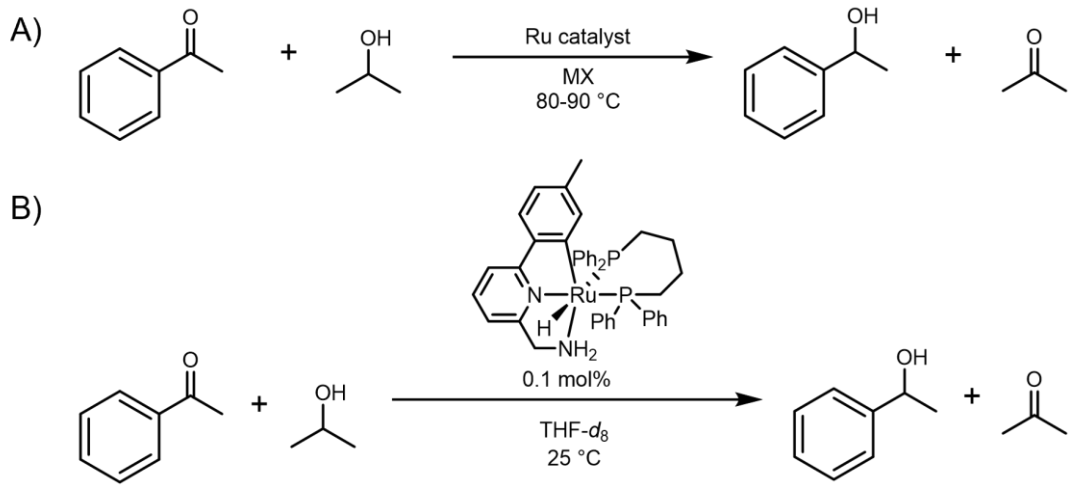


**Scheme 5.1.** Transfer hydrogenation of acetophenone to 1-phenylethanone using IPA as a hydrogen source. (A) General scheme using MX as a strong base that is required to activate the Ru catalyst; (B) Example using a ruthenium hydride as the catalyst and no base.

The only example of a Ru-catalyst for this reaction that does not require addition of a strong base is an isolated ruthenium hydride, and in this case adding a large excess of potassium *tert*-butoxide had no effect (Scheme 5.1B).[16] The role of the base had been considered to be increasing the concentration of the isopropoxide ion, which coordinates with the metal centre of the pre-catalyst, and then β-eliminates leaving a metal-hydride reducing species as an active catalyst, and acetone as a by-product. This previously accepted mechanism was challenged when Noyori and co-workers found the base was necessary to generate the 16e active catalyst from the 18e pre-catalyst *via* elimination of chloride.[17] It is plausible that weak *N*-coordination of the azophosphine in a $\kappa^2$*P,N* ruthenium complex may enable this process to occur in a base-free manner.

*Oxidation of Olefins*

Ruthenium can catalyse numerous oxidative transformations owing to its versatility in which a range of transient oxidation states, −1 to +8, are accessible.[18] Catalytic

oxidation of olefins is an important transformation to access carbonyl-containing compounds by inserting the oxygen functionality into their backbone. The use of ozonolysis to cleave the C=C bond and replace it with a carbonyl group led to the development of catalytic metal-based systems for application in olefin oxidation, of which ruthenium catalysts have been widely investigated.[19] As a typical carbonyl-containing compound, benzaldehyde has extensive application in the perfumery, foodstuff and pharmaceutical industries; however, preparation by hydrolysis of α,α-dichlorotoluene, which produces chlorine-containing products, is unsuitable for these industries. To circumvent this, the selective oxidation of toluene, benzyl alcohol and styrene to benzaldehyde with various oxidants has been explored, of which styrene is the preferred option due to its higher reactivity and lower cost.[20] Previous research on the oxidation of styrene has found oxidation at the side chain can lead to C=C cleavage into benzaldehyde or epoxidation depending on the catalyst and reaction conditions (Scheme 5.2).[18]

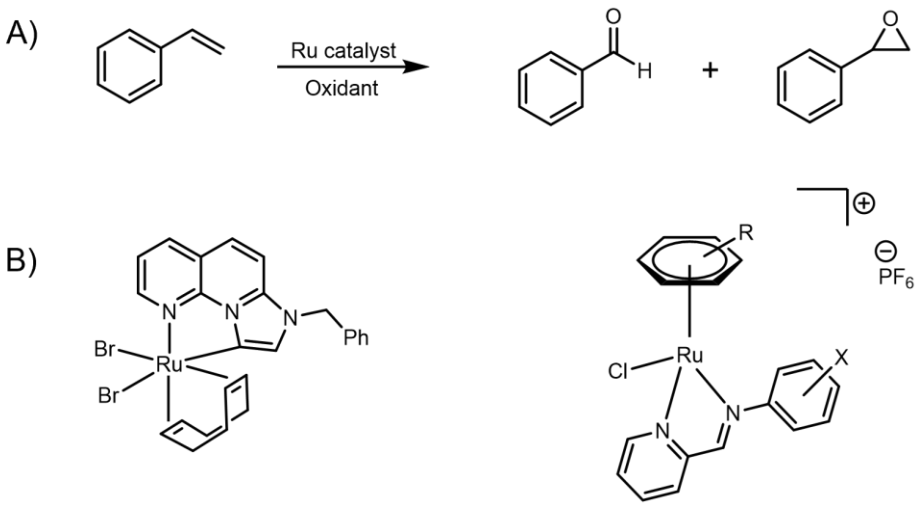


**Scheme 5.2.** (A) Oxidation of styrene to benzaldehyde and the corresponding epoxide; (B) Structures of example catalysts. X = halide group.

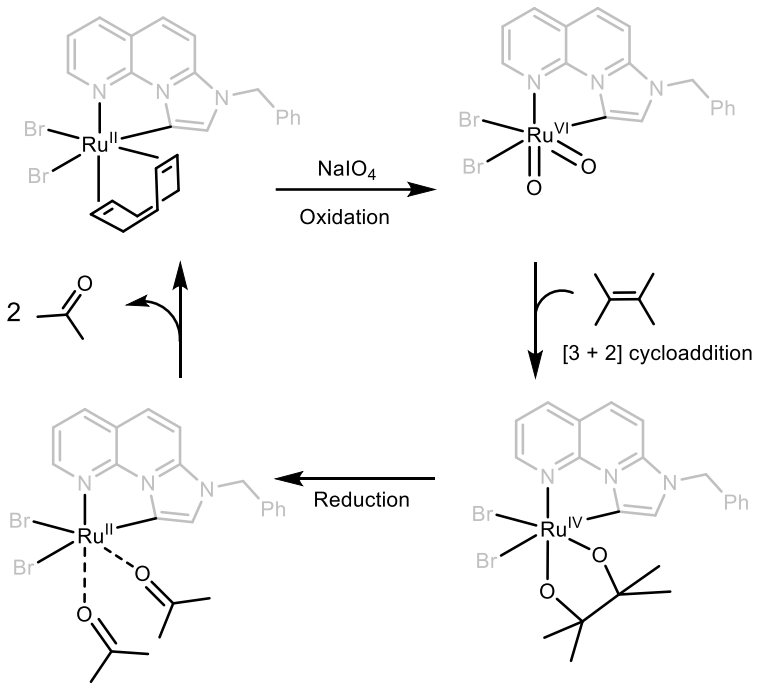


**Scheme 5.3.** Proposed mechanism for olefin oxidation by Bera and co-workers.[21]

As depicted in Scheme 5.3, a proposed mechanism for selective aldehyde formation involves ligand displacement by oxidative addition to form a Ru(VI)(=O)$_2$ species in the first step.[21] Optimisation of the selective oxidation of styrene to benzaldehyde has found conversions of >90% can be achieved after 3 h when using a Ru(II)(COD) catalyst with $NaIO_4$ as an oxygen source and mild temperatures.[21,22]

To test whether the Ru-azophosphine complexes displayed catalytic activity the transfer hydrogenation of acetophenone and the oxidation of styrene were used as two proof-of-concept studies and will be discussed in turn in Section 5.2.

### 5.1.2 Gold Complexes in Catalysis

Gold commonly exists in two stable oxidation states (I and III) and, as a soft, third row transition metal, has a binding affinity for soft donor atoms, such as phosphorus.[23] Au(I) complexes are typically represented by L–Au–Cl (L, neutral ligand) in which the

linearly-coordinated chloride requires abstraction by a silver salt (AgX) to generate the catalytically active [L–Au]$^+$ species *in situ*.[24] The cationic Au(I) complex readily coordinates alkenes, allenes, and alkynes, demonstrating utility as a catalyst for the functionalisation of C–C multiple bonds by activating these substrates toward nucleophilic attack (Scheme 5.4).[25]

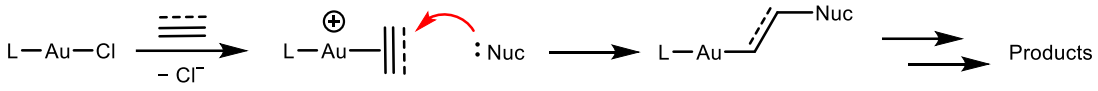


**Scheme 5.4.** General mechanism for Au(I) π-activation catalysis involving a [L–Au]$^+$ complex.

The synthetic utility and desirable combination of high π acidity and low oxophilicity of [L–Au]$^+$ has led to focus moving away from Au(III) catalysts in favour of Au(I) catalysts. The high lattice enthalpy of AgCl makes addition of AgX a facile means of activating the L–Au–Cl pre-catalyst but is not without problems. Known as the 'silver effect', addition of AgX can negatively impact the reaction outcome due to the Ag(I) cation not being catalytically innocent.[26] Incomplete abstraction of chloride and practical issues, such as light and moisture sensitivity, are additional drawbacks to using *in situ* catalyst activation by AgX.[27] Generation of a catalytically active species in solution without the need for activation by addition of a silver salt is therefore highly advantageous in catalysis.

In the presence of bidentate ligands, binuclear Au(I) complexes can be obtained. Here, a distinction must be made between binuclear Au(I) complexes, which have Au···Au centres linked by a bidentate ligand, and digold catalysis, which typically involves two independent Au(I) centres that do not come from the same pre-catalyst. Au···Au aurophilic interactions impart a distinctly different nature to binuclear complexes compared to their mononuclear counterparts. A comprehensive review of binuclear

gold catalysis by Xie and co-workers highlighted their unique catalytic ability in coupling reactions, asymmetric catalysis and photocatalysis.[28] The two binuclear centres may have different formal oxidation states and steric environments, which leads in some cases to better catalytic performance than mononuclear Au(I) complexes. It has been proposed that activation of one Au centre provides the opportunity to leave behind a coordinated counteranion to convey chiral information (Scheme 5.5).[29]

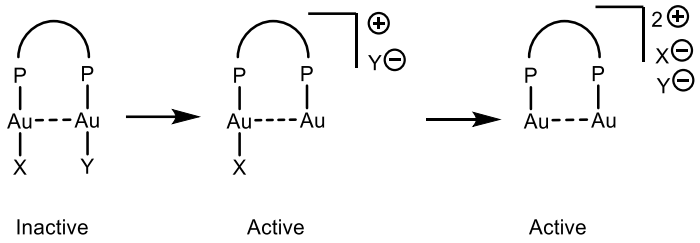


**Scheme 5.5.** Inactive and active catalyst forms of binuclear Au(I) complexes proposed by Toste and co-workers.[29]

As discussed in Chapter 4 (Sections 4.1.2 and 4.3.2), there are limited examples of 1,3-P,N ligands forming binuclear μ*P,N* dimer complexes with Au(I) due to their tendency to form trinuclear arrangements which are found to be catalytically inactive. As a consequence, catalytic efficiencies of $\kappa^1$*P* L–Au–Cl monomers, upon activation by AgX, can be restricted by trimerisation and catalyst deactivation depending on the coordinating ability of X. In the Markovnikov hydration of terminal alkynes using 1 mol% $PyPh_2P$–Au–Cl as the pre-catalyst (Py, pyridine), the yield decreased from 61% to 40% upon changing the silver salt from AgOTf to $AgBF_4$ (Scheme 5.6).[30]

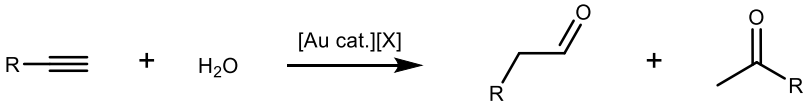


**Scheme 5.6.** Markovnikov hydration of terminal alkynes. X = OTf or $BF_4$.

Single crystal X-ray analysis of crystalline material on the glass surface after the reaction confirmed the [(μP,N)$_3$–Au$_3$] trinuclear arrangement in which each of the three Au atoms was coordinated by P of the initial PPh$_2$Py ligand and N of the Py group of the adjacent PPh$_2$Py ligand. Increasing the catalyst loading to 5 mol% resulted in quantitative yields for both [PyPh$_2$P–Au][OTf] and [PyPh$_2$P–Au][BF$_4$]. Attempting Markovnikov hydration of terminal alkynes using 5 mol% of [L–Au][OTf] (L, imidazolyl-based 1,3-P,N ligands) obtained conversions of only 6 – 30%.[31] Similarly, catalyst deactivation was attributed to the structurally characterised [(μP,N)$_2$–Au$_3$(Cl)$_2$][Cl] trimer. Formation of the trimer in the presence of OTf as a coordinating anion occurs, in contrast to the μ-PyPh$_2$P-based Au$_3$ trimer, because of the stronger electron-donating ability of imidazolylphosphines over pyridylphosphines.

The ability to form binuclear Au(I) dimer complexes with μP,N coordination of an azophosphine was demonstrated in Chapter 4 (Section 4.3.1). It was considered whether the weak coordinating properties of N would, firstly: diminish the potential for trimerisation and catalyst deactivation of the azophosphine-Au monomer upon activation by silver salt and, secondly; by using the azophosphine-Au dimer as catalyst, allow the generation of a catalytically active species in solution without the need for activation by addition of a silver salt. These investigations are discussed in Sections 5.3.1 and 5.3.2.

### 5.1.3 Ligand Knowledge Bases

Ligands play a central role in catalysis, and their steric and electronic properties are crucial in metal- and ligand-based reactivity. A combination of structural and computational chemistry can elucidate the coordination and reactivity of organometallic catalysts, and the Ligand Knowledge Base (LKB) is an approach rooted in this

concept.[32] LKBs are a collation of knowledge on ligands in metal complexes, both inherent to the free (pro-)ligand and dependent on its coordination, reported by a consortium of authors. From a prototype developed in a proof-of-concept study,[33] LKBs have now been developed for monodentate phosphorus(III) ligands (LKB-P),[34] carbenes (LKB-C),[35] bidentate *P,P*- and *P,N*-donor ligands (LKB-PP),[36,37] and, more recently, a wider range of bidentate ligands featuring combinations of *P*-, *N*-, *O*- and *C*- donor atoms (LKB-Bid).[38] Steric and electronic descriptors of ligand properties, combined with Principal Component Analysis (PCA) as a multivariate statistical technique to reduce the dimensionality of the data, enables insight into the part of chemical space a given ligand is located by generating a so-called map of ligand space. Knowledge of the location in ligand space for a given ligand ideally would allow prediction of its behaviour in a metal complex and ultimately provide predictions for its application in catalysis or guide the rational design of suitable catalysts. Fey, Pringle and co-workers demonstrated the successful prediction of fluorophosphines of the type $R_2PF$ as ligands in catalytic hydroformylation and hydrocyanation when coordinated to rhodium and nickel, respectively (Scheme 5.7).[39] Proximity in ligand space to triaryl phosphites ($P(OAr)_3$) – ligands typically deployed in hydroformylation and hydrocyanation – was used as an indicator of catalytic potential. This represented the first application of $R_2PF$ ligands in catalysis, performing in some cases as well as, or better than, commercial $PPh_3$-rhodium catalysts for hydroformylation and tritolyl phosphite ($P(O\text{-}o\text{-}Tol)_3$) nickel catalysts for hydrocyanation.[39] Fluoroaryl phosphines ($P(Ar^F)_3$) were clearly distinguished from aryl phosphites on the ligand map and, when tested, $P(C_6F_5)_3$ gave catalysts with essentially zero activity in hydroformylation and hydrocyanation.

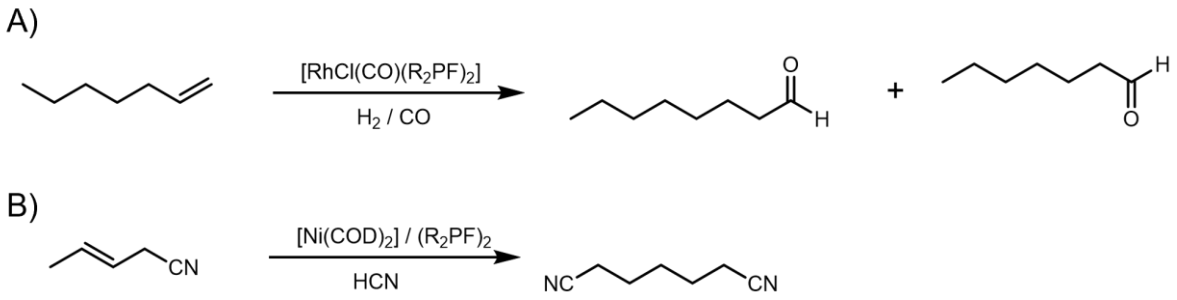


**Scheme 5.7.** (A) Hydroformylation of 1-heptene; (B) Hydrocyanation of 3-pentenenitrile.

The LKB-Bid database uses descriptors closely related to those in LKB-PP and were selected to capture different coordination environments. These are discussed by Durand and Fey.[32] In brief, the selected descriptors were derived from Density Functional Theory (DFT) calculations on the ligand in both free and chelated conformations in the tetrahedral [$ZnCl_2$(LL)] and square planar [$PdCl_2$(LL)] complexes (LL is a bidentate ligand with *P,P*- or *P,N*-donor atoms). The interaction energy between the ligand in its chelating conformation and a rigid wedge of eight helium atoms is a steric descriptor, termed $He_8$_wedge, which simulates the steric bulk of other ligands in an octahedral coordination environment. As it was found that $He_8$_wedge tended to overestimate the size of some large but “compressible” ligands, a second steric descriptor, n$He_8$, was introduced to accommodate the flexible response of ligands to steric hindrance. Applicable to only LKB-PP, frontier molecular orbital energies and ligand proton affinities were also calculated for each donor atom, derived from truncated ligand fragments.[32,37] Fey and co-workers note that the chelate effect and ligand hemilability could be challenging to capture computationally; however, the trends in ligand effects are likely to be reasonably robust, even where energy effects were not fully captured.[38]

The LKB-PP and LKB-Bid now contain approximately 324 and 224 ligands, respectively,[32] and is highly relevant in understanding the applications of azophosphines as *P,N*-donor ligands in catalysis. This will be discussed further in Section 5.2.4.

### 5.1.4 Chapter Outline

The coordination chemistry studies, discussed in Chapter 4, found that the azophosphines with the more electron-donating *N*-aryl substituents (in particular, *p*-($NMe_2$)$C_6H_4N_2P^tBu_2$ (**11**) and *p*-(OMe)$C_6H_4N_2P^tBu_2$ (**12**)) made stronger donor ligands, affording monodentate complexes Ru(benzene)(κ$^1$*P*-(**11**))$Cl_2$ (**24**) and Ru(*p*-cymene)(κ$^1$*P*-(**12**))$Cl_2$ (**26**). Clean conversion of **24** and **26** to their respective bidentate complexes [Ru(benzene)(κ$^2$*P,N*-(**11**)Cl][$BPh_4$] (**25**) and Ru(*p*-cymene)(κ$^2$*P,N*-(**12**)Cl][$BPh_4$] (**27**) was achieved by addition of $NaBPh_4$. Coordination of **12** to a gold(I) centre also produced clean conversion to the bridging ([Au(μ*P,N*-**12**)][$SbF_6$])$_2$ dimer (**30**) from the corresponding Au(κ$^1$*P*-**12**)Cl monomer (**29**). In this chapter, ruthenium complexes **26** and **27** are explored as catalysts in the transfer hydrogenation of acetophenone (Section 5.2.2) and in the oxidation of styrene (Section 5.2.3). Ruthenium complex **25** is tested in a Diels-Alder reaction, guided by a computational study which mapped a range of azophosphines onto the LKB-PP and LKB-Bid databases for bidentate *P,N*-donor ligands (Section 5.2.4). Finally, in Section 5.3, gold complexes **29** and **30** are tested as catalysts in the functionalisation of C–C multiple bonds.

### 5.1.5 Acknowledgements

ReactIR experiments discussed in Section 5.2.2 were carried out in collaboration with Bethan Greene (PhD student, Davies group, University of Birmingham). The computational study referenced in Section 5.2.4 is titled '*Exploring the Ligand Properties of Azophosphines*' by Lewis J. Oram (MSci student, Jupp group, University of Birmingham),[40] with supervision by Dr Laura English (Jupp group), in collaboration with Dr Natalie Fey at the University of Bristol, in partial fulfilment of the requirements of the Honours degree of MSci at the University of Birmingham. Section 5.3.1 contains research by Ellen M. Tait (MSci student, Jupp group),[41] with supervision by the author, in partial fulfilment of the requirements of the Honours degree of MSci at the University of Birmingham. Section 5.3.2 discusses an active collaboration with the Davies group at the University of Birmingham in which catalytic runs were performed by Bethan Greene using samples of **29** and **30** synthesised by the author.

### 5.1.6 Published Research

Research in this chapter (Section 5.2.2) has been published in *Organometallics*.[42] The remainder of the chapter is currently unpublished research.

## 5.2 Ruthenium

Ruthenium κ$^1$*P* complex **26** and κ$^2$*P,N* complexes **25** and **27** were prepared according to the synthetic methods outlined in Chapter 4 (Sections 4.6.1 and 4.6.2, respectively) (Figure 5.1).

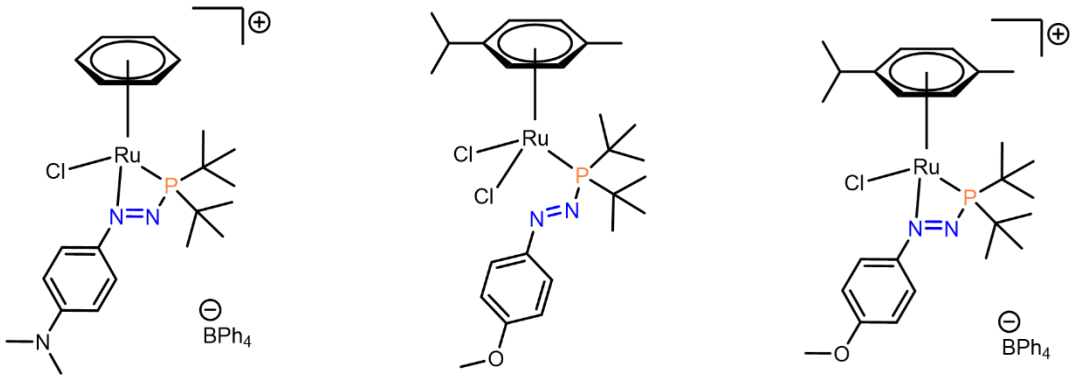


**25** **26** **27**

**Figure 5.1.** Structures of ruthenium complexes **25** – **27** tested as catalysts.

### 5.2.1 Transfer Hydrogenation of Acetophenone[42]

Mono- and bidentate complexes **26** and **27**, respectively, were explored as catalysts in the transfer hydrogenation of acetophenone to 1-phenylethanol. It was hypothesized that the azophosphine could act as a hybrid ligand to enable this process to occur in a base-free manner. To this end, the transfer hydrogenation of acetophenone using IPA as a hydrogen source was carried out using 1 mol% of **26** or **27** as catalyst (Figure 5.2A), and the reactions followed by FTIR spectroscopy using ReactIR. ReactIR allows for *in situ* monitoring of reactant and/or product, without the need for offline analysis.[43] The use of standard addition (see experimental) enabled quantification of acetophenone concentration and calculation of its conversion by following the isolated, characteristic peak at 1267 cm$^{-1}$ (C–C(O)–C) stretch). As the peaks in the FTIR spectra

assigned to 1-phenylethanol were not sufficiently resolved, reliable quantification of product yield was not possible by this method. $^{1}$H NMR spectroscopy instead provided an integration ratio of acetophenone: 1-phenylethanol in the reaction mixture to provide their relative % composition. Note this value does not equate to a % yield of 1-phenylethanol as it assumes selective conversion of acetophenone, although no other side-products were observed in the $^{1}$H NMR spectra.

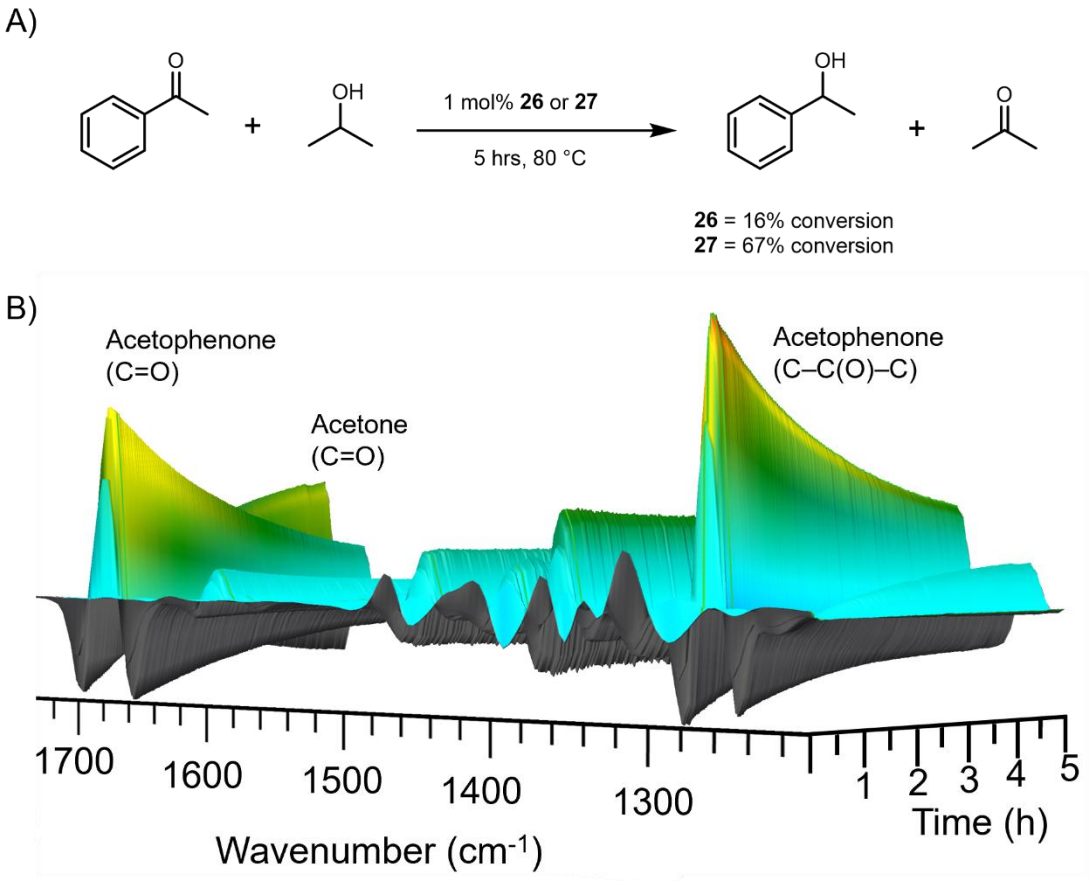


**Figure 5.2.** (A) Base-free transfer hydrogenation of acetophenone with catalysts **26** and **27**. (B) FTIR surface plot showing changes in IR spectra over time for reaction using **27** as catalyst.

When using $\kappa^{1}$*P* **26** as the catalyst the rection was sluggish, although it is noteworthy that some of the target 1-phenylethanol was observed despite the lack of external base in the reaction. The FTIR reaction monitoring for this reaction reproducibly showed

erratic spikes in the spectra at various timepoints, which precludes any detailed discussion of kinetics, but after 5 hours approximately 16% of the acetophenone had been converted. An aliquot of the reaction mixture taken after 16 hours was analysed by $^{1}$H NMR spectroscopy and showed a 79:21 ratio of acetophenone:1-phenylethanol. The experiment using $\kappa^{2}$*P,N* **27** as the catalyst was far more promising. The surface plot of **27** showed the consumption of acetophenone, represented by a decrease in the peak at 1681 cm$^{-1}$ (C=O stretch, acetophenone) and the tracked peak at 1267 cm$^{-1}$ with time (Figure 5.2B). The production of acetone as a by-product immediately after addition of **27** was observed, represented by the characteristic peak at 1710 cm$^{-1}$ (C=O stretch). After 5 h, the conversion of acetophenone was 67%. $^{1}$H NMR spectroscopic analysis after 16 h showed a relative composition of 11% acetophenone to 89% 1-phenylethanol. Further studies briefly explored the scope of the transfer hydrogenation with a second substrate and $H_2$ source. Benzaldehyde can be reduced to benzyl alcohol similarly to acetophenone (17% benzaldehyde to 83% benzyl alcohol). However, formic acid is not a suitable hydrogen source in place of IPA for this transfer hydrogenation chemistry, and 0% conversion for the reduction of acetophenone was observed in this case. These results provide a proof-of-concept that the azophosphine ligand is capable of promoting the base-free transfer hydrogenation of acetophenone and benzaldehyde, and that the $\kappa^{2}$*P,N* complex **27** is a more active catalyst than $\kappa^{1}$*P* complex **26**. We hypothesise that the hard N donor in **27** can detach from the Ru centre, creating a vacant coordination site for binding of the substrate during the catalytic cycle. Further work using analysis and quantification by GC-MS would provide kinetic data and a product yield from which turnover numbers (TON) and turnover frequencies (TOF) could be calculated, in addition to optimisation of catalyst loading

and reaction conditions. Subtle differences to the electronics of azophosphines by modulating the *p*-substituent on the *N*-aryl group have major implications on their ligand properties, as discussed in Chapter 4 (Section 4.2.2). An examination as to whether these implications on ligand properties are extended to influencing conversion rates would be an insightful addition to this proof-of-concept study.

### 5.2.2 Oxidation of Styrene

The oxidation of styrene to benzaldehyde using $NaIO_4$ as an oxygen source was carried out using 1 and 5 mol% of $\kappa^1$*P* complex **26** and $\kappa^2$*P,N* complex **27** as the catalyst (Scheme 5.8), and the reactions followed by $^1$H NMR spectroscopy.

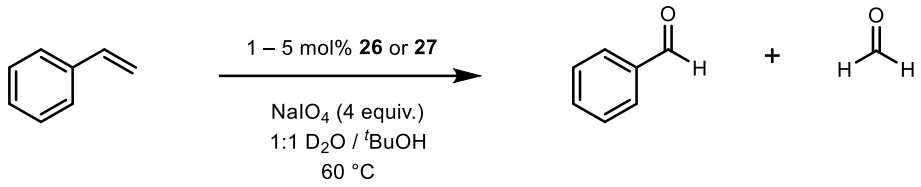


**Scheme 5.8.** Oxidation of styrene to benzaldehyde with catalysts **26** and **27**. Based on a literature procedure reported by Friedrich and co-workers.[22]

Aliquots of the reaction mixtures taken 2 h after addition of 5 mol% of **26** or **27** and $NaIO_4$ showed full consumption of styrene and the appearance of a characteristic aldehyde signal at 9.99 ppm in the corresponding $^1$H NMR spectrum. Reducing the catalyst loading to 1 mol% maintained full consumption of styrene after 2 h and the appearance of a signal at 9.99 ppm in the $^1$H NMR spectrum (Figure 5.3). Repeating the reaction with no catalyst and addition of only $NaIO_4$ showed less than 1% conversion of styrene after 2 h (Table 5.1). Note full consumption of styrene does not equate to its full conversion to benzaldehyde as it assumes selective conversion, although no other side-products were observed in the $^1$H NMR spectra.

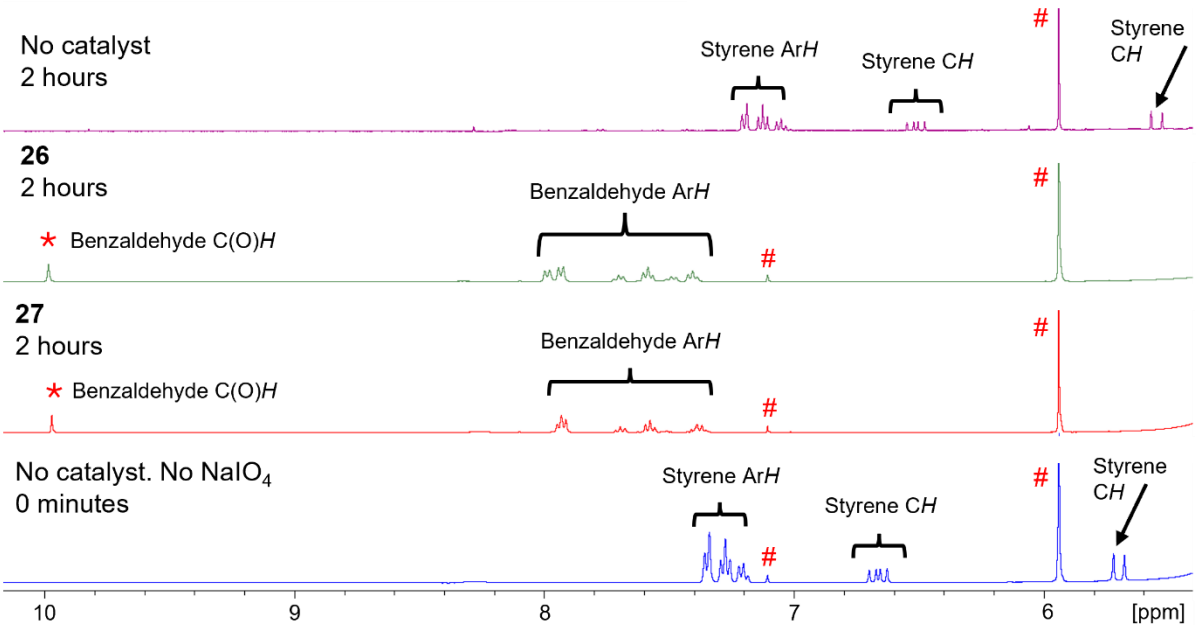


**Figure 5.3.** Stacked $^{1}$H NMR spectra of (bottom) styrene in 1:1 $D_2O$ / $^{t}$BuOH at time 0 minutes; (middle) full consumption of styrene after addition of catalyst **26** or **27** in 1 mol%; (top) consumption of styrene after addition of $NaIO_4$ only. * Singlet at 9.99 ppm assigned to benzaldehyde C(O)*H* proton; #, trimethoxybenzene and $CDCl_3$ in sealed capillary tube.

**Table 5.1.** Oxidation of styrene catalysed by Ru complexes **26** or **27**

| Entry | Catalyst | Loading (mol%) | $NaIO_4$ (equiv.) | Conversion (%) |
|---|---|---|---|---|
| 1 | **26** | 5 | 4 | 100 |
| 2[a] | **26** | 1 | 4 | 100 |
| 3 | **27** | 5 | 4 | 100 |
| 4[a] | **27** | 1 | 4 | 100 |
| 5[b] | - | - | 4 | < 1 |
| 6[c] | **26** | 5 | - | 0 |
| 7[c] | **27** | 5 | - | 0 |

Conditions: styrene, 0.25 mmol (0.25 M in 1:1 $H_2O$ / $^{t}$BuOH); catalyst, 5 mol%; $NaIO_4$, 1.0 mmol; styrene/$NaIO_4$/Ru(II) cat. = 20:80:1; 60 °C. [a] catalyst, 1 mol%; styrene/$NaIO_4$/Ru(II) cat. = 100:400:1. [b] no catalyst. [c] no $NaIO_4$.

Collection of kinetic data using ReactIR was not possible due to the mixed-phase reaction mixture that interfered with the absorbance measured by the ATR crystal. Similarly, preparing the reactions on an NMR scale for collection of kinetic data was

not possible due to the mixed-phase reaction mixture that required filtration through a silica plug prior to analysis by NMR spectroscopy. Trimethoxybenzene in a sealed capillary within each NMR tube was used to calibrate the spectra. The conversions observed are comparable to those reported by Friedrich and co-workers in which over 90% conversion was obtained after 1 – 3 h, depending on ruthenium catalyst.[22] Quantitative yields of benzaldehyde, obtained after 30 min, have been reported, albeit with a different solvent system.[21] However, comparison of **26** and **27** with other ruthenium catalysts reveal they performed better as lower conversions (23%) and longer reaction times (24 h) have been obtained under the same reaction conditions.[44] $\kappa^1$*P* complex **26** and $\kappa^2$*P,N* complex **27** were both active as catalysts in the oxidation of styrene which is in contrast to the transfer hydrogenation of acetophenone, in which **27** was a more active catalyst than **26**. A proposed mechanism for the selective aldehyde formation involves the displacement of a chelating ligand by oxidative addition to form a $Ru(VI)(=O)_2$ species in the first step. Considering the oxidation of styrene uses excess $NaIO_4$ as an oxygen source, the oxidation of $\kappa^1$*P* **26** and concomitant displacement of ligand **12** and chloride can likely be assigned to the increased activity of the catalyst relative to that observed in the transfer hydrogenation which did not use a co-catalyst. Oxidation at the side chain of styrene can result in oxidative C=C cleavage to obtain benzaldehyde, or epoxidation to obtain styrene oxide.[45] Of the former, benzoic acid can be a side-product postulated to form by further reaction of benzaldehyde.[22] No evidence of epoxidation or formation of benzoic acid was observed in the $^1$H NMR spectra of the oxidation of styrene using **26** or **27** as catalyst.

Repeating the experiments and taking aliquots of the reaction mixture after 4 hours again observed no formation of benzoic acid as a side-product. The interference of trimethoxybenzene as an internal standard has precluded calculation of a product yield to determine TON and TOF and discussion of kinetic data. This can be readily rectified by screening for alternative internal standards, followed by quantitative NMR spectroscopy as a method of analysis. Testing a lower catalyst loading and larger substrate scope could be considered in future.

### 5.2.3 Diels-Alder Cycloaddition

A computational study by Lewis J. Oram (MSci student, Jupp group, University of Birmingham), in collaboration with the University of Bristol, modelled a selection of azophosphines using DFT calculations,[40] enabling them to be mapped onto the LKB-PP and LKB-Bid databases developed by Fey and co-workers that were discussed in section 5.1.3.[36,37] The methodology used was the same as that used by Fey and co-workers as these methods have been tried and tested to be robust, reliably capturing trends between ligands.[32,37,38,46] From building upon and utilising the many contributions to the LKBs, comparison of the properties of azophosphines to pre-mapped ligands was intended to predict potential applications in catalysis. For complete discussion of the methodology and results of the computational study the reader is referred to reference [40].

As discussed in Section 5.1.3, the prediction by the LKB of fluorophosphines as alternative ligands to triaryl phosphites for hydrocyanation gave catalysts with similar or superior activity to an analogous P(O-*o*-Tol)$_3$-Zn catalyst.[39] It was considered whether the successful prediction of a catalytic application of a ligand, by its close

proximity in ligand space to a catalytically-established ligand, was responsive to subtle changes in coordination environment.

Azophosphine **11** mapped onto the LKB-PP in proximity in ligand space to the electron-poor bis(pentafluorophenyl)-phosphine ligand (R)-BINOP-F (Figure 5.4).

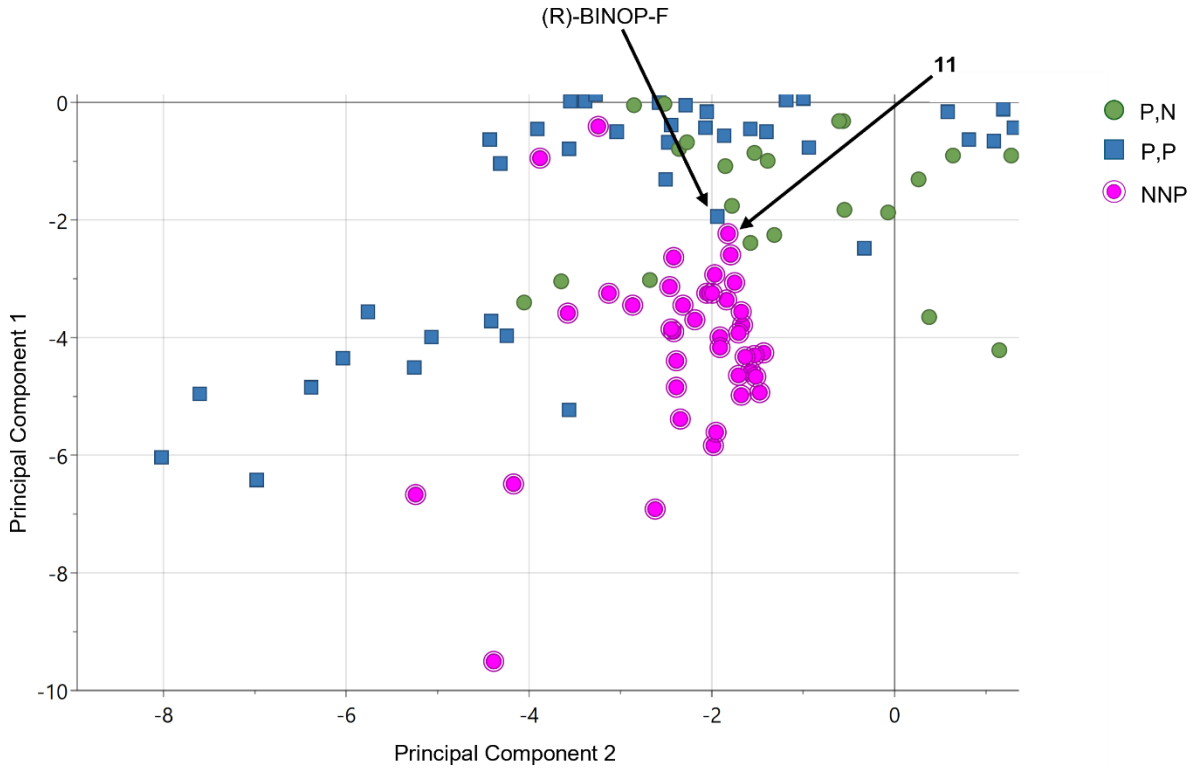


**Figure 5.4.** (A) LKB-PP showing mapped location of ligand **11** relative to (R)-BINOP-F. P,N and P,P are pre-mapped bidentate ligands, NNP represents the mapped location of a selection of azophosphines modelled using DFT calculations by Lewis Oram. Map adapted from reference [40].

The $\kappa^2$*P,P* Ru(II)(Cp) complex of (R)-BINOP-F has been found to activate methacrolein and catalyse the Diels-Alder reaction with cyclopentadiene to give the [4 + 2] cycloadduct in 92% yield, with an exo:endo diastereomeric ratio of 99:1, an enantioselectivity of 92% ee (exo) and 2*S* absolute configuration (Scheme 5.9).[47]

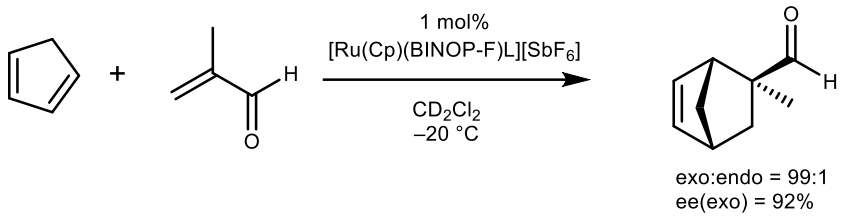


**Scheme 5.9.** Diels-Alder reaction of cyclopentadiene with methacrolein using [Ru(Cp)(BINOP-F)L][$SbF_6$] as the catalyst, reported by Kündig and co-workers.[47] L, acetone or $H_2O$.

Coordination of azophosphine **11** in a Ru(II)(benzene) framework of the form [Ru(benzene)(κ$^2$*P,N*-(**11**)Cl][$BPh_4$] (**25**) introduced subtle differences in coordination environment compared to the Ru(II)(Cp) framework for (R)-BINOP-F (Figure 5.5).

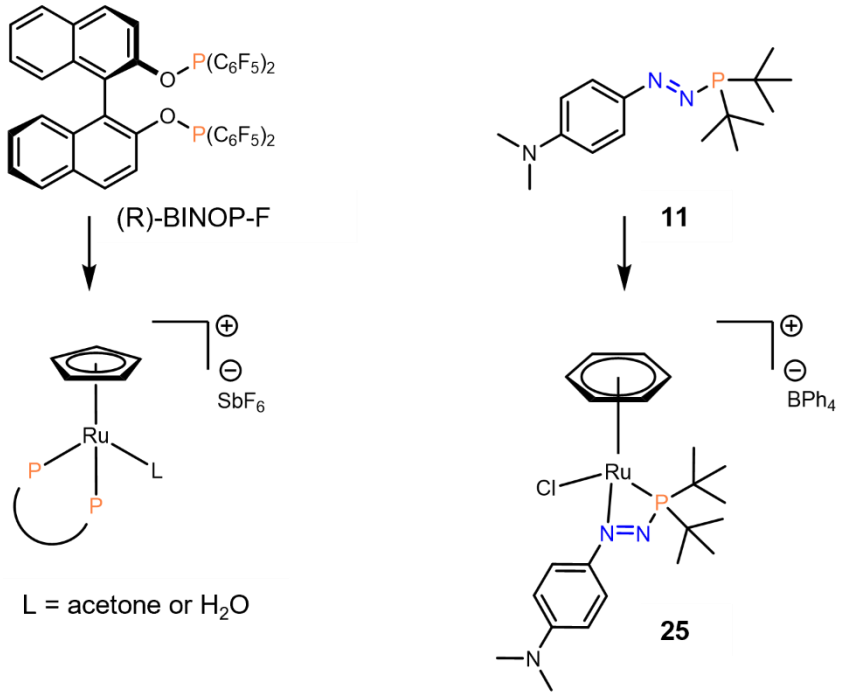


**Figure 5.5.** Structures of (R)-BINOP-F ligand and azophosphine **11**, and their respective Ru(II)(arene) complexes used as the catalysts in the Diels-Alder reaction of methacrolein with cyclopentadiene.

To this end, **25** was tested as a catalyst in the Diels-Alder reaction of methacrolein with cyclopentadiene, guided by LKB-PP (Scheme 5.10). The objective was to assess the activity of the catalyst, not to replicate the asymmetric catalysis.

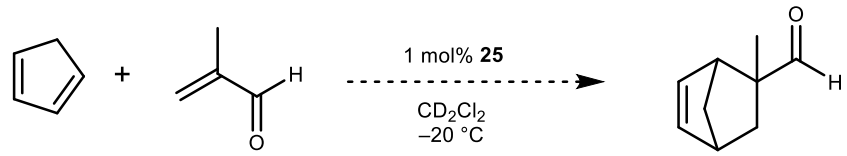


**Scheme 5.10.** Attempted Diels-Alder reaction using **25** as catalyst.

Ru complex **25** as catalyst was added to a pre-cooled solution of methacrolein and cyclopentadiene in $CD_2Cl_2$, with n-decane as an internal standard, and the reaction monitored at −20 °C by $^1$H NMR spectroscopy over 12 h. Analysis of the $^1$H NMR spectra before addition of **25** as catalyst and after 12 h showed no difference between spectra indicating no cycloaddition had occurred (Figure 5.6). Cyclopentadiene was used in the reaction in 1.2 equivalents therefore its presence in the $^1$H NMR spectrum would be expected if cycloaddition had occurred; however, no additional signals that can be assigned to the cycloadduct are observed.

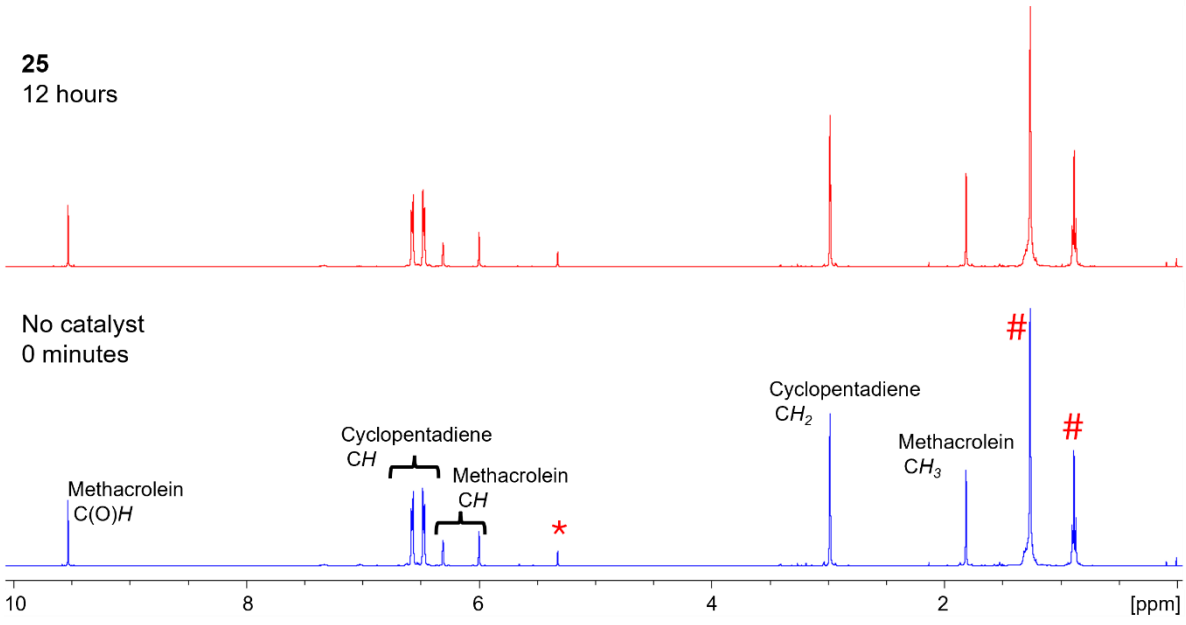


**Figure 5.6.** Stacked $^1$H NMR spectra of methacrolein and cyclopentadiene in $CD_2Cl_2$ at (bottom) time 0 minutes; (top) 12 hours after addition of **25** as catalyst. *, residual $CDHCl_2$; #, n-decane (jnternal standard).

Disappointingly, azophosphine **11** when $\kappa^2$*P,N* coordinated in a Ru(II)(benzene) framework gives complexes with no catalytic activity in the Diels-Alder reaction of methacrolein with cyclopentadiene. It would be premature to take these data as a failed indication of how broadly the predictions of LKB-PP can be applied and formulate a discussion based on only this rudimentary evidence. When identifying azophosphine **11** as being in proximity in ligand space to the (R)-BINOP-F ligand, the metal framework the ligand is coordinated to when used in catalysis is not taken into account and, in the case of cationic complexes, neither is the counter anion. Fey and Durand note that the prediction of a 'best' catalyst for a given substrate remains a formidable challenge as few catalytic routes are mechanistically robust, nor are they fully mapped.[32] In the Diels-Alder reaction of methacrolein with cyclopentadiene, both the capping arene and the counter anion has been found to have an effect on the rate of catalysis.[48] An anion of smaller steric bulk interacted with the bound substrate and cationic catalyst retarding the substrate/product exchange, whereas when this proximity was not possible, due to increased steric bulk of the anion and/or arene, the rate of catalysis was faster. Another significant difference is that (R)-BINOP-F forms a nine-membered metallacycle upon coordination to ruthenium, in contrast to the four-membered metallacycle of **25**; however, these are inherent properties of the ligands that should influence its modelling when mapped onto the LKB-PP. Repeating the Diels-Alder reaction of methacrolein with cyclopentadiene using azophosphine **11** $\kappa^2$*P,N* coordinated to the same Ru(Cp)(L) framework (L = $H_2O$ or acetone) with $SbF_6^-$ as counter anion is first necessary, in addition to testing a ligand not mapped in proximity in ligand space to (R)-BINOP-F. Testing a wider range of ligands would also be prudent; however, at the time of writing, the other ligands which mapped in proximity

to existing and/or synthetically accessible azophosphines other than **11** were theoretical with no published application in catalysis.

## 5.3 Gold

Section 5.3.1 discusses research conducted by the author and an MSci student under my supervision (Ellen M. Tait) on the catalytic activity of gold κ$^1$*P* monomer **29** and μ*P,N* dimer **30**.[41] Section 5.3.2 discusses an active collaboration on the catalytic activity of **29** and **30** with the Davies group at the University of Birmingham using samples synthesised by the author.

### 5.3.1 Preliminary Investigation[41]

Au-azophosphine complexes **29** and **30** (Figure 5.7) were prepared according to the synthetic methods outlined in Chapter 4 (Sections 4.6.3 and 4.6.4, respectively). To benchmark the catalysis investigations, κ$^1$*P* complexes of JohnPhos–AuCl and $PPh_3$–AuCl, as two well-established Au(I) catalysts, were purchased or synthesised according to the literature, respectively (Figure 5.7).[49] JohnPhos–AuCl was chosen for its structural similarity to **29** and $PPh_3$–AuCl for its prevalence in Au(I) catalysis. For a full discussion of the project the reader is referred to reference [41]. Here, only the most pertinent results will be discussed.

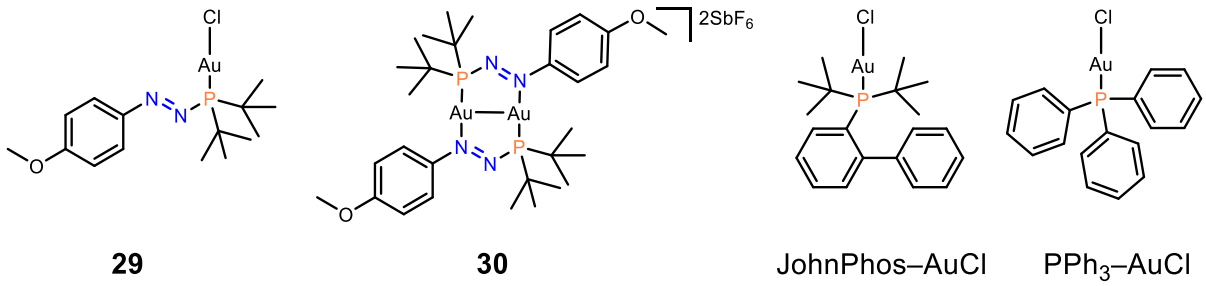


**Figure 5.7.** Structures of **29** and **30** tested for their catalytic activity and benchmarked against the well-established Au(I) catalysts JohnPhos–AuCl and $PPh_3$–AuCl.

During a series of reactions which featured **29** as the catalyst it was observed that addition of silver salt resulted in a colour change from reddish-pink to yellow. This colour change is indicative of dimer formation and is observed in the synthesis of **30** from **29**. It was considered how *in situ* dimer formation upon chloride abstraction from **29** could affect catalytic performance as it is known that trimerisation can deactivate Au(I) catalysts featuring 1,3-P,N ligands.[30,31] When tested in the cycloisomerisation of aryl propargyl ether (Scheme 5.11) it was found that **30** out-performed **29** as catalyst by obtaining product yields of 41 – 44% compared to 29 – 30%, respectively (Table 5.2). Addition of $AgNTf_2$ to the reaction mixture of **30** confounds these data.

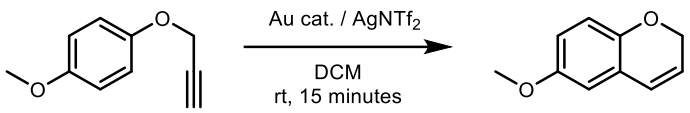


**Scheme 5.11.** Cycloisomerisation of aryl propargyl ether. Au cat. = **29** or **30.**

**Table 5.2.** Conversion (%) and product yields (%) obtained by **29** and **30** when applied as catalysts in the cycloisomerisation of aryl propargyl ether.

| Catalyst | Conversion | Product Yield |
|---|---|---|
| **29** | 59 | 29 |
| | 64 | 30 |
| **30** | 82 | 44 |
| | 81 | 41 |
| $PPh_3$–AuCl | 74 | 34 |
| | 75 | 35 |

Catalyst loading = 0.5 mol% for binuclear complex **30**.

When analysed by $^{31}P\{^1H\}$ NMR spectroscopy to assess whether the substrate disrupted the dimer no change in chemical shift was observed. Similarly, no change

was observed for a solution of **30** in DCM. In a solution of acetonitrile (MeCN), a more coordinating solvent, **30** exists as the MeCN-coordinated Au(κ$^1$*P*-**12**)MeCN monomer and is accompanied by a significant change in chemical shift from 108.1 ppm (**30**) to 126.6 ppm, comparable to the chemical shift of **29** (124.6 ppm) (Figure 5.8).

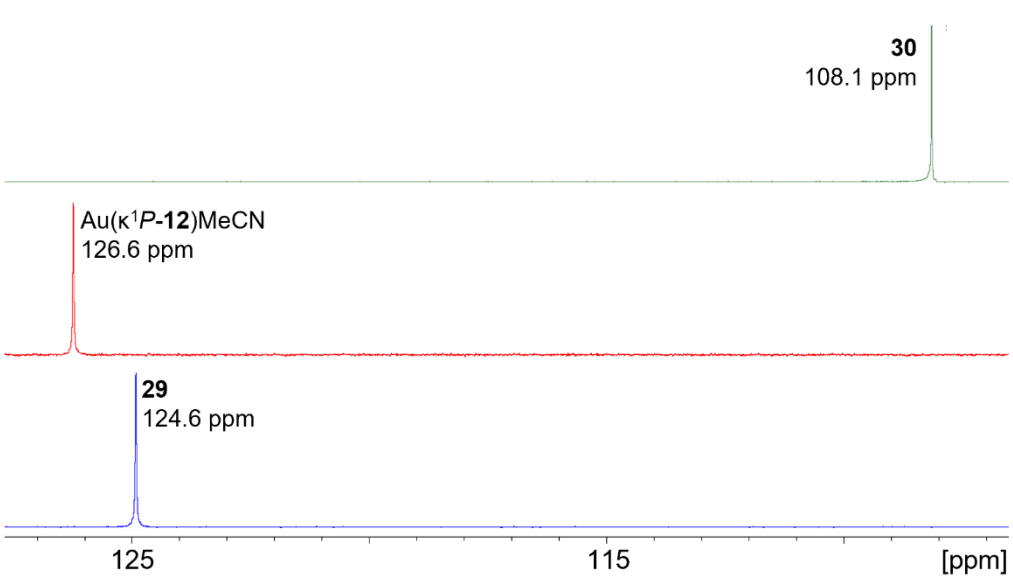


**Figure 5.8.** Stacked $^{31}P\{^1H\}$ NMR spectra of dimer **30** in $CD_2Cl_2$ (top) and $CD_3CN$ (middle), and monomer **29** in $CD_2Cl_2$ (bottom).

Analysis by $^{31}P\{^1H\}$ NMR spectroscopy and single-crystal X-ray diffraction found that removal of acetonitrile *in vacuo* regenerates dimer **30**. Generation of a catalytically active species in solution without the need for activation by addition of a silver salt is highly advantageous in catalysis.

These preliminary investigations found that **29** and **30** were catalytically competent, with a comparable performance to well-established catalysts. This prompted a more in-depth collaborative study and is discussed in the next section.

### 5.3.2 Collaborative Investigation

Au-azophosphine complexes **29** and **30** were prepared according to the synthetic methods outlined in Chapter 4 (Sections 4.6.3 and 4.6.4, respectively). To serve as a benchmark, $PPh_3$–AuCl was synthesised from literature procedures.[49] The reactions performed are shown in Scheme 5.12. Reactions A – D were run in duplicate for each catalyst with 1 mol% catalyst loading and activation by chloride abstraction from **29** and $PPh_3$–AuCl by addition of a silver salt. After 14 h, an aliquot of the reaction mixture was filtered through a silica plug and analysed by $^1H$ NMR spectroscopy. Conversions (%) and spectroscopic product yields (%) are tabulated in Table 5.3.

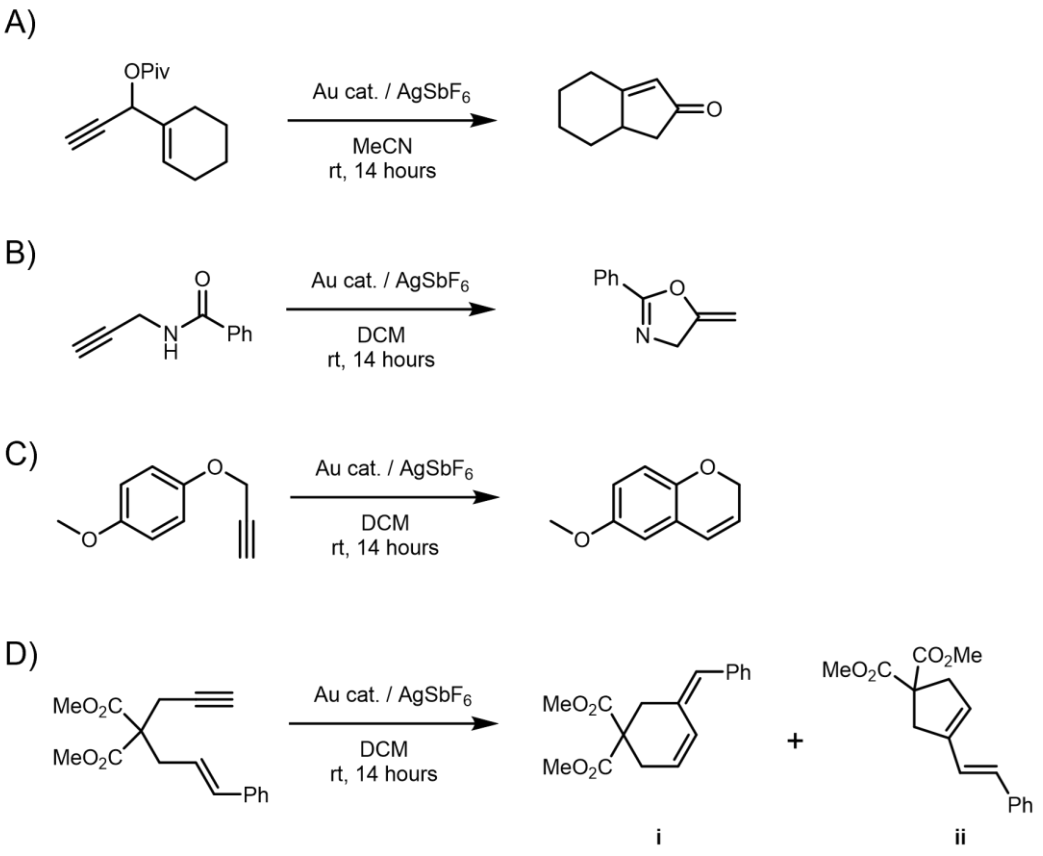


**Scheme 5.12.** Reactions tested using **29** and **30** as catalysts and $PPh_3$–AuCl as a benchmark. Conversion (%) and product yields (%) are tabulated in Table 5.3. Au cat. = **29**, **30** or $PPh_3$–AuCl (A – C), JohnPhos–AuCl (D). When Au cat. = **30** = no $AgSbF_6$.

**Table 5.3.** Conversion (%) and product yields (%) obtained by **29**, **30** and $PPh_3$–AuCl when applied as catalysts in reactions A – D, as depicted in Scheme 5.12.

| Reaction | Catalyst | Conversion | Product Yield |
|---|---|---|---|
| **A**[a] | **29** | 75 | 24 |
| | | 99 | 28 |
| | **30** | 100 | 27 |
| | | 100 | 26 |
| | $PPh_3$–AuCl | 73 | 33 |
| | | 80 | 33 |
| **B**[b] | **29** | 100 | 69 |
| | | 100 | 74 |
| | **30** | 92 | 50 |
| | | 82 | 43 |
| | $PPh_3$–AuCl | 100 | 50 |
| | | 100 | 60 |
| **C**[b] | **29** | 100 | 56 |
| | | 100 | 63 |
| | **30** | 100 | 63 |
| | | 100 | 68 |
| | $PPh_3$–AuCl | 100 | 55 |
| | | 100 | 62 |
| **D**[b] | **29** | 100 | 26 (i) 21 (ii) |
| | | 100 | 30 (i) 23 (ii) |
| | **30** | 100 | 20 (i) 11 (ii) |
| | | 100 | 21 (i) 18 (ii) |
| | JohnPhos–AuCl | 100 | 24 (i) 19 (ii) |
| | | 100 | 25 (i) 20 (ii) |

[a] MeCN as solvent; [b] DCM as solvent.

Overall, the performances of **29** and **30** as catalysts were very similar and comparable to that of $PPh_3$–AuCl. No significant variation in values is observed across reactions A – D. Reaction A was performed in MeCN whereas reactions B – D were performed in DCM. As discussed in section 5.3.1, analysis by $^{31}P\{^1H\}$ NMR spectroscopy had found that, in solutions of MeCN or DCM, **30** existed as the Au($\kappa^1$*P*-**12**)MeCN monomer or dimeric species, respectively. These data show that MeCN, as a coordinating solvent, is not imperative to elicit catalytic activity from **30**. However, in reaction A, although the product yields obtained by **29**, **30** and $PPh_3$–AuCl are similar, only **30** has a conversion of 100% after 14 hours. This could be due to a faster reactivity of **30**, as in MeCN it exists in the catalytically-active state, or incomplete halide abstraction from **29** and $PPh_3$–AuCl preserving residual catalyst in their inactive pro-catalyst states. In reaction B, performed in DCM, the opposite is seen in that only **30** has incomplete conversion after 14 hours. Again, this could be attributed to the rate of disruption of dimer **30** as, conversely to reaction A, disruption of the dimer is less influenced by the solvent and is more dependent on disruption by the substrate. For reaction C, **29**, **30** and $PPh_3$–AuCl all reached 100% conversion of substrate after 14 h, with **30** obtaining marginally higher product yields (63%, 68%) than **29** (56%, 63%) and $PPh_3$–AuCl (55%, 62%). In reaction D, product **i** was favoured over product **ii** for each catalyst with comparable **i**:**ii** ratios and 100% conversion of substrate; however, **30** obtained marginally lower yields (20:11%, 21:18%) than **29** (26:21%, 30:23%) and JohnPhos–AuCl (24:19%, 25:20%).

Reactions A – D provide proof-of-concept of the catalytic activity of Au-azophosphine complexes **29** and **30**, with no significant differences in performance to that of $PPh_3$–AuCl and Johnphos–AuCl as well-established Au(I) catalysts. Dimer **30** was not

rendered inactive when using DCM as solvent, although using a coordinating solvent such as MeCN may increase the rate of reaction. Pleasingly, this demonstrated that, for reactions A – D, the application of **30** as catalyst negates the use of a silver salt for *in situ* catalyst activation. The observation discussed in section 5.3.1 of a colour change from reddish-pink to yellow upon addition of $AgSbF_6$ to each reaction which featured **29** as catalyst prompted further investigation into the effect of *in situ* dimer formation on conversion and product yield. As discussed in Section 5.1.2, when employing Au(I) complexes featuring 1,3-P,N ligands as catalysts, *P*,*N*-Au(I) trimerisation has been attributed to deactivation of the catalyst. This is not the fate for **29** as these data show that dimer **30** obtains comparable conversions and product yields when applied as catalyst. Instead, these data suggest the mechanism of action of **29** goes *via in situ* formation of dimer **30**.

## 5.4 Conclusion

In this chapter it was demonstrated that Ru-azophosphine complex **26** is catalytically active in the transfer hydrogenation of acetophenone and benzaldehyde without the need for a strong base additive, and both **25** and **26** were active as catalysts in the oxidation of styrene to benzaldehyde with formation of no side-products. Guided by a computational study, LKB-PP suggested the Diels-Alder reaction of methacrolein with cyclopentadiene would be a viable reaction using **25** as catalyst. Reaction monitoring by $^1$H NMR spectroscopy provided no evidence that cycloaddition had occurred; however, this result is tentative and further testing is required. Investigations into the catalytic activity of Au-monomer **29** suggested *in situ* generation of the corresponding dimer **30** upon addition of a silver salt for activation of the catalyst. Further investigations demonstrated that **29** and **30** are both catalytically active in a range of

reactions and advantageously **30** obtains comparable conversions and yields without requiring *in situ* activation by a silver salt.

This chapter has discussed the first-time application of Ru-azophosphine and Au-azophosphine complexes in catalysis and marks the culmination of research carried out for this thesis in the synthesis, coordination chemistry and catalytic applications of azophosphines. Suggestions for further work in the research of azophosphines are provided in Chapter 6.

## 5.5 Experimental

Room temperature (RT) refers to reactions where no thermostatic control was applied and the temperature was recorded as 16–25 °C. Unless otherwise stated, overnight reactions refer to a period of 16 h.

Commercial reagents were purchased, suitably stored as specified by the supplier, and used as received, unless otherwise stated, from Sigma-Aldrich (acetophenone, 99%; benzaldehyde, >99%; JohnPhos, 97%; styrene, 99.9%), Thermoscientific (dicyclopentadiene, 95%; methacrolein, 95%) or Fisher Scientific (n-decane, 99+%; sodium periodate, 99.8%). Solvents were purchased and used as received, unless otherwise stated, from Sigma-Aldrich (acetonitrile-$d_3$, 99.8 atom % D, contains 0.03% (v/v) TMS; dichloromethane-$d_2$, 99.5 atom % D; deuterium oxide, 99.9 atom % D; isopropanol, 99.5%; tert-butanol, 99.0%).

All NMR spectra were collected on a Bruker 400 MHz AV_NEO Avance NMR Spectrometer. Chemical shifts are reported in ppm, coupling constants (*J*) are reported in Hz. Unless otherwise stated, $^1$H NMR spectra were referenced internally to the most up-field solvent peak.

### 5.5.1 Ruthenium Catalysis

Ruthenium $\kappa^1$*P* complex **26** and $\kappa^2$*P,N* complexes **25** and **27** were prepared according to the synthetic methods outlined in Chapter 4 (Sections 4.6.1 and 4.6.2, respectively).

#### Procedure for *in situ* ReactIR Measurements

Standard addition was used to quantify *in situ* FTIR reaction data according to literature procedures without the need for offline sampling and analysis.[43] For this, acetophenone

was added in two portions, allowing for five consecutive scans after each addition, and the average of these two calibrations was reported. The average temperature during the reactions was recorded by the FTIR probe. Changes in the IR spectra were monitored over time *via* the solvent abstraction feature of the iCIR software. To select an appropriate peak to monitor, IR spectra of acetophenone, acetone, and 1-phenylethanol in IPA were taken. Using the iCIR software, the reference spectra were stacked, and the most isolated peaks were selected for monitoring. The acetophenone was monitored using the height of the signal at 1267 $cm^{-1}$ relative to a two-point baseline (1284 and 1252 $cm^{-1}$). Due to a lack of isolated peaks for 1-phenylethanol, quantification of the formation of the product by FTIR was not possible. Therefore, an aliquot of the reaction was taken for analysis by $^{1}H$ NMR spectroscopy to confirm the presence and relative reaction composition of acetophenone to 1-phenylethanol.

**General Procedure for Transfer Hydrogenation (ReactIR) (GP14)**

A vial, equipped with stirrer bar and the ReactIR probe, was placed in an aluminium heating block, set at 80 °C, and charged with IPA (2.0 mL). Three consecutive spectra were collected after the addition of IPA. A stock solution of acetophenone (1 M in IPA) was added in two 0.5 mL portions (overall 1.0 mL, 1.0 mmol, 120 mg) to give 3.0 mL of solution. Five consecutive spectra were taken after both additions of stock acetophenone before **26** (1 mol%, 0.01 mmol, 6 mg) or **27** (1 mol%, 0.01 mmol, 9 mg) was added to initiate the reaction. Addition of the solid required the reaction vial to be briefly lowered from the FTIR probe; this FTIR data point was removed for clarity. Parafilm was secured around the vial and FTIR probe to minimise evaporation, and the reaction was stirred and heated at 80 °C for 5 h with spectra collected every 60 s until the rection appeared to end by visual analysis. After monitoring by FTIR had

ceased, the reaction was left stirring at 80 °C overnight (16 h) and an aliquot, filtered through Celite, was analysed by $^1$H NMR spectroscopy to obtain a composition ratio of acetophenone:1-phenylethanol.

$^1$H (400 MHz, $CDCl_3$): $\delta$ = 2.58 (s, 3H (substrate)), 1.43 (d, 3H (product)). For spectra see appendix.

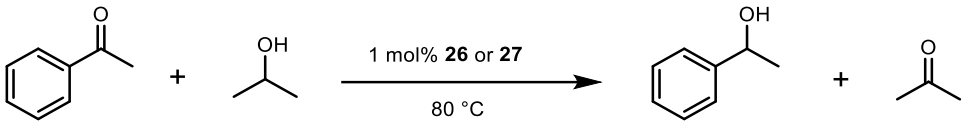


| **Catalyst** (1 mol%) | **Composition Ratio** (acetophenone:1-phenylethanol) |
|---|---|
| **26** | 79:21 |
| **27** | 11:89 |

**General Procedure for Transfer Hydrogenation (NMR Scale) (GP15)**

A pre-mixed solution of hydrogen source (IPA or formic acid, 0.5 mL) and substrate (acetophenone or benzaldehyde, 0.17 mmol, 1.0 equiv.) was added to a vial containing **27** (1 mol%, 1.7 μmol, 1.5 mg). The reaction vial was capped, para-filmed, and stirred at 80 °C in a sand bath overnight (16 h), after which an aliquot, filtered through Celite, was analysed by $^1$H NMR spectroscopy to obtain a composition ratio of product:substrate.

**Benzaldehyde as Substrate:** Following GP15 using benzaldehyde (17.0 μL, 0.17 mmol), IPA (0.5 mL) and **27** (1 mol%, 1.5 mg, 1.7 1.7 μmol). Composition ratio of benzaldehyde:benzyl alcohol was determined by $^1$H NMR spectroscopy.

$^1$H (400 MHz, $CDCl_3$): $\delta$ = 9.99 (s, 1H (substrate)), 4.64 (s, 2H (product)). For spectrum see appendix.

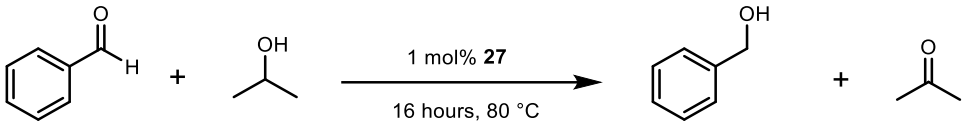


| Substrate | $H_2$ source | Composition Ratio (substrate:product) |
|---|---|---|
| Benzaldehyde | IPA | 17:83 |

**Formic Acid as Hydrogen Source:** Following GP15 using acetophenone (20 µL, 0.17 mmol), Formic acid (0.5 mL) and **27** (1 mol%, 1.5 mg, 1.7 µmol). Composition ratio of acetophenone:1-phenylethanol was determined by $^1$H NMR spectroscopy.

$^1$H (400 MHz, $CDCl_3$): $\delta$ = 2.58 (s, 3H (substrate)). For spectrum see appendix.

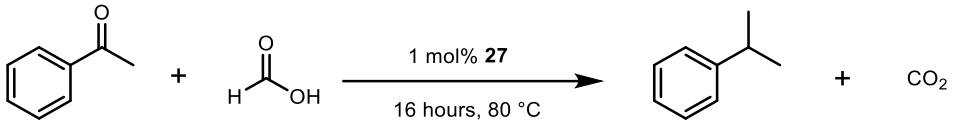


| Substrate | $H_2$ source | Composition Ratio (substrate:product) |
|---|---|---|
| Acetophenone | Formic acid | 100:0 |

**General Procedure for Oxidation of Styrene (GP16)**

A pre-mixed solution of styrene in 1:1 $D_2O$/$^t$BuOH (0.25 M, 3.0 mL, 1.0 equiv.) was added to a vial containing **26** (1-5 mol%) or **27** (1-5 mol%). To this stirring solution, $NaIO_4$ (4.0 equiv.) was added to initiate the reaction and the mixture stirred vigorously at 60 °C for 2 h, after which an aliquot, filtered through Celite, was analysed by $^1$H NMR spectroscopy to obtain a composition ratio of styrene:benzaldehyde.

$^1$H (400 MHz, $D_2O$): $\delta$ = 9.99 (s, 1H (product)), 5.70 (d, 1H (substrate)). For spectra see appendix.

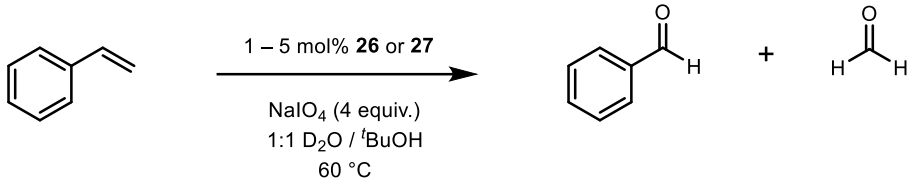


| Catalyst (1 and 5 mol%) | Composition Ratio (styrene:benzaldehyde) |
|---|---|
| **26** | 0:100 |
| **27** | 0:100 |

**General Procedure for Diels-Alder Cycloaddition (GP17)**

Methacrolein (40 µL, 0.3 mmol, 1 equiv.) and n-decane (0.1 mL, 0.3 mmol, 1 equiv.) were added to a vial with $CD_2Cl_2$ (0.5 mL) and cooled to –20 °C. To this, cold cyclopentadiene (50 µL, 0.4 mmol, 1.2 equiv.), prepared by cracking dicyclopentadiene (see below for details), was added and the solution stirred at –20 °C. To this stirring solution, **25** was added and the reaction mixture transferred to a pre-cooled NMR tube for reaction monitoring at –20 °C by $^1$H NMR spectroscopy.

$^1$H (400 MHz, $CD_2Cl_2$): $\delta$ = 9.53 (s, 1H (substrate)). For spectra see appendix.

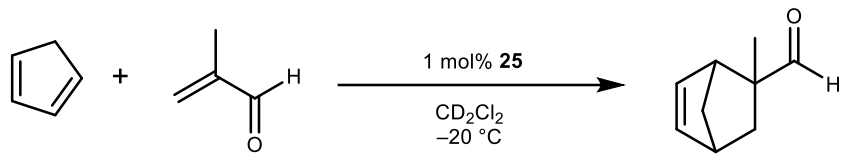


| Catalyst (1 and 5 mol%) | Composition Ratio (methacrolein:bicycloaldehyde) |
|---|---|
| **25** | 0:100 |

**General Procedure for Cracking Dicyclopentadiene (GP18)**

Using a short-path distillation, dicyclopentadiene (5 mL) was added to a round-bottomed flask equipped with a temperature probe and heated in a sand bath set to 160 °C. Cyclopentadiene started to distil when the temperature probe read 35 °C. The

receiving flask was placed in a cold bath maintained between –20 and –40 °C. Cold cyclopentadiene was then syringed into the reaction vial according to GP4.

### 5.5.2 Gold Catalysis

Au-azophosphine catalysts **29** and **30** were prepared according to the synthetic methods outlined in Chapter 4 (Sections 4.6.3 and 4.6.4, respectively). $PPh_3AuCl$ was prepared according to the literature.[49] Substrates were prepared according to the literature: reaction A;[50] reaction B;[51] reaction C;[52] reaction D.[53]

All experimental details relating to Section 5.3.1 can be found in the experimental section of reference [41].

**General Procedure for Collaborative Investigation (GP19)**

Stock solutions of substrate (0.2 M in *solvent*, 0.5 mL, 0.1 mmol), $PPh_3AuCl$ (4 mM in *solvent*, 0.25 mL, 1 µmol), **29** (4 mM in *solvent*, 0.25 mL, 1 µmol), **30** (1 mM in *solvent*, 0.5 mL, 0.5 µmol) and $AgSbF_6$ (4 mM in *solvent*, 0.25mL, 1 µmol) were prepared. Substrate and [Au] catalyst were added to a vial followed by $AgSbF_6$ if needed. The reaction was stirred overnight (14 h) at r.t. The reaction was diluted with DCM (2 mL) and passed through a pad of silica, eluting with DCM (8 mL). The solvent was evaporated under reduced pressure.

**Reaction A:** Following GP19 using pivolate (0.2 M, 0.5 mL, 0.1 mmol), $PPh_3AuCl$ (4 mM, 0.25 mL, 1 µmol), **29** (4 mM, 0.25 mL, 1 µmol), **30** (1 mM, 0.5 mL, 0.5 µmol) and $AgSbF_6$ (4 mM, 0.25mL, 1 µmol) in acetonitrile. Product yield was determined by $^1H$ NMR spectroscopy relative to an internal standard 1,2,4,5-tetramethylbenzene and with comparison to the literature $^1H$ NMR spectrum of the product.[53]

$^1$H (400 MHz, $CDCl_3$): $\delta$ = 5.84 (s, 1H (product)), 5.74 (s, 1H (substrate)). For spectra see appendix.

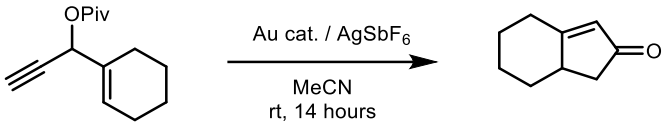


| Catalyst | Ag Salt | Yield (%)[a] | SM Recovery (%)[a] |
|---|---|---|---|
| **29** | $AgSbF_6$ | 26 | 13 |
| **30** | - | 27 | 0 |
| $PPh_3AuCl$ | $AgSbF_6$ | 33 | 24 |

[a] average of two runs

**Reaction B:** Following GP19 using propargyl amide (0.2 M, 0.5 mL, 0.1 mmol), $PPh_3AuCl$ (4 mM, 0.25 mL, 1 µmol), **29** (4 mM, 0.25 mL, 1 µmol), **30** (1 mM, 0.5 mL, 0.5 µmol) and $AgSbF_6$ (4 mM, 0.25mL, 1 µmol) in DCM. Product yield was determined by $^1$H NMR spectroscopy relative to an internal standard 1,2,4,5-tetramethylbenzene and with comparison to the literature $^1$H NMR spectrum of the product.[50]

$^1$H (400 MHz, $CDCl_3$): $\delta$ = 4.82 (q, *J* = 3.0 Hz, 2H (product)), 4.26 (dd, *J* = 5.2, 2.6 Hz, 2H (substrate)). For spectra see appendix.

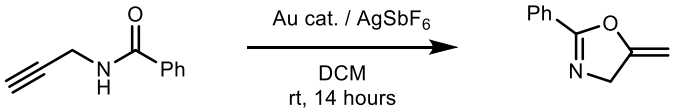


| Catalyst | Ag Salt | Yield (%)[a] | SM Recovery (%)[a] |
|---|---|---|---|
| **29** | $AgSbF_6$ | 72 | 0 |
| **30** | - | 47 | 13 |
| $PPh_3AuCl$ | $AgSbF_6$ | 55 | 0 |

[a] average of two runs

**Reaction C:** Following GP19 using propargyl ether (0.2 M, 0.5 mL, 0.1 mmol), $PPh_3AuCl$ (4 mM, 0.25 mL, 1 µmol), **29** (4 mM, 0.25 mL, 1 µmol), **30** (1 mM, 0.5 mL, 0.5 µmol) and $AgSbF_6$ (4 mM, 0.25mL, 1 µmol) in DCM. Product yield was determined by $^1H$ NMR spectroscopy relative to an internal standard 1,2,4,5-tetramethylbenzene and with comparison to the literature $^1H$ NMR spectrum of the product.[54]

$^1H$ (400 MHz, $CDCl_3$): $\delta$ = 4.75 (dd, *J* = 3.7, 1.8 Hz, 2H (product). For spectra see appendix.

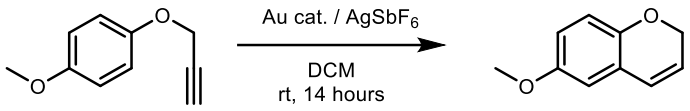


| Catalyst | Ag Salt | Yield (%)[a] | SM Recovery (%)[a] |
|---|---|---|---|
| **29** | $AgSbF_6$ | 60 | 0 |
| **30** | - | 68 | 0 |
| $PPh_3AuCl$ | $AgSbF_6$ | 59 | 0 |

[a] average of two runs

**Reaction D:** Stock solutions of enyne (0.2 M in DCM, 0.5 mL, 0.1 mmol), JohnPhosAuCl (4 mM in DCM, 0.25 mL, 1 µmol), **29** (4 mM in DCM, 0.25 mL, 1 µmol), **30** (1 mM in DCM, 0.5 mL, 0.5 µmol) and $AgSbF_6$ (4 mM in DCM, 0.25mL, 1 µmol) were prepared. The enyne substrate and [Au] catalyst were added to a vial containing 4Å molecular sieves, followed by $AgSbF_6$ if needed. The reaction was stirred overnight (14 h) at r.t. The reaction was diluted with DCM (2 mL) and passed through a pad of silica, eluting with DCM (8 mL). The solvent was evaporated under reduced pressure. Product yield was determined by $^1H$ NMR spectroscopy relative to an internal standard 1,2,4,5-tetramethylbenzene and with comparison to the literature $^1H$ NMR spectra of product i[55] and ii.[52]

$^1$H (400 MHz, $CDCl_3$): $\delta$ = 6.34 (s, 1H (Product **i**)), 5.72 (s, 1H (Product **ii**)), 6.01 (dt, *J* = 15.5, 7.6 Hz, 1H (substrate)). For spectra see appendix.

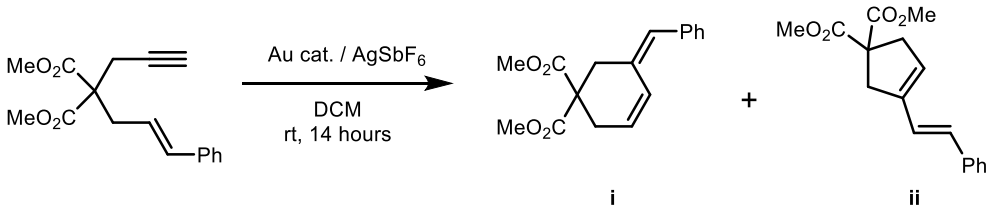


**i** **ii**

| Catalyst | Ag Salt | Yield i (%)[a] | Yield ii (%)[a] | SM Recovery (%)[a] |
|---|---|---|---|---|
| **29** | $AgSbF_6$ | 28 | 22 | 0 |
| **30** | - | 21 | 15 | 16 |
| JohnPhosAuCl | $AgSbF_6$ | 25 | 20 | 0 |

[a] average of two runs

## References


1 J. Hafeez, M. Bilal, N. Rasool, U. Hafeez, S. Adnan Ali Shah, S. Imran and Z. Amiruddin Zakaria, *Arab. J. Chem.*, 2022, **15**, 104165.

2 M. Bashir, I. A. Mantoo, F. Arjmand, S. Tabassum and I. Yousuf, *Coord. Chem. Rev.*, 2023, **487**, 215169.

3 M. K. Rong, F. Holtrop, J. C. Slootweg and K. Lammertsma, *Coord. Chem. Rev.*, 2019, **380**, 1–16.

4 G. Brieger and T. J. Nestrick, *Chem. Rev.*, 1974, **74**, 567–580.

5 U. Matteoli, P. Frediani, M. Bianchi, C. Botteghi and S. Gladiali, *J. Mol. Catal.*, 1981, **12**, 265–319.

6 D. Wang and D. Astruc, *Chem. Rev.*, 2015, **115**, 6621–6686.

7 G. Zassinovich, G. Mestroni and S. Giadiali, *Chem. Rev.*, 1992, **92**, 1051–1069.

8 H. Chai, T. Liu, Q. Wang and Z. Yu, *Organometallics*, 2015, **34**, 5278–5284.

9 F. Zeng and Z. Yu, *Organometallics*, 2008, **27**, 6025–6028.

10 Z. Fanlong and Y. Zhengkun, *Organometallics*, 2009, **28**, 1855–1862.

11 Q. Wang, H. Chai and Z. Yu, *Organometallics*, 2017, **36**, 3638–3644.

12 S. Hashiguchi, A. Fujii, J. Takehara, T. Ikariya and R. Noyori, *J. Am. Chem. Soc.*, 1995, **117**, 7562–7563.

13 V. Rautenstrauch, X. Hoang-Cong, R. Churlaud, K. Abdur-Rashid and R. H. Morris, *Chem. – Eur. J.*, 2003, **9**, 4954–4967.

14 C. M. Moore, B. Bark and N. K. Szymczak, *ACS Catal.*, 2016, **6**, 1981–1990.

15 P. R. Singh, A. Maji, O. Singh, U. P. Singh and K. Ghosh, *Appl. Organomet. Chem.*, 2020, **34**, e5615.

16 K. M. Waldie, K. R. Flajslik, E. McLoughlin, C. E. D. Chidsey and R. M. Waymouth, *J. Am. Chem. Soc.*, 2017, **139**, 738–748.

17 R. Noyori, M. Yamakawa and S. Hashiguchi, *J. Org. Chem.*, 2001, **66**, 7931–7944.

18 I. W. C. E. Arends, T. Kodama and R. A. Sheldon, *Ruthenium Catalysts and Fine Chemistry*, Springer-Verlag Berlin Heidelberg, 2004.

19 D. Yang and C. Zhang, *J. Org. Chem.*, 2001, **66**, 4814–4818.

20 Y. Zhang, H. Wang, S. Li, B. Lu, J. Zhao and Q. Cai, *Mol. Catal.*, 2021, **515**, 111940.

21 J. M. Gichumbi, H. B. Friedrich and B. Omondi, *J. Organomet. Chem.*, 2016, **808**, 87–96.

22 P. Daw, R. Petakamsetty, A. Sarbajna, S. Laha, R. Ramapanicker and J. K. Bera, *J. Am. Chem. Soc.*, 2014, **136**, 13987–13990.

23 A. Collado, D. J. Nelson and S. P. Nolan, *Chem. Rev.*, 2021, **121**, 8559–8612.

24 J. H. Teles, S. Brode and M. Chabanas, *Angew. Chem. Int. Ed.*, 1998, **37**, 1415–1418.

25 R. E. M. Brooner and R. A. Widenhoefer, *Angew. Chem. Int. Ed.*, 2013, **52**, 11714–11724.

26 D. Wang, R. Cai, S. Sharma, J. Jirak, S. K. Thummanapelli, N. G. Akhmedov, H. Zhang, X. Liu, J. L. Petersen and X. Shi, *J. Am. Chem. Soc.*, 2012, **134**, 9012–9019.

27 A. Franchino, M. Montesinos-Magraner and A. M. Echavarren, *Bull. Chem. Soc. Jpn*, 2021, **94**, 1099–1117.

28 W. Wang, C. L. Ji, K. Liu, C. G. Zhao, W. Li and J. Xie, *Chem. Soc. Rev.*, 2021, **50**, 1874–1912.

29 R. L. Lalonde, B. D. Sherry, E. J. Kang and F. D. Toste, *J. Am. Chem. Soc.*, 2007, **129**, 2452–2453.

30 C. Khin, A. S. K. Hashmi and F. Rominger, *Eur. J. Inorg. Chem.*, 2010, **2010**, 1063–1069.

31 C. Wetzel, P. C. Kunz, I. Thiel and B. Spingler, *Inorg. Chem.*, 2011, **50**, 7863–7870.

32 D. J. Durand and N. Fey, *Acc. Chem. Res.*, 2021, **54**, 837–848.

33 N. Fey, A. C. Tsipis, S. E. Harris, J. N. Harvey, A. G. Orpen and R. A. Mansson, *Chem. – Eur. J.*, 2006, **12**, 291–302.

34 J. Jover, N. Fey, J. N. Harvey, G. C. Lloyd-Jones, A. G. Orpen, G. J. J. Owen-Smith, P. Murray, D. R. J. Hose, R. Osborne and M. Purdie, *Organometallics*, 2010, **29**, 6245–6258.

35 N. Fey, M. F. Haddow, J. N. Harvey, C. L. McMullin and A. G. Orpen, *Dalton Trans.*, 2009, 8183–8196.

36 N. Fey, J. N. Harvey, G. C. Lloyd-Jones, P. Murray, A. G. Orpen, R. Osborne and M. Purdie, *Organometallics*, 2008, **27**, 1372–1383.

37 J. Jover, N. Fey, J. N. Harvey, G. C. Lloyd-Jones, A. G. Orpen, G. J. J. Owen-Smith, P. Murray, D. R. J. Hose, R. Osborne and M. Purdie, *Organometallics*, 2012, **31**, 5302–5306.

38 N. Fey, A. Koumi, A. V. Malkov, J. D. Moseley, B. N. Nguyen, S. N. G. Tyler and C. E. Willans, *Dalton Trans.*, 2020, **49**, 8169–8178.

39 N. Fey, M. Garland, J. P. Hopewell, C. L. McMullin, S. Mastroianni, A. G. Orpen and P. G. Pringle, *Angew. Chem. Int. Ed.*, 2012, **51**, 118–122.

40 L. J. Oram, Exploring the Ligand Properties of Azophosphines, University of Birmingham, 2024.

41 E. M. Tait, Exploring the Coordination and Catalytic Applications of Azophosphines, University of Birmingham, 2023.

42 E. J. Jordan, E. D. E. Calder, B. L. Greene, H. V. Adcock, L. Male, P. W. Davies and A. R. Jupp, *Organometallics*, 2024, **43**, 2674–2685.

43 G. Hutchinson, C. D. M. Welsh and J. Burés, *J. Org. Chem.*, 2021, **86**, 2012–2016.

44 M. Poyatos, J. A. Mata, E. Falomir, R. H. Crabtree and E. Peris, *Organometallics*, 2003, **22**, 1110–1114.

45 V. Kogan, M. M. Quintal and R. Neumann, *Org. Lett.*, 2005, **7**, 5039–5042.

46 J. Jover and N. Fey, *Dalton Trans.*, 2012, **42**, 172–181.

47 V. Alezra, G. Bernardinelli, C. Corminboeuf, U. Frey, E. P. Kündig, A. E. Merbach, C. M. Saudan, F. Viton and J. Weber, *J. Am. Chem. Soc.*, 2004, **126**, 4843–4853.

48 E. P. Kundig, C. M. Saudan, V. Alezra, F. Viton and G. Bernardinelli, *Angew. Chem. Int. Ed.*, 2001, **40**, 4481–4485.

49 D. Barik and R. S. Liu, *J. Org. Chem.*, 2022, **87**, 7097–7105.

50 S. Orbisaglia, B. Jacques, P. Braunstein, D. Hueber, P. Pale, A. Blanc and P. De Frémont, *Organometallics*, 2013, **32**, 4153–4164.

51 I. Volchkov and D. Lee, *J. Am. Chem. Soc.*, 2013, **135**, 5324–5327.

52 J. W. Faller and P. P. Fontaine, *J. Organomet. Chem.*, 2006, **691**, 1912–1918.

53 C. Bürki, A. Whyte, S. Arndt, A. S. K. Hashmi and M. Lautens, *Org. Lett.*, 2016, **18**, 5058–5061.

54 T. Danelzik, S. Joseph, C. Mück-Lichtenfeld, C. G. Daniliuc and O. García Mancheño, *Org. Lett.*, 2022, **24**, 6105–6110.

55 C. Nieto-Oberhuber, M. P. Muñoz, S. López, E. Jiménez-Núñez, C. Nevado, E. Herrero-Gómez, M. Raducan and A. M. Echavarren, *Chem. – Eur. J.*, 2006, **12**, 1677–1693.

# CHAPTER 6

# Conclusions and Further Work

## 6.1 Conclusions

The research presented in this thesis explored azophosphines (N=N–P) as a heavier analogue of triazenes (N=N–N) which, at the time of commencement of research, had been scarcely explored in the literature. Broadly, the themes of research discussed have related to their synthesis, coordination chemistry and application in catalysis.

The development of a general synthetic route to azophosphine $MesN_2PR_2$ (R = phenyl, Ph and *t*-butyl, $^t$Bu), *via* the corresponding azophosphine-borane, was provided in Chapter 2. A comparison of the stability and fundamental structure of $MesN_2PR_2$ found that the *P*-aryl azophosphine was significantly less stable than the *P*-alkyl analogue and could be attributed to homolytic cleavage of the P–N bond. Based on this finding, and using the same general synthetic route, the library of azophosphines was expanded in Chapter 3 by maintaining $^t$Bu as the P substituent and introduced versatility at the *para*-position of the N-aryl substituent with the general formula *p*-$(Z)C_6H_4N_2P^tBu_2$. Systematically modulating Z to span the electron-donating to electron-withdrawing range (Z = $NMe_2$, OMe, Me, H, F, $CF_3$) found structural trends in single-crystal X-ray diffraction, spectroscopic and computational studies. Significantly, the pyramidal structure at phosphorus, and availability of its lone pair, was confirmed by single-crystal X-ray diffraction data, highlighting the viable application of azophosphines as ligands. In general, azophosphines were found to be relatively weak phosphine donors, and that within this chemical space it was possible to fine-tune the donor properties by varying the Z group.

The coordination chemistry of azophosphines was discussed in Chapter 4. Selective monodentate $\kappa^1P$ and controlled bidentate $\kappa^2P,N$ coordination to a Ru(II)(arene)

framework was demonstrated, in stark contrast to the triazene analogues. The effect of Z on the donor properties of azophosphines was found to extend to their ability to act as a competent $\kappa^2$*P,N* ligand, where the stronger donors afforded $\kappa^2$*P,N* coordination more cleanly. Steric bulk in the *ortho*-positions of the *N*-aryl group of azophosphines inhibited N coordination to Ru required to form a bidentate complex. When coordinated to Au(I), selective $\kappa^1$*P* and controlled μ*P,N* coordination was demonstrated to give monomeric and dimeric complexes, respectively. Ultimately, the replacement of the tri-coordinate nitrogen centre in triazenes with a phosphorus atom to yield azophosphines is of dramatic consequence to the ligand properties. Azophosphines can be considered a new member of the family of 1,3-P,N ligands that have a bridging N atom, rather than C atom, between the P and N sites.

The photo-switching properties of azophosphines, on account of its N=N azo group, were investigated in Chapters 2 – 4. No conclusive experimental data indicative of photoisomerisation were obtained, and a computational study, in collaboration with the Curchod group at the University of Bristol, found no viable pathway to photoisomerisation. The most compelling evidence of photo-switching was provided experimentally by $\kappa^1$*P* coordinated *p*-(OMe)$C_6H_4N_2P^tBu_2$ azophosphine to Au(I); however, further work is required to demonstrate and understand what photochemical and photophysical processes may be occurring.

Finally, the first-time application of Ru-azophosphine and Au-azophosphine complexes in catalysis was provided in Chapter 5. Pleasingly, Ru-azophosphine complexes were catalytically active in the transfer hydrogenation of acetophenone and benzaldehyde without the need for a strong base additive, and in the oxidation of styrene to benzaldehyde with formation of no side-products. Au-azophosphine monomer and

dimer were catalytically active in a range of reactions and advantageously the dimer obtained comparable conversions and yields without requiring activation by a silver salt.

## 6.2 Further Work

*Practical Solutions*

The general synthetic procedure to azophosphines provided in Chapter 2 goes *via* deprotection of the azophosphine-borane to the corresponding azophosphine using pyrrolidine as a borane-scavenging Lewis base. Full conversion from the azophosphine-borane to the azophosphine is achieved; however, removal of the pyrrolidine·$BH_3$ adduct requires filtration through a silica plug giving yields as low as 50% depending on the derivative of azophosphine. Scaling up the reaction can be cumbersome and time-consuming due to the filtration being performed in the glovebox. Attempts to circumvent the use of silica to remove the amine adduct were not successful – for example, cooling a hexane solution of the deprotection reaction mixture to precipitate pyrroldine·$BH_3$; removal *in vacuo* at ambient and slightly elevated temperatures; and substituting pyrrolidine for solid-supported piperazine. Due to the slight acidity of silica and the basicity of the azophosphines, decomposition could possibly be resolved by instead using alumina in the plugs, which is slightly basic. Other solid-supported amines could also be explored. Alternatively, it could be that the assumed air-sensitivity of azophosphines is tolerable to temporary exposure to air expediting the silica plug filtration and minimising the silica-azophosphine contact time thus reducing the decomposition. This work does not directly expand the knowledge of

azophosphines but benefits the researcher, in product yield and time, contributing to the continued and efficient research of azophosphines.

*Photo-switching Properties*

As concluded in Section 6.1, no conclusive evidence of the photo-switching properties of azophosphines – as an azophosphine-borane, azophosphine or when ligated to a Ru(II) or Au(I) centre – was obtained. Discussed in Chapter 4 (Section 4.3.2), irradiating L–Au–Cl monomer (L = $\kappa^1$*P* *p*-(OMe)$C_6H_4N_2P^tBu_2$) showed similarities to azobenzene, a well-established photo-switch, in the UV/Vis spectrum consistent with *trans* → *cis* isomerisation. These changes did not appear to be reversible; however, decomposition of the complex was not immediately obvious when analysed by $^{31}P\{^1H\}$ NMR spectroscopy. Certainly, the combination of experimental and computational data so far collected makes the photo-switching properties of azophosphines a high risk but high reward thread of research to pursue. It would, therefore, be prudent to repeat the experiments of Chapter 4 Section 4.3.2 with different conditions – for example, testing in different solvents and, when testing for decomposition of the complex by $^{31}P\{^1H\}$ NMR spectroscopy, increasing the irradiation time of the sample and spectral width of the spectrum. Based on these results, further experiments could employ a 2,6-dihalo derivative of the azophosphines as the analogous derivatives of azobenzene are known to increase the half-life of the *cis*-isomer.[1,2]

*Azophosphines as Ligands*

The combination of a soft P donor with a hard N donor provide rich coordination chemistry to azophosphines. Modulating the *para*-position of the N-aryl group can fine-tune the donor properties whilst steric bulk in the *ortho*-positions hinders access to

$\kappa^2$*P,N* coordination. Overall, P–$^t$Bu$_2$ azophosphines are relatively weak phosphine donors and the steric bulk of phosphine ligands can be proportional to their dissociation from a metal centre. As discussed in Chapter 4 (Section 4.2.3), a Tolman plot of electronic parameter ($\nu_{CO}$) against cone angle shows the $\nu_{CO}$ of PCy$_3$ and P$^t$Bu$_3$ are equal differing only in the cone angle of PCy$_3$, which is approximately 10° smaller than that of P$^t$Bu$_3$. Research within the Jupp group has found that the P–Cy$_2$ azophosphine MesN$_2$PCy$_2$ (Cy, cyclohexyl) can be synthesised *via* the general synthetic method provided in Chapter 2.[3] It is therefore plausible that this synthetic method could be used to synthesise a range of *p*-(Z)C$_6$H$_4$N$_2$PCy$_2$ azophosphines from which a simple examination of the P and N donor properties would be possible using the methods demonstrated in this thesis. Substituting the $^t$Bu groups for Cy groups maintains the electron-rich alkyl groups at P concomitantly reducing steric bulk, potentially reducing dissociation of the azophosphine from a metal centre and enhancing its stability towards hemilability (Scheme 6.1).

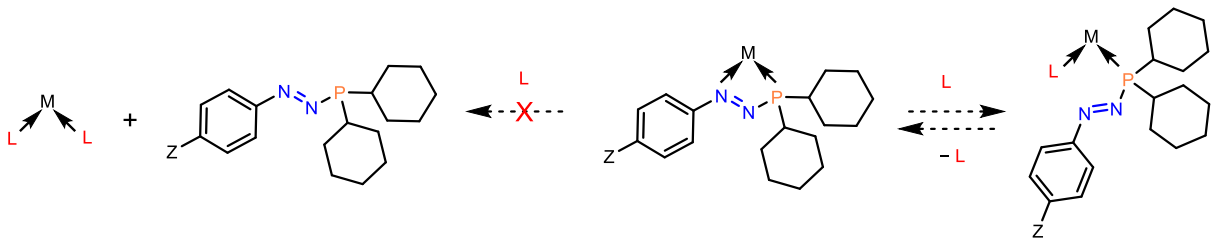


**Scheme 6.1.** Hypothesised selective displacement of N from a metal M centre by a competing ligand L.

The research towards this thesis focussed on azophosphines bearing the same P–R$_2$ substituents - that is, P–Ph$_2$ or P–$^t$Bu$_2$. Azophosphines bearing different P–RR' substituents would provide the opportunity to explore chiral at P azophosphines and the effects on coordination chemistry and asymmetric catalysis. The general synthetic method provided in Chapter 2 could be tested as a route to P–RR' azophosphines; however, a synthesis of the HPRR' phosphine or corresponding phosphine-borane

would first need to be developed. Alternatively, the anionic 'ate' derivative of azophosphines could be pursued. Deprotonation of RN=N–PHR' is a possible pathway to $[RN{=}N{-}PR']^-$. If using the general synthesis of azophosphines provided in Chapter 2, this would require the use of primary phosphines which have a reputation as being difficult to handle on account of their high sensitivity to oxidation and noxious character.

*Coordination Chemistry*

In addition to exploration of the coordination chemistry of RN=N–PRR' and $[RN{=}N{-}PR']^-$ derivatives of azophosphines, discussed above, the coordination chemistry of *p*-(R)$C_6H_4N_2P^tBu_2$ azophosphines with Pd(II) and Ir(III) could be explored, continuing the research introduced in Chapter 4 section 4.4. No evidence of $\kappa^2$*P,N* coordination to $PdCl_2$ was observed instead obtaining the bis-monodentate complex **32** and decomposition product **33** (Figure 6.1A and B, respectively)

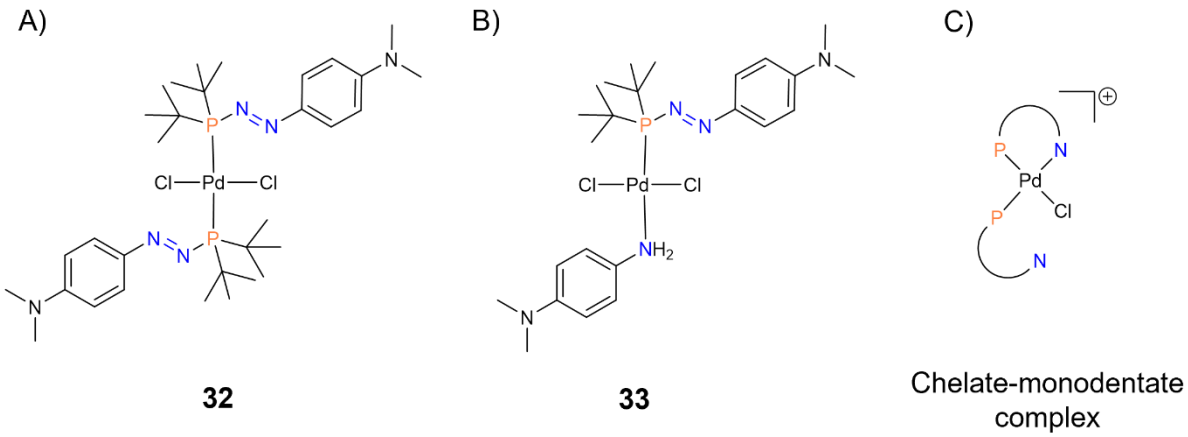


**32** **33**

**Figure 6.1.** (A) *trans*-Pd($\kappa^1$*P*-L)$_2Cl_2$ **32 (L =** *p*-($NMe_2$)$C_6H_4N_2P^tBu_2$); (B) decomposition product **33**; (C) chelate-monodentate coordination reported in the literature.

Consulting the literature suggested that $\kappa^2$*P,N* coordination occurs as a 'chelate-monodentate' complex for other 1,3-P,N ligands *via* the *cis*-Pd($\kappa^1$*P*-L)$_2Cl_2$ complex (L = $PPh_2Py$) (Figure 6.1C). In Chapter 4 Section 4.4.2, it was proposed that upon 'chelate-

monodentate' coordination of an azophosphine, the shorter covalent radius of the central nitrogen would give a distorted square-planar geometry with a P–Pd–N bond angle that was strongly deviated from 90°. Combined with the steric bulk of P–$^{t}$Bu$_2$, which would inhibit the prerequisite *cis*-isomer of **32**, this may preclude κ$^2$*P,N* coordination and be implicated in the formation of **33**. This 'chelate-monodentate' mechanism could be explored further starting with a series of variable temperature NMR experiments, providing valuable insight into potential decomposition pathways.

*Catalysis*

Chapter 5 presented the first-time application of Ru(II)- and Au(I)-azophosphine complexes as catalysts, demonstrating scope for further applications in catalysis. This could be in the form of reaction and substrate scope or catalyst optimisation. Iridium complexes are proven to be very effective catalysts.[4,5] The Ir(III)-azophosphine complexes introduced in Chapter 4 Section 4.4.3 could be expanded and tested for their catalytic performance.

*Medicinal Applications*

This research in this thesis concluded by testing the application of the Ru(II) and Au(I)-azophosphine complexes, presented in Chapter 4, in catalysis (Chapter 5). Since the discovery of Pt-based cisplatin as an anticancer drug, transition metal complexes consisting of organic ligands have been studied extensively in the field of medicinal inorganic chemistry. Most recently, ruthenium[6,7] and gold[8] complexes have been prominent, demonstrating superior antineoplastic and antimetastatic properties, in addition to potential as drug delivery systems (Figure 6.2). Indeed, gold-based anti-arthritic therapeutics, such as aurothiomalate, aurothioglucose and auronofin, are

already being prescribed in the clinic. Previously, a collaboration with Dr Isolda Romero-Canelon in the School of Pharmacy at the University of Birmingham sought to investigate the anticancer properties of the Ru(II)-azophosphine complexes. Time and resource constraints hampered the progress of this project beyond preliminary experiments. Nevertheless, initiation of another collaborative investigation of the Ru(II)- and Au(I)-azophosphine complexes for their anticancer properties would provide an interesting research project with the potential to obtain exciting results.

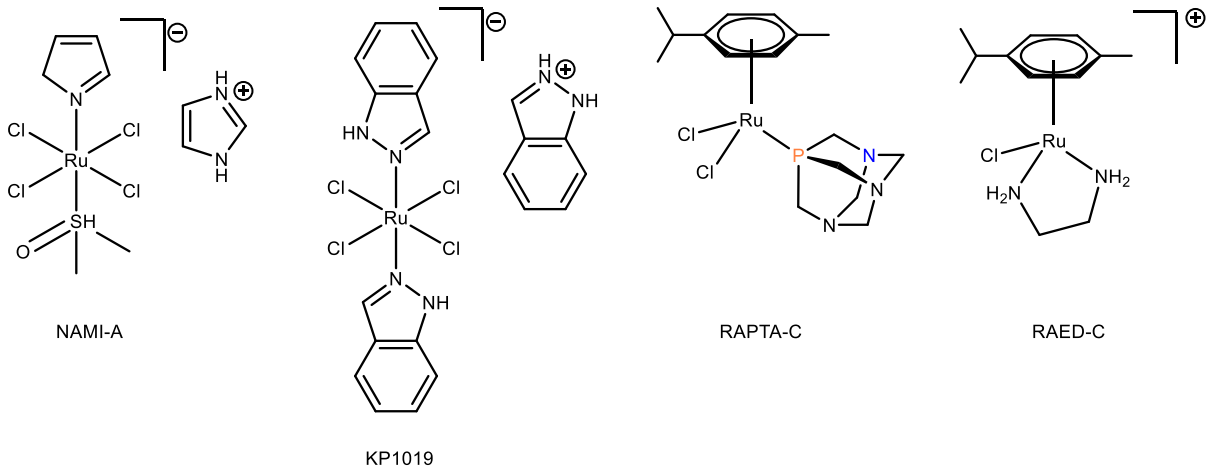


**Figure 6.2.** Structures of leading Ru-anticancer complexes.

## References


1 E. V. Brown and G. R. Granneman, *J. Am. Chem. Soc.*, 1975, **97**, 621–627.

2 C. Courtine, I. Hamouda, S. Pearson, L. Billon, P. Lavedan, S. Ladeira, J. C. Micheau, V. Pimienta, E. Nicol, N. Lauth de Viguerie and A. F. Mingotaud, *J. Colloid Interface Sci.*, 2023, **629**, 670–684.

3 E. D. E. Calder, L. Male and A. R. Jupp, *Dalton Trans.*, 2024, **53**, 15032–15039.

4 Q. Cheng, H. F. Tu, C. Zheng, J. P. Qu, G. Helmchen and S. L. You, *Chem. Rev.*, 2019, **119**, 1855–1969.

5 C. Wang, A. Schechter and L. Feng, *Nano Res. Energy*, 2023, **2**, e9120056–e9120056.

6 S. Y. Lee, C. Y. Kim and T. G. Nam, *Drug Des. Devel. Ther.*, 2020, **14**, 5375.

7 M. Bashir, I. A. Mantoo, F. Arjmand, S. Tabassum and I. Yousuf, *Coord. Chem. Rev.*, 2023, **487**, 215169.

8 G. Moreno-Alcántar, P. Picchetti and A. Casini, *Angew. Chem. Int. Ed.*, 2023, **62**, e202218000.